Durham E-Theses

Measurement of surface and sub-surface damage by x-ray scattering

Pape, Ian

Measurement of Surface and Sub-Surface Damage by X-Ray Scattering

by

Ian Pape

**A thesis submitted in partial fulfilment of the requirements
for the degree of Doctor Of Philosophy**

The University Of Durham

1997

Abstract

The study of surface and interface structure of thin film devices is becoming increasingly important in industrial applications today. In this thesis, the technique of grazing incidence x-ray scattering (GIXS) is developed and its validity examined for many different materials. In addition, the technique of Born wave analysis introduced by Lagally has been extended, showing that in certain cases surface roughness can be obtained without full simulations of the data.

GIXS measurements performed on float glass revealed that the density of the tin and air sides were 2.7 ± 1 and 2.3 ± 1 g/cc respectively across the entire ribbon. For all samples studied a surface layer on the order of a few nanometers was in evidence. When similar measurements were made on container glass it was seen to be layer free. In addition, excellent agreement was found between the roughness deduced from the simulations and the Born wave analysis. In all samples, the surface roughness deduced from the diffuse scatter was less than that from the specular, indicating that a vertical density gradient was present. When x-ray scattering measurements were performed on CVD layers deposited on glass it was noted that two sets of Yoneda wings existed in the diffuse scatter. From these it was concluded that lateral density variations existed in the SnO_2 layer which were on the order of 0.5mm in diameter. Furthermore, excellent specular simulations were obtained. These indicated that the control of both layer thickness and interface roughness between samples was on the Angstrom level.

Specular and diffuse x-ray scattering measurements were performed on Cu/Co multilayers grown on sapphire using a Nb buffer. Here the effect of anomalous dispersion was employed in order to highlight the scattering from the Cu/Co interfaces. From these data, Born wave analysis was used to characterise the roughness of the samples. It was found that little change took place for anneals of 45 minutes at temperatures up to $300^{\circ}C$. In addition, it would appear that the measured GMR bore no relationship to the component of uncorrelated roughness within the samples. GIXS measurements perfumed on Cu/Co multilayers grown on Si, using a Cu_3Si buffer, revealed an asymmetry in the diffuse

scatter, which was attributed to terracing within the layers. Simulations were obtained to the data using a slight modification of the fractal model for several scattering vectors with a single set of parameters. From this, a model of step bunching has been proposed which allows the diffuse scatter to be described using such a fractal surface.

Diffuse x-ray scattering studies performed on Al_2O_3, which had been ground in different ways, indicted that the surface density as measured from the Yoneda wings followed the bearing area as measured from optical techniques. Comparisons performed between these results and those from optical microscopy and surface acoustic wave techniques allowed a model to be proposed which was consistent with all the findings.

Finally, GIXS measurements were performed on GaAs which had been subjected to various polishing techniques. Simulations revealed that a nanometer scale surface layer was present on all samples. Born wave analysis was successfully applied to the diffuse scatter and the effect of surface layers on the deduced roughness was investigated. In addition, symmetric and asymmetric triple axis diffraction studies revealed that the distribution of strains was independent of the type of polishing used whereas the tilts were not. A model has been proposed in which the surface consists of unstrained mosaic blocks separated by cracks.

Acknowledgements

Over the past four years, I have worked with over one hundred people in collaboration with a dozen institutions. In consequence, it is only possible to thank those directly related to the material which has been included in this thesis. They are as follows.

Firstly, I must thank Prof. B.K. Tanner and Prof. D. Bloor for the provision of the excellent facilities of the Physics department. Also BEDE Scientific Instruments Ltd., DTI, Logitech Ltd., Morgan Matroc Ltd., Pilkingtons plc. and the Physics department for provision of funds during the time of my PhD. In addition to being the head of department, Prof. B.K. Tanner has also provided me with excellent supervision during the course of my PhD.

Next, thanks goes to all those that have worked with me on the LINK project, which was headed by Prof. D.K. Bowen and Mr. M. Robertson. Without the support of these people with regards to technical information, specimens and further measurements, much of the work presented in this thesis could not have been started. Especially I must thank Mr. M. Wormington, who wrote the specular and diffuse scatter simulation code. Without his work, most of the analysis of the data presented in this thesis would have remained qualitative.

As many of the people I have worked with have been experts in their field, much of the information learnt about the samples and processes has been from discussions rather than from the literature. As a result, there are many people that I am indebted to for 'bringing me up to speed' during my first six months. For the information on the manufacturing of glass, I must thank Dr. J. Bradshaw, Mr. R. Davies, Miss J. Greengrass, Dr. S.J. Hurst and Mr. N. Murphy. Whilst Dr. C. Hampson, Mr. A. Hey and Mr. C. Paine gave vital information regarding the ceramic specimens. Finally in this section, Mr. M. Robertson must be thanked for allowing me to take part in the Logitech training course on the polishing of GaAs.

List Of Publications Relating To This Thesis

Giant magnetoresistance and interface structure of Cu/Co multilayers grown by MBE on Si(111) substrates with copper silicide buffers, **I Pape**, T P A Hase, B K Tanner, H Laidler, C Emmerson, T Shen and B J Hickey, J. Magn. Mag. Mater. 156 (1996) 373-4

Evidence of grading at polished surfaces from grazing incidence X-ray scattering, M Wormington, **I Pape**, T P A Hase, B K Tanner and D K Bowen, Phil. Mag. Letts 74 (1996) 211-216

X-ray and magnetoresistance measurements of annealed Co/Cu multilayers, H Laidler, **I Pape**, C I Gregory, B J Hickey and B K Tanner, J Magn. Mag. Mater. 154 (1996) 165-174

Interface effect in grazing incidence X-ray scattering from transition metal magnetic multilayers, B K Tanner, M Wormington, T P A Hase and **I Pape**, Surface - X-ray, synchrotron and neutron investigations (Gordon and Breach) 12 (1996) 1189-1199: also published as Proc. Russian Academy of Sciences 3-4 (1996) 10-20

Triple axis X-ray diffraction study of polishing damage in III-V semiconductors, C D Moore, **I Pape** and B K Tanner, Il Nuovo Cimento (in press)

Grazing incidence X-ray measurements of interface roughness in sputtered Cu/Co multilayers, B K Tanner, D E Joyce, T P A Hase, **I Pape** and P J Grundy, Adv. X-ray Analysis 40 (1997) (in press).

Triple axis X-ray diffraction study of polishing damage in III-V semiconductors, C D Moore, **I Pape** and B K Tanner, ACTA Crystallographica, Vol. A52 (in press)

Declaration

I declare that this thesis is original and that no part of it has been submitted previously for a degree at any other University. All work presented in this thesis is my own unless otherwise stated. This thesis is within the word limit set by the examining body.

The samples analysed in this thesis were obtained from the following sources;

Chapter IV

Float glass 'Therm'	:	Pilkington plc Group Research, Pilkington Technology Centre, Ormskirk.
Container glass	:	Confidential

Chapter V

Brown Alumina	:	Morgan Matroc Ltd., Stourport-on-Severn.

Chapter VI

GaAs	:	MCP Wafer Technology Limited, Milton Keynes. Polished by Logitech Ltd., Glasgow.

Chapter VII

'Cu/Comultilayers grown on sapphire'	:	H. Laidler, Physics, University of Leeds.
'Cu/Co multilayers grown on silicon'	:	T. Shen, C. Emmerson, Physics, University of Leeds.

Contents

Chapter I

Review of selected non destructive surface sensitive techniques

1.1 Introduction

The study of interfaces and near surface structure is of vital importance in many areas of industry and technology today. In crystals, surfaces represent a break in the periodicity of the lattice and so often exhibit properties and lattice spacings quite different from those of the bulk [1,2]. The roughness on surfaces and buried interfaces is seen to effect the optical [3], electrical [4] and mechanical properties [5] of devices and the control of layer thickness is necessary for optimum performance in many applications [6]. As it is often necessary to perform further measurements after structural characterisation has occurred, any technique that is to be used should ideally be non-destructive in nature. In addition, such a technique, or combinations of techniques, should be sensitive to elemental composition, buried interfaces, roughness correlations and strain within the samples under investigation.

1.2 Electron probe techniques

Electron probe techniques [7] give several types of information on the surface, near surface and bulk structure of samples. In the scanning electron microscope (SEM), images of the surface can be obtained by looking at the secondary electron yield generated in the surface. As the primary electrons are impinging on the surface with an energy between 1 and 50 KeV the secondary electrons are generated in the top 500 Å of the sample. Contrast is obtained through shadowing, generated by roughness as the secondary electrons escape the material. As a result, the image produced can only ever be of the near surface region of the sample. The resolution of this technique is related to the spot size, which decreases for larger accelerating voltages. An upper limit on the accelerating voltage to be used is given by the escape depth of the secondary electrons. Beyond a certain voltage, the primary electrons penetrate so deep before ionising atoms

1

that the secondary electrons created do not have enough energy to escape. In consequence, the accelerating voltage is limited to a few tens of kilovolts, which relates to a beam of a couple of hundred Angstroms in diameter. This spot size limits the resolution of the machine and in this way the standard SEM technique is not able to probe surfaces features less than a few hundred Angstroms.

Elemental analysis is also possible using SEM, by studying the Auger and x-ray fluorescence yield, excited from the sample by the primary electron beam. In the case of Auger electrons, which are released from the atoms with little kinetic energy, the elemental information arises from the top 10 Å of the sample. In addition, the Auger yield is only significant for elements with atomic numbers less than 14, beyond which the relaxation process is dominated by fluorescence. X-ray fluorescence can be detected from much deeper inside the sample. Typically this can give elemental information on the top 1000 Å to 1 μm of the material.

Electrons do not require the sample to be crystalline for imaging, but need a high level of conductivity in order to stop charging effects, which distort the image. For non conducting specimens, this problem can be alleviated by coating the sample with a thin layer of gold. However, in certain circumstances, such as when further electrical measurements need to be made on semiconductors, this is not possible.

There are a two large drawbacks associated with the use of electrons as a means of characterising samples. Firstly, the whole experiment must be performed in high vacuum ($<1 \times 10^{-5}$ Torr) and as such corresponding evacuated chambers, bellows and load locks must be incorporated into the design. Secondly the technique cannot image interfaces that exist below the surface. One variation, which allows buried interfaces to be studied is cross sectional transmission electron microscopy. In this, a 1000 Å vertical slice of the sample is made, and a depth profile of the interface structure can be performed. An unfortunate consequence of this technique is that a laborious stage of 'back thinning' must take place before analysis can occur and as such the sample is destroyed.

If electron diffraction is performed, it is found that many waves are excited for each angle of incidence on the sample. This is due to the electrons having a very short wavelength, typically in the region of 0.03 Å for TEM. The resulting Ewald sphere has an extremely large radius of curvature and thus cuts through many points in reciprocal space. As a result many diffraction spots are produced and often a complicated dynamical interaction ensues.

1.3 Symmetric and asymmetric x-ray diffraction

In the case of x-rays, the wavelengths involved are much longer, typically on the order of 1 Å. As a result the number of diffracted beams produced for each incident wave is usually restricted to one [8,9]. This reduces the complexity of the analysis of the diffraction pattern dramatically, removing the need for dynamical analysis completely if the crystal is thin or highly dislocated. In addition, x-rays can be used outside of vacuum and do not produce charging effects. Unfortunately, focusing is difficult, and as such an average over the entire interface is produced.

For crystalline materials, the termination of the lattice is probed by the fall off of the crystal truncation rod (CTR) [10]. This arises due to the finite number of atomic planes being probed in the direction normal to the surface. As a result, the x-ray diffraction condition, which equates to a Fourier transform of the spatial frequencies in the sample is broadened. When the termination of the crystalline lattice is not so abrupt, fewer Fourier components are required to fit the step and the crystal truncation rod falls off more rapidly away from the Bragg peaks. Physically this can be interpreted as atoms which are above the plane, interfering destructively away from the Bragg condition.

As the crystal truncation rod arises by virtue of the termination of the crystal lattice, an amorphous overlayer present on the surface of the crystal will not be detected. If crystalline overlayers are present, their thickness can be determined from fringes which appear in the CTR [11]. These arise from the kinematical addition of diffracted waves that are produced from the bulk and overlayer respectively. If the epilayer is exactly

3

matched to the substrate, then its Bragg peak occurs at the same angle. However, in many cases, some degree of relaxation has taken place within the epilayer and its Bragg peak is shifted slightly [12]. Such relaxation in the plane of the surface can be detected by performing symmetric scans (figure 3.4, section 3.1.5) since the vertical and horizontal lattice parameters are related though Poisson's ratio. On a large number of occasions, the epilayer being studied is extremely thin and as such, in the symmetric geometry, the number of crystal planes being probed is very limited. In consequence, the width of the epilayer peak in the direction perpendicular to the surface ($\theta/2\theta$ direction) is extremely large and correspondingly, its intensity is low. Due to this lack of intensity, it is possible that the epilayer peak can be lost under the tails of the substrate Bragg peak and the general background, arising from thermal diffuse scattering in the bulk. A possible way to reduce the substrate Bragg peak relative to the epilayer is to choose a reflection which is strong for the layer but weak for the bulk [13]. However, this does not alleviate the problem of thermal diffuse scatter, which can only be reduced (at constant temperature) by changing the penetration depth of the x-rays [1] . This can be achieved by studying asymmetric reflections (section 3.1.9) arising from sets of planes inclined at an angle to the surface of the sample [14,15]. Such reflections, reduce dramatically the penetration depth of the x-rays and so decrease both the thermal diffuse scattering and the substrate Bragg peak intensity. In addition, such scans probe a component of the in-plane lattice parameter and as such measure a larger change as relaxation occurs.

1.4 Grazing incidence x-ray diffraction

In order to decrease the bulk contribution still further Grazing incidence diffraction (GID) can be employed [1,2,16,17]. In this arrangement, the reflecting planes lie perpendicular to the surface of the sample and the resulting scattering vector is in the plane of the surface. The incident wave impinges on the sample surface at an angle, α_i, which is close to the critical angle of total external reflection, and also at the Bragg angle with respect to the planes. The experimental arrangement is shown in figure 3.13. If α_i is less than the critical angle, an evanescent wave is produced which runs parallel to the surface of the sample [18]. This wave satisfies the Bragg condition of the planes within the sample and

4

diffraction occurs. As the evanescent wave is strongly damped into the material, the technique is extremely surface sensitive. Depth profiling can be achieved by changing the angle of incidence, α_i, with respect to the sample's surface. In this way depths can be probed ranging from 20 Å to 0.1 µm if the incident beam is highly collimated in the vertical direction. This requirement for good collimation is one reason why the majority of GID is performed at synchrotron sources. Another reason for the preferred use of synchrotron radiation is the diffracting volume of the sample is very low and thus the resulting signal is rather small. An advantage of this technique is that unlike the symmetric and asymmetric reflections, a large number of epilayer planes are involved in the diffraction process. As a result, the epilayer peak becomes much sharper and correspondingly easier to detect. Since the scattering vector is in the plane of the surface this technique is extremely sensitive to the in-plane lattice parameter of the epilayer. In addition, the surface streak (CTR) is oriented perpendicular to the direction of relaxation of the epilayer in reciprocal space, so reducing the effect of the substrate still further. When this is combined with the increased signal to noise over other diffraction methods in the thin films regime, this produces a technique which is sensitive to even the smallest degrees of epilayer relaxation.

1.5 X-ray reflectivity

Another grazing incidence technique is that of x-ray reflectivity (section 3.2) [19,20]. This is sensitive to the variations in the electron density normal to the surface within the sample and so probes the interface structure of the layers deposited on the substrate. Apart from some very special cases, where the GID condition is satisfied [21] or the lattice parameter of the crystal is extremely large, the modelling of the scatter is identical whether the sample is crystalline, polycrystalline or amorphous in nature. If roughness is present on these interfaces, x-rays are scattered out of the reflected beam and diffuse scatter is produced. Simulations of this diffuse scatter can yield information not only on the degree of roughness, but also the correlations that exist within the roughness on and between interfaces.

1.6 Neutron reflectivity

Reflectivity can also be performed at neutron sources [22,23]. In neutron reflectivity increased contrast can be sometimes obtained by deuterating the constituent atoms of one of the layers. The analogy in the x-ray case is anomalous dispersion [24]. This produces much lower levels of contrast, but can be used on all elements. The fluxes that are available at neutron sources are typically in the order of 10^6 c.p.s. which is between two and five orders of magnitude lower than at synchrotrons. A significant advantage in using neutrons is that they are very much more penetrating than x-rays. In consequence, they lend themselves to experiments where reaction chambers are present and the beams must pass through windows in the experimental vessels. Another advantage of using neutrons, once spin polarised, is that they are sensitive to the magnetisation of the layers within the samples. In consequence, they can yield information on the magnetic orientation of the layers. As an example, if a magnetic multilayer was in the ferromagnetic configuration then a Bragg peak would be observed corresponding to the structural (electron density) period within the sample. However, if the magnetic layers were aligned antiferromagnetically, then a second Bragg peak would be observed at half the angle corresponding to a repeat unit of twice the layer/spacer period [25].

In white beam neutron reflectivity, mainly produced by spallation sources, each point on the reflectivity curve is smeared out over a range of angles. As a result, the specular scatter is recorded using a position sensitive detector. The scattering vectors are determined from the angle with which the neutrons leave the sample and the time they take to reach the detector. Area detectors are used to record the diffuse scatter out of plane. This technique, is similar to that used by Metzger in x-ray reflectivity which is reviewed in section 3.2.16. Unfortunately, a consequence of the lower intensities arising from neutron sources is the diffuse scatter associated with the roughness of the interfaces is extremely small.

1.7 The study of diffuse scatter arising in grazing incidence techniques

The problem of low intensities of diffuse scatter is also present when using the techniques of symmetric diffraction, asymmetric diffraction and GID to study in-plane roughness correlations. In all these cases the low intensity arises since the x-rays are being scattered out of a Bragg peak, which is already two or three orders of magnitude less intense than the incident beam. However, even though the intensities are small, work has been carried out on the modelling of the diffuse scatter [26] produce by correlations in the interface roughness in all these techniques. Such simulations show the same features as seen in GIXS, but to our knowledge have never been observed to exist with any degree of certainty.

1.8 Conclusion

In conclusion, the technique which is most suitable is related to the type of information that is wanted from the sample. For bulk single crystals, a combination of symmetric and asymmetric reflections will characterise the in and out of plane lattice parameters. In addition, if the range of q being probed is large enough, they will provide information on the sharpness of truncation of the crystal lattice. For thin layers on substrates, again symmetric and asymmetric reflections can be used to probe the degree of relaxation which has taken place. However, for extremely small relaxations the layer peak cannot be distinguished from the bulk even with the correct choice of reflection. This problem can be solved using GID if high intensity sources are available. In this mode the bulk Bragg peak and thermal diffuse scattering are strongly suppressed relative to the epilayer peak. In addition depth profiling of the strain profile is possible. If information is required about interface roughness then the best technique to use is specular and diffuse reflectivity. This gives the advantage that the diffuse scatter is of much higher intensity than in the other techniques and is also sensitive to roughness of amorphous overlayers. One particular case exists where the use of CTR measurements are better. This is when crystalline layers are present over a micrometer in thickness and interference from the

7

bottom surface can only be achieved if the path length of the x-rays through the medium is reduced substantially.

Chapter II

Experimental techniques of x-ray scattering

2.1 X-ray reflectivity

2.1.1 Experimental configuration of station 2.3

Grazing incidence x-ray scattering measurements were performed using the two circle powder diffractometer on station 2.3 at the Synchrotron Radiation source (SRS) at Daresbury Laboratory [1,2]. Figure 2.1 shows a schematic diagram of the station when set up for grazing incidence reflectivity measurements. Sample axis (θ) and detector axis (φ) were optically encoded, permitting an accuracy of 0.72 and 0.36 arc seconds respectively. A water cooled, double bounce, Si 111 monochromator [3] was used to select the wavelength and gave a dispersion ($\Delta\lambda/\lambda$) of 1.5×10^{-4} at a wavelength of 1.4 Å. The dispersion, $\Delta\lambda/\lambda$, is given by:

$$\frac{\Delta\lambda}{\lambda} = \cot(\theta_B)\Delta\theta \qquad\qquad 2.1$$

where $\Delta\lambda$ is the wavelength spread in the beam, $\Delta\theta$ is the angular spread of the beam and θ_B is the Bragg angle of the reflecting planes. With incident beam slits after the monochromator 100 μm in height and 4 mm in width, this produced count rates of typically 10^8 c.p.s. at the sample. By the use of a thickness calibration gauge a precision of $\pm$ 0.1 μm was achieved on all slits.

The Si monochromator was used in the (+ -) non dispersive setting. Due to the relativistic nature of the electrons within the storage ring, a 'white' x-ray beam of vertical divergence approximately 200 arc seconds, tangential to the electrons orbit, was incident upon it [4]. When diffracted by this crystal, a beam of $\Delta\lambda/\lambda = 1.5 \times 10^{-4}$ (1.4Å) was emitted. As the x-rays passed the 100μm beam defining slits, a 100μm high beam of angular divergence 1 arc second was selected.

EDRa (lead encased)

analyser slits

scatter slits (lead)

detector axis

scatter slits

evacuated can

sample stage

Kapton foil

Slits

Slits

Beam intensity monitor

Si 111 monochromator

Slits

X-ray Beam
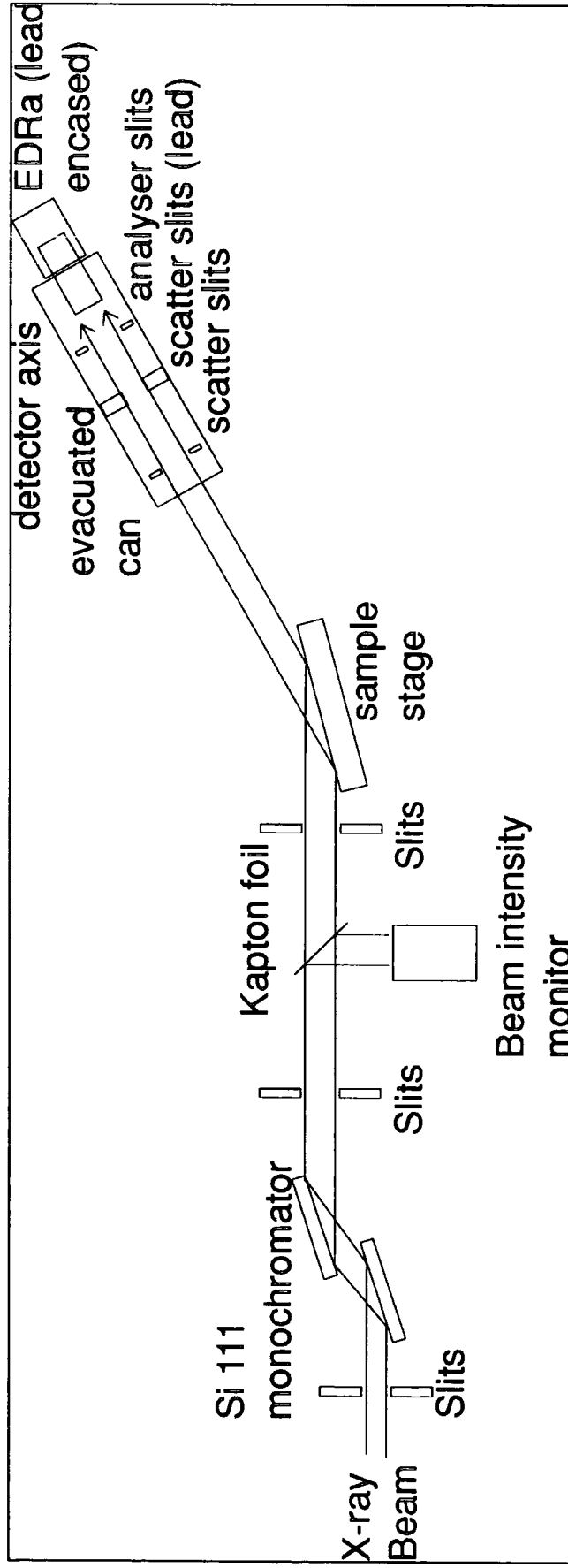
Fig 2.1

Configuration of station 2.3 at the Daresbury SRS

The monochromator was not offset for higher harmonic suppression. For this reason, contamination from higher harmonics coming from the Si 111 monochromator was present. However the lower intrinsic widths of these rocking curves significantly reduced their intensity. The strongest harmonic, the 333 reflection was calculated to have an integrated intensity a factor of 13 lower than the 111 fundamental (figure 2.2). This was then convolved with the synchrotron radiation spectrum ($\lambda_{333} = \lambda_{111}/3$) (figure 2.3) to give the true intensity of the harmonics to be between one and two orders of magnitude lower than the fundamental. Thus the higher harmonics gave a negligible contribution to reflectivity except in the very low angle region when an attenuator was present which absorbed preferentially the fundamental component of the beam.

As the beam defining slits were after the monochromator, varying the angular setting of the monochromator to change the wavelength did not significantly alter the position of the beam incident on the sample. Scanning the wavelength through its full range caused the beam position at the analyser slits to change less than 20 arc seconds. This produced a variation of the beam at the sample stage of ± 15 μm.

A further set of tungsten carbide slits, width 3 mm, was placed 450 mm after the beam defining slits. These served to remove any stray Laue reflections, or powder rings, that evaded the initial 100 μm beam defining slits.

The critical alignment of the rotation axis with the incident beam was achieved by optical alignment of the specimen holder with the rotation axis (± 25μm) and then displacing the whole diffractometer until the sample half-cut the beam (± 2μm). Subsequent height adjustments to accommodate any differences in specimen thickness were made with the sample holder translation only. Once the initial alignment had been achieved, changing of the samples was very straightforward. The large distance between the sample and the small source size produced a large projected lateral coherence length, which for typical sample angles was in the region of 100 μm.
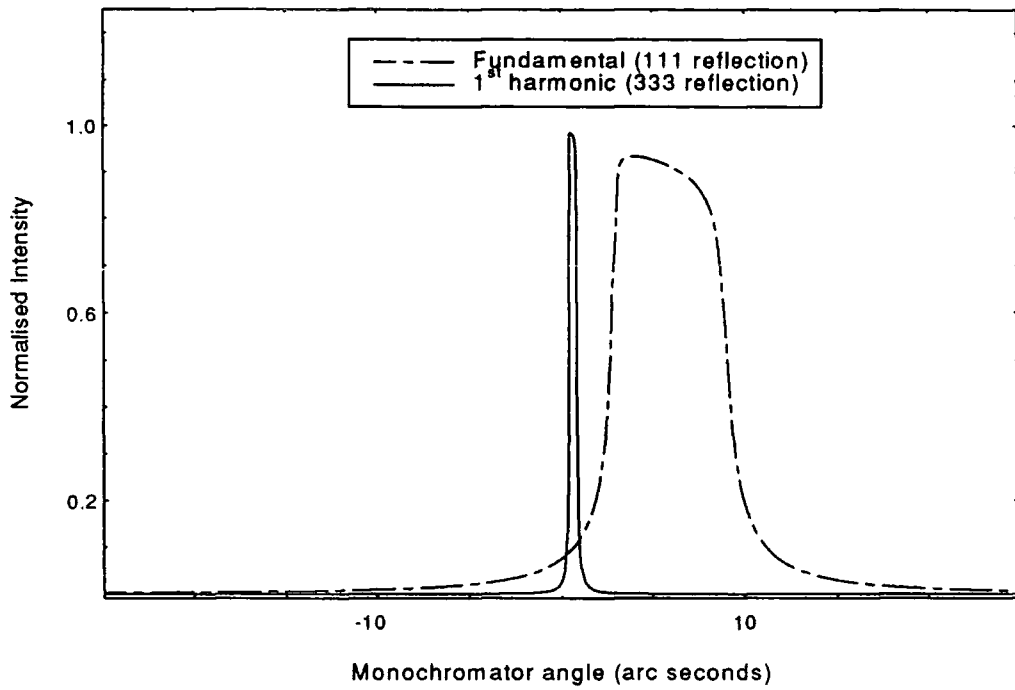
Figure 2.2   Fundamental (λ=1.4Å) and first harmonic (λ=0.47Å) reflections
from a Si 111 crystal.
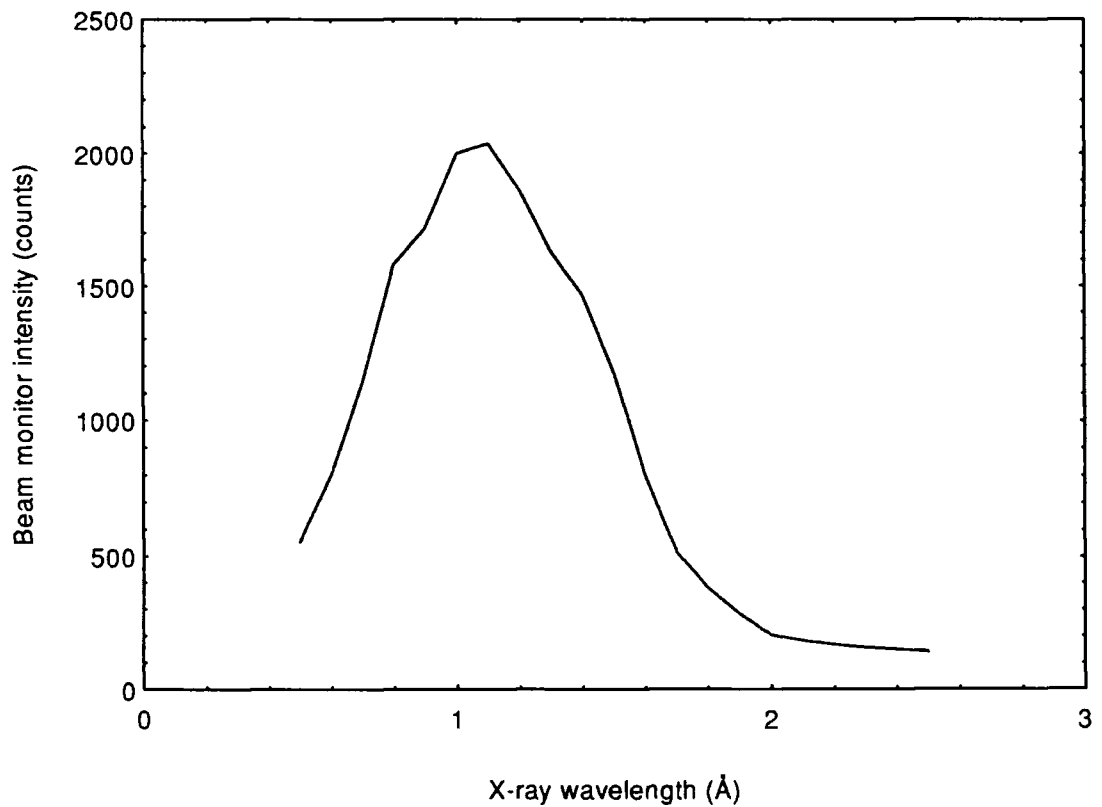
Figure 2.3 Synchrotron radiation spectrum for the S.R.S as measured from station 2.3

Analyser slits immediately in front of the detector were set to 100 μm, giving a (minimum) measured instrumental resolution function in transverse (specimen only) scan which was a Gaussian and of 15 arc seconds at full width half height maximum (FWHM). A further set of detector slits, width 1000 μm, was mounted on the detector arm closer to the sample in order to reduce scatter from the air path between the monochromator and the sample. The path between the two sets of detector slits was evacuated with an aluminium can, fitted with Kapton® windows, in order to reduce further the effect of air scatter. Two peaks of scatter at ± 4 to 5 degrees were initially observed due to the direct beam passing under or over 1000 μm slits and scattering off the inside of the vacuum can (figure 2.4a). These were eliminated by the introduction of lead shielding inside the can arranged so as to reduce the angular acceptance of the 100 μm slits to exclude any beam except that coming from directly behind the 1000 μm slits. Evidence for the origin of the increased scatter along with the effect of the introduction of the lead shielding is shown in figure 2.5. From this figure it is clear that even with the anti scatter slits completely closed the peak in the diffuse scatter is still present. For this reason the source of the noise must be arising from behind the front set of slits and thus the primary beam must be passing over or under their housing.

Finally, the detector and vacuum can were encased in a 1 mm thick lead sheet to reduce the background still further. With a BEDE scientific EDRa scintillation detector, which has an intrinsic background of 0.15 c.p.s. [5], the experimental background of 0.5 c.p.s. (fully optimised) was finally limited by scatter of the main beam within the air path in the hutch passing through both sets of detector slits. Typical background counts for experimental runs using variable wavelengths were around 1 c.p.s. at scattering angles of 5° (figure 2.4b). Despite being able to count to 2 MHz, in order to determine the specular reflectivity close to the critical angle, we had to insert an aluminium foil of thickness 1 to 2 mm into the beam to reduce the intensity and scale the results accordingly. All such scaling was found to overlap effectively with no glitches in the data sets.
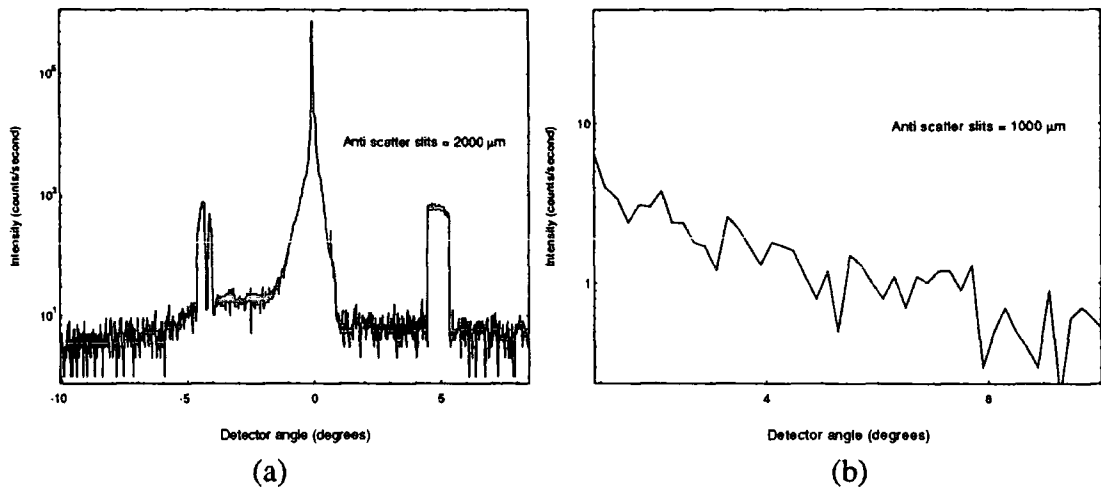
Fig 2.4 The background of station 2.3 before (a) and after (b) the inclusion
of lead shielding inside the vacuum can
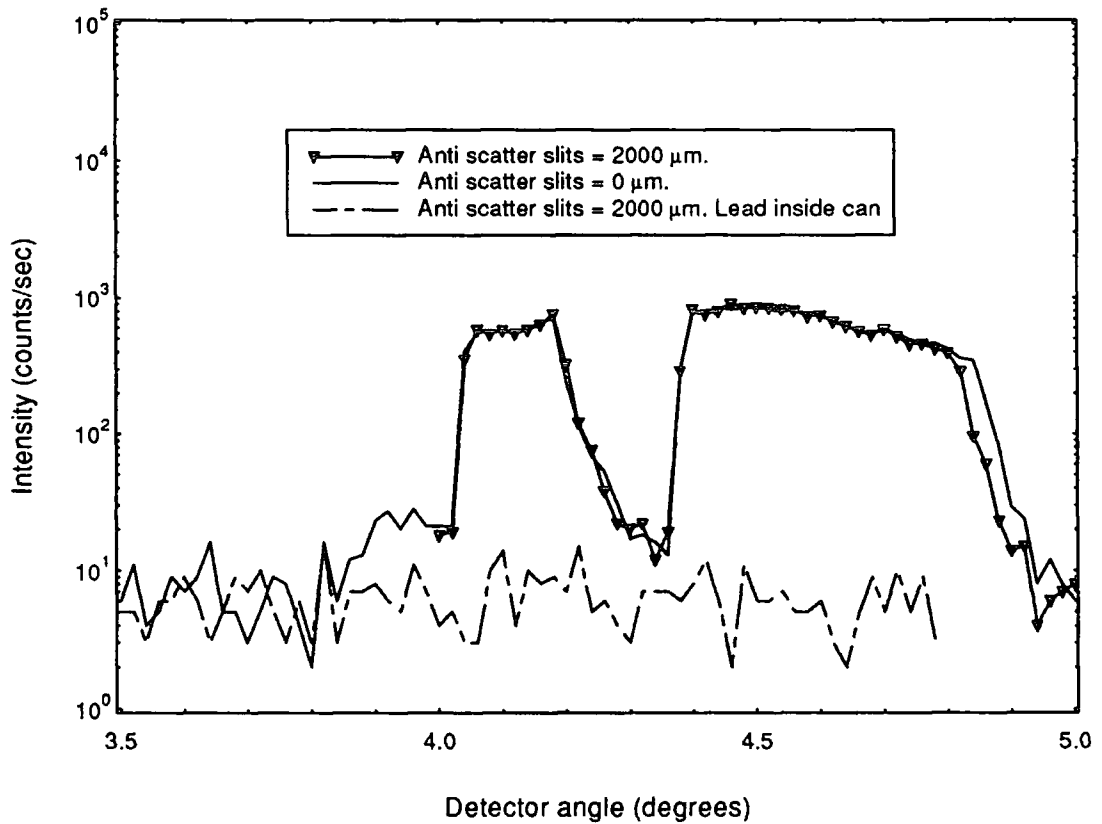
Fig 2.5 The effect of closing the anti scatter slits on the noise at 4.5 degrees.
Clearly the scatter must be passing around the side of this initial slit

We could not rely on the absolute accuracy of the diffractometer for studies exploiting the tunability of synchrotron radiation to enhance the scattering from the interfaces by the use of anomalous dispersion [6]. As the variation in the anomalous dispersion correction changes very rapidly, it was essential to locate reproducibly the wavelength with respect to the absorption edges of Cu or Co. This was achieved by recording a near-edge X-ray absorption fluorescence (NEXAFS) spectrum from standard samples. A peak in the NEXAFS spectrum of copper was clearly visible in the fluorescence detector and was a very convenient reference point. For this reason it was the Cu (figure 2.6b), rather than the Co (figure 2.6a) edge which was used to perform the experiments described here. The wavelength reproducibility using this method was one part in 10^4 and three parts in 10^4 for during the same and between the electron storage ring fills respectively (figure 2.7a,b).

2.1.2 Alignment of specimens for GIXR on station 2.3

The aim of the alignment procedure was to ensure that the sample surface was both within a few tens of micrometers of the centre of rotation of the diffractometer and that it was flat with respect to the scattering plane. If the sample was not flat with respect to the x-ray beam and the detector slits, then a off specular $\theta/2\theta$ scan would have been performed. If the sample was tilted along the axis of the beam then there would be an intensity loss when the tilted beam passed through the detector slits. However in this case, for a beam of width 4 mm and height 100μm passing through a slit also of height 100μm, a tilt of 360 arc seconds gave a loss of intensity of only 3%. Typical samples showed tilts in the region of 100 to 250 arc seconds and so optimisation in this plane did not prove necessary.

The optimised alignment procedure for a sample on the diffractometer thus was as follows.

1) Initially an aluminium absorber was placed in the beam and the detector arm was scanned so as to place the detector slits in the centre of the beam and the position calibrated to zero. This was particularly important if the wavelength had been changed since the beam moved slightly.

a)

Reproducible peak
used as reference point
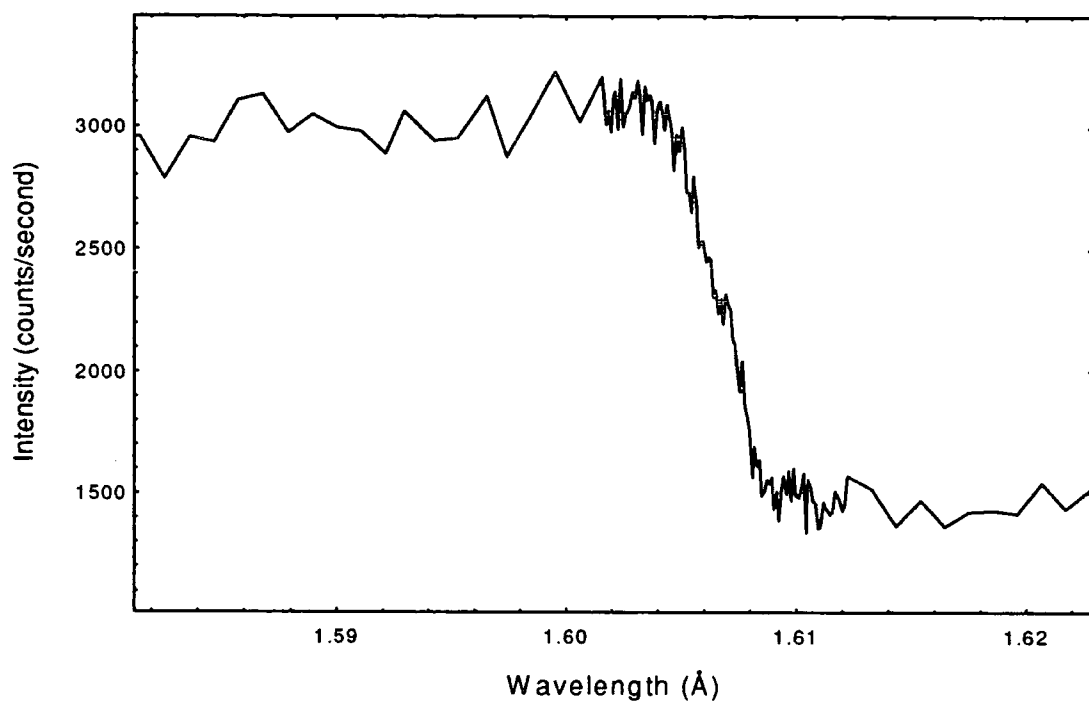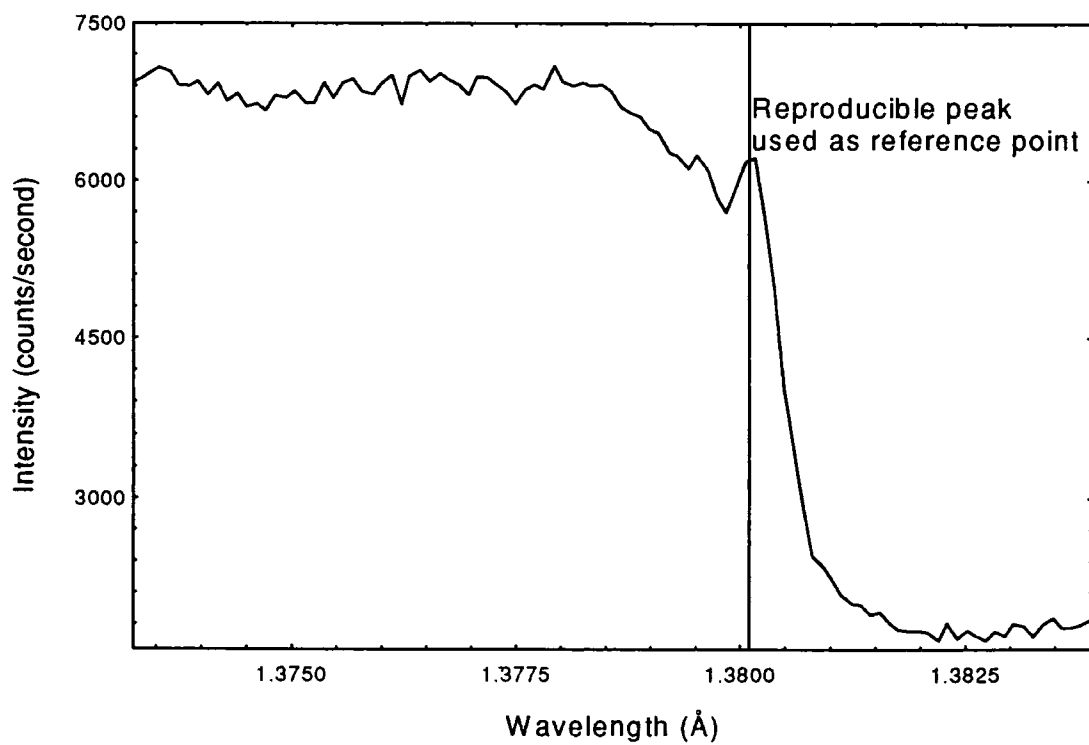
b)

Fig 2.6   X-ray fluorescence recorded from the Co (a) and Cu (b) standards
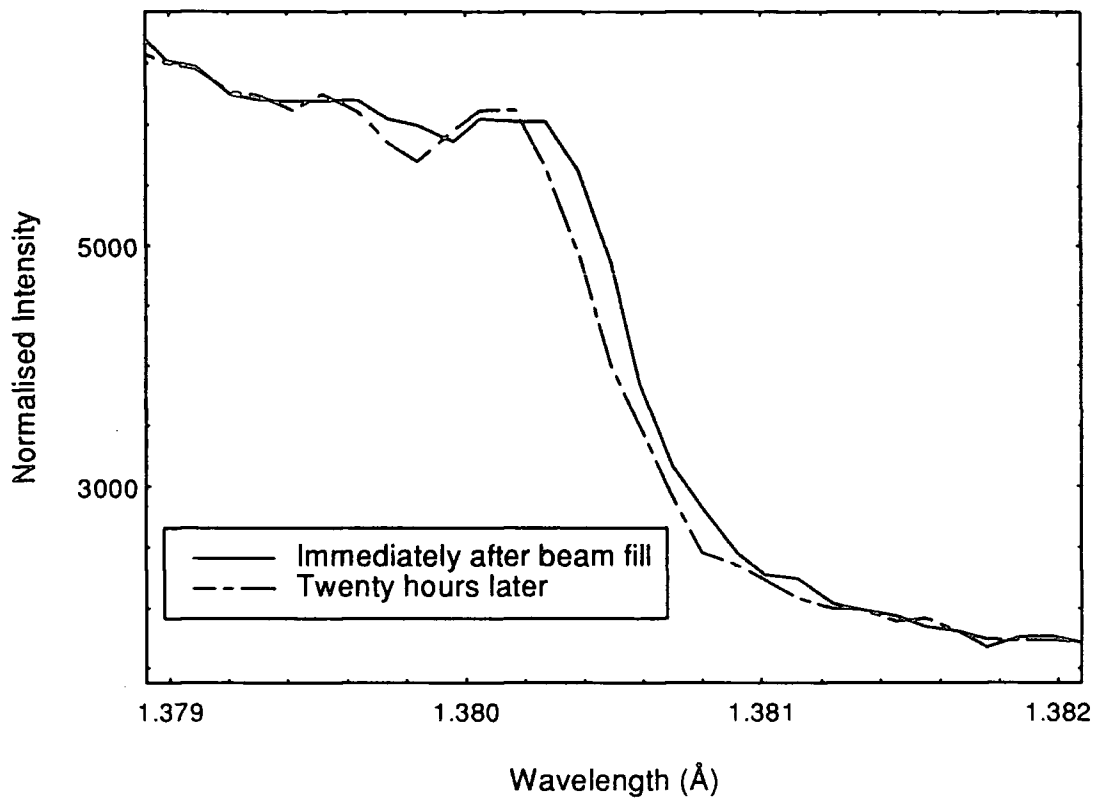
a)
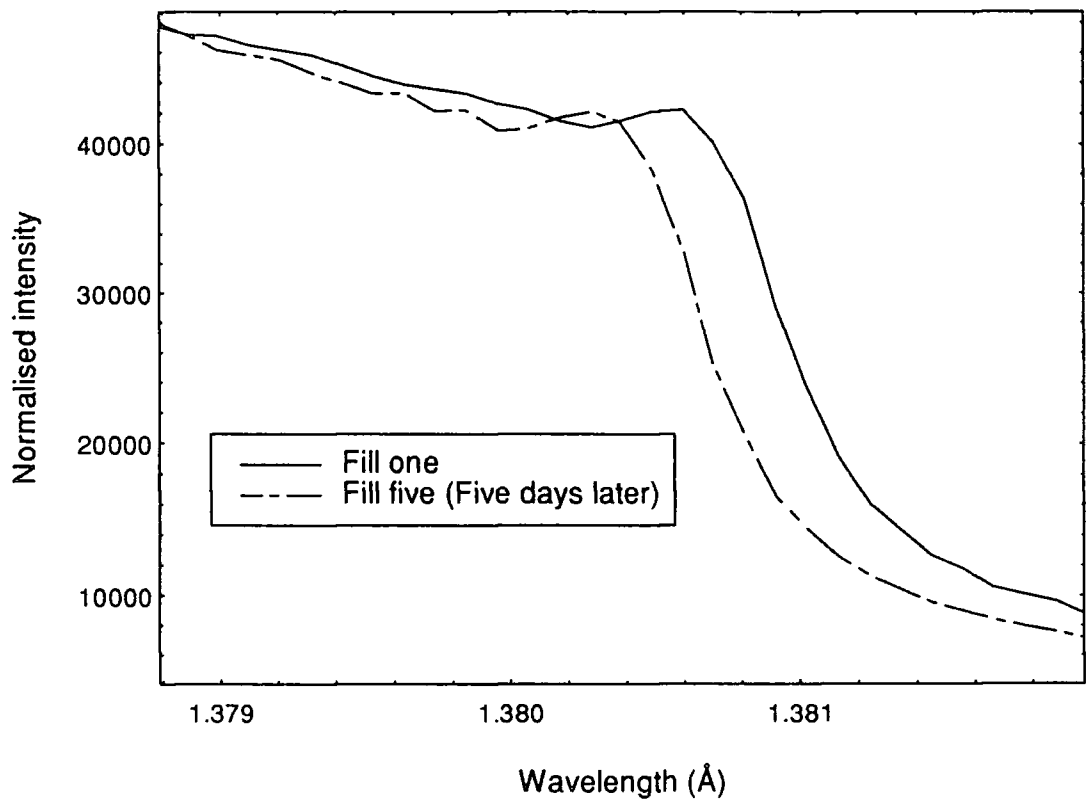
b)

Fig 2.7   Reproducibility of the Cu edge fluorescence data during (a) and
           between (b) synchrotron ring beam injections.

2) The sample was mounted and raised using the stage so that it half cut the beam. At this point it was done roughly to ±10% of the beam intensity.

3) The sample axis was rocked until maximum was recorded, this was then calibrated to zero. At this point sample surface and beam were approximately parallel. Again the steps were 'large', approximately 36 arc seconds.

4) The beam was again half cut with the sample. This time accurately, to ±2% of the beam intensity.

5) The aluminium absorber was removed and the sample and detector were moved to 2 and 4 degrees respectively. The sample axis was rocked in 1.8 arc second steps to find maximum intensity. At this point, the detector slits were aligned with the specularly reflected beam and the samples surface was at half the angle of the detector. This final sample position was calibrated to half the detector value.

6) Sample was then aligned. The process took approximately 15 minutes.

2.1.3 Experimental configuration of the GXR1 reflectometer

X-ray reflectivity measurements were performed in Durham using the laboratory based GXR1 reflectometer. A schematic of the instrument is shown in figure 2.8. Details of the equipment and alignment procedures have been covered in great depth elsewhere [7]. However the main differences between this and Daresbury are as follows.

X-rays were produced using a fixed Cu tube run at 40 KV, 30 mA. These were monochromated to Cu K_β using a 75μm slit and an asymmetrically cut Si 111 crystal (figure 2.9) with an angle of incidence of 2 degrees. The grazing geometry of this monochromator produced higher count rates than a symmetrically cut crystal due to the increased angular acceptance of its rocking curve [8]. The slits limited the angular acceptance of the monochromator, which in turn limited the wavelength range

X-ray source

Beam conditioner block

Combined Z (up and down) and tilt
motions on sample stage

Detector

Sample stage drive

Translation stage (out of page)

Detector arm drive

Sample stage rotation drive
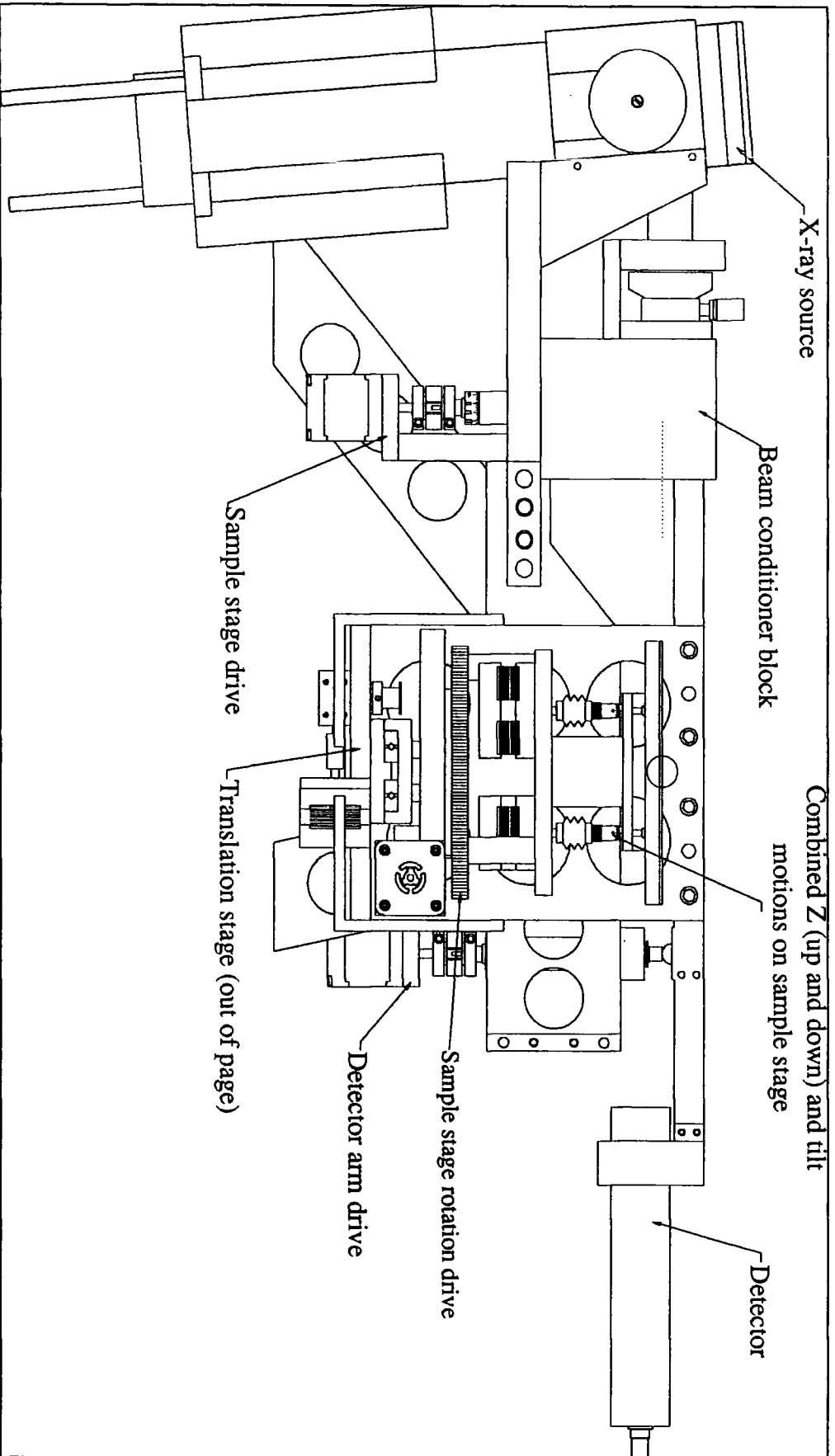
Fig 2.8
Courtesy of BEDE Scientific Instruments

Schematic of the GXR1 reflectometer

available for diffraction (figure 2.10). Finally, a beam of 75μm height and 100 arc seconds divergence emerged, delivering count rates at the sample in the region of 1.2×10^6 c.p.s, with a $\Delta\lambda/\lambda = 2 \times 10^{-3}$.

The reason for the increase of intensity using the grazing incidence geometry was due to the larger angular acceptance of the reflection. This angular acceptance is governed by the width of the rocking curve and is predicted by the following result of dynamical theory [9]:

$$\omega_i = \omega_s \left[\frac{\sin(\theta + \alpha)}{\sin(\theta - \alpha)} \right]^{1/2} \qquad 2.2$$

Here ω_i is the width of the asymmetric rocking curve, ω_s is the width of the corresponding symmetric reflection and θ is the Bragg angle of the reflecting planes. The offcut of the Bragg planes with respect to the surface is given by α. From this equation it can be seen that the width of a asymmetric reflection in the grazing incidence geometry is higher than the symmetric reflection, whereas that in the grazing exit diffraction it is less.

In figure 2.10 the DuMond diagram [10,11], which is a graphical representation of Bragg's law, is calculated for the symmetric and asymmetric Si 111 reflections. From this figure, the grazing incidence reflection (dotted lines) is seen to have a larger intrinsic width than the symmetric reflection (full lines). Using this DuMond diagram, the intensity of the diffracted beam can be calculated by measuring the area defined by the width of the rocking curve and the angular acceptance of the slits. Thus the intensity of the diffracted beam is correspondingly higher for the crystal cut in the grazing incidence geometry.

Alignment to Cu K_β ($\lambda = 1.393$ Å) radiation was unintentional, and a result of an initial miscut in the monochromating crystal. Due to the larger Bragg angle of Cu K_α radiation, this miscut caused the x-rays to hit the inside of the brass housing and be absorbed.
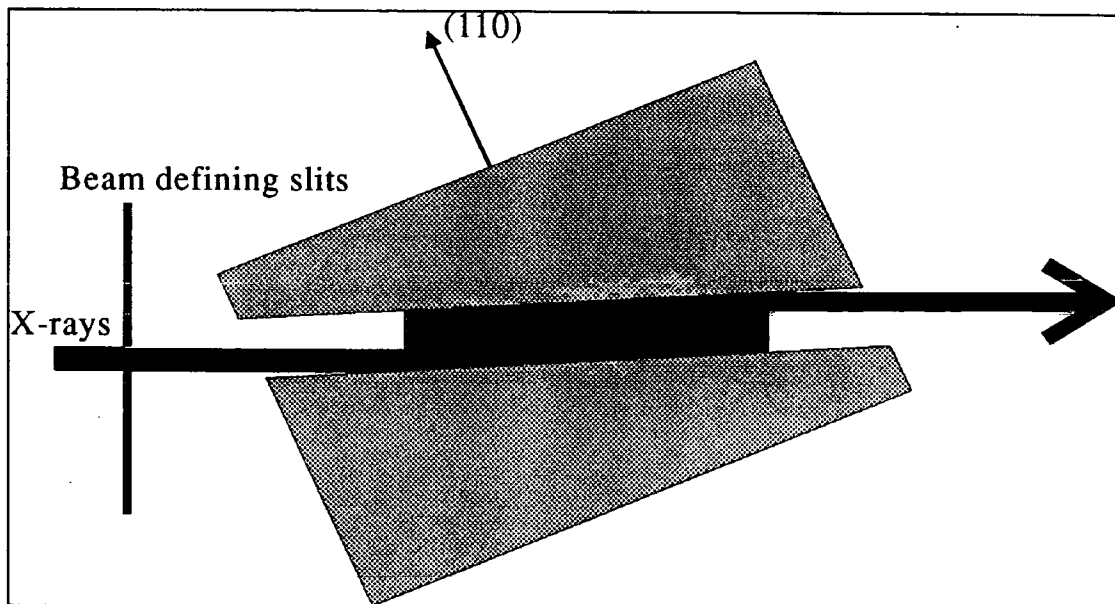
Fig 2.9   Schematic of the asymmetric cut channel collimator on the GXR1
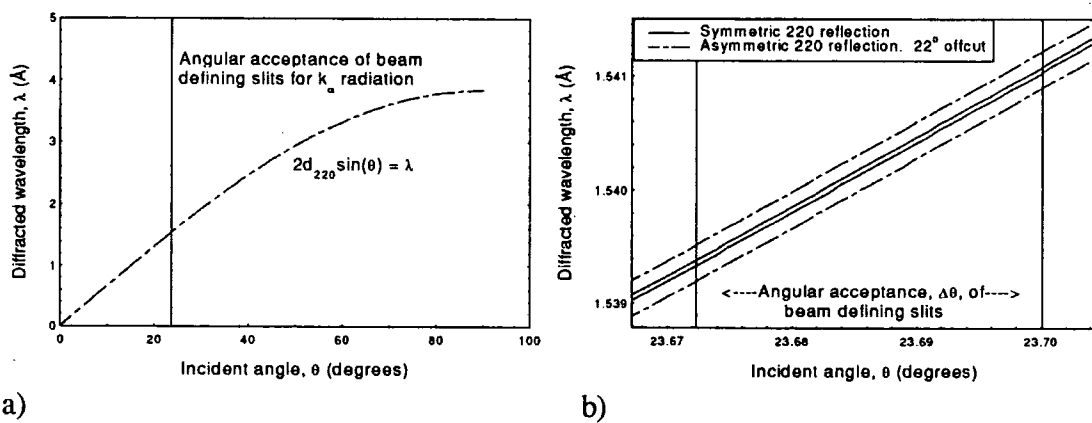
Fig 2.10 The duMond diagram for the symmetric and asymmetric Si 220 reflections (a) and an enlargement of the region of Cu K_β (b).

Sample (θ) and detector (ϕ) axis were controlled via stepper motors and a BEDE MINICAM II interface with back lash correction. The resulting accuracy of the sample and detector motions were 0.25 and 0.5 arc seconds respectively.

In order to utilise the high intensity of the instrument, an EDRa scintillation detector was again employed. In front of this was mounted a single set of 100μm (±0.1μm) slits. These produced an instrumental resolution of 100 arc seconds in transverse (specimen only) scans.

The background of the instrument was seen to include a broad shoulder to one side of the primary beam. This arose from x-rays clipping the bottom of the monochromator block as they emerged. The noise could be removed to a large extent by including a set of anti scatter slits just behind the monochromator, set to exclude everything except the primary beam itself. The effect of the slits on the background is shown in figure 2.11 and the increase in clarity from a typical glass sample in figure 2.12.

2.1.4 Alignment of specimens on the GXR1

The alignment of the sample on the GXR1 took place in exactly the same way as at Daresbury except for two points.

a) The lower resolution of the detector slits on the GXR1 relaxed the need for such accuracy on the sample alignment. On this machine, the sample needed (and could) only to be aligned to ± 15 arc seconds.

b) The presence of a rotation axis around the samples surface normal and separate tilt motions on the sample stage allowed the sample to be aligned flat with respect to the x-ray beam in both tilt directions and there was no need to calibrate the sample axis. The accuracy of these tilt motions were ± 15 arc seconds, whilst that of the height adjustment was 0.003 mm.
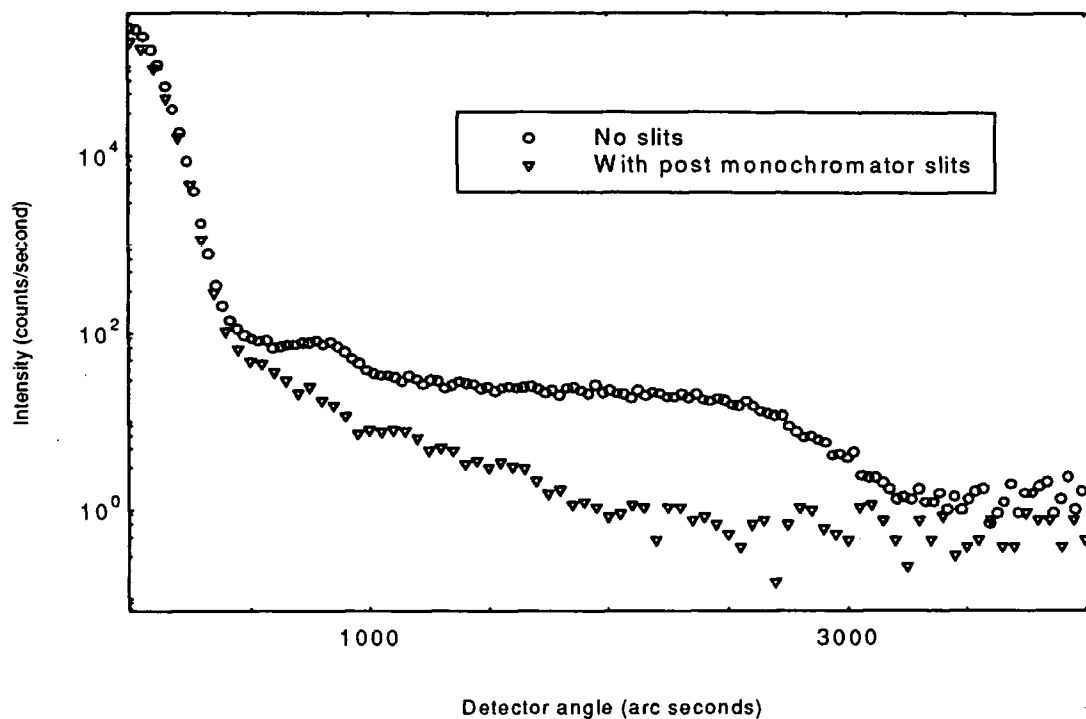
Fig 2.11   The effect of including slits after the monochromator on the
background of the GXR1
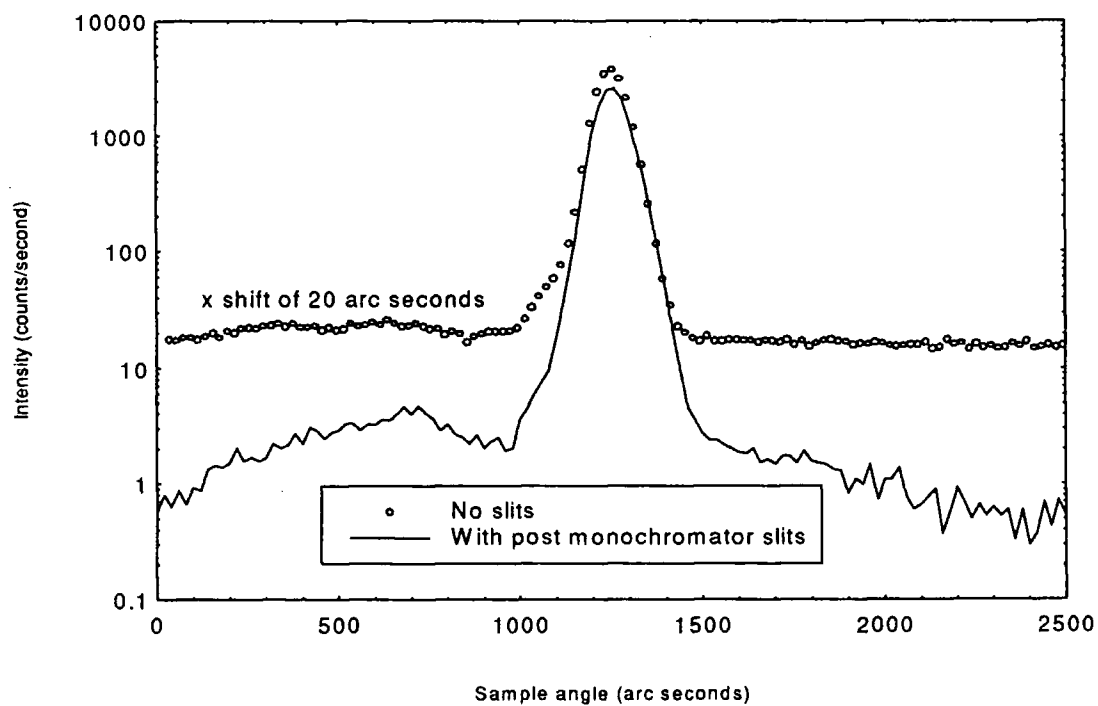
Fig 2.12   The effect of post monochromator slits on a transverse diffuse scan
taken from a typical glass specimen (S15)

2.2 X-ray diffraction

2.2.1 Configuration of the Model 200 diffractometer

The Model 200 triple crystal diffractometer has been described in great detail elsewhere [7]. X-rays from a fixed Cu tube were first given a low angular divergence and wavelength spread by passing through a four bounce Si 022 channel cut collimator (c.c.c.). Monochromation to Cu $K_{\alpha 1}$ was then performed using a single bounce Ge 111 crystal, in the dispersive (- -) setting, which gave an angular divergence of 16 arc seconds and $\delta\lambda/\lambda = 3 \times 10^{-4}$. The analyser crystal used was a four bounce Si 022.

All motor axis were again moved by stepper motors, controlled by a MINICAM II electronics interface with backlash correction. This gave a resolution of both the sample (θ) and analyser (ϕ) axes of 0.3 arc second.

Finally the detector used was a BEDE EDR [12]. This was the same as the EDRa detector except it had a NaI(Tl) crystal in it instead of Yttrium aluminium oxide to convert the x-rays into light. This had a longer deadtime and meant that although it too had an intrinsic background of 0.15c/s, its saturation count rate was in the region of 8×10^5 c.p.s. However, due to the lower intensities involved with triple crystal diffraction, such count rates were never obtained.

2.2.2 Configuration of the D3 diffractometer

On the D3 triple axis diffractometer, monochromation was performed using a DuMond monochromator. This consisted of two 022 Si crystals with symmetrically and asymmetrically cut channels [8]. The symmetrically cut channels were used in the dispersive (+ - + - - + - +) setting, giving an angular divergence of 5 arc seconds and a wavelength dispersion of $\delta\lambda/\lambda = 5.5 \times 10^{-5}$. In addition, the large number of bounces gave a rocking curve with highly suppressed tails. The analyser used was a four reflection 111 Si crystal. A schematic of the diffractometer is given in figure 2.13.
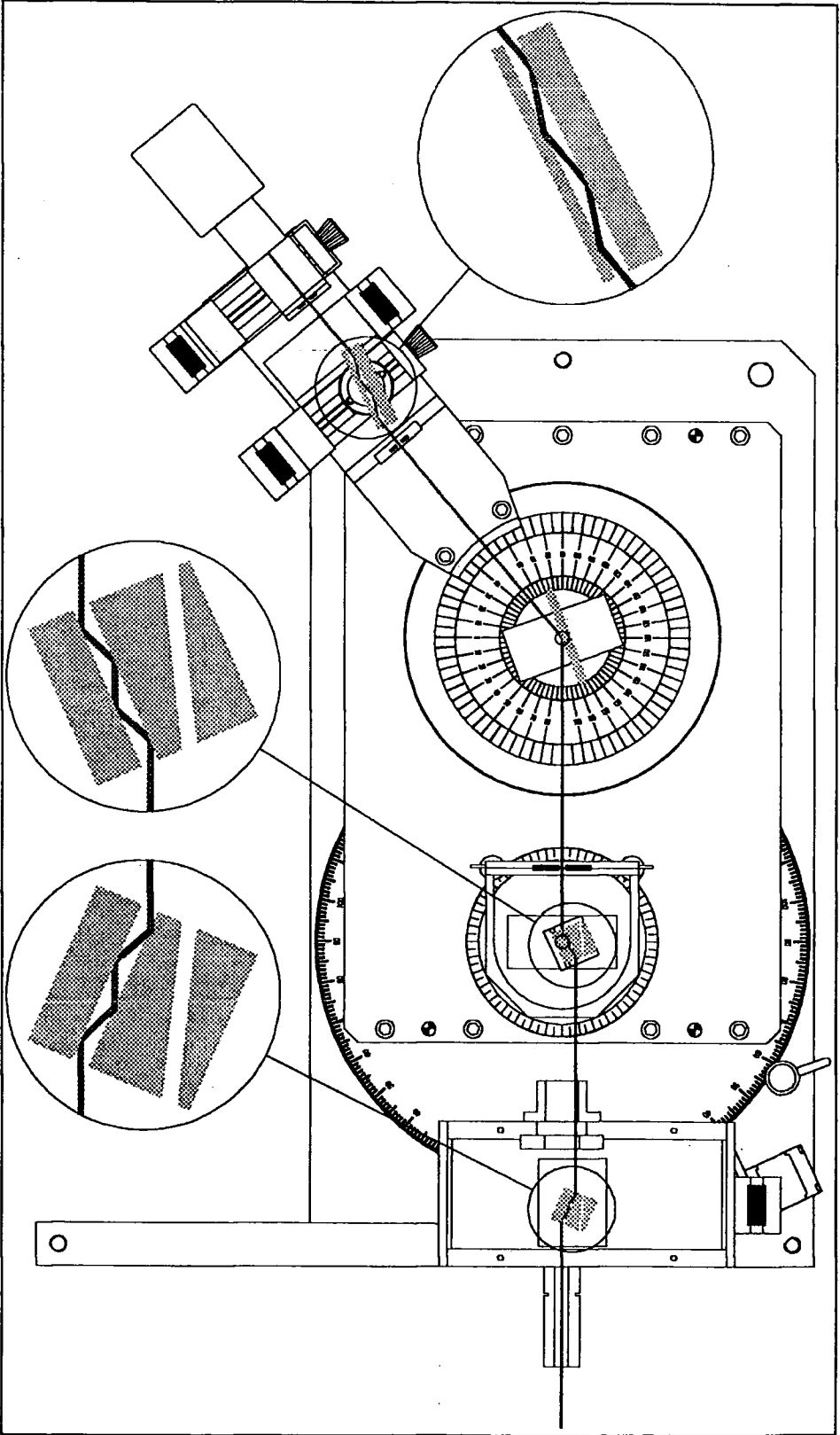
Fig 2.13
Courtesy of BEDE Scientific Instruments Ltd.

Plan view of the D3 diffractometer

On this machine, the sample and detector axes were encoded, giving each a resolution of 0.06 arc seconds. In addition, the detector used was a BEDE EDRa of the same specifications as the one on the GXR1 and the SRS station 2.3.

2.2.3 Specimen alignment on the Model 200 and D3 diffractometers

The alignment of a sample on both machines was identical and it has been described in depth for the D200 elsewhere [7].

Chapter III

Theory of x-ray scattering

3.1 X-ray diffraction

3.1.1 The Kinematical theory

In this theory [1,2], the atoms within the crystal are assumed to be point scatterers. These are coherently illuminated by an x-ray beam which is incident on the sample. The spatial periodicities of these scatters, described by the structure factor, leads to a phase difference being introduced between the scattered waves. As a result, summing the phases of these scattered waves gives strong diffracted amplitudes arising in certain directions.

There are two large assumptions made within the kinematical theory. The first is that there has been no interaction between the incident and diffracted waves (i.e. no rediffraction has occurred). The second is that all the atoms have been illuminated to the same degree. These conditions are only satisfied in small or highly dislocated crystals and as a result, a new theory must be introduced for thick or highly perfect crystals. An example of the breakdown of the kinematical theory is seen when Laue diffraction is performed on perfect crystals for increasing thickness' (figure 3.1). For small thickness' the kinematical theory predicts the diffracted intensity extremely well. However as the thickness is increased the intensity predicted by the kinematical theory tends to infinity whereas in reality it saturates.

3.1.2 The Dynamical theory

In the kinematical theory, it has been assumed that no interaction between the incoming and diffracted beam has occurred. However, in reality, rediffraction of x-rays occurs by other, parallel crystal planes. This causes diffracted x-rays, which are coherent with respect to the incident beam, to be placed back in the incoming
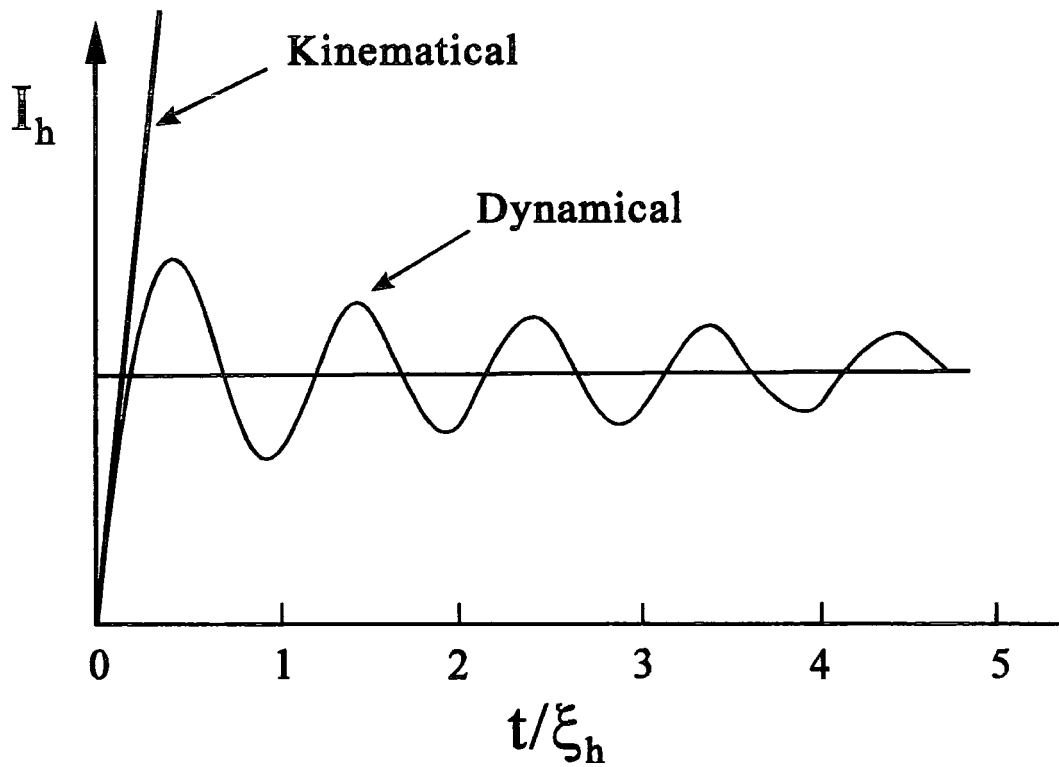
Fig 3.1 Comparison of the kinematical theory intensity I_h with the type of intensity variation seen experimentally. The thickness t is scaled to the extinction distance ξ_h.

direction. In consequence, an energy exchange occurs and a coupling of the two wavefields results.

In order to describe the above situation, we must solve Maxwell's equations in a periodic medium [2,3]. The crystal is assumed to consist of a certain electronic distribution, described by the structure factor, which acts as a perfect dielectric as it is polarised under the influence of the electromagnetic field. Due to the medium being periodic on the same scale as the E-M waves, the electric susceptibility, χ, is able to be expanded as a Fourier series.

$$\chi = \sum_h \chi_h \exp(2\pi i\, h.r) \qquad\qquad 3.1$$

The wave equation for an E-M wave propagating in a linear isotropic homogeneous medium is given by:

$$\Delta E = \frac{1}{c^2}\frac{\partial^2 E}{\partial t^2} \qquad\qquad 3.2$$

Assuming that the electrical conductivity and the magnetic permeability are zero and using the electric displacement ($D = \varepsilon_0\varepsilon_r E$) this reduces to the form.

$$curlcurl D = -\frac{(1+\chi)}{c^2}\frac{\partial^2 D}{\partial t^2} \qquad\qquad 3.3$$

In the kinematical theory, it is plane waves that propagate through the medium. Since in the thin crystal case, dynamical theory must yield the same results as the kinematical theory, we may expect that its solutions are linear combinations of these waves.

$$D = \sum_g D_g \exp(-i\, k_g.r)\exp(i\omega t) \qquad\qquad 3.4$$

After substitution of (3.4) and (3.1) into (3.3) and assuming that there is only one diffracted beam, two simultaneous equations are produced, the solutions of which are

the basic equations of the plane wave dynamical theory. A graphical representation that encompasses solutions of the dynamical theory equations for wavevectors is called the dispersion surface (figures 3.2, 3.3). This decides the locus of wavevectors of any wave allowed inside the crystal. Far from the exact diffraction condition, the Lorentz point, the equations give the same results as would be expected from the laws of reflection and refraction. However when diffraction occurs, dynamical effects take over and two distinct wavefields exist within the crystal. These 'Bloch waves' themselves consist of the superposition of two waves (the transmitted and diffracted waves) and propagate unchanged through the medium. These waves are of a similar origin as standing waves within such a medium, but in addition they must respect the periodicity of the lattice. If such a wave existed that tried to contravene this periodicity, interactions with the atoms would redistribute it's energy and it would be suppressed.

When the Bloch waves reach the exit surface, they must again have their tangential components matched across the interface (i.e. get refracted). In addition, the periodic medium, which supported the existence of the solitons is removed and they split into their respective wavefields. As a result, for each polarisation, four waves emerge from the crystal for every one incident upon it.

3.1.3 Reciprocal space

Due to the crystal being a periodic medium it is an ideal situation for Fourier analysis [1]. In 1-D, the Fourier series of a function, n(x), with periodicity 'a' is given by [4].

$$n(x) = \sum_p n_p \exp(i2\pi px/a) \qquad 3.5$$

As a result, this period is described in reciprocal space as a series of points, whose separation from the origin of reciprocal space is 0, $2\pi/a$, $-2\pi/a$, $4\pi/a$ $-4\pi/a$ etc. The value $2\pi x/a$ is called the reciprocal lattice length. When this is extended to 3-D, the $2\pi x/a$, is replaced with a vector G, which is called the reciprocal lattice vector.
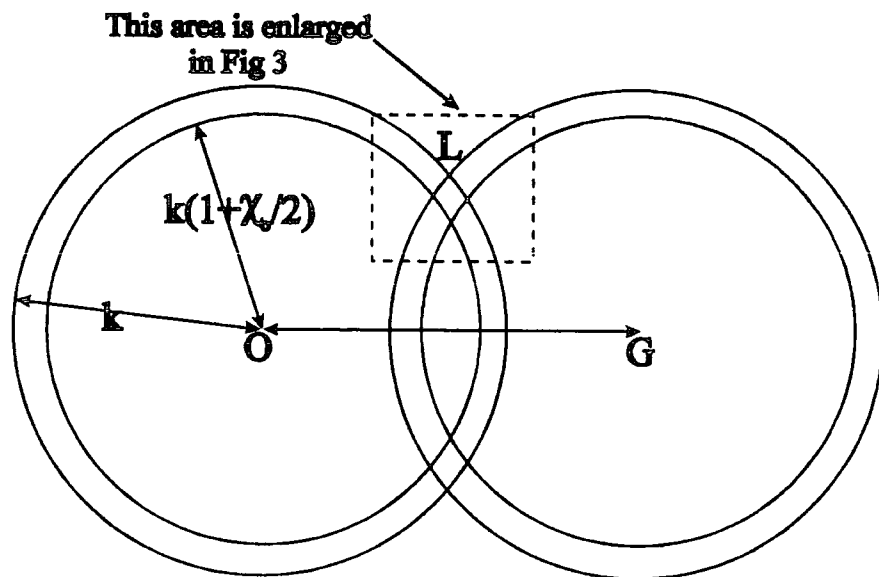
Fig 3.2 The dispersion surface - a graphical representation of dynamical theory
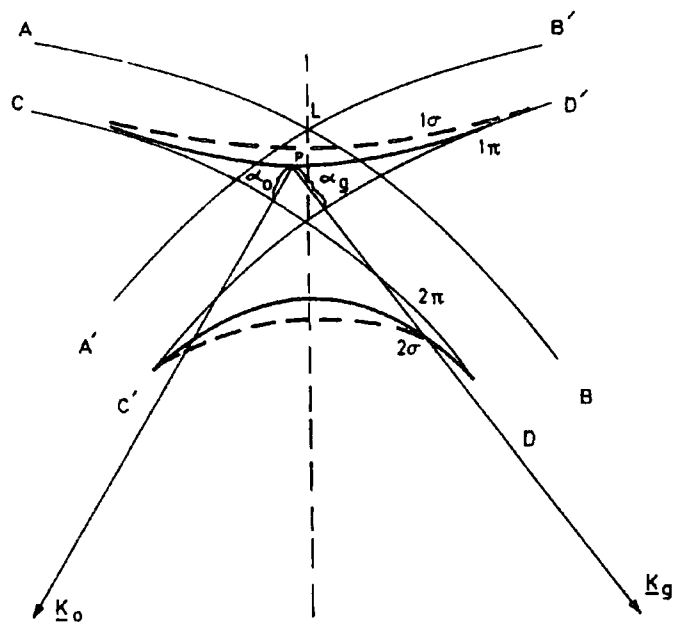
Fig 3.3 An enlarged region of the dispersion surface around the Lorentz point

For simplicity, the primitive vectors of the reciprocal lattice are defined in the following way with respect to the primitive vectors of the real lattice.

$$b_1 = 2\pi \frac{(a_2 \times a_3)}{(a_1 \cdot a_2 \times a_3)}; b_2 = 2\pi \frac{(a_3 \times a_1)}{(a_1 \cdot a_2 \times a_3)}; b_3 = 2\pi \frac{(a_1 \times a_2)}{(a_1 \cdot a_2 \times a_3)} \qquad 3.6$$

As a result, the primitive reciprocal vectors are orthogonal to two primitive vectors in the real lattice. Also, the direction of a reciprocal lattice vector from a single set of planes is in the same direction as the surface normal of those planes. Using these vectors, the points in the reciprocal lattice are mapped by the following:

$$G = v_1 b_1 + v_2 b_2 + v_3 b_3 \qquad 3.7$$

In addition, every wavelength in real space corresponds to a reciprocal vector, or k vector, in reciprocal space of magnitude:

$$|k| = \frac{2\pi}{\lambda} \qquad 3.8$$

Due to the above construction of the primitive vectors, the direction of this vector is the same in both real and reciprocal space.

In summary, reciprocal space is a 3-D mathematical construction, in which spatial frequencies in real space are converted to points. The direction of these points from the origin, is the same as the direction that the spatial frequency was propagating in real space. In addition, the distance of these points from the origin is proportional to the inverse of the wavelength of their corresponding spatial distribution. The origin of reciprocal space is arbitrary, since the crystal possesses translational symmetry. Shown in figure 3.4 is a slice through reciprocal space. Included in the figure are the regions that can be probed by various scans reviewed in this chapter.

In order to show how important reciprocal space is for diffraction, we must return to the kinematical theory for a moment. In this, it is assumed that the scattered amplitude
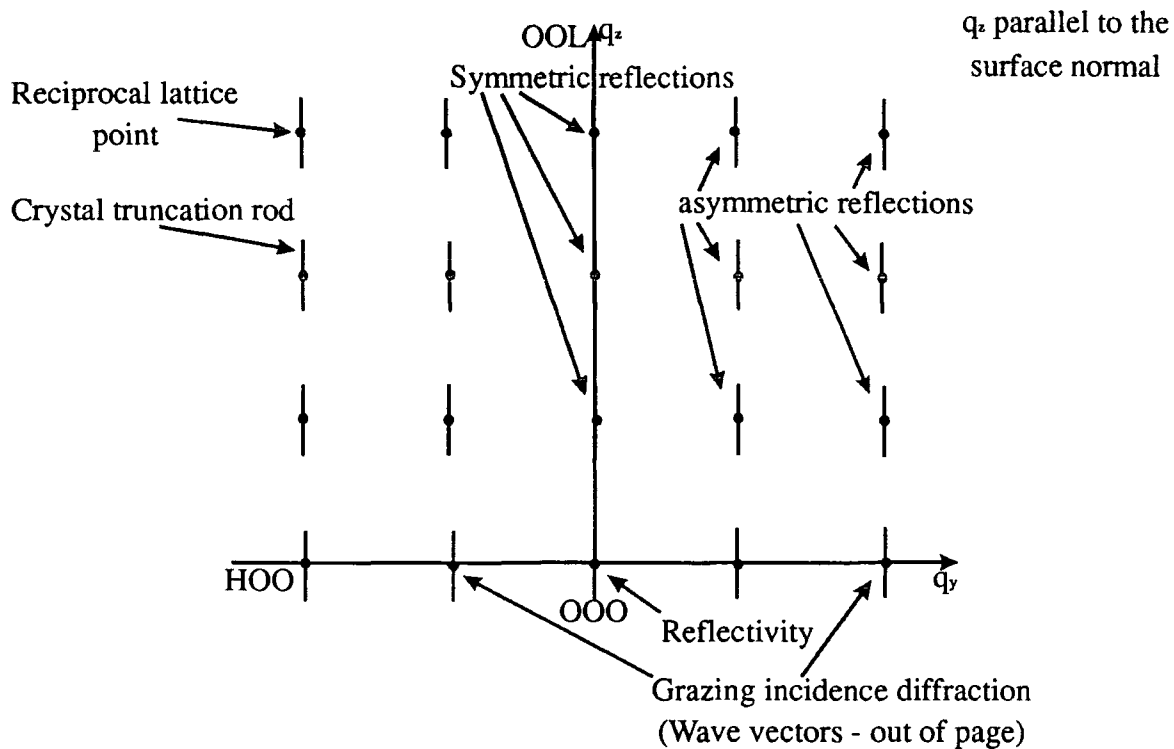
Fig 3.4   A slice through reciprocal space showing the regions probed by the
scans reviewed in this chapter

of the x-rays are just a sum of the phases from the atoms in the crystal lattice, weighted by their electron density [1]. As a result:

$$F = \int dV \, n(r) \exp[i(k_o - k_h) \cdot r] = \int dV \, n(r) \exp(-iQ \cdot r) \qquad 3.9$$

$$k_o + Q = k_h \qquad 3.10$$

where k_o is the incident wavevector, k_h is the diffracted wavevector and Q is the scattering vector.

Combining (3.5) and (3.9) produces

$$F = \sum_G \int dV \, n_G \exp[i(G - Q) \cdot r] \qquad 3.11$$

When $G = Q$, the argument of the exponential vanishes and $F = Vn_G$. In consequence, it is the set of reciprocal lattice vectors, G, which determines the possible x-ray reflections. A very transparent graphical representation was developed by Ewald. This clearly demonstrates the diffraction effect and Bragg's law can be derived from it. The construction is shown in figure 3.5.

3.1.4 Transforms from real to reciprocal space

Figure 3.6 shows an enlarged section of the Ewald sphere. The wavevector k_o is incident upon the diffracting planes at an angle, θ and is diffracted as the wavevector, k_h. Again, the change in wavevector is defined as Q.

From geometry
$$Q \approx 2k_o \sin(\frac{\phi}{2}) \approx (\frac{4\pi}{\lambda}) \sin(\frac{\phi}{2}) \qquad 3.12$$

Now
$$q_z = Q \cos\delta \qquad 3.13$$
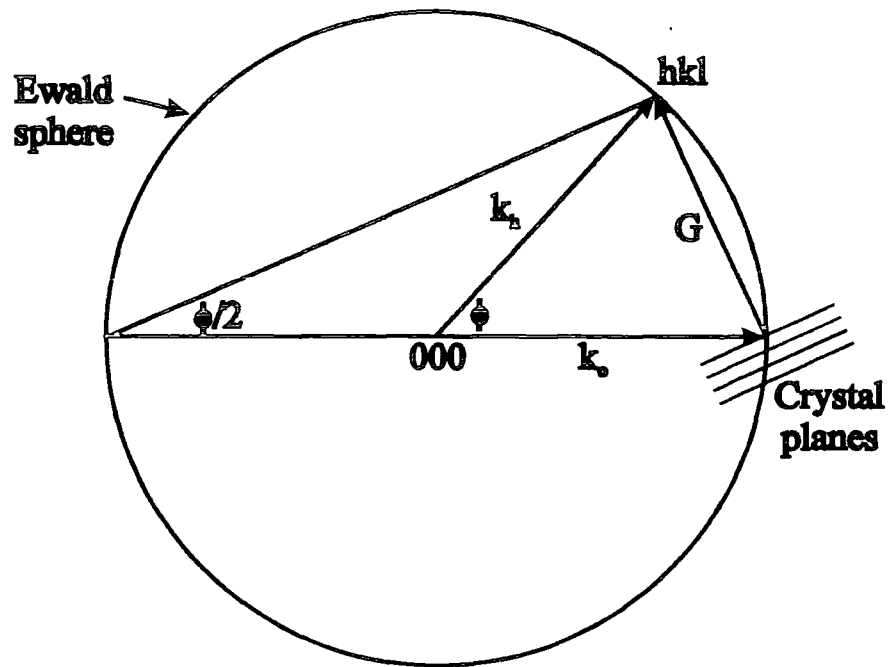
Fig 3.5   The Ewald construction (or Ewald sphere)
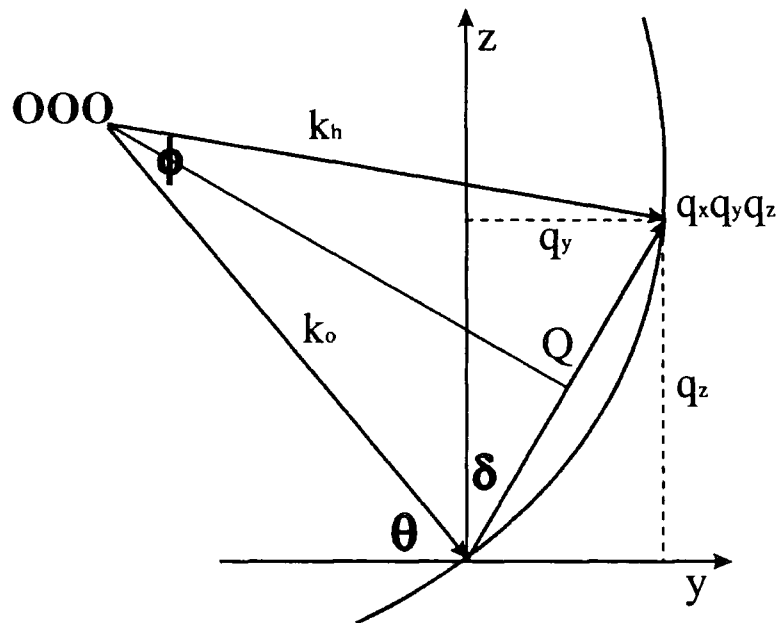
Fig 3.6   Enlargement of Ewald sphere

This diagram is completely general for both symmetric and asymmetric reflections.   If the symmetric geometry is assumed, the normal of the surface and the diffraction spot hkl both lie on the Z axis.

and

$$q_y = Q \sin\delta \qquad\qquad 3.14$$

where

$$\delta = \theta - (\phi/2) \qquad\qquad 3.15$$

So

$$q_z = (\frac{4\pi}{\lambda}) \sin(\frac{\phi}{2}) \cos\delta \qquad\qquad 3.16$$

and

$$q_y = (\frac{4\pi}{\lambda}) \sin(\frac{\phi}{2}) \sin\delta \qquad\qquad 3.17$$

3.1.5 The effect of lattice dilations and tilts in reciprocal space [5]

Consider a monochromatic beam, of small angular divergence, incident upon a perfect crystal. If the angle of incidence is chosen so that θ, the Bragg angle, is satisfied, then a diffracted wave is produced. If it is also assumed that by some means (say a very fine slit) both the intensity and direction of the diffracted beam can be measured, then we have a situation which describes what is displayed in the Ewald construction.

In order to find what effect lattice tilts and dilations have on the diffracted intensity, it is instructive to consider the two most extreme cases.

In the first case, assume the lattice parameter of the crystal is left constant but a tilt is put into the lattice planes. It is clear from figure 3.7, that if such a tilt exists, then in order to get the second part of the crystal to diffract, it must be rotated by an amount, equivalent to the angular offset between the two sets of crystal planes. On rotation of the crystal to this position, x-rays are diffracted in the same direction as before. These pass through the analyser slits and are detected. As a result, a 'sample only', or theta scan, maps out the tilt distribution within the crystal.

The second extreme example is to consider a crystal whose planes are perfectly flat, but the lattice parameter of one region is different to that of another. This scenario is shown in figure 3.8. Assume initially that region 1 is diffracting. In order to get region 2 to diffract, the crystal must be rotated to the Bragg angle corresponding to the second set of lattice planes, θ'. However, this time, when diffraction takes place, the scattered beam is at an angle $2\theta'$ with respect to the incident beam. In order for the x-rays to be detected the detector slits must be moved to the new exit angle, $2\theta'$. As a result, a scan in which the detector and sample axes are coupled in a ratio 2:1 maps out the range of dilation's within the sample. This type of scan is conventionally called a theta-two theta scan.

In terms of reciprocal space. From equation 3.16, it can be seen that if the sample and detector axis are scanned in a ratio 2:1, then δ $(= \theta - (\phi/2))$ becomes equal to zero. As a result the q_y component in reciprocal space is zero and a scan along q_z is performed. If however, only the sample is scanned, then the scan proceeds as a circle about the origin in reciprocal space. For small displacements in θ:

$$q_z \approx (\frac{\phi}{\lambda})(1 - \frac{\delta^2}{2}) \approx (\frac{\phi}{\lambda})(1 - \frac{1}{2}(\theta - \frac{\phi}{2})^2) \approx const \qquad 3.18$$

and so it becomes a scan in a straight line in q_y.

Due to the reflections here being symmetric, the surface normal and $\theta/2\theta$ scan are parallel in reciprocal space. For simplicity, later in the reflectivity section, we will define now the direction of q_z to be parallel to the surface normal, and not relate it in any way to the crystal planes.

X - rays

Region 1, d   **Region 2, d**
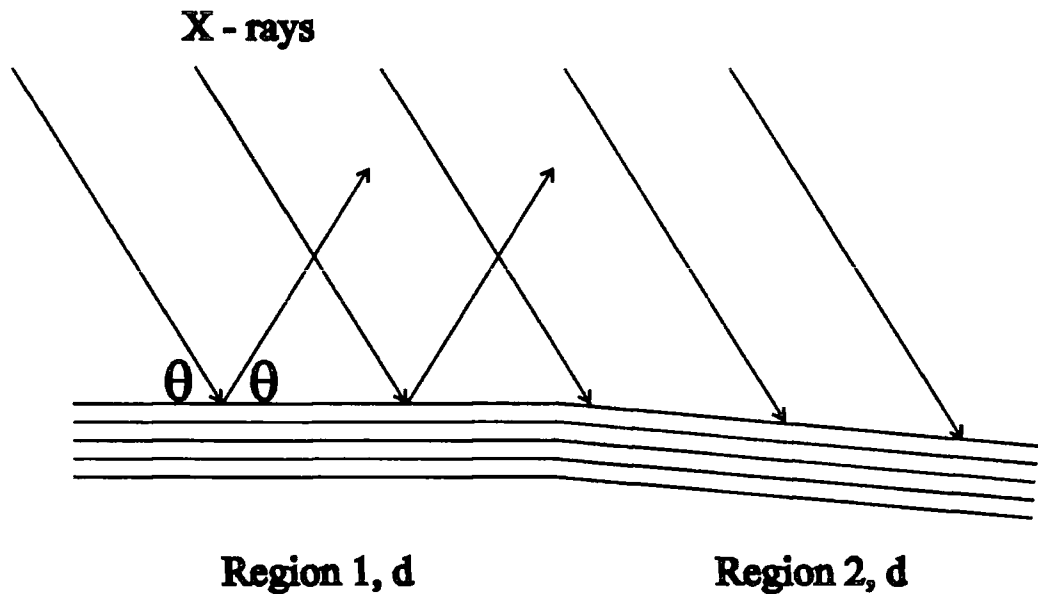
Fig 3.7   Diffraction from a crystal containing only lattice tilts

In order for region 2 to diffract, the crystal must be rotated by an amount equivalent to the angular offset between the planes. The diffracted beam will then emerge at an angle 2θ with respect to the incident beam and be detected at the same scattering angle.

X - rays

Region 1, d   **Region 1, d'**
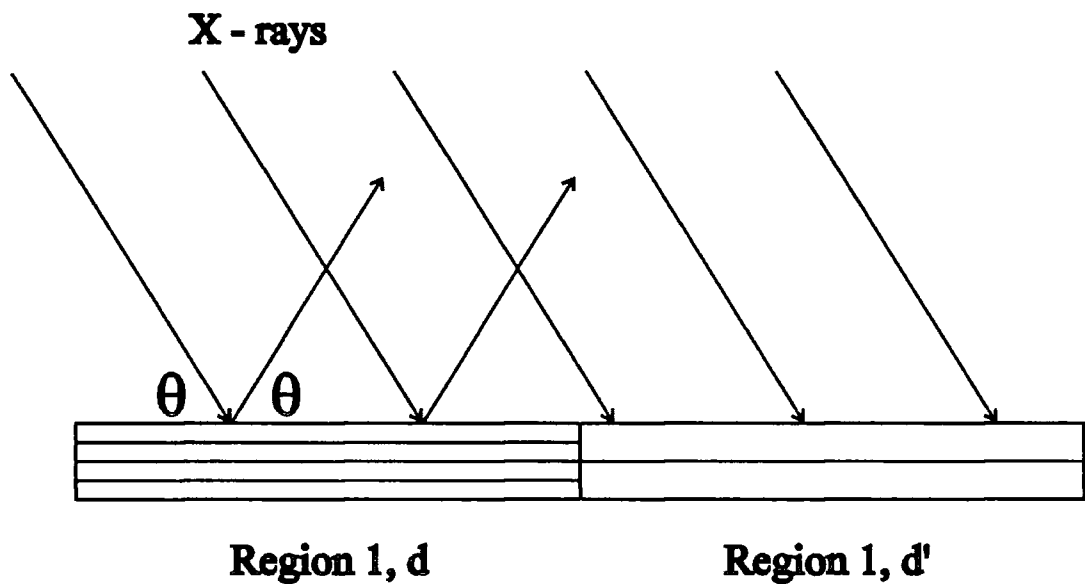
Fig 3.8   Diffraction from a crystal containing only lattice dilations

In order for region 2 to diffract, the crystal must be rotated to it's Bragg angle, θ'. If this is done, the diffracted beam will exit at an angle $2\theta'$ with respect to the incident beam. In consequence, the detector must be moved to a new angle of $2\theta'$ in order for the diffracted x-rays to be detected.

3.1.6 Double axis diffraction

In double axis diffraction (HRXD) [5] a monochromatic beam of small angular divergence is incident upon the sample. If the Bragg condition is satisfied, a diffracted beam is produced which is detected (figure 3.9). Due to there being no form of discrimination of the direction of the exit beam, an integration of the directions of all diffracted beams is observed. As a result, double axis diffraction cannot distinguish between a sample containing tilts or lattice dilations. In order to combat this, some form of angular discriminator must be introduced in front of the detector.

3.1.7 Triple axis diffraction

In triple axis diffraction [5], the direction of the diffracted radiation is determined by using a slit or an analyser crystal (figure 3.10). In such a way, $\theta/2\theta$ and specimen only scans can be used, as described above, to determine which distortions are giving rise to the observed diffuse scatter. It is often the case that a whole series of $\theta/2\theta$ scans are performed for a range of sample angles. In this way the entire region of reciprocal space around the selected diffraction spot may be mapped [5,6].

3.1.8 Artefacts observed in symmetric triple axis diffraction

As seen in figure 3.11, a star can form around the reciprocal lattice point when a triple axis map is taken [5]. The streak extending from top left to bottom right is due to a lack of resolution on the analyser. As a result, the Bragg peak is smeared out along the Ewald sphere. The second streak is due to a lack of monochromation or a large angular spread of the beam. This results in a variety of Bragg angles being satisfied and in consequence, a streak along the k_h direction is observed.

The third streak along the q_z direction is due to the crystal being non infinite. As reciprocal space is a Fourier transform of spatial frequencies, having a non infinite array in one direction will broaden the spot into a rod [7].
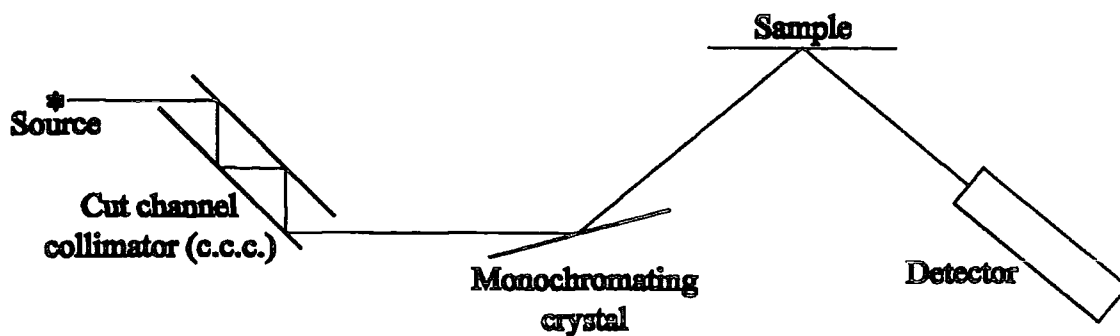
Fig 3.9   Schematic of the experimental set up for double axis diffraction
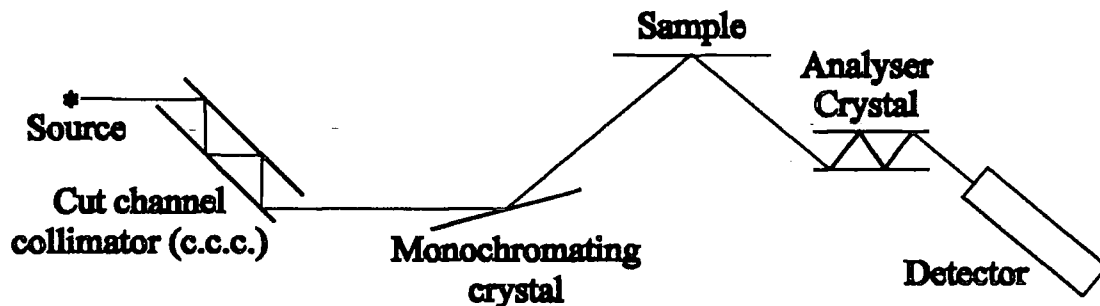
Fig 3.10   Schematic of the experimental set up for triple axis diffraction
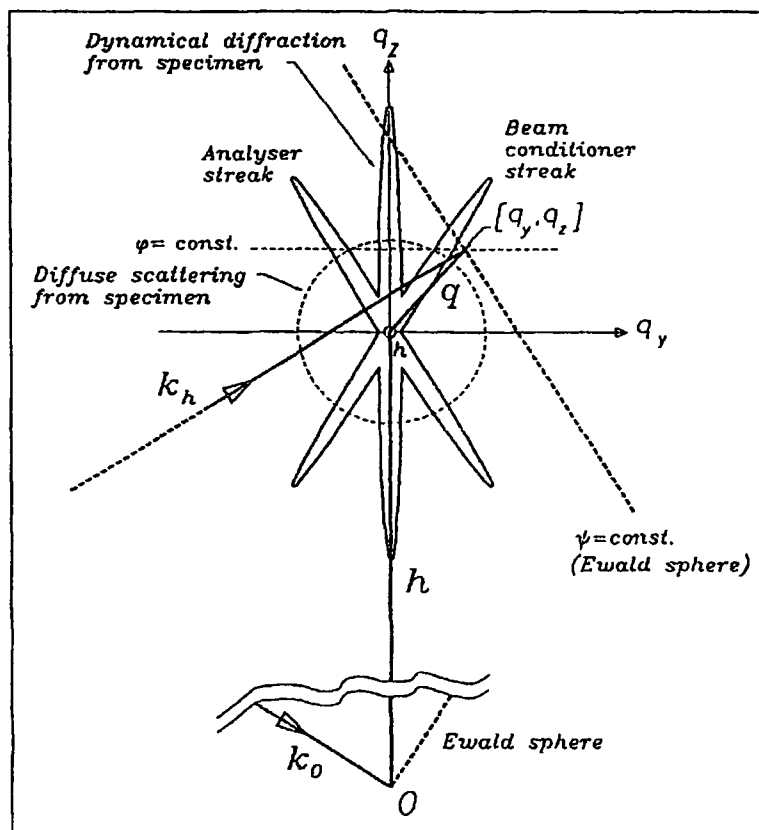
Fig 3.11   Region of reciprocal space around the hkl diffraction spot

3.1.9 Triple axis diffraction from asymmetric reflections

In an asymmetric reflection, the $\theta/2\theta$ and specimen only scans still map out the distributions of strains and tilts in the reflecting planes. However, this time there is an angular offset with respect to the surface. Due to q_z in reciprocal space being anchored to the surface normal, the resulting scans move through it in different directions to the symmetric case.

Consider the situation as shown in figure 3.12. Here the angle of incidence, θ' is related to the Bragg angle, θ, via $\theta' = \theta - \alpha$, where, α, is the angle of offcut. In addition, $\phi' = \phi$ and $\delta' = \delta + \alpha$. Ignoring refraction, the resulting transformation equations become.

$$q_z = \frac{4\pi}{\lambda}\sin(\frac{\phi}{2})\cos\delta' \qquad 3.19 \qquad\qquad q_y = \frac{4\pi}{\lambda}\sin(\frac{\phi}{2})\sin\delta' \qquad 3.20$$

In consequence, a $\theta/2\theta$ scan, moves on the radial line joining the origin of reciprocal space with the diffraction spot being studied, whereas a specimen-only scan moves orthogonally to this. The surface streak is still orientated along the q_z direction, by definition, and so is now at an angle, α, to the $\theta/2\theta$ scan.

3.1.10 Grazing incidence x-ray diffraction

Although Grazing incidence x-ray diffraction (GID) [8-11] has not been used in this study, its theoretical interpretation was used for the basis of x-ray diffuse scattering theory and so it is briefly reviewed here. In this arrangement, the reflecting planes lie perpendicular to the surface of the sample and the resulting scattering vector is in the plane of the surface. The incident wave impinges on the surface at an angle, α_i, which is close to the angle of total external reflection. In addition, the wave makes the Bragg angle with respect to the reflecting planes. The experimental arrangement is shown in figure 3.13. If α_i is less than the critical angle, an evanescent wave is produced which runs parallel to the surface of the sample. This wave satisfies the
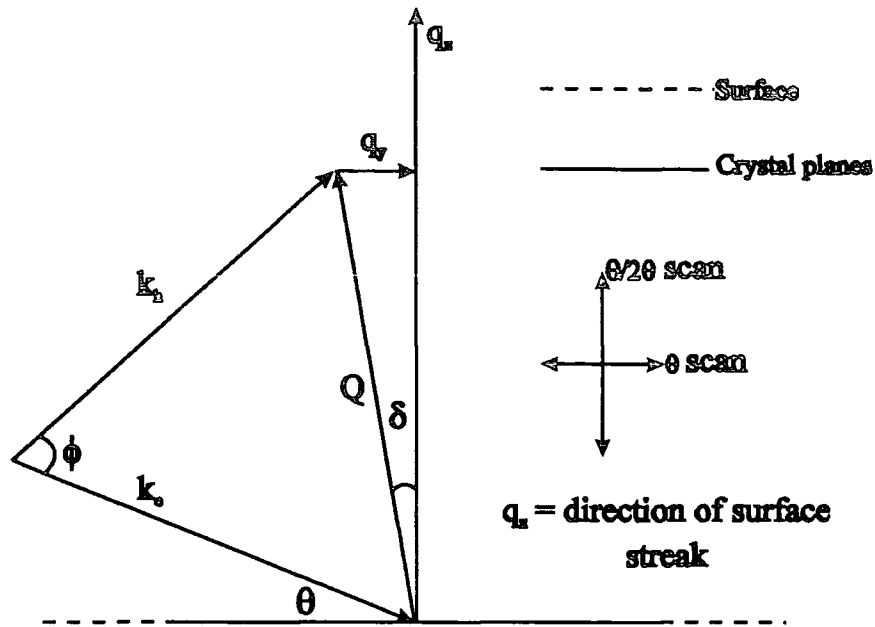
Fig 3.12a Calculation of the reciprocal vectors q_z and q_y for a symmetric reflection.

Here θ is both the angle of incidence with respect to the surface and the Bragg angle, ϕ is the scattering angle and δ is the angular offset from the q_z direction. k_o is the incident wavevector, k_h is the diffracted wavevector and Q is the scattering vector.
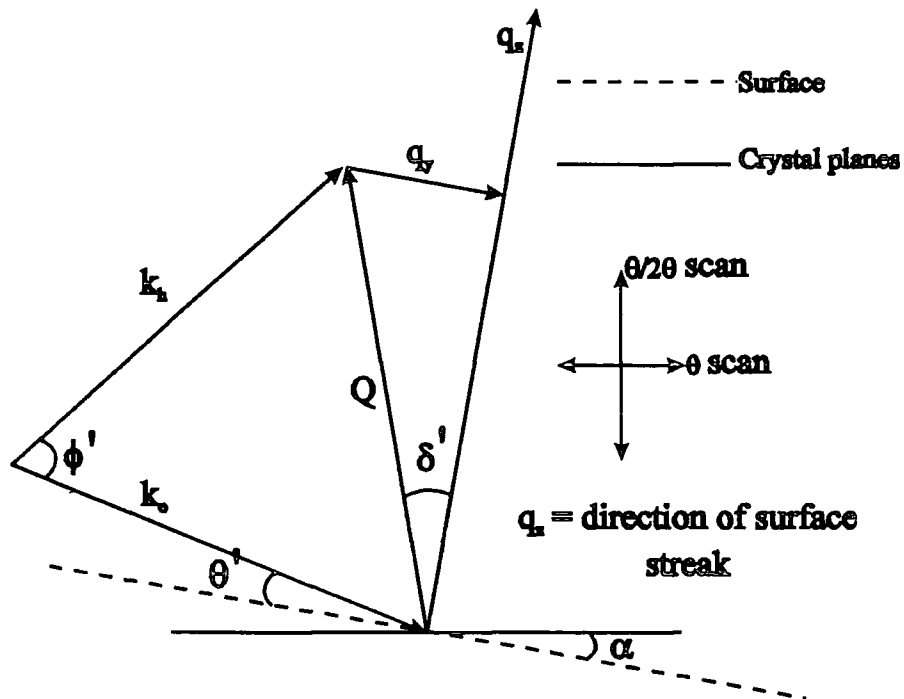
Fig 3.12b Calculation of the reciprocal vectors q_z and q_y for the same crystal planes, but with a surface off cut of angle α. Here refraction effects have been ignored.

The measured incident angle becomes $\theta' = \theta - \alpha$, the scattering angle remains constant and the angle with respect to q_z becomes $\delta' = \delta + \alpha$ since q_z is defined with respect to the surface.
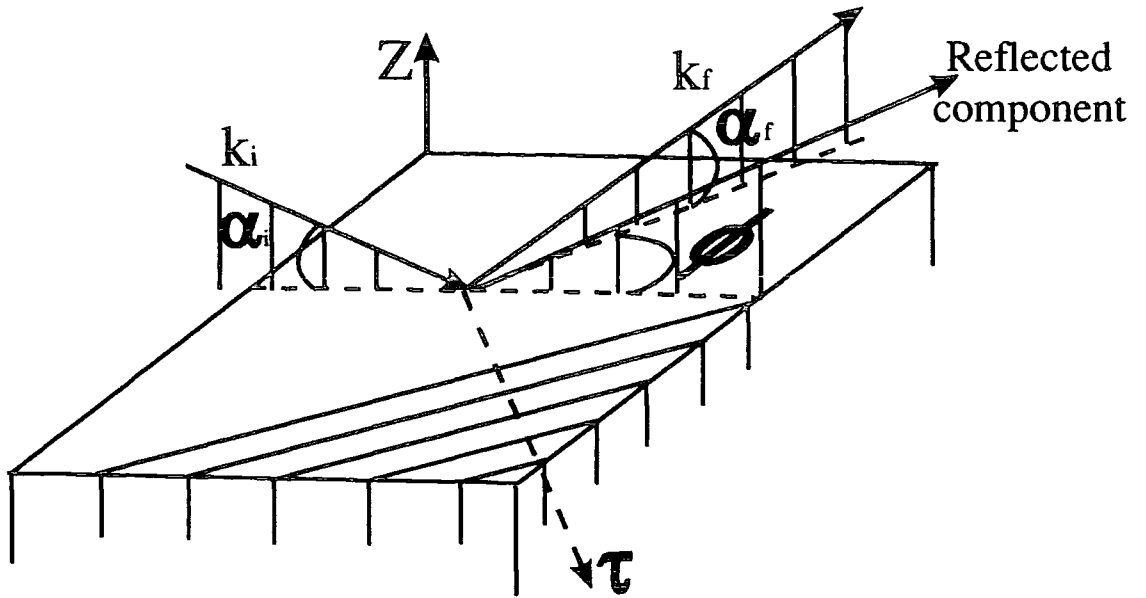
Fig 3.13 Experimental arrangement of the incident (k_i) and diffracted (k_f) waves vectors in grazing incidence diffraction. In addition there is the transmitted wave (τ) and the reflected wave which are in the same plane as k_i.

Bragg condition of the planes within the sample and diffraction occurs. As the evanescent wave is strongly damped into the material, the technique is extremely surface sensitive. The equation that describes the propagation of this wave is given below [12].

$$E_t = E_{ot} \exp(-\beta y) \exp\left(i\left(\frac{k_t x \sin\theta}{n} - \omega t \right) \right)$$

3.21

Here x represents the direction along the interface, y the penetration into the interface and θ the angle of incidence with respect to the surface normal. The value of β in the first exponential is a damping factor, whilst k_t is the wavevector of the transmitted wave and n is the refractive index of the medium. Finally E_{ot} and E_t are the amplitude and instantaneous value of the electric field vector within the medium.

Depth profiling can be achieved by changing the angle of incidence, α_i, with respect to the sample's surface. In this way depths can be probed ranging from 20 Å to 0.1 μm. Due to the depth of penetration and therefore the scattering volume being small, the intensity of the absolute intensity of the GID is small. As a result, the majority of such measurements take place at synchrotrons.

The usual kinematical theory is not valid in the regime of GID since very large refraction effects are present. Vineyard [13] avoided this problem by employing the distorted wave Born approximation (DWBA). Using this he split the permittivity of the sample into two. Firstly, he calculated the wavefields from the ideal continuum surface by using Fresnel's equations. Then he illuminated the atoms within the crystal with this ideal wavefield and calculated the scattering using the kinematical model, assuming that no further interactions occurred with the scattered waves and the medium. The resulting Bragg peak was predicted at an angle parallel to the surface of the sample ($\alpha_f = 0$). In reality however, this is not the case; the observed Bragg peak occurs at the critical angle with respect to the samples surface ($\alpha_f = \alpha_c$). This breakdown of the theory was explained four years later by Dosch [14]. He demonstrated that due to the reciprocity theorem, for exit angles less than the critical angle, only the very near surface can be probed (i.e. there is strong refraction). As the

angle of exit is increased towards the critical angle, a slightly deeper penetration is allowed. In consequence, more of each scattering plane is seen, and as the intensity of the diffracted wave is proportional to the scattering volume of the crystal, the observed Bragg intensity increases. For larger detector angles, when the angle, α_f, increases beyond the critical angle, the x-rays which are being detecting are originating from deeper inside the crystal. Since the diffracted wave is running parallel to the surface of the crystal, it cannot exit at an angle greater than θ_c and as such it contributes less to the observed scatter. In consequence, the observed intensity decreases and a peak of intensity is observed at the critical angle.

3.2 X-ray reflectivity

3.2.1 Introduction

At small incident angles, it is observed experimentally that x-rays are totally externally reflected from solid surfaces. Above some critical angle, penetration into the medium occurs and the (specular) reflectivity falls sharply (figure 3.14). For a single, perfectly flat, non absorbing interface, this fall off beyond the critical angle, θ_c, is proportional to $(2\theta)^{-4}$ [19].

For real interfaces, roughness is always present. The effect of roughness is to scatter some x-rays out of the specular direction, and so the observed reflectivity falls off more rapidly. As can be seen from figure 3.15, x-ray reflectivity is extremely sensitive to such roughness, making it one of the most sensitive technique for such measurements.

If a thin layer is present, interference (Kiessig) fringes are seen as shown in figure 3.16. The fringe period due to a layer of thickness, t, for a specific incident wavelength, λ is given by $\Delta\theta \cong \lambda/2t$, for $\theta \geq 2\theta_c$. The contrast of these fringes is related to the electron density difference at the air/layer and layer/substrate interfaces. If roughness is present on one, or both of the interfaces, then x-rays are scattered out of the specular direction, and the amplitude of the fringes changes, usually decreasing. For a multilayer system, low angle Bragg peaks are seen in the specular scans (figure 3.17). Again these arise from constructive interference from reflected waves from the bilayer interfaces.

When the diffuse scatter either side of the specular is probed, several effects are immediately apparent (figure 3.18). Firstly, the intensity of this is seen to increase as more roughness is present on the surface, and secondly, interference fringes are sometimes observed within it. In addition, two increases of intensity, or Yoneda wings, are seen whenever the incident or scattered beam makes the critical angle with the surface.
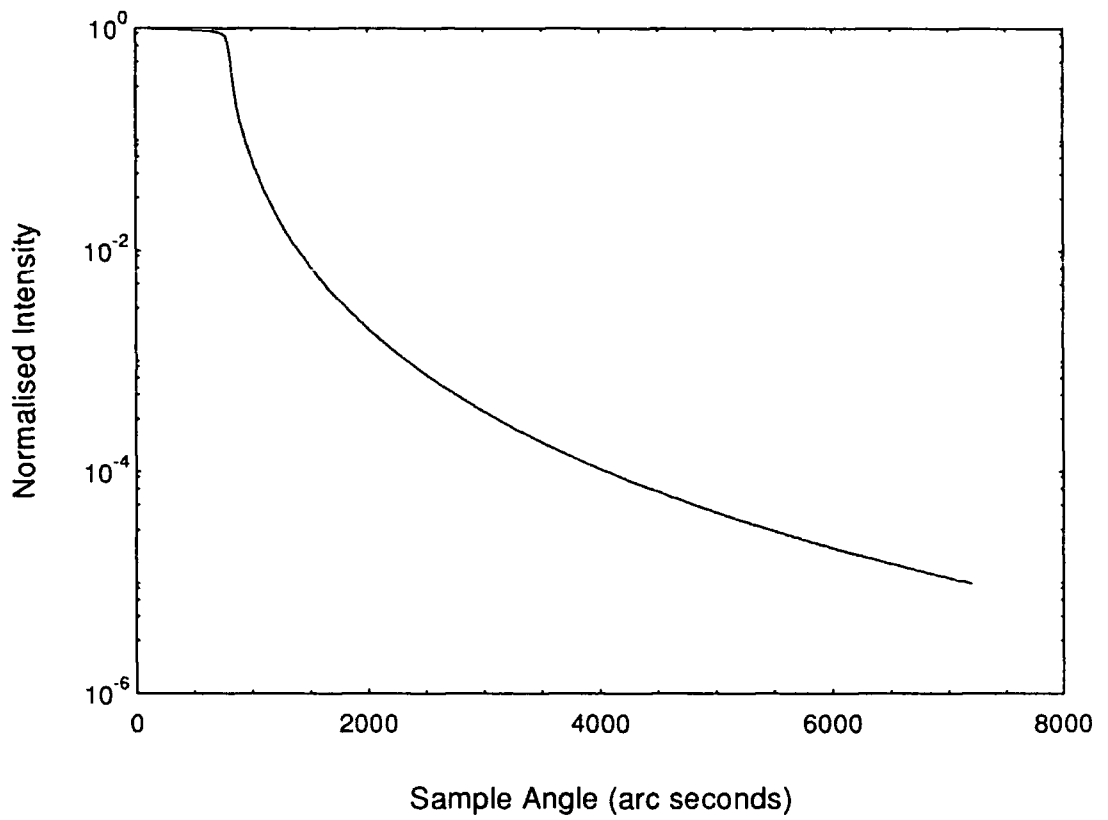
Fig 3.14   Calculated reflectivity from a perfectly smooth Si surface
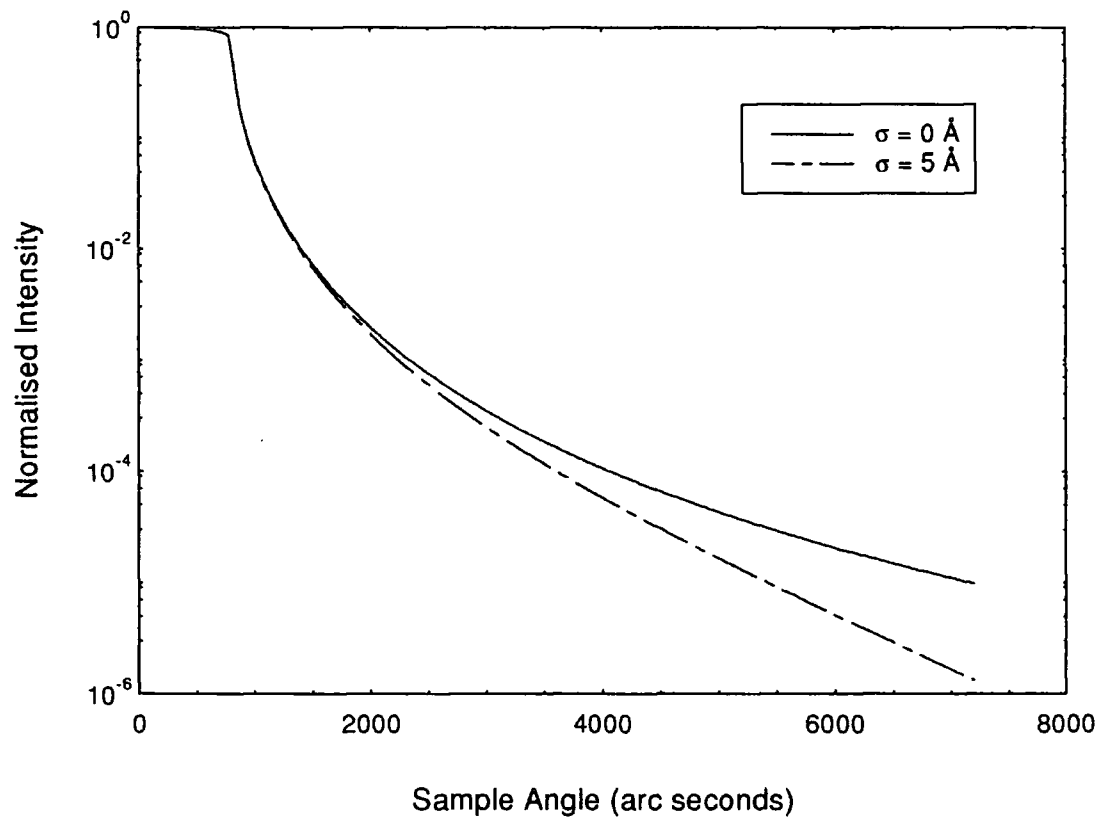
Fig 3.15   Calculated reflectivity from a perfect Si surface and one which
has 5 Å of roughness
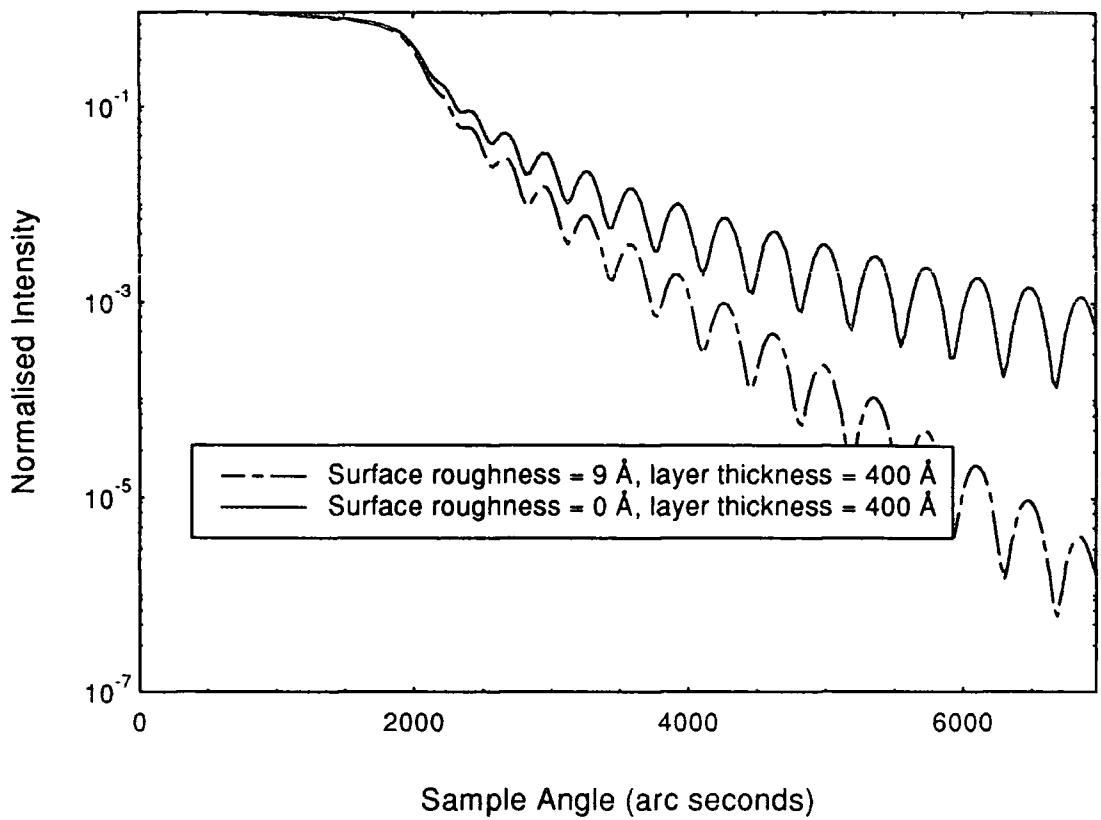
Fig 3.16   Calculated reflectivity from a 400 Å Au layer deposited on Si
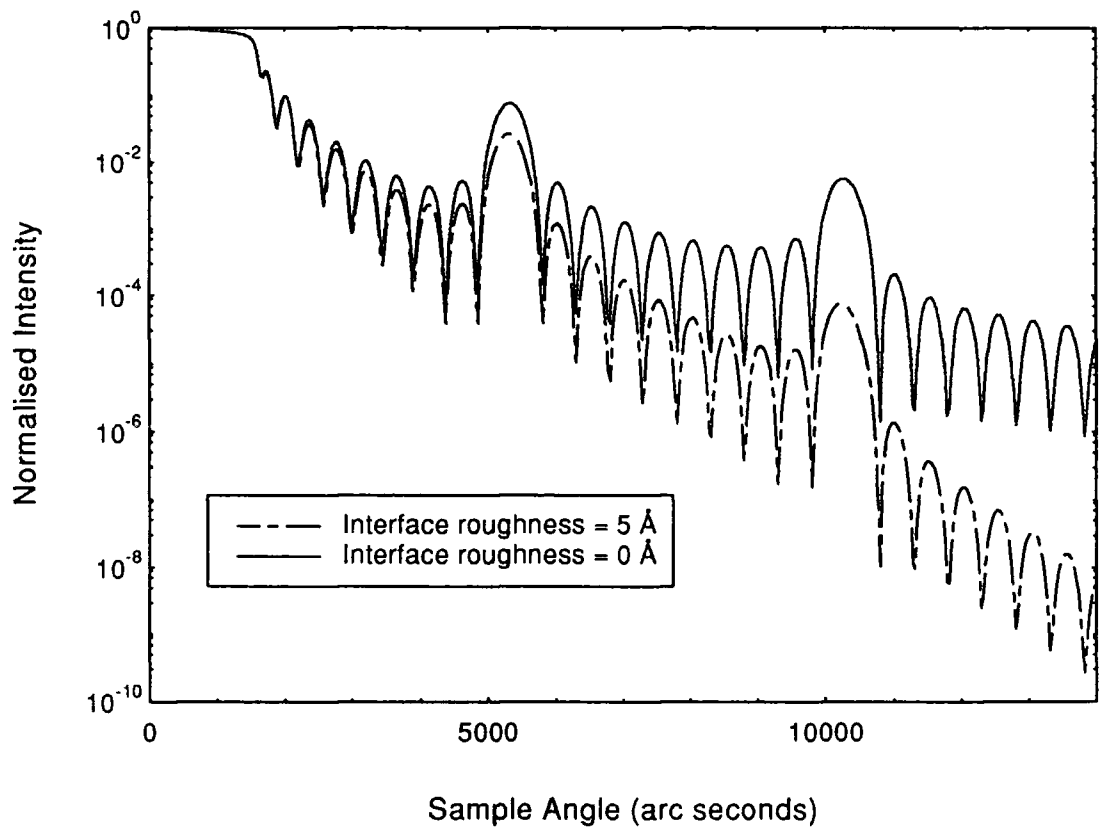
Fig 3.17 Calculated reflectivity from a ten period Au/Cu multilayer deposited on Si

As mentioned above, x-ray reflectivity depends simply on the electron density of the material and the way this varies with depth. As a result it can be used not only on crystalline materials, but also on amorphous or even liquid samples. It is a highly versatile technique, able to be used on layers from 1nm to 1μm in thickness.

3.2.2 History of x-ray reflectivity

References [15,16]

The first reports of x-ray reflectivity came from Compton in 1923 when he wrote about the total external reflection of x-rays from the surfaces of solids. Nothing much new happened for the next ten years until, in 1931, Kiessig, working on thin deposited layers, noticed that fringes were present in the x-ray reflectivity. Then, in 1940, DuMond reported that the reflectivity from periodic multilayers could give rise to Bragg peak, just like crystalline solids.

The foundations for modelling of specular reflectivity from multilayers were laid in 1954 when Parratt [17] generalised Fresnel's equations [12] to included layered systems. Later, in 1972, Nevot and Croce developed techniques for the inclusion of roughness.

The first reports on the observation of diffuse scatter came from Yoneda, in 1963 [18]. He noticed two anomalous lines, on his x-ray films, which he attributed to scatter out of the specular beam, due to dirt on the samples surface. However, it was in 1988, when Sinha [19] published his paper on the modelling of specular and diffuse scatter that the explosion in grazing incidence x-ray scattering studies (GIXS) occurred. Although the basis for this work had been done by Vineyard, in 1982 [13], the developments in computing power and diffractometers [20] in the late 80's made the technique much more widely available. Even so it was a couple of years before papers relating to diffuse x-ray scattering began to emerge in large numbers.

In the early 1990's, Lagally's group [21-26] developed methods for the determination of roughness by using a kinematical approximation and integrating diffuse scatter.

During the same time (1989) Sinha went on to try and include vertical correlations of the roughness in his models [27]. Great advances in the application of GIXS to multilayers came in 1992, when Holý et al turned their efforts from diffraction to reflectivity. Within two years, both uncorrelated [28,29] and correlated roughness [30,31] had been included in models, which provided graphically, explanations of the modulations in the observed diffuse scatter [28-32]. Such modulations like interference fringes in transverse diffuse scans and Bragg like peaks were quickly explained in terms of generalised Yoneda scattering [33]. The Bragg-like peaks had been seen some years before, but wrongly interpreted as amorphous scattering [34]. It is interesting to note, that the standing waves which generated these effects had long been known about in the fluorescence community [35].

Once the bones of the simulation techniques were in place, people moved on to the validity of modelling of surfaces. Work by people like Palasantzas [36-38] proposed different self affine models which perhaps could describe surface better than Sinha's version. At the same time, others checked the existing model against complementary surface sensitive techniques [39], with varying degrees of success.

Present day work has seen new models proposed for certain domain like materials which are not described as fractal surfaces [40]. Also terrace [41], island [16] and domain models [42] are in preparation. Finally, new types of data collection techniques have been investigated which get around some of the inherent problems with the present x-ray reflectivity geometry [43-46], whilst theories for which diffraction and reflection are occurring simultaneously are also under development [47].

3.2.3 Experimental requirements of x-ray reflectivity

A beam with an angular divergence less than a few tens of arc seconds and a low dispersion, $\Delta\lambda/\lambda = 1 \times 10^{-3}$, is required. Its vertical extent must be small, typically in the region of $100\mu m$, so that it is all intercepted by the sample, even at very small angles. The centre of rotation of both the specimen and detector axis must be within a few tens of microns and the beam must be incident at that point to the same accuracy.

3.2.4 Experimental procedure

There are four typical types of data collection strategies (figure 3.19). The most common is to scan the specimen and detector in a coupled $\theta/2\theta$ motion. Such a scan probes the vertical periodicities within the sample and moves along the q_z direction.

A similar scan to the $\theta/2\theta$, or specular scan, is the off specular longitudinal diffuse scan. This is performed, by offsetting slightly the initial position of the sample angle. Ideally this offset is by an amount, just large enough to avoid the specular scatter. Such a scan moves radially in reciprocal space. As a result, it probes certain surface frequencies (parallel to the x-ray beam), which display a vertical period as well, i.e. correlated roughness.

Sample only, or transverse diffuse scans, can also be performed. Due to the angular range of these scans being small, approximately a straight line in q_y is probed. This type of scan is not sensitive to vertical periodicities, but instead, solely the horizontal spatial frequencies across the surface. Such a scan therefore maps out the type of roughness on the interfaces.

Finally, detector only scans can be made. In these scans it is the sample that is held fixed, whereas the detector is scanned through the diffuse scatter. Such scans follow the effective Ewald sphere in reciprocal space and so map out both vertical and horizontal spatial frequencies. The constant sample angle means that the penetration depth and projected beam size on the sample are held constant.

3.2.5 Centre of rotation and its importance

A schematic diagram of a sample stage that is off the centre of rotation is shown in figure 3.20. On rotation of the sample stage by $\Delta\theta$, the reflected beam from a sample stage that is on the centre of rotation changes its angle by $2\Delta\theta$. However, the reflected beam from the stage that is off the centre of rotation has an additional lateral displacement. In order for this to pass through the analyser slits, the detector must be moved by an amount greater than $2\Delta\theta$. As a result, a $\theta/2\theta$ motion produces an
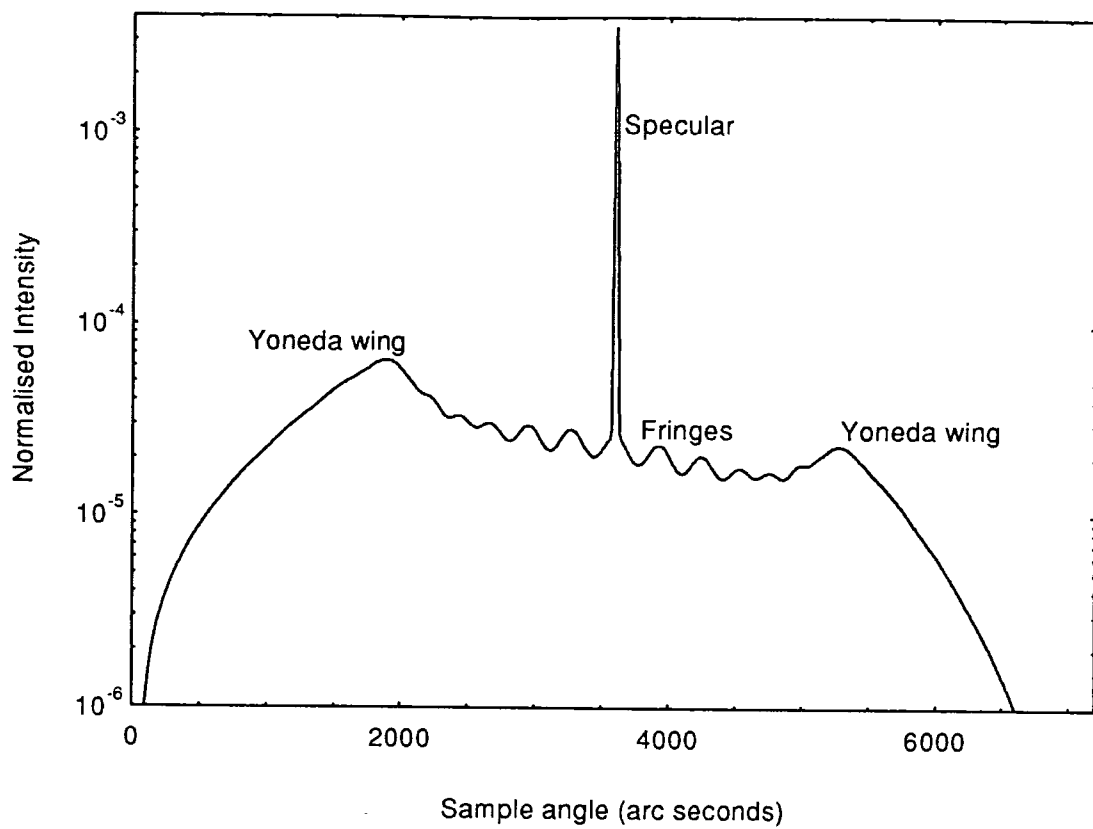
Fig 3.18   Typical transverse diffuse scan
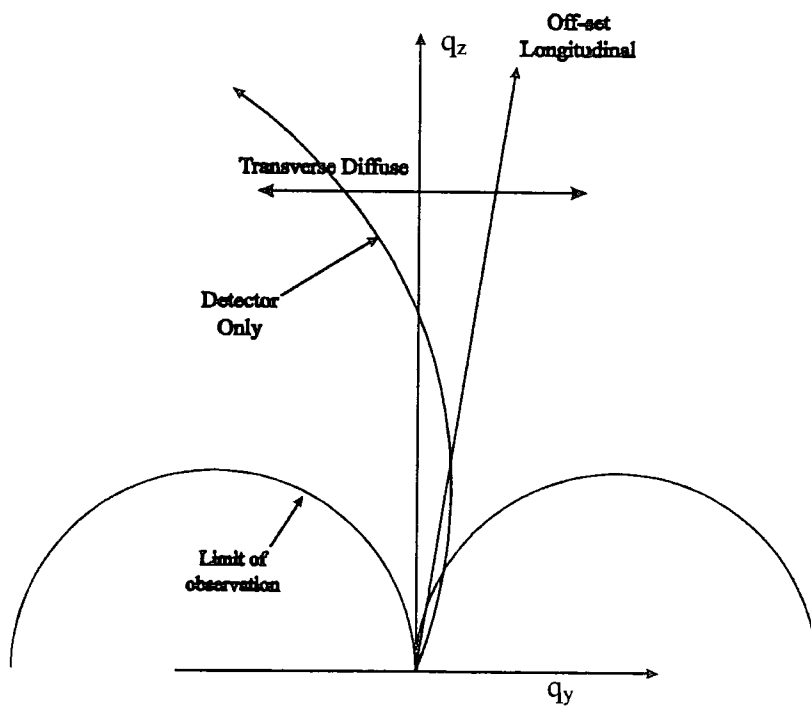
Fig 3.19   Movements of scans in reciprocal space

effective diffuse scan. Since the lateral offset increases with time, this gives rise to a quadratic movement in reciprocal space. The apparent angular offset Ω, is given by:

$$\Omega = \frac{x\theta}{z} \qquad\qquad 3.22$$

where θ is the sample angle, x is the distance from sample stage surface to the centre of rotation and z is the distance from the centre of rotation to the detector slits.

At the SRS, the FWHM of the beam is 15 arc seconds, the sample detector distance is 0.65 m and the largest sample angles are 5 degrees. In order to stay on the ridge ($\Omega < 3$ arc seconds) to these high angles, the surface of the sample stage must be on the centre of rotation within 100 micrometers.

3.2.6 The coherence length

Assuming that the source is radiating according to Fraunhofer diffraction, the lateral coherence length is defined as the spacial extent of the first Airy disk [12].

For such an extended source we have [48],

$$\varsigma_{\perp} = \frac{\lambda R}{r_s} \qquad\qquad 3.23$$

where R is the source sample distance and r_s is the source size.

Experiments such as Young's slits [12] demonstrate the existence of this effect (as does diffraction!) and it has been measured on certain instruments by using diffraction gratings [48] and pin holes [49].

Temporal coherence arises because, within the beam, wave trains emerge that are coherent for a certain length of time, and then suddenly randomly change their phase. The temporal coherence, $\zeta_\parallel$ is given by [48]:-

$$\zeta_\parallel \cong \frac{\lambda^2}{2\Delta\lambda} \qquad 3.24$$

3.2.7 Theory and simulation of x-ray reflectivity

X-rays are a form of electromagnetic radiation, and as a result their propagation is described using Maxwell's equations [50]. Maxwell's equations require that the tangential components of E and H to must be continuous across an interface [12]. From these boundary conditions Snell's law and Fresnel's equations can be derived.

The refractive index [51], n, of a material, is given by:

$$n = 1 - \delta - i\beta \qquad 3.25$$

where $\delta + i\beta$ may be written in terms of the atomic scattering factors of atoms of type a, of which there are N_a in unit volume of the material:

$$\delta + i\beta = \frac{\lambda^2 r_e}{2\pi} \sum_a \frac{\rho_a}{A_a} \left(Z_a + f_a' + if_a'' \right) \qquad 3.26$$

Here, δ is related to the dispersion within the medium and β the absorption. Z_a and

34

A_a are the atomic and mass numbers of the atomic species a, and f' an f'' are the real and imaginary parts of the dispersion corrections. Finally, r_e is the Bohr radius of an electron and ρ_a is the density of the species a.

In the region of the electromagnetic spectrum corresponding to x-rays, the refractive index is slightly less than unity. As a result, total external reflection of x-rays occurs at small angles of incidence. Assuming that there is no absorption in the medium, an equation for the critical angle can be derived from Snell's law.

$$\theta_c = \sqrt{2\delta} \qquad\qquad 3.27$$

However, since the refractive index for x-rays in solids is only slightly less than 1 ($1-n \approx 1 \times 10^{-5}$), the critical angle is small. Above this critical angle, penetration into the medium occurs and the reflectivity falls sharply. For a perfect interface the amplitude of the reflected wave is governed by Fresnel's laws.

Parratt [17] extended the formalism derived by Fresnel to include any number of interfaces. By matching the tangential components of E across an arbitrary (planar) interface (figure 3.21) he showed that the tangential components at the interface must be:

$$a_{n-1}E_{n-1} + a_{n-1}^{-1}E^R_{n-1} = a_n^{-1}E_n + a_nE^R_n \qquad\qquad 3.28$$
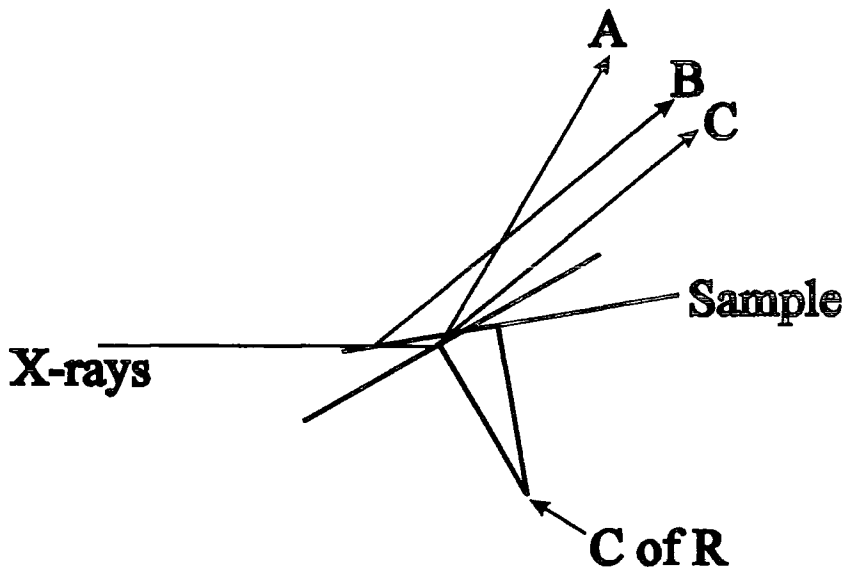
Fig 3.20. On rotation of this sample stage by an angle $\Delta\theta$, the reflected beam moves from position A to position B. However, for a sample which was on the centre of rotation, the reflected beam would have been in direction C. As a result, the detector angle is required to be increased by an amount $2\Delta\theta + f(\Delta\theta)$ in order to intercept the specularly reflected beam, B.
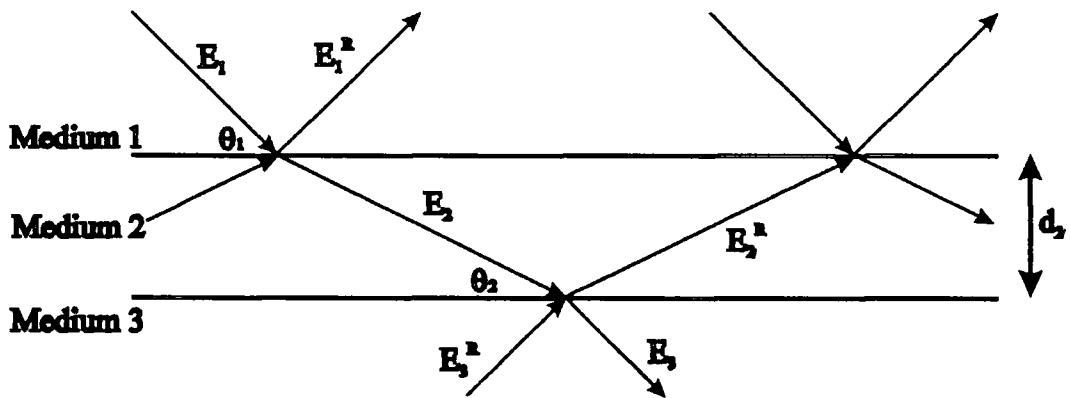
Fig 3.21   Ray diagram of x-rays within a layered system

The differential of (3.28) leads to a second simultaneous equation. The solution of these gives a recursive formula for the reflection amplitude $R_{n-1,n}$ of the stack of layers from the substrate to the interface between the nth and the $n-1^{th}$ layers:

$$R_{n-1,n} = a_{n-1}^4 \left[\frac{R_{n,n+1} + r_{n-1,n}}{R_{n,n+1} r_{n-1,n} + 1} \right]$$

3.29

$$R_{n,n+1} = a_n^2 \left[\frac{E_{n,n+1}^R}{E_{n,n+1}} \right]$$

3.30

$$r_{n-1,n} = \frac{(f_{n-1} - f_n)}{(f_{n-1} + f_n)}$$

3.31

$$f_n = (\theta^2 - 2\delta_n - 2i\beta_n)^{1/2}$$

3.32

and a_n is the phase factor for half the layer thickness d_n

$$a_n = \exp\left(\frac{-i\pi f_n d_n}{\lambda} \right)$$

3.33

The recursive formula is solved by starting at the substrate (layer N), whose thickness is assumed infinite and therefore has no reflected wave in it; hence $R_{N,N+1}$ is zero.

The equations are solved with n=N and continued recursively until the top layer of the material is reached (n=1) where a_n is unity, giving the reflectivity

$$R_{0,1} = \frac{E_{0,1}^R}{E_{0,1}}$$

3.34

The ratio of the reflected to incident x-ray intensities is given by the product of $R_{0,1}$ with its complex conjugate.

$$\frac{I_r}{I_o} = |R_{0,1}|^2 \qquad\qquad 3.35$$

3.2.8 Inclusion of roughness in specular simulation

Real surfaces and interfaces are not infinitely sharp, as in the ideal case described above, but have some roughness and some gradual change in electron density as shown in figure 3.22. This can be taken into account by perturbation theory in terms of both the Born and Distorted Born Wave Approximations (sections 3.2.11, 3.2.12).

A form for the reflection amplitude that matches both the DWBA and the Born approximation in their respective regimes of validity is given by [19,52]:

$$r = r_F \exp\left(-\frac{1}{2}\sigma^2_{n-1,n}Q_nQ_{n-1}\right) \qquad\qquad 3.36$$

where σ is the roughness on the interface, and $Q_n = k_n' - k_n$.

By substituting the above expression into the recursive theory described above gives the result that:

$$r_{n-1,n} = \left[\frac{f_{n-1} - f_n}{f_{n-1} + f_n}\right]\exp\left(-\frac{1}{2}\sigma^2_{n-1,n}Q_nQ_{n-1}\right) \qquad\qquad 3.37$$

for the reflection amplitudes from the n-1th and n[th] layers. This modified theory of Parratt works up to a roughness given by the limit of the DWBA.

37

3.2.9 Modelling of vertical grading

Another situation in which the interface is not sharp is when there is vertical grading. In this case, no lateral density variations are present, but instead a gradual change from one density to the next is observed. Due to there being only vertical density variations, no diffuse scatter is created. However, this grading has a significant effect on the observed specular scatter.

Specular scatter arises as a result of a discontinuity in electron density. In the case of grading, a myriad of small density changes occur in moving between the two regions (figure 3.23). As a result, many specularly reflected beams are produced, which are all slightly out of phase and therefore interfere destructively. Mathematically this is modelled as [19,53]:

$$r = r_F \int_{-\infty}^{\infty} \left(-\frac{1}{\rho_{-\infty}} \frac{d\rho(z)}{dz} \right) \exp(-iQz) dz \qquad 3.38$$

where r is the observed reflectivity, r_F is the Fresnel reflectivity and $\rho(z)$ is the density at height z.

It is clear from the above equations and figures 3.22 and 3.23 that by performing solely specular scans, no distinction can be made between true roughness and grading. In order to separate these two effects, simulations of the diffuse scatter must be undertaken.

3.2.10 Simulating diffuse scatter

Diffuse scatter arises, due to lateral inhomogeneities in electron density, which introduce a lateral component of momentum transfer into the reflected (and transmitted) beam. Due to the wavelength of the x-rays being on an atomic scale, macroscopic quantities cannot initially be assumed, and the surface must be simulated as a multitude of point scatterers. However, since the wavefield is coherent, for a
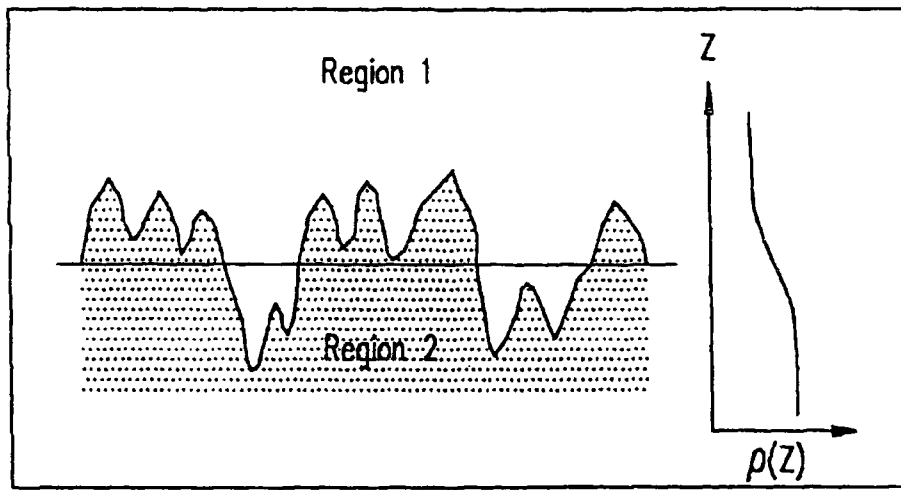
Fig 3.22   Variation of density, ρ, with z, for a rough interface
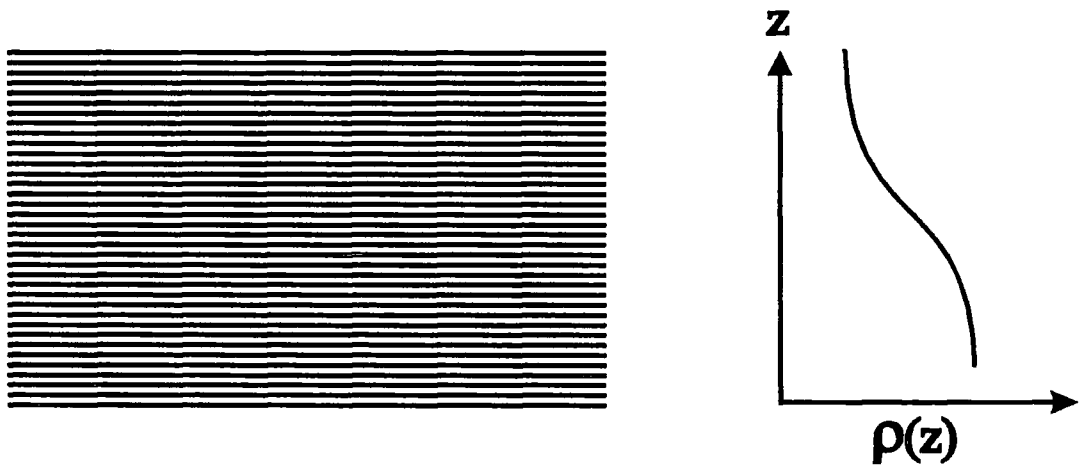
Fig 3.23 Variation of density, ρ, with z for a interface with vertical grading

smooth interface this averages back to the Fresnel equations, as is observed experimentally.

When roughness is present, an additional interference function is generated, which corresponds to the distribution of spatial frequencies across the sample. This interference function is what is observed as the diffuse scatter.

As a result, models for the simulation of diffuse scatter must include both the statistical distribution of the roughness and be able to sum the scattered waves. The bones of the summation is introduced using the Born Wave and Distorted Wave Born Approximations. Whilst the statistical distribution of the surface heights (and therefore the surface potential) is modelled here using random variables and a self affine description of the surface.

3.2.11 The Born wave approximation

The Born wave approximation [54] is a specific use of 'Fermi's golden rule' [55] to calculate the transition probability from a wavevector k to k' in the vicinity of an additional localised potential, v(r). These two states are defined to be plane waves incident upon a general potential. As the surface itself [47] can be described as a scattering potential of the form:

$$v(r) = k^2[1-n(r)] = \text{constant within a medium of uniform n.} \qquad 3.39$$

and

$$v(r) = \begin{cases} 0, r > a \\ \text{const}, r < a \end{cases} \qquad 3.40$$

The Born wave approximation

$$\frac{d\sigma}{d\Omega} = \int_V \int_V V(r) \exp\left[-iq(r-r')\right] dr dr' \qquad 3.41$$

can be thus reduce to [19]:

$$\frac{d\sigma}{d\Omega} = N^2 b^2 \int_V \int_V \exp\left[-iq \cdot (r-r')\right] dr dr' \qquad 3.42$$

where $d\sigma/d\Omega$ is the differential cross section, N is the scattering particle density and b is the scattering length.

These volume integrals can be translated to surface integrals using Stokes' theorem [4] and the dependence on $r(x,y,z)$ split into its horizontal (x,y) and vertical $z(x,y)$ components. Once this is done, the roughness can be introduced as a statistical variation on the surface heights and as a result, the exact region over which $v(r)$ extends.

The resulting differential cross section can be converted to a power spectrum and for surfaces which posses a cut off (section 3.2.15) the scatter splits into a specular and a diffuse component. The definition of the power spectrum is as follows:

$$S(q) = \frac{d\sigma}{d\Omega} \frac{1}{N^2 b^2 L_x L_y} \qquad 3.43$$

Here $S(q)$ is the power spectrum and the product $L_x L_y$ is the area of illumination on the surface of the sample.

The result of doing this is that the equation for the specular component of reflectivity becomes:

$$|R^2| = \left[\frac{(1-n^2)}{4\sin^2 \frac{\phi}{2}} \right] \exp(-q_z^2 \sigma^2) \qquad 3.44$$

whilst the power spectrum of the diffuse scatter is given by:

$$S_{diff}(q) = \frac{2\pi}{q_z^2} \exp(-q_z^2 \sigma^2) \int_0^\infty dR R F(q_z, \theta, R) J_o(q_r R) \qquad 3.45$$

where J( ) is a Bessel function and F( ) is given by:

$$F(q_z^2, R) = \exp\left\{ \sigma^2 q_z^2 \exp\left[-\left(\frac{R}{\xi}\right)^{2h} \right] \right\} - 1 \qquad 3.46$$

where ξ is the correlation length and h is the fractal exponent.

In summary, the Born wave approximation assumes that each piece of surface acts as a point scatter (all scatterers inside the medium cancel). By knowing the relative (statistical) positions of these scatters, the diffuse scatter can be calculated by adding the phases of their scattered waves (c.f. kinematical diffraction theory, section 3.1.1). This approximation is only valid for high scattering vectors or low roughness. High scattering vectors are required so that there is no strongly reflected component and this makes sure that the situation is restricted to the two beam case. The low roughness is required so that the perturbation does not become too large. Finally since the theory is kinematical (i.e. no transmitted wave) no rereflections (i.e. dynamical effects) are considered.

3.2.12 The distorted wave Born approximation

This approximation assumes that in the zero roughness state, three waves are present, as described by Fresnel's laws. In this case the surface scattering potential can be split into two [19].

$$V = V_1 + V_2 \qquad 3.47$$

where V_1 is the average (perfect) surface for which the solution is known to be Fresnel's laws, i.e.

$$V_1 = \begin{cases} k_o^2(1-n^2), & -a < z < 0 \\ 0, & z > 0 \end{cases} \qquad 3.48$$

and V_2 is the perturbation due to roughness, i.e.

$$V_2 = \begin{cases} k_o^2(1-n^2), & 0 < z < z(x,y) \text{ if } z(x,y) > 0 \\ -k_o^2(1-n^2), & z(x,y) < z < 0 \text{ if } z(x,y) < 0 \\ 0 & \text{elsewhere} \end{cases} \qquad 3.49$$

Here $z(x,y)$ is the statistical distribution of the roughness and k_o is the magnitude of the wavevector in free space.

This second potential, V_2, is illuminated by the plane waves given by the solution of Fresnel's laws and deforms them (hence the name 'distorted wave'). The resulting transition probability is thus:

$$< 2|T|1 > = < \tilde{\psi}_2|V_1|\phi_1 > + < \tilde{\psi}_2|V_2|\psi_1 > \qquad 3.50$$

where ϕ_1, is the incident plane wave, ψ_1, is the solutions to Fresnel's laws and $\tilde{\psi}_2$ is the time reversed final state. The time reversed state is required so that a well defined final state exists [56].

After 'some' manipulation the DWBA reduces to:

$$|\tilde{R}(k_1)|^2 \cong |R(k_1)|^2 \exp(-q_z q_z' \sigma^2)$$ 3.51

for the specular scatter, where q_z and q_z^t is the momentum transfer for the reflected and transmitted beams respectively

and

$$\left[\frac{d\sigma}{d\Omega}\right]_{diff} = (L_x L_y)\frac{|k_o^2(1-n^2)|^2}{16\pi^2}|T(k_1)|^2|T(k_2)|^2 S(q_t)$$ 3.52

for the diffuse scatter where $L_x L_y$ is the area of illumination on the surface, $|T(k_1)|^2$ and $|T(k_2)|^2$ are the Fresnel transmission coefficients for the time forward and time reversed cases respectively. Here k_1 and k_2 are the incident and scattered wavevectors respectively ($q = k_2 - k_1$). In addition, $S(q_t)$, the power spectrum or structure factor is given by:

$$S(q_t) = \frac{\exp\{-[(q_z^t)^2 + (q_z^{t*})^2]\sigma^2/2\}}{|q_z^t|^2}\iint_{s_o} dXdY(e^{|q_z^t|^2 C(X,Y)} - 1)e^{i(q_x X + q_y Y)}$$ 3.53

where $X = (x - x')$ and $Y = (y - y')$ on the surface of the sample.

The inclusion of Fresnel's equations, brings in also the results of Maxwell's laws for the reflection, refraction, and transmission of waves at an interface. In doing so, a knowledge of the critical angle is included in the theory. Some people have suggested [57,58] that when roughness is present the Fresnel amplitudes should be reduced by multiplying them by an exponential, whose argument includes the rms roughness and the scattering vector.

In summary, the DWBA works on the same principles as the BWA. However in addition it encompasses Fresnel's laws and does not require two plane waves as the final state. The DWBA gives a much better description of the scattering at small q_z,

because its initial state better describes the wavefields in reality than the Born approximation. In addition, this theory can be used to higher roughness values (nanometers) since only the roughness is acting as a perturbation and not the entire surface. However, the DWBA deviates for values of $(q_z\sigma)$ greater than 1. This is due to the expansion of the Gaussians that have been made whilst deriving the equation for reflectivity (3.51).

Some comparisons of the predictions of the distorted wave Born approximation with the Born wave approximation and the 'adhoc Debye Waller factor', used in the extension of Parratt's theory, are shown in figures 3.24 and 3.25. From these calculations it can be clearly seen that the BWA breaks down at high roughness values or low scattering vectors and as such any measurements using the BWA require correcting using the DWBA.

3.2.13 Self Affine surfaces

Self affine surfaces [39] are a broad class of functions, of which, the better known self similar, or fractal surfaces are just one subset. As with fractals, self affine surfaces display a scaling behaviour as the length scale of observation is changed. However unlike fractal surfaces, this scaling behaviour is anisotropic and follows the form.

$$z(x) \approx b^h z(bx) \qquad\qquad 3.54$$

Here, $z(x)$ is the height of the interface at the point x and h is the self affine (or Hölder) exponent. In the case of 2-D surfaces, h can vary between 0 and 1. For the special case of $h = 1$, the transformation is isotropic and the surface becomes self similar.

If by some means, the length scale, x, on which the height separations can be measured is changed, it is found that the height separation changes as a power law, $\Delta(l) \approx l^h$. Methods are available to calculate this [39] such as the ball method, box method or measurements from the correlation function. Such techniques involve plotting log-log graphs in order to extract the fractal exponent from the slope.
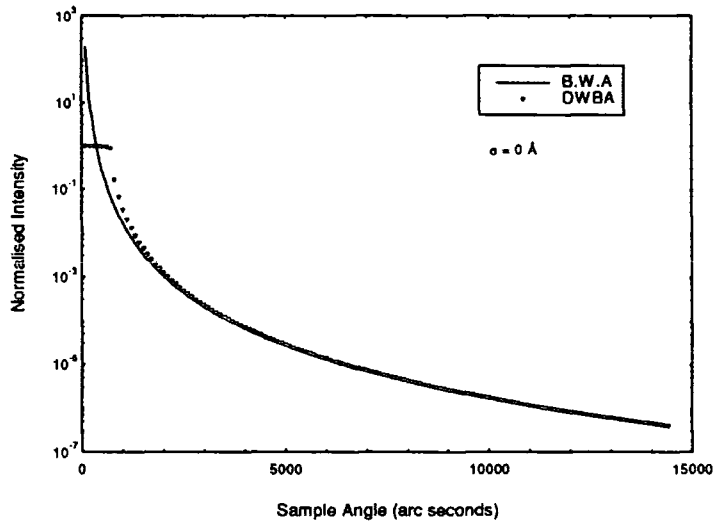
a   0 Å of surface roughness
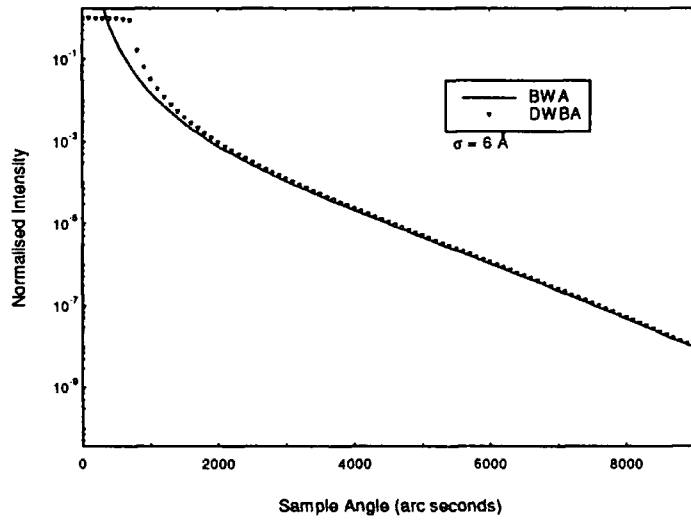
b   6 Å of surface roughness
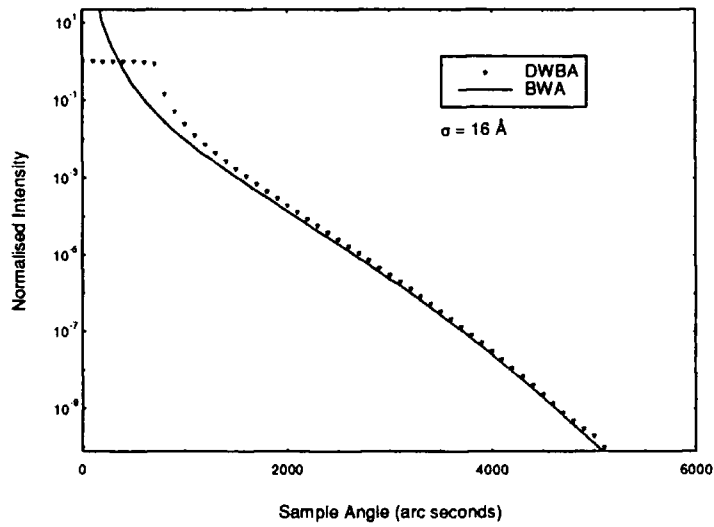
c   16 Å of surface roughness

Fig 3.24 Comparison of the predicted reflectivity from a single Si surface using the DWBA and the BWA
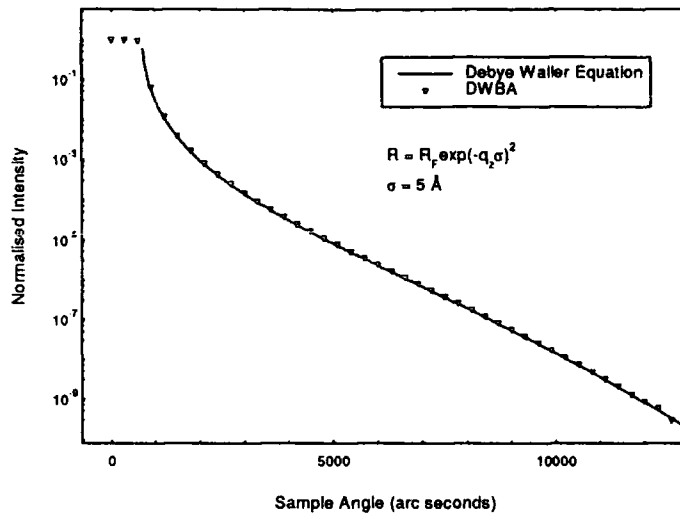
a   5 Å of surface roughness
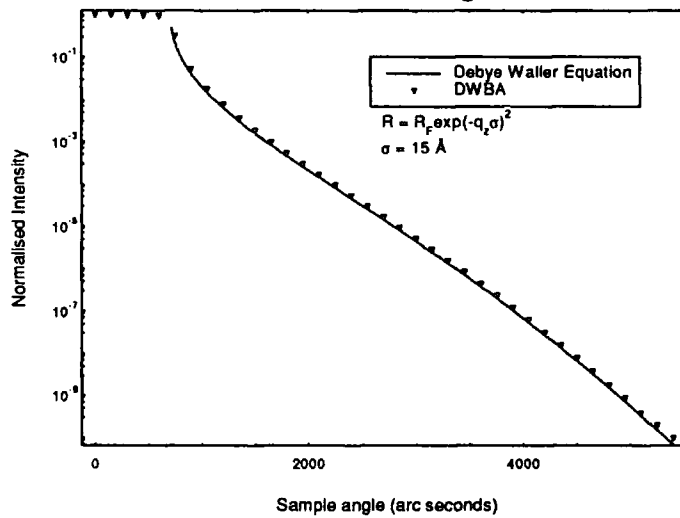
b   15 Å of surface roughness
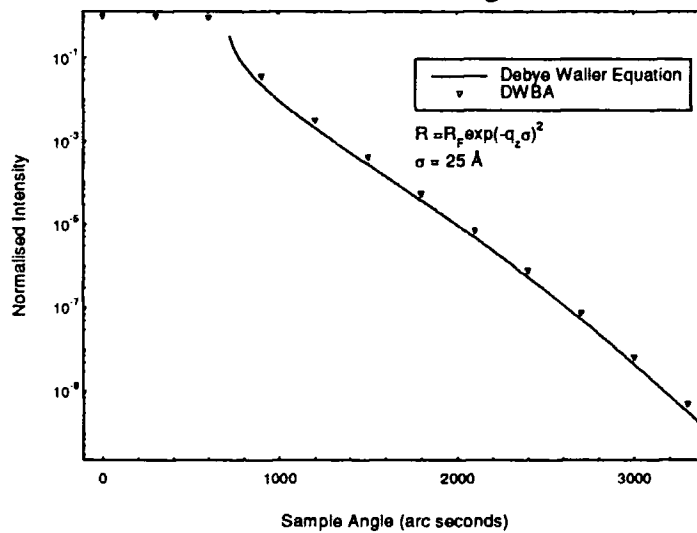
c   25 Å of surface roughness

Fig 3.25   Comparison of the predicted reflectivity from a single Si surface using the DWBA and the Debye Waller reflectivity equation

The type of interfaces discussed so far are known as a deterministic self affine surfaces. This is because, if they are scaled by the required transformation, then they overlay a larger magnification exactly. However, in the case of deposition processes, which lead to statistical surfaces, a more useful form is the statistical self affine surface. This does not physically overlap but shows statistical properties which scale as a power law. An example is the trajectory of a random walker (i.e. Brownian motion) which is shown in figure 3.26. For this it is found that the deviation of its position from the mean varies as:

$$<[x(t_2) - x(t_1)]^{1/2}> \propto \Delta t^{1/2} \qquad\qquad 3.55$$

3.2.14 The results of growth models

Over the years, many models have been used to try and simulate the effect of growing interfaces by the use of ballistic deposition processes [39]. From these, a rough interface is observed[†], which has a particular lateral correlation length. This correlation length continues to increase with growth time, eventually saturating when it reaches the system size. The roughening of the interface arises physically from the random nature of the incident particle flux. The origin of the lateral correlation length is not fully understood. However, it seems to stem from the fact that since a single particle can produce offshoots diagonally over time it can give 'knowledge' of its position to other regions of the interface as growth progresses. In consequence, a lateral correlation between the roughness develops. (figure 3.27)

[†] The interface roughness also scales as a power law, for short time scales. It saturates when the correlation length stops increasing. Again this is not fully understood.
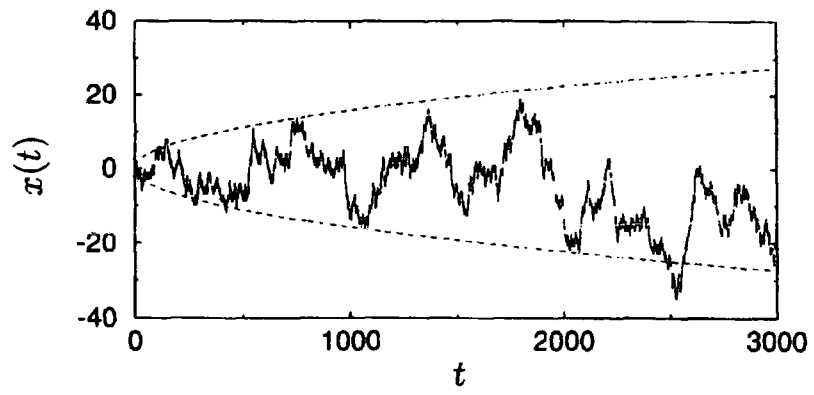
Fig 3.26   Self affine scaling behaviour of the rms deviation from the
mean in Brownian motion
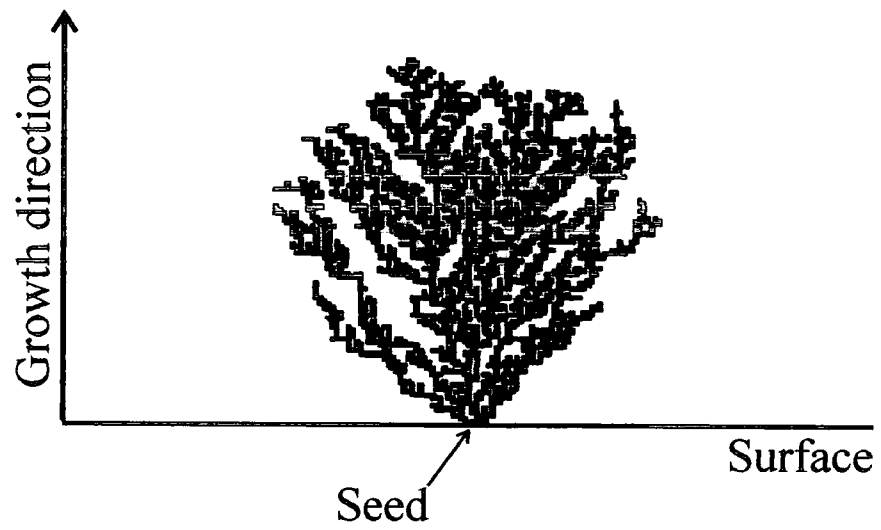
Fig 3.27   Growth of a self similar surface by ballistic deposition.   Lateral
off shoots are clearly visible.

3.2.15 Statistical descriptions of surfaces

For true statistically self similar functions [19,39], the height difference correlation function:

$$g(X,Y) \equiv <[z(x',y')-z(x,y)]^2> \equiv g(R) = AR^{2h} \quad ; (X,Y) \equiv (x'-x,y'-y) \qquad 3.56$$

shows a self similar scaling behaviour for all length scales observed (figure 3.28).

However, in growth processes, this scaling is cut short by the existence of a correlation length on the surface. In real systems, this cut off occurs well below the system size due to other dominating finite size effects. An example of these is the grain size in MBE or sputter grown samples. Since the individual grains have developed completely separately, when they finally coalesce they can be statistically independent.

As a result, functions of the form[19,36-38]:

$$g(R) = 2\sigma^2[1-exp(-(R/\xi)^{2h})] \qquad 3.57$$

have been introduced. Where σ is the RMS roughness of the surface, h is the fractal exponent and ξ is the lateral correlation length of the roughness. These equations show true self similar behaviour for $R<<\xi$, but saturate to a particular RMS roughness for $R>>\xi$. As a result ξ gives a cut off length between the regimes of self similarity and saturation. Figure 3.29 shows g(R) plotted for different values of h.

In x-ray scattering experiments, however, it is not the height difference that is measured but the Fourier transform of the spatial frequencies on the surface. It is therefore convenient to define a height-height lateral correlation function, C(X,Y).
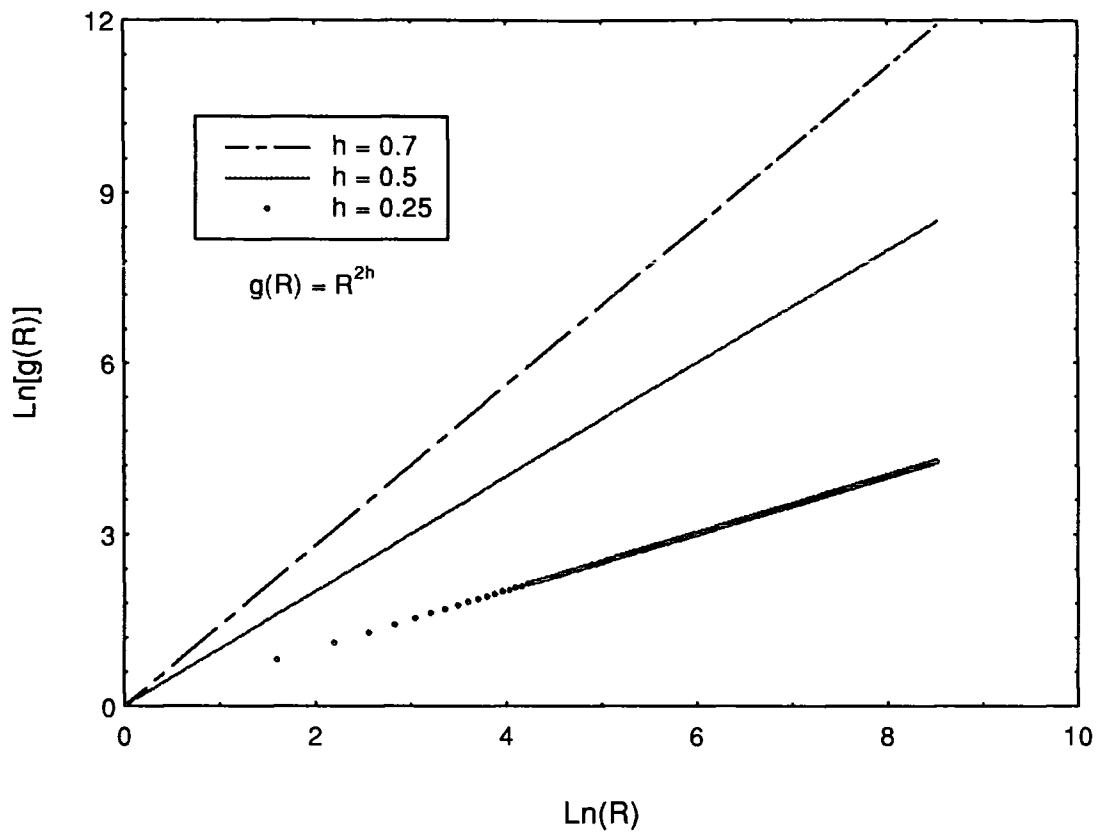
Fig 3.28   Scaling behaviour of a self affine surface with no cut off
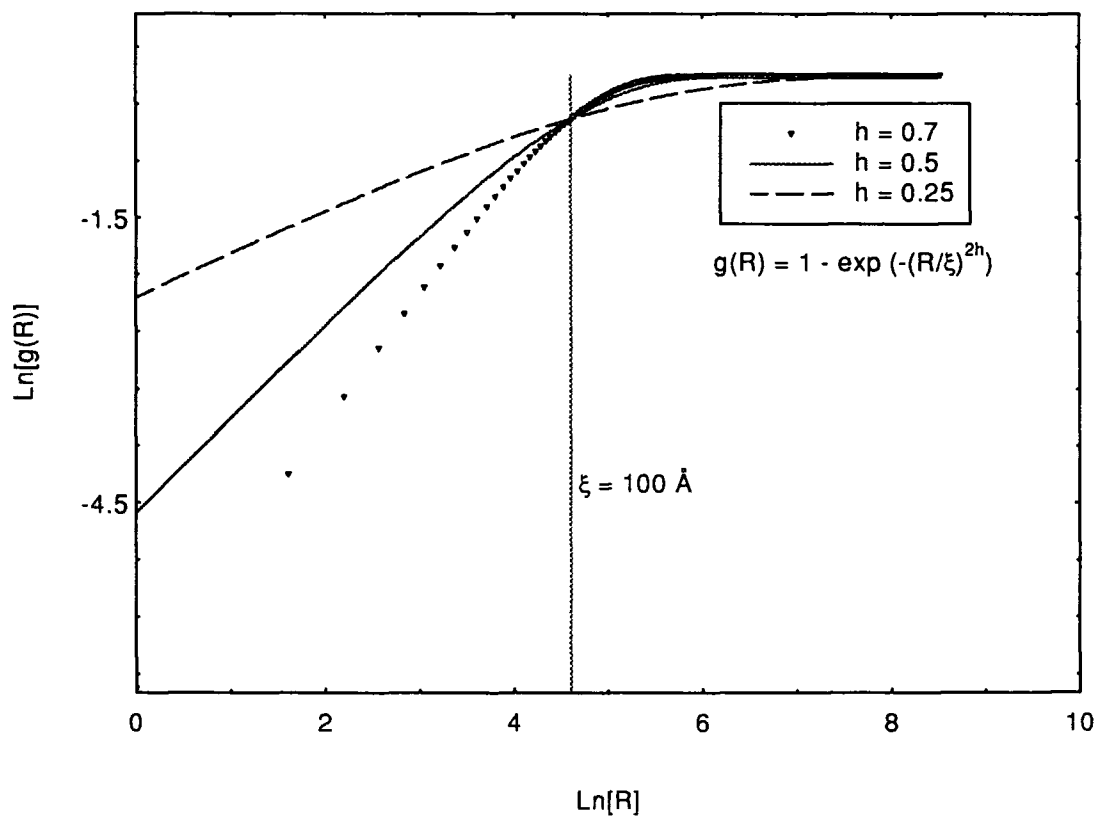
Fig 3.29   Scaling behaviour of a self affine surface with a cut off

This gives the degree of correlation (or knowledge) that one point has of another over a particular lateral length scale, R and is defined as:

$$C(X,Y) \equiv \langle z(X,Y)z(0,0)\rangle = \sigma^2 - (1/2)g(X,Y) \qquad 3.58$$

As a result the lateral correlation function which is derived from (3.57) becomes:

$$C(X,Y) = \sigma^2 \exp(-(R/\xi)^{2h}) \qquad 3.59$$

Figure 3.30 shows this correlation function for various values of h. It can be seen from this, that the lateral correlation length, ξ, is a tie point, defining the point at which the correlation function has dropped to a value of 1/e.

As it is the frequencies of the roughness that are being measured in a x-ray scattering experiment, it is expected that varying the parameters in g(R) will affect the distribution of the diffuse scatter. The results of such variations in σ, ξ and h are shown in figures 3.31 a,b,c respectively. The effect of raising σ, is to increase the amount of scatter out of the specular direction, and thus the diffuse intensity increases. As can be seen from figure 3.29, increasing the correlation length moves the distribution of roughness to longer wavelengths. As a result, a general rise in the low q_y region is observed. Finally changing h, alters the fall off with R and so changes the shape of the decrease in intensity with q.

Due to the relationship between the length scales on the surface and h, it is possible that its value may be determined from a log-log plot of intensity vs. q [19,43,46]. This arises because the intensity and q are related to g(R) and R respectively and that g(R) displays a power law for R<<ξ. However, due to the reciprocal nature of such experiments, in order to approach the region in which self affine scaling is occurring, very large q values must be measured. The effect of moving out to high $q_{(x,y)}$ is shown in figure 3.32. Here a log-log plot of the Fourier transform of the surface frequencies clearly shows a power law scaling behaviour for large q as a function of R. It must be noted that the approximation of the power spectrum, $S(q_t)$ in a transverse scan, to the Fourier transform of the correlation function is only valid in the region
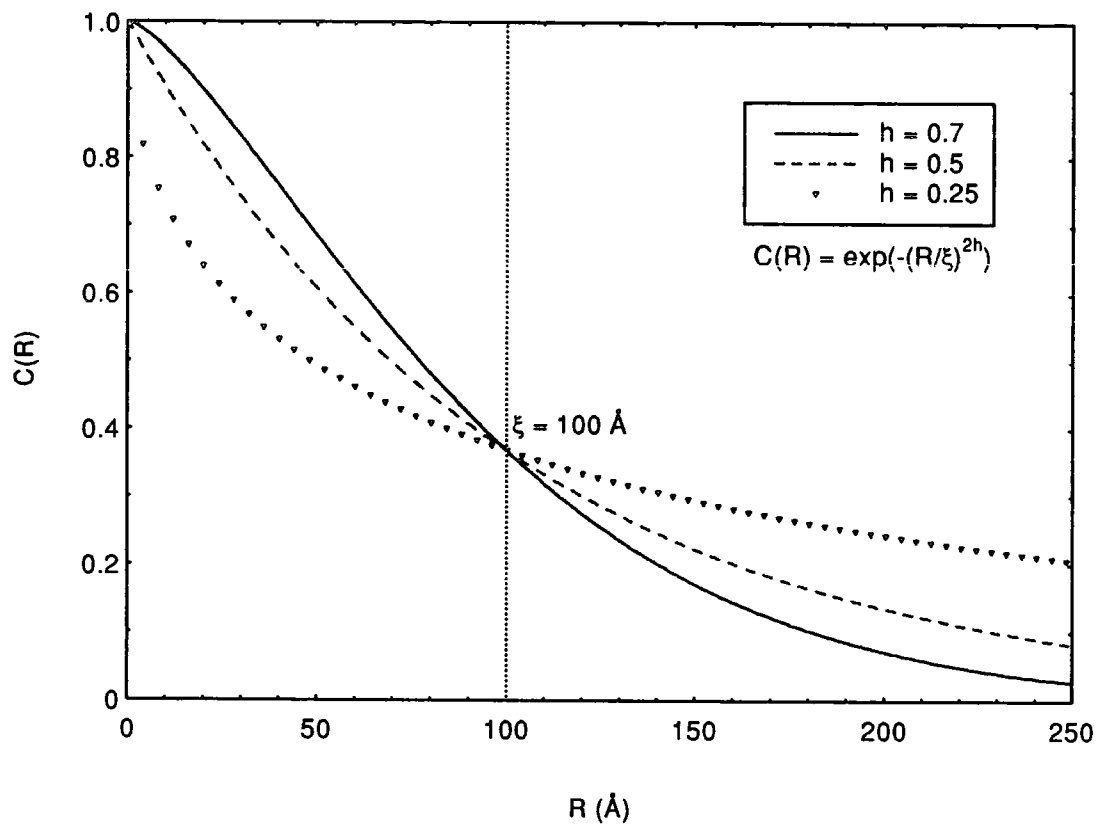
Fig 3.30   Variation of C(R) for a self affine surface with a cut off
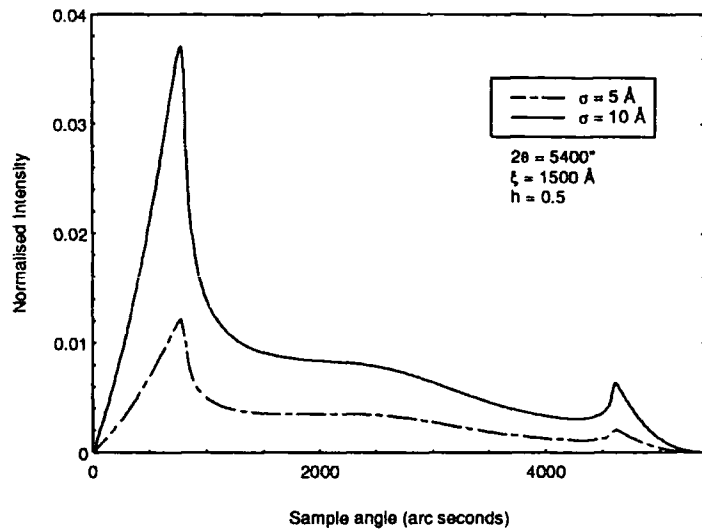
a   Variation of diffuse scatter with surface roughness, σ
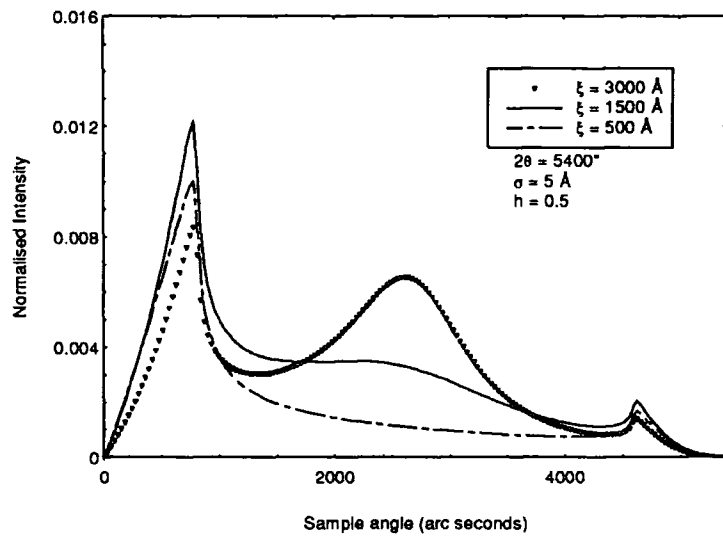
b   Variation of the diffuse scatter with the correlation length, ξ
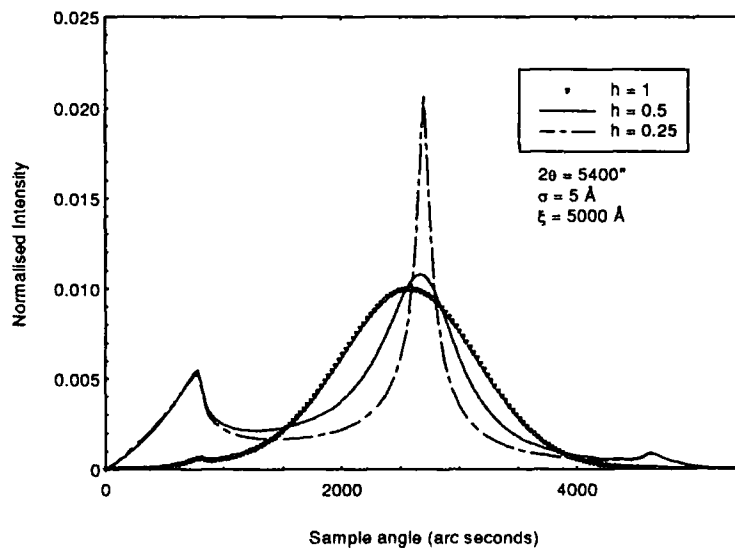
c   Variation of the diffuse scatter with fractal exponent, h.

Fig 3.31   Simulations of diffuse scatter from a silicon substrate

$q_z^2\sigma^2 < 1$. This is due to the expansion of an exponential containing C(R) which took place in deriving the Fourier transform described above.

The power law scaling as a function of q also occurs in the q_z direction. At first sight it seems extremely strange that a lateral spatial frequency distribution can affect the vertical scattering vector. However, this is explained when the weak limit approximation is considered. Beyond the region of validity of this approximation the diffuse scatter is no longer described exactly by a Fourier transform. As a result when $\sigma^2 q_z^2 > 1$ a 'h' dependent, power law scaling is observed as a function of q_z.

For $R \gg \xi$, the roughness acts as independent scatterers. As a result, it is the amplitudes and not phases that are added. This is seen in transverse diffuse scans taken from materials with a very low lateral correlation length. Such scans are merely an incoherent (constant) intensity, modulated by the Fresnel transmission coefficients.

3.2.16 Sensitivity of diffuse scans to the value of h

Transverse diffuse scans are limited in the range of q that they can probe due to the cut off given by the Yoneda wings. As a result, the large values of q required to observe the power law decay are rarely reached. In addition, if both h and ξ are small, then the restricted range of q_y probed in a transverse diffuse scan makes simulations of them highly insensitive to h [46]. This is shown in figure 3.33. Fortunately, for the correlation lengths of the samples studied here this was not the case. Off specular longitudinal diffuse scans have no such high q cut off, but have a large component of q_z in their motions. Unfortunately, due to the intensity of the x-ray diffuse scatter falling as q_z^{-2} [19,46], such scans are lost in the experimental noise at quite low q. As a result, typical scans may not probe sufficiently small length scales to see the effect of h. Finally, detector only scans have no cut off due to the sample, on the high angle side, but again, have a large q_z component to their paths through reciprocal space.

As a result, in order for the fractal exponent to be pulled out of any of the diffuse scans used in this study, intensities must be used that are greater than those available at the Daresbury synchrotron radiation source. Metzger has got around this problem by
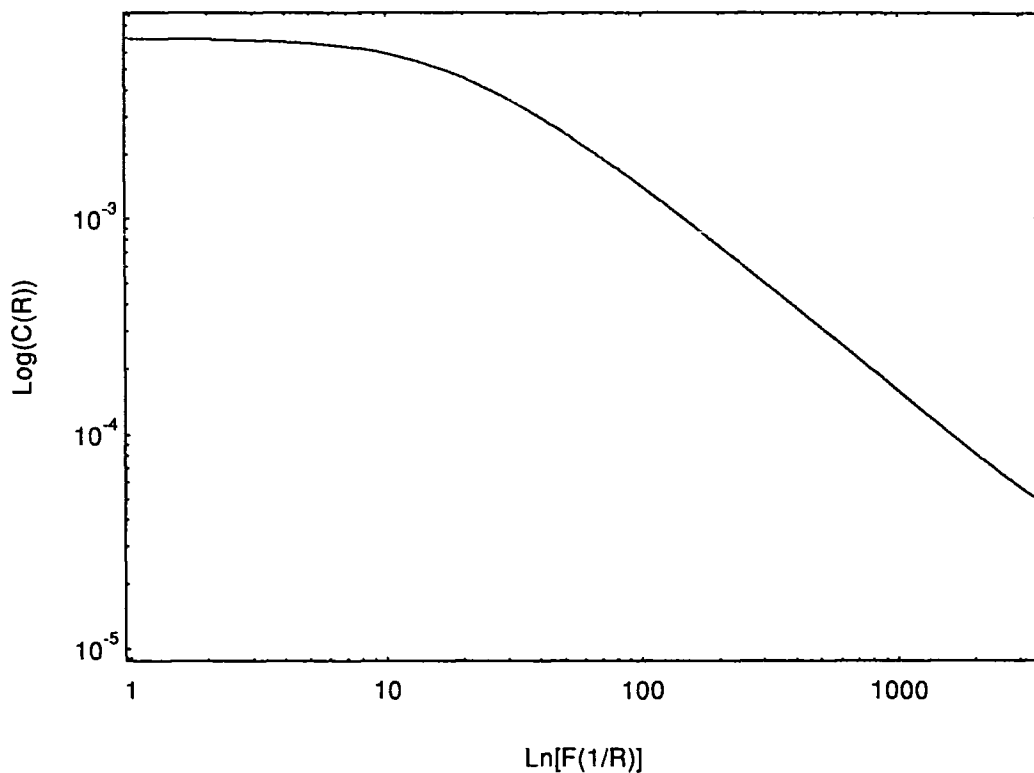
Fig 3.32 Illustration of the power law in the diffuse scatter for large q
($h = 0.5$, $\xi = 100$ Å)
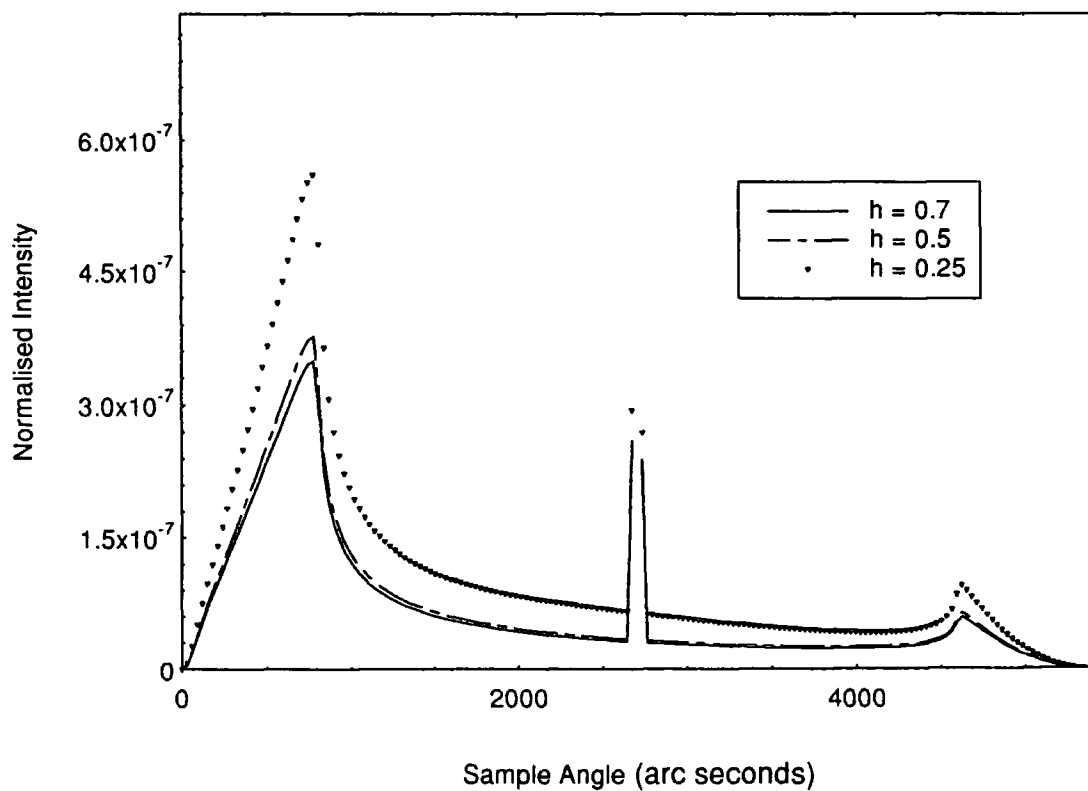
Fig 3.33 Insensitivity of transverse diffuse scans (from a Si surface) to h, when they are taken at low angles ($2\theta = 5400$") and also have a small ξ (100Å)

performing out of plane scans [43-46]. In these he uses a position sensitive detector to measure detector only scans. With the incident beam fixed near the critical angle, he scans the detector round the surface normal of the sample. Due to the low angle of incidence high levels of intensity are present and no limit on the value of q_x, q_y is imposed, since there are no edges of samples to be crossed.

3.2.17 The validity of the fractal model

The question of whether interfaces are self affine is still under debate and in many instances there is a wealth of contradictory evidence. An example of this was when simulations were performed on Langmuir blogget films [40]. In this case, a domain model was successfully employed to simulate the diffuse scatter. However, at the same time measurements of the Bragg peak width by other researchers showed a self affine scaling behaviour in similar materials [59]. MBE has its own specific problems when stepping occurs below the coherence length [16,39,41], although again there are a large number of papers that have reported self affine surfaces on such materials [39,60,61]. The specific problems of simulating MBE surfaces are discussed further in section 7.4.6.

3.2.18 Non physical solutions

As h is reduced on a self affine interface, a general increase in high frequency roughness is observed. In addition, for a real system, as the frequency of the roughness is increased it gets more and more difficult to replicate the roughness from one layer to another [21]. Eventually, the frequencies on the surface become too high to be replicated and the layer must become uncorrelated. Thus simulations that require extremely low h, in conjunction with a short correlation length, and give a significant degree of correlation are physically unrealistic. In addition, if the rms roughness in such a system approaches 1/3 of the layer thickness then the layer would cease to exist since the roughness of the two interfaces would overlap. Only if the correlation length is long, or h is high, can the necessary correlations be physically introduced into the roughness in order to stop the layer being washed out.

3.2.19 Effects of vertical grading on diffuse scatter

The effect of including vertical grading in the simulation of diffuse scatter, from an already rough surface, is seen in figure 3.34. The inclusion of grading, reduces the (electron) density of the material near the surface. Since this is related to the refractive index, the Yoneda wings are seen to move to smaller critical angles. In addition, due to the blurred contrast of the interface, a reduction in the diffuse intensity is observed. The equation for diffuse scatter [62] is seen to become:

$$I_d = I_\infty \frac{k^3 \delta\theta_i}{8\pi \sin(\theta_i)} \left| T(k_{1z})T(k_{2z})(1-n^2) \int_{-\infty}^{\infty} \left[\frac{d\rho_e(z)}{dz} \right] e^{iq'_z z} dz \right|^2 \times \frac{e^{-\left[(q'_z)^2 + (q'^*_z)^2 \right] \sigma^2/2}}{|q'_z|^2} \int_0^{\infty} \left(e^{|q'_z|^2 C(X)} - 1 \right) \cos(q_x X) dX \qquad 3.60$$

where the grading is modelled as a density modulation described by an error function.

3.2.20 Scaling of the diffuse scatter and figuring

It is vitally important that when the diffuse scatter is simulated the correct incident intensity is used. If this is incorrect, two problems can occur when attempting to fit the diffuse scatter. Firstly if the incident intensity is allowed to vary arbitrarily, then there are a multitude of solutions that can be made to fit the same diffuse scatter (figure 3.35). Secondly, if the incident intensity is assumed to be higher than in reality, the fit will require additional grading to make both the specular and diffuse scatter fit simultaneously.

For large flat samples, the incident intensity can be assumed to be the same as the intensity at the critical angle. This is because total external reflection of x-rays is occurring and all the x-ray beam is incident upon the sample. However, if the sample is figured, i.e., bent on a length scale greater than the coherence length, then a convolution will be performed on the data. This is because every separate tilt will act as a separate sample and the specular and diffuse scatter will be blurred out.
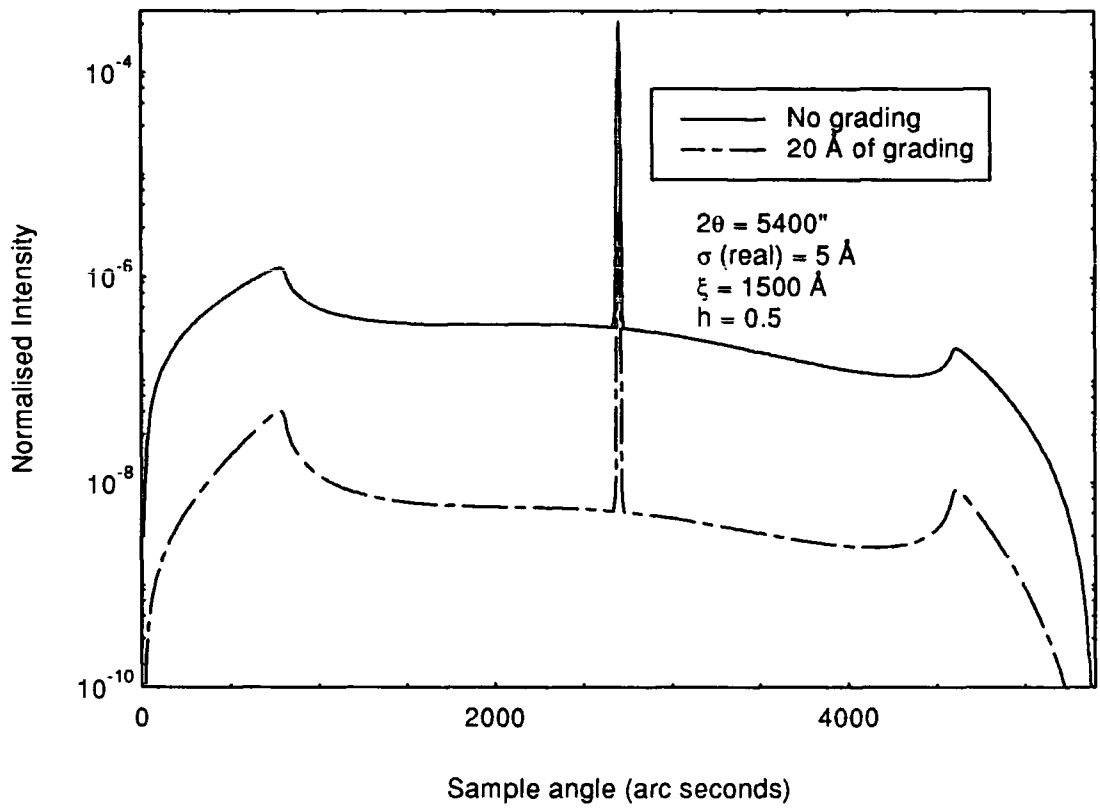
Fig 3.34   The effect of vertical grading on the diffuse scatter from a Si substrate
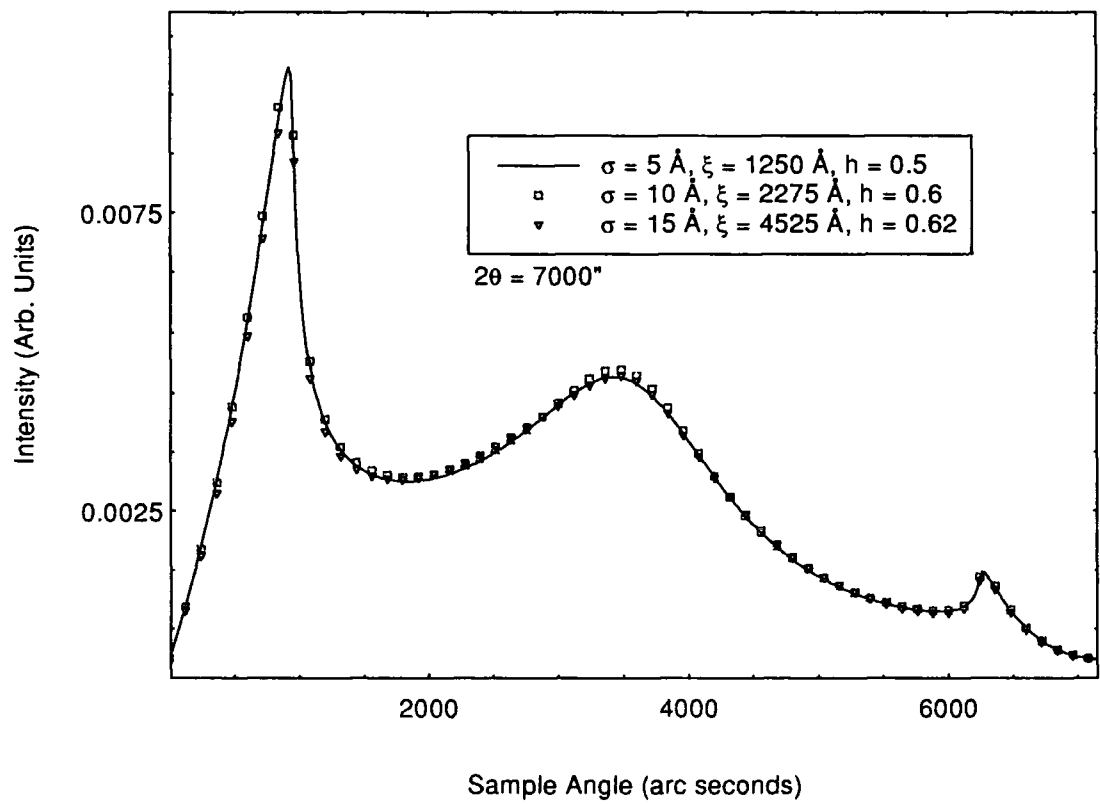
Fig 3.35   The effect of arbitrarily scaling the intensity of the diffuse scatter.
(Example silicon substrate)

Now consider a transverse diffuse scan. It is clear that it is comprised of two distinct components. Firstly there is the specular scatter, which is essentially a delta function, and secondly there is the diffuse, which is essentially a box. When a convolution is applied to the specular it is seen to broaden and reduce in height (to satisfy conservation of energy). However, when the same convolution is applied to a box the height remains constant, except for a slight blurring at the edges. As a result, if figuring is present on the sample, the specular intensity is reduced, whilst the diffuse intensity is left almost unchanged. In this way the intensity at the critical angle cannot be assumed to be that of the incident beam and so cannot be used in the diffuse simulations. Therefore in order to produce high quality simulations it is vital that the incident intensity of the instrument is measured for use in the diffuse scans.

3.2.21 Deducing roughness using the Born wave approximation

A method of extracting the roughness of an interface without simulation was developed by Lagally *et al* [21]. In this they used the results of the Born wave approximation to calculate the rms. roughness on the surface. A brief description of this method and corrections to it is given below.

From the Born wave approximation, the intensity of the specular scatter for a single rough surface is given by the Fresnel reflectivity damped by an exponential (3.44). This intensity is lower than predicted by Fresnel's laws since some of the x-rays have been scattered diffusely. From conservation of energy, it therefore follows that the diffuse intensity, I_{diff}, is given by:

$$I_{diff} = I_o - I_{spec} = I_o - I_o \exp\left(q_z^2 \sigma^2\right) \qquad 3.61$$

where I_{spec} is the specular intensity for this particular scattering angle and I_o is the Fresnel reflectivity for the perfect surface.

From this the ratio of I_{diff}/I_{spec} is:

$$\frac{I_{diff}}{I_{spec}} = 1 - \exp[(q_z \sigma)^2]$$ 3.62

where σ is the rms roughness of the surface and q_z is the scattering vector.

Thus by measuring the diffuse and specular integrated intensities in a transverse diffuse scan, the roughness of the surface can be deduced. However, a problem that exists with this is that in reality not all the diffuse scatter is measured. This is because the values of q_y that can be probed are cut off by the shadow of the specimen edges. As a result, the measured diffuse is slightly lower that the true diffuse and thus the rms roughness deduced is an underestimate.

By comparing the results given by (3.62) with the diffuse scatter predicted from the distorted wave Born approximation, this underestimate can be corrected. To our knowledge, such corrections to the roughness deduced from the Born wave approximation have not been employed by any other group than our own to date. Shown in figures 3.37 and 3.38 is the roughness deduced from the BWA for simulations of diffuse scatter given by the DWBA for various scattering angles. It can be seen that as the scattering angle increases, the roughness given by the BWA improves since more of the diffuse scatter is probed by the scan.

Variations of diffuse scatter with roughness, lateral correlation length, and h are shown in figures 3.36, 3.37 and 3.38 respectively. From figure 3.37 it can be seen that as the correlation length decreases, more diffuse scatter is pushed out of the observation window of the transverse diffuse scan and the deduced roughness falls. From figure 3.36, it can be seen that as the roughness increases, the accuracy of the deduced roughness again falls. This is due to the break down of the BWA as the perturbation on the perfect situation increases. Finally in figure 3.38, it can be seen that almost no effect is given by h on the roughness of the surface deduced from the Born wave approximation.
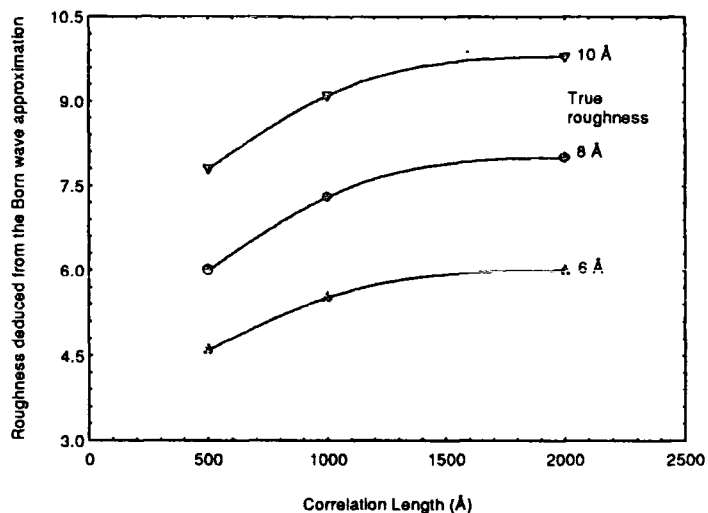
Fig 3.36   Variation with correlation length and surface roughness
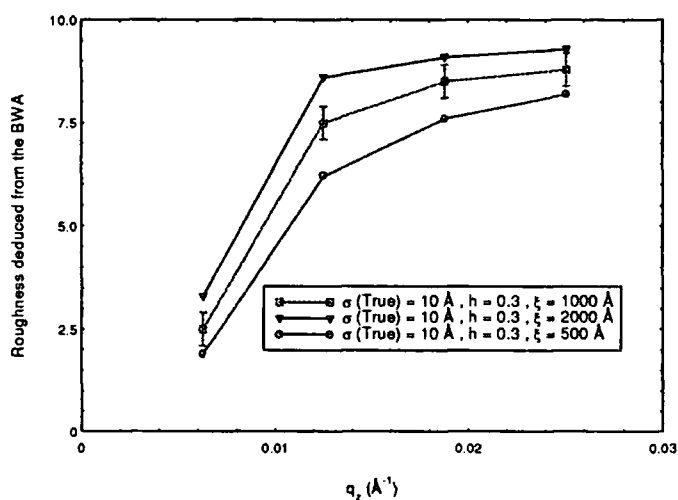
Fig 3.37   Variation with correlation length and scattering vector
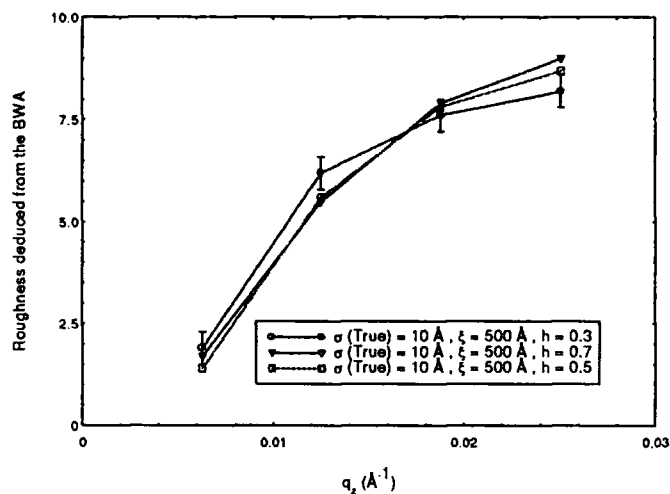
Fig 3.38   Variation with fractal exponent and scattering vector

Figs 3.36 to 3.38.   Roughness deduced using the BWA from DWBA
      simulations (for a GaAs surface) of the diffuse scatter with a known roughness

An advantage of this method is that it is almost unaffected by grading. This is because the specular and diffuse scatter are damped by the same amount on the application of a vertical density variation. The deduced roughness of a surface with an additional density grade present is shown in figure 3.39. When combined with figure 3.34, it is clear that although there is a large change in diffuse scatter on the application of grading, very little change in the deduced roughness has occurred. The small changes that have taken place are due to the movement of the Yoneda wings, due to a change in top surface density. This results in a different amount of diffuse being multiplied up at the critical angles and the total amount of diffuse scatter changes slightly.

3.2.22 Features seen in x-ray diffuse scattering

3.2.22.1 Yoneda wings

These increases in intensity are seen when the sample or detector angle is equal to the critical angle of the interface. Mathematically, they correspond to the maximum values of the two Fresnel transmission coefficients included in the DWBA. However, two physical ways of understanding how they arise are possible.

The first description is given by Fresnel's laws. Consider a surface with a slight amount of roughness on it as shown in figure 3.40. Initially at high angles of incidence, a reflected and transmitted beam are produced as shown in figure 3.40a. However, as the sample angle is decreased, the transmitted component becomes closer and closer to the surface. Finally, at the critical angle, the transmitted component runs parallel to the surface and scatters very strongly (figure 3.40b). As a result an increase in diffuse scatter is seen.

The second description is given by considering the wavefield above the surface. This is a combination of the incident and reflected waves which are coherent. As a result, a dynamic interaction takes place, and a standing wave is set up above the surface as shown in figure 3.41. As the angle of incidence is changed, the nodes and antinodes of this wavefield move vertically. When the critical angle is reached, calculations
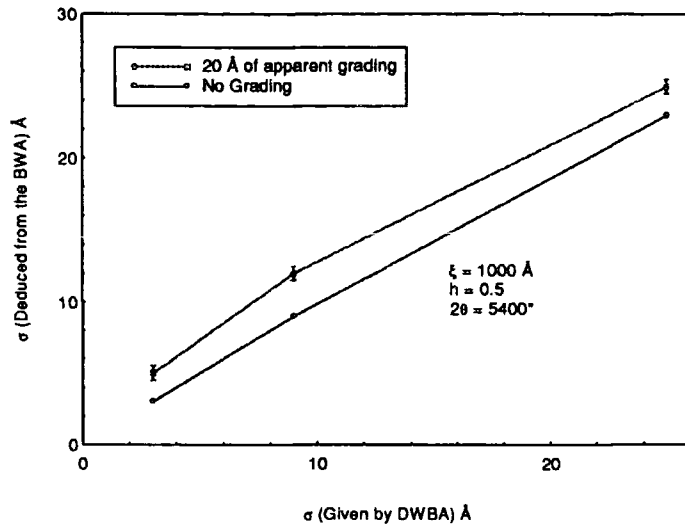
Fig 3.39 Effect of grading on the roughness deduced from the B.W.A.
(Example surface GaAs)
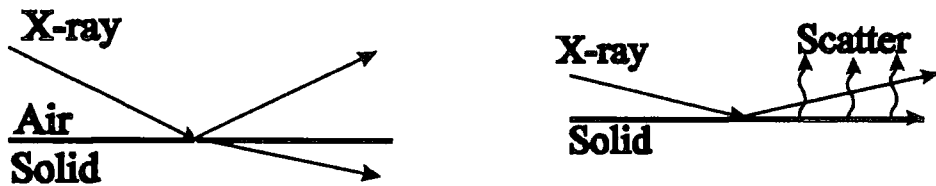
Fig 3.40 Ray diagram of an x-ray beam entering a solid at various
angles of incidence

a) Above θ_c, penetration occurs.   b) At θ_c, transmitted wave scatters
strongly off the roughness
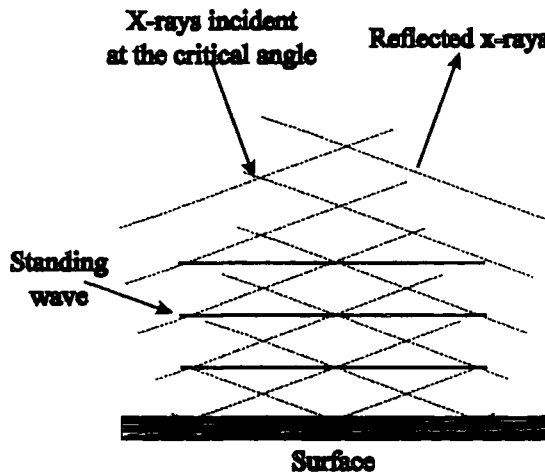
Fig 3.41 Standing waves generated above the surface of a sample

show that a standing wave antinode lies on the surface. This corresponds to a maximum of intensity and so the roughness on the surface scatters very strongly.

Neither of these two physical arguments give a feel to why the right hand side Yoneda wing exists. This is a result of the Reciprocity Theorem, which requires that the x-ray diffuse scatter must be symmetric around the specular (ignoring geometric effects). An explanation of this theory is given below.

3.2.22.2 The reciprocity theorem

The reciprocity theorem arises as a consequence of Maxwell's equations being symmetric in time. As an example consider a refracting beam as shown in figure 3.42a. If the beam was sent in the opposite direction then, from intuition, you would expect it to behave in the same way as shown in figure 3.42b. This is a statement that the results of Maxwell's equation are independent of the direction in which time is run. Now consider a situation where an x-ray beam is incident upon the sample as shown in figure 3.43. The x-rays leaving the sample at the critical angle would have to behave the same as the x-rays coming in at this angle. As a result, a second Yoneda wing must exist.

A parallel situation is observed when grazing incidence x-ray diffraction is performed. This was reviewed in section 3.1.10 and was the source of the error in the calculation of the position of the Bragg peak.

3.2.22.3 Diffuse Bragg peaks (or resonant Bragg sheets)

These are increases in intensity, observed in the diffuse scatter at the same q_z value as the specular Bragg peaks, but extending out as bars in q_y (figure 3.44). In addition, they are seen to shift their position to higher q_z as they approach the Yoneda wings. As a result of their appearance they have been named 'Holy bananas', by de Boer, after V. Holý who first explained their existence [28]. Such distinct periods in q_z, which also extend out in q_y, are clearly the result of a variety of spatial frequencies across an interface which are also being periodically replicated in the vertical direction. These vertical periodic replications correspond to roughness which has

Incident x-rays

Transmitted x-rays
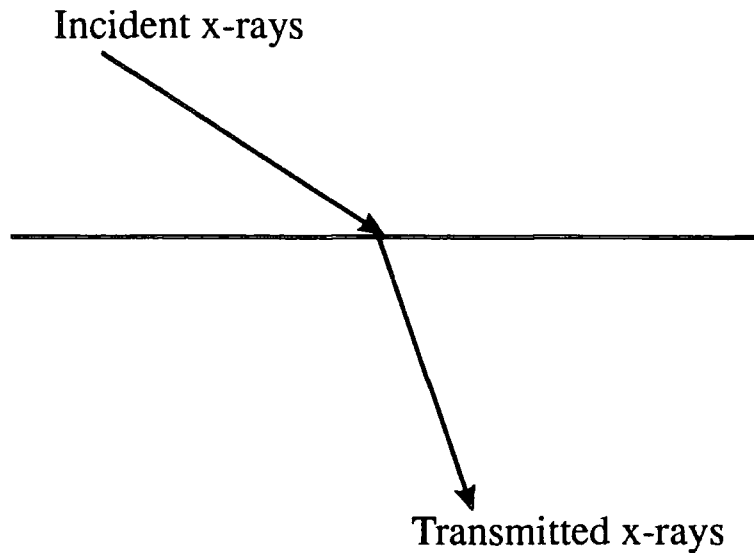
Fig 3.42a   Ray diagram for x-rays incident upon a solid surface

Transmitted x-rays

Incident x-rays
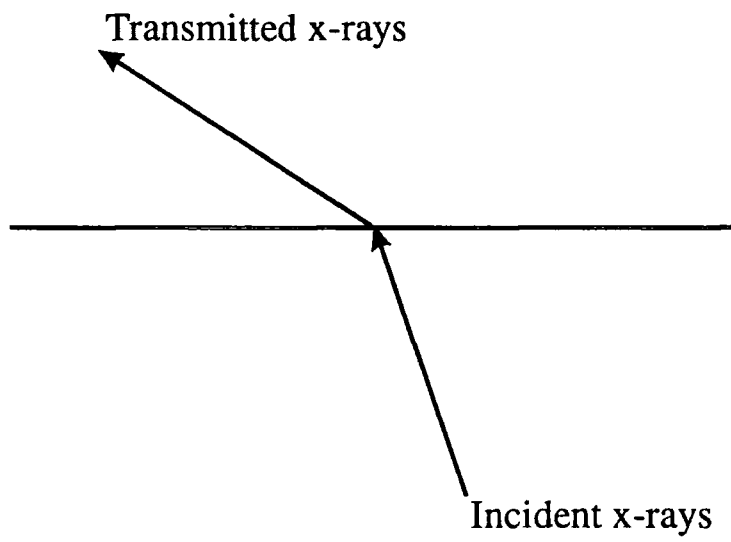
Fig 3.42b   Ray diagram for x-rays emanating from a solid surface

Incident x-rays

Diffuse scatter

θ_c

Transmitted wave
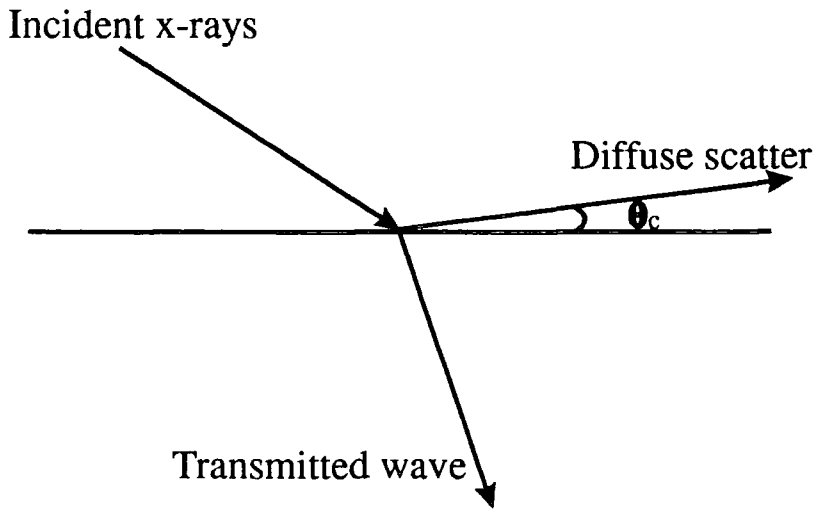
Fig 3.43 Ray diagram for diffuse scatter leaving a solid surface at the critical angle
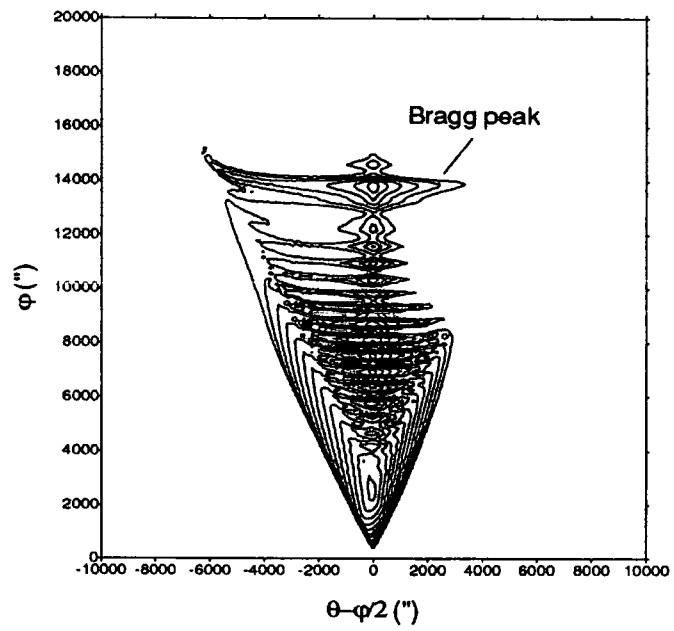
Fig 3.44   The diffuse Bragg peak due to correlated roughness

been correlated from layer to layer through the multilayer stack. At high q_y, these humps are sometimes seen to decay in height. This corresponds to the highest frequency roughness that is able to propagate vertically through the stack [21].

3.2.22.4 Off specular Kiessig fringes

These are similar in origin to the diffuse Bragg peaks, but this time the frequency of the modulations in the q_z direction is much higher. These correspond to spatial frequencies on the interfaces, which have been replicated between the bottom and top surfaces giving a long vertical spatial period.

3.2.22.5 Kiessig fringes in the transverse diffuse scan

These fringes do not correspond to an interference effect. Instead they are a result of generalised Yoneda scattering. Such fringes arise for the same reason as the Yoneda wings and are best envisaged in terms of standing waves.

Consider a single layer upon a substrate. Within the medium there are two coherent wavefields, firstly a transmitted wave from the top surface and secondly a reflected wave from the layer/substrate interface. As a result, a dynamic interaction takes place and standing waves are formed. As with the Yoneda wings, the nodes and antinodes of this wavefield move vertically as the sample angle is changed and the path difference between the waves alters. When these maxima pass a rough interface, the x-ray intensity rises and an increase in diffuse scatter is produced. Since this effect is not generated by interference in the diffuse scattered wave, fringes in transverse diffuse scans occur even if no correlated roughness is present. Corresponding maxima also occur at periodic detector angles due to the standing wave been set up from the coherent addition of diffuse scatter. The amplitude of these detector angle peaks is again the same as those for the sample angles due to the reciprocity theorem.

3.2.22.6 Bragg like peaks

Like the fringes in the transverse diffuse scans these are a result of generalised Yoneda scattering. Again they occur every time the sample or detector angle equals the Bragg angle of the multilayer. As before, they correspond to the maxima of the standing wave generated in the medium. However this time it is related to the path difference generated within each bilayer and so its wavelength is much shorter since the layers are thinner. In this case the Bragg like peaks arise when the standing wave maximums coincide with the separate interfaces with in the bilayer repeat units. Their effect is largest when there is no vertical correlation within the roughness. As the degree of correlation increases, they are seen to decay in intensity as their energy is redirected into the resonant Bragg sheets.

Chapter IV

X-ray scattering studies of float glass and CVD

deposited layers

4.1 An introduction to float glass

4.1.1 The history of glass making

References [1,2]

The earliest reports of the use of glass came from the Egyptians. Here, glass was used to make vessels for perfume, by trailing it, in molten form, around a shaped core. Another 2000 years passed, before the next advances in the uses of glass emerged. These were in Romans times when glass was blown, moulded, painted and engraved. This colouring of glass continued, and by the middle ages it was being widely used in stained glass windows.

By the late 1600's, two competing methods of glass production were in operation. The first type of glass was 'window' glass. This was cheap and quick to make, but was dogged by many imperfections. The competitor, 'plate' glass, gave a much smoother finish, but was extremely expensive to produce.

The first type of 'window' glass to be made was using the 'crown' process. This involved the placing of a glass 'gob' onto the end of a metal pole and spinning it into a sheet. Before use, the glass was required to be cut into plates a few inches square. The 'bullion' in the centre of the disk, where the rod was attached, was also used and can still be seen in older houses today. By 1850, the 'crown' process had largely been superseded by the 'cylinder' process. In this, large cylinders were blown and then split along their axis and flattened. This produced much larger amounts of glass, typically $8m^2$, but was again full of distortions.

In 1914, the 'sheet' process was developed. This involved drawing glass vertically from a molten bath into a sheet. The edges of the glass were stiffened by two sets of cold rollers, allowing it to be drawn to a height of several metres. The resulting glass was cheap, but again contained many distortions. Such glass could not be used for high quality applications, and as such, a large market was still available for a better quality process. The 'plate' glass process was first used in 1688. In this, molten glass was poured onto a table, rolled flat and then left to cool. The resulting glass was highly damaged and so underwent annealing before a laborious grinding and polishing stage. In consequence, such glass took a long time to make and was highly expensive. By 1773, large casting halls were in operation, producing glass in plates of 100m x 46 m. In 1918, automation of the process began with the introduction of a continuous rolling mechanism. Further developments came in 1920, when Pilkingtons added a continuous melting furnace. Finally, in 1923, continuous mechanical grinding 'off line' was introduced, which was incorporated on the line in 1935.

This was the heyday of plate, in which a 300m long glass ribbon was continuously ground with progressively finer sand as it progressed along the line. Sheet glass could not compete in terms of the quality of the finished product, and as a result, plate glass was used up until the 1960's for all thick and distortion free windows. Unfortunately, as mentioned previously, a large drawback of the plate process were the overhead costs. Typically a glass plant required 1.5 MW of power and 20% of the glass made was ground away. As a result, the glass was extremely expensive.

For many years it was thought that the ideal situation would be to be able to combine the above two techniques. Such an idealised process would produce glass which would have the fire finish and inexpensiveness of sheet, but also the quality of plate. These ideas were realised in 1959, when the first float glass tank came on line. This first line could only make 6 mm thick glass, but advances were quickly made. One example was the production of 3 mm glass in 1961, which was done by stretching the glass in a controlled

manner. Such improvements continued, and by 1969, commercial glass was available in the range 3 to 15 mm.

The main breakthrough of the float process was that the glass did not require a grinding and polishing stage. As a result, vast savings were made, and the competing 'plate' glass process was no longer economically viable. This lesson from history is the justification for studying the polishing and grinding stages in other materials, such as ceramics, today. As even if only a small reduction can be made in the grinding, lapping and polishing times, this will constitute major savings on the production line.

4.1.2 The float glass process

In this process, a continuous ribbon of glass moves out of the melting furnace, and floats along the surface of an enclosed bath of molten tin. The ribbon is held in a chemically controlled atmosphere, at a high enough temperature for all the irregularities to melt out, and the surface to become flat and parallel. The glass is cooled whilst still on the tin and when it is case hardened moves onto rollers. The resulting product has a bright 'fire' finish and is of uniform thickness. There is no need for subsequent grinding and polishing. The float glass tank is comprised of fire bricks; on start up glass flows between these and solidifies as a mortar. Once running the line cannot easily be shut down (they have a tendency to collapse!) and typically they must run for several years.

4.1.3 The chemical composition of float glass [3]

During the formation of glass, a mixture of oxides are melted together and then slowly cooled. On cooling, no crystallisation takes place and a supercooled liquid is formed. If crystallisation occurs the resulting glass becomes opaque (as is sometimes seen in old windows) and devitrification is said to have occurred. The viscosity of the melt is

carefully controlled, so that any bubbles that are contained within it are absorbed. The actual oxides present in a standard sample of Pilkington float glass are shown in table 4.1.

Oxide	% weight	Oxide	% weight
SiO_2	72.7	Al_2O_3	1.0
Na_2O	12.9	K_2O	0.6
CaO	9.3	SO_3	0.2
MgO	3.1	Fe_2O_3	0.1

Table 4.1   Constituents of a standard float glass sample

As the glass cools it passes through several stages of viscosity which determine what physical changes can take place. They are as follows:-

1	Melting point	Material is a liquid.
2	Working point	Glass is easily deformed.
3	Softening point	Max temperature, before handling causes damage to surface
4	Annealing point	Atomic diffusion sufficiently rapid to remove residual stress
5	Strain point	Fracture occurs before plastic deformation.

When glasses cool, differences in cooling rates cause different regions to contract at different speeds. As a result, thermal stresses are introduced in the glass which lead to weakening or fracture, termed thermal shock. Such stresses can be reduced or eliminated by raising the glass temperature to its annealing point and then cooling it slowly.

During processing in the float tank, incorporation of tin occurs in both sides of the float glass. On the bottom side of the glass, incorporation of the tin occurs by diffusion from the melt underneath. On the air side, tin is still in contact with the glass from the tin vapour, which has found its way into the atmosphere.

Several different techniques have been used to characterise the tin concentrations within the two surfaces of the float glass [4-8]. The exact predicted concentrations vary, but two general features are noted. Firstly, on the air side there is very much less tin incorporated than on the tin side. This concentration falls away rapidly as a function of distance into the glass. Secondly, on the tin side, an anomalous peak in SnO_2 density is observed a few micrometers into the glass. The origin of this is not known.

4.1.4 The need for defect free glass

Reference [9]

As alluded to previously, one of the major selling points about glass is its fire finish. One example of the importance of this is in cars. With the increasing requirements for aerodynamic shapes, the windscreens of cars have become ever more sloped. As a result, the view of the driver is through an increasingly oblique angle to the glass. Since imperfections in the glass surface are magnified as the angle of incidence is reduced, car manufacturers have become increasingly stringent of the type of glass they accept. The most extreme example is the Japanese car industry. They have stated that they will only except 100% defect/haze free glass and as a result the requirements for high surface finish (angstrom level) is ever stronger.

Methods such as CCD cameras and laser scattering are available for the detection of defects such as nuclei and bubbles in the glass. However, no method is yet available to assess the surface finish of the glass. As mentioned above this is responsible for producing 'haze', but is also vitally important for applications requiring coatings, such as CVD deposited layers.

The technique of grazing incidence scattering is ideally suited to the measurements of surface roughness on the angstrom level, and as such it was an obvious technique to apply to the study of float glass.

4.2 X-ray scattering studies of the surface of float glass

4.2.1 Specular and diffuse studies of the tin side of float glass

Grazing incidence x-ray scattering measurements were performed on a standard float glass sample, taken from the centre of the float glass line, using the GXR1. Shown in figures 4.1 and 4.2 are specular reflectivity curves from the air and tin sides respectively. Both reflectivity curves were modelled assuming only a substrate with no layers present. From these simulations, the roughness on the air and the tin side were found to be 14 Å and 8 Å respectively. Such roughness were higher than the typical 5 Å measured by scanning probe techniques and in order to study this further, diffuse x-ray scattering measurements were performed. From these, it was then hoped to determine the true roughness using the Born wave analysis, developed by Lagally *et al.* [10] and as such, a rapid characterisation technique could be produced.

Preliminary work was performed on the tin side of the sample. A typical transverse diffuse scan, taken at a scattering angle of 3000 arc seconds, is shown in figure 4.3 and the results of the Born wave analysis for various scattering angles are shown in table 4.2.

Detector angle (arc seconds)	Deduced roughness (Å)
2000	6 ± 1
2500	10
3000	8

Table 4.2 Roughness of the tin side of float glass deduced using Born wave analysis

From the shape of the diffuse scatter and from previous simulations, it was deduced that the lateral correlation length of the roughness was in the region of a few hundred angstroms. In consequence, it was expected that a large q_y would have to be probed, in order to see all of the diffuse scatter. As the range of q_y probed on the GXR1 is quite small, one would assume that a lot of the diffuse scatter would be missed, and therefore
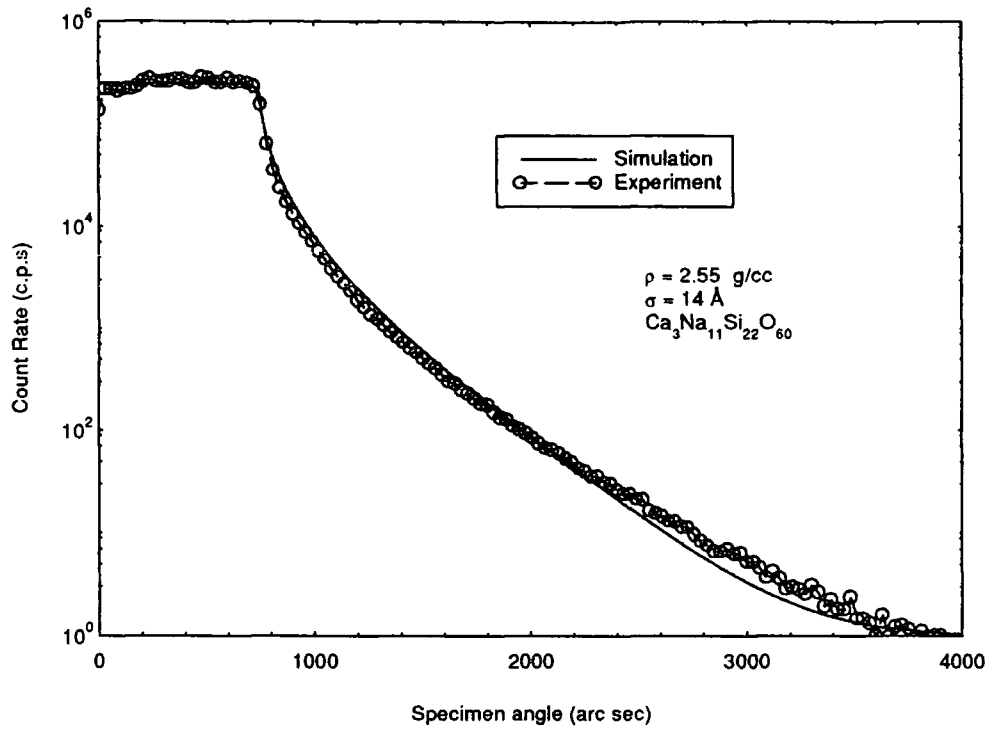
Fig 4.1   Simulation of the air side of a float glass sample

LINK0186 specular
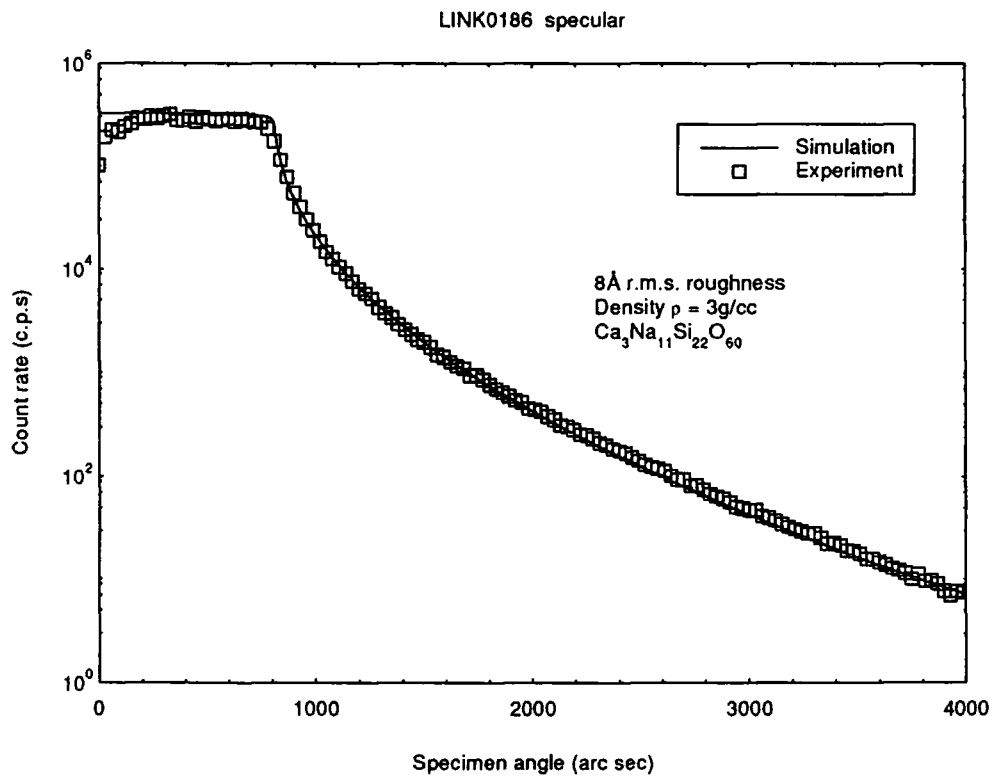
Fig 4.2   Simulation of the tin side of a float glass sample

the roughness on the surface would be underestimated (section 3.2.21). In order to compensate for this underestimate, calibrations of the roughness deduced from the Born wave approximation were produced by comparing it with the DWBA.

In order to produce a calibration curve, the DWBA was initially used to simulate the specular and diffuse scatter for various combinations of roughness, correlation length and fractal exponent. From these simulations, the roughness as given by the BWA, was calculated using equation 4.1, and compared with 'true' roughness from the DWBA. As the DWBA gives a better description of the wavefields around the sample and has a 'knowledge' of the Yoneda wings built in, it works up to a higher value of surface roughness. As a result, a calibration curve can be produced between the true and deduced surface roughness if the correlation length is known within reasonably tight bounds. Such a calibration curve for glasses with a correlation length in the range expected, and for a scattering angle of 3000 arc seconds, is shown in figure 4.4. The equation that results from the BWA which relates the amount of diffuse (I_{diff}) and specular (I_{spec}) scatter seen to the surface roughness (σ) and scattering vector (q_z) is given below:

$$\frac{I_{diff}}{I_{spec}} = \exp(q_z^2 \sigma^2) - 1 \qquad 4.1$$

Returning to the roughness values deduced from the BWA, shown in table 4.2, two things are very noticeable:

Firstly, the roughness values are very high. From the calibration curve (figure 4.4) one would expect the calibrated roughness values to be at least a factor of two higher than the values deduced from the BWA due to the small scattering vector being probed. For the 8 Å of roughness given here by the BWA, for a scattering angle of 3000 arc seconds, this would give a true (corrected) roughness in the order of 17 Å ± 3 Å. Such roughness values would be higher than predicted by the specular scatter and thus theoretically impossible!
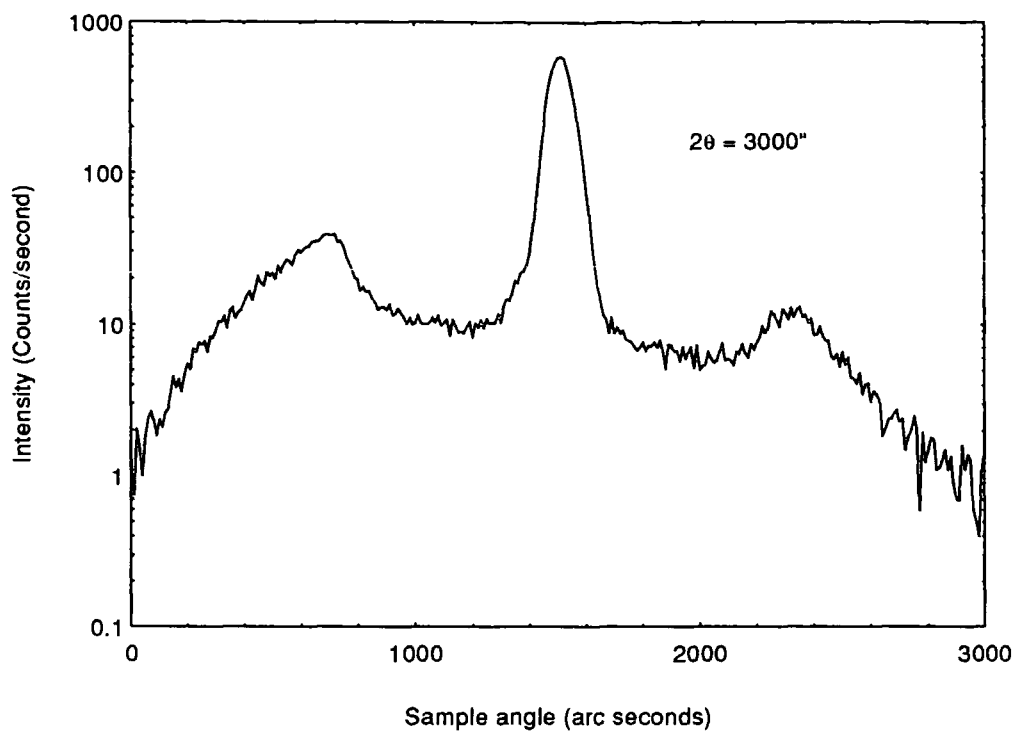
Fig 4.3   Transverse diffuse scan taken from the tin side of float glass on the GXR1
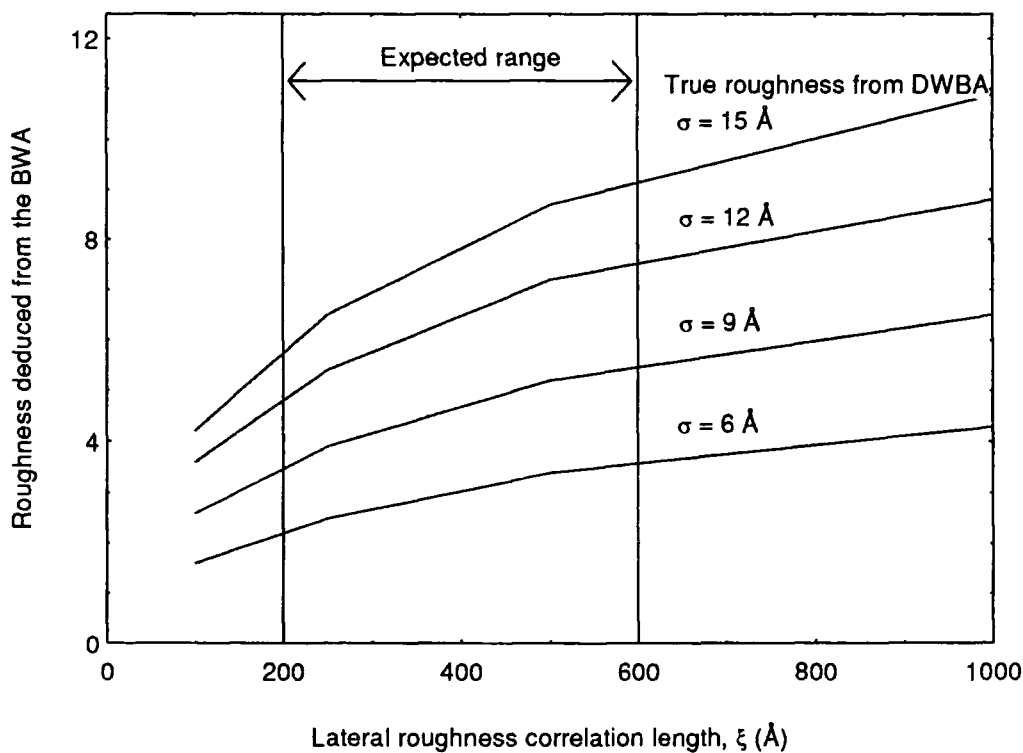
Fig 4.4   Calibration curve for the roughness values determined by the BWA
Scattering angle = 3000 arc seconds

Secondly, there is very little in the way of a consistent trend in the roughness deduced from the BWA as a function of scattering angle. From the calculations shown in section 3.2.21, one would expect the deduced roughness to increase as a function of scattering angle as more of the diffuse scatter was probed. However as shown in table 4.2, the roughness values appear to show no such increase. If it is to be believed that genuinely all the diffuse scatter has been seen by the time the detector angle reaches 2500 arc seconds, then a lateral correlation length of several thousand angstroms must be present on the surface. As was shown in section 3.2.15, this would lead to a large rise in the centre of the diffuse scatter which is clearly not in evidence here.

4.2.2 Studies of a cross section taken from the float glass line

In order to study this apparent breakdown of the Born approximation, grazing incidence x-ray scattering measurements were performed at the Daresbury SRS on a series of samples taken from a cross section of the float glass line. The wavelength used was 1.3926 Å in order to be consistent with the laboratory GXR1. With the higher intensity provided by the Daresbury SRS, clean data could be obtained up to a much higher scattering vector. As such, the variation of the roughness as deduced from the BWA could be observed over a much larger range.

Shown in figures 4.5 and 4.6 are the specular and off specular reflectivity curves, taken from the tin and air sides of a float glass sample respectively. Fringes are clearly visible in both specular scans and from these, it can be deduced that a thin layer exists on both sides of the sample. Such fringes were seen on all samples across the float line. Simulations (figure 4.7) showed that this layer was approximately 20 Å thick which is in the same order of magnitude as other studies of float glass [11]. It is unfortunate that even with the high intensity of the Daresbury SRS, insufficient signal was available to record the offspecular longitudinal diffuse scan in the region of the specular fringes. Thus, using solely specular scatter, it cannot be said conclusively whether the roughness in the surface layer is correlated with respect to that on the glass or not.
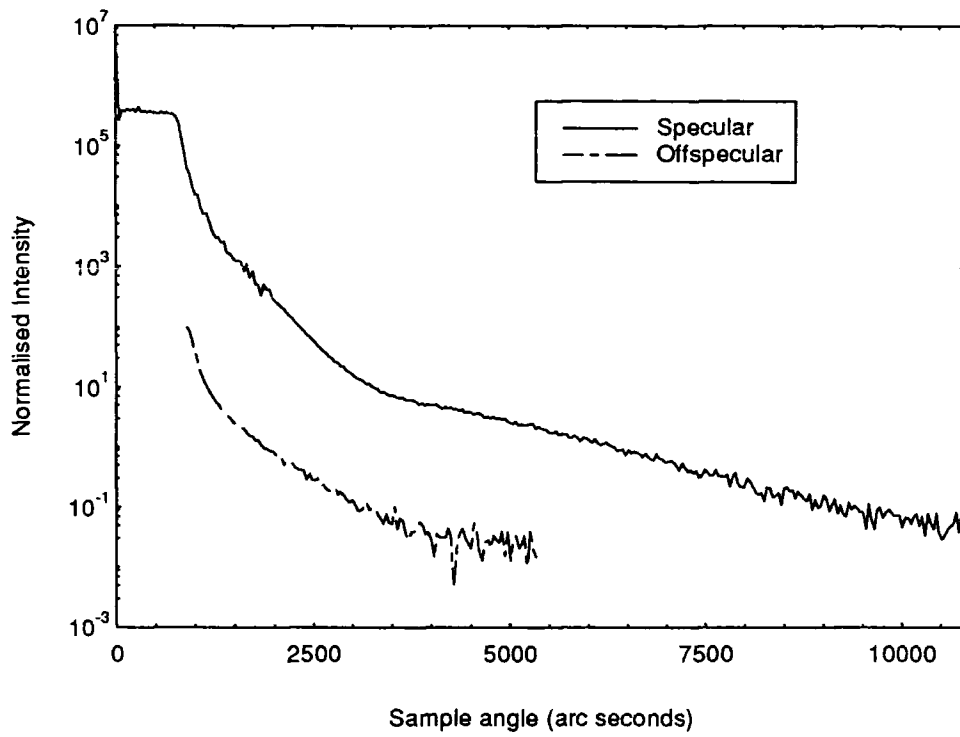
Fig 4.5   Comparison of the specular and offspecular scatter from the tin side of
a sample taken from the edge of the float glass line
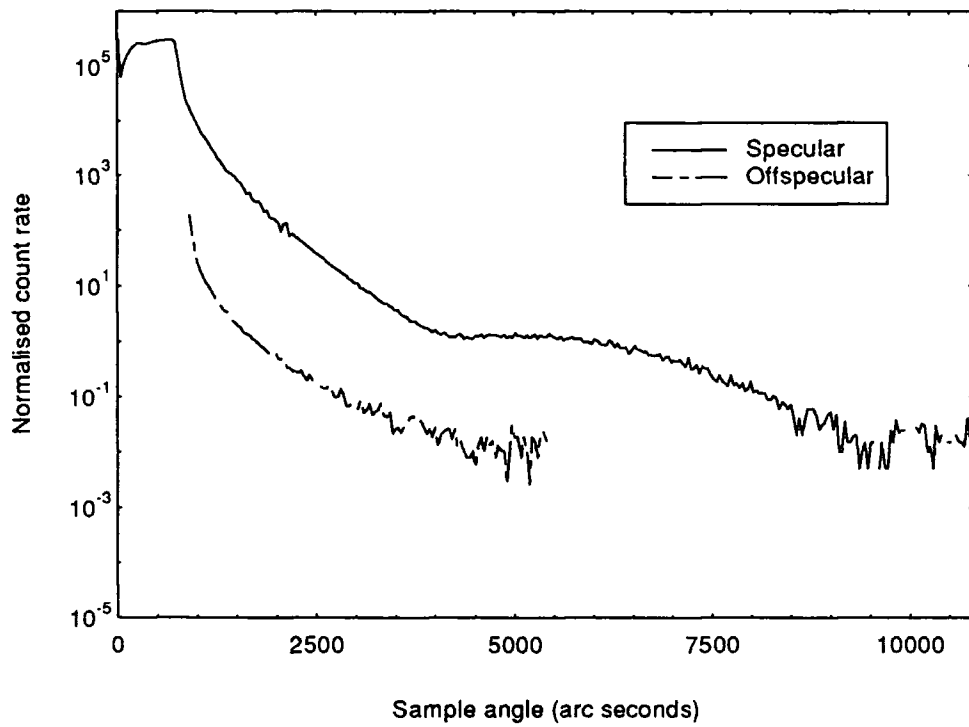
Fig 4.6   Comparison of the specular and offspecular scatter from the air side of
a sample taken from the edge of the float glass line

Diffuse scatter measurements were also taken as a function of position across the float glass line (figure 4.8). From this it can be seen that no significant trend in density is observed across the line and that the two Yoneda wings predict the same density. However, it is noted that the surface density of the tin side is consistently higher than the air side.

4.2.3 The effect of a surface layer on the positions of the Yoneda wings

From simulations of systems where a top surface layer contains heavier elements than the bulk, it is found that at the Yoneda wings, the x-rays are sensitive to the top 50 to 75 Å of the surface (figure 4.9). For layer thickness less than this, the resulting position of the Yoneda wings is related to the average density in the top 50 to 75 Å. In contrast, for samples which have a layer of lower density than the bulk, it can be shown that the position of the Yoneda wings corresponds to the density of the bulk material even when the top surface layer is on the order of 0.1 microns thick (figure 4.10). This would imply that the density measured on the surface of the glass samples is in actual fact the density of the next 50 to 75 Å of material below the carbonaceous layer. Calculations show that this is explained by a 6% increase of SnO_2 in the near surface region of the tin side of the float glass. As mentioned previously (section 4.1.3), such increases in the SnO_2 concentration have been observed by a variety of other element sensitive techniques.
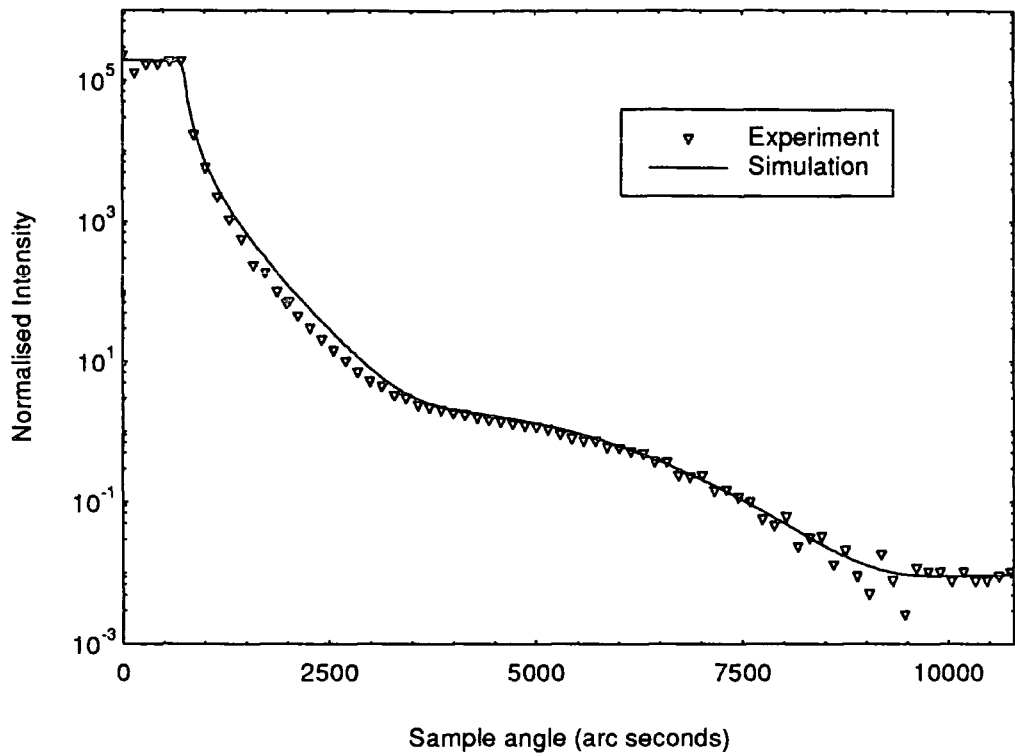
Fig 4.7 Simulation of the air side of a glass sample, taken from the edge of the float line. The layer thickness was found to be 22 Å
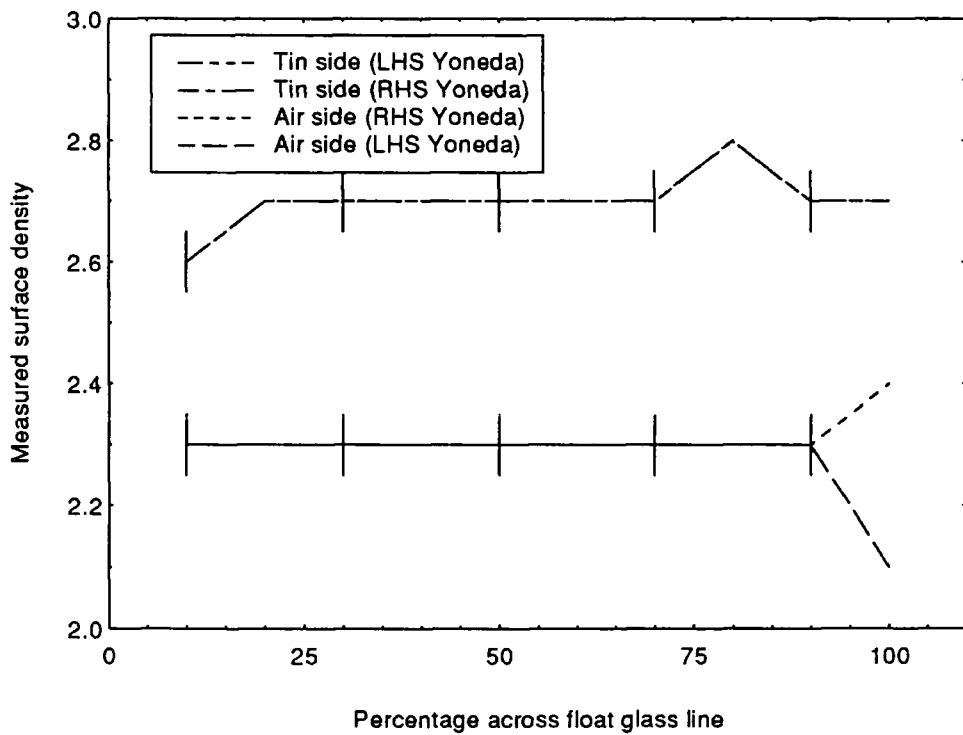
Fig 4.8   Calculated surface density of the air and tin sides of float glass
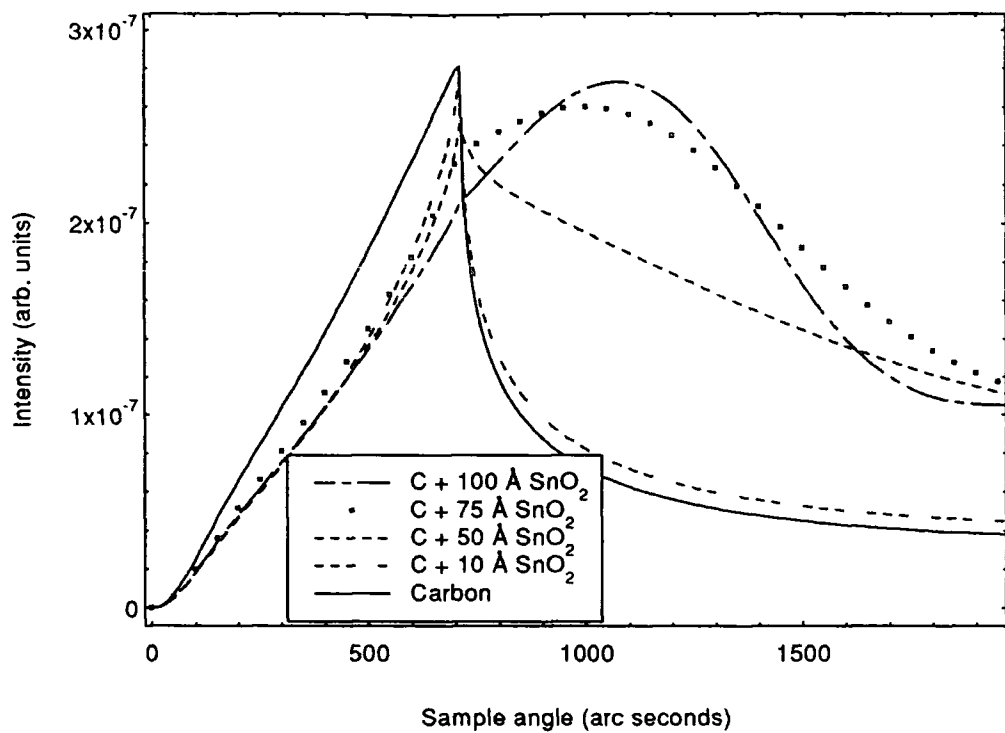
Fig 4.9 Variation of the measured critical angle with layer thickness for a SnO_2 layer deposited on carbon substrate
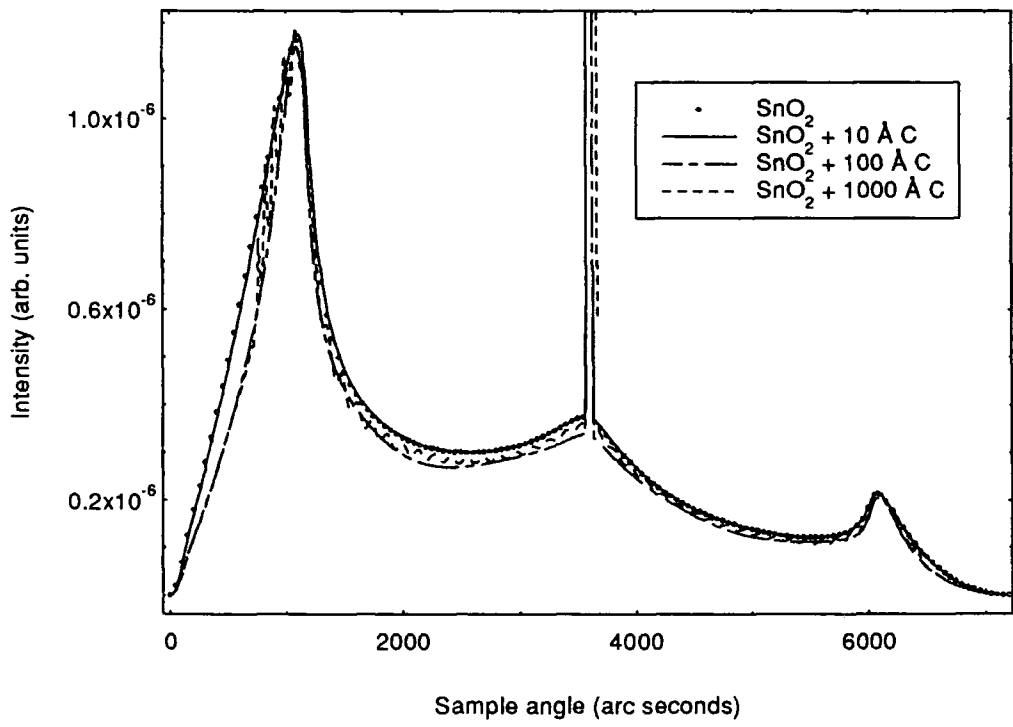
Fig 4.10 Variation of the measured critical angle with layer thickness for a carbon layer deposited on an SnO_2 substrate

4.2.4 Born wave analysis of the float glass as a function of scattering vector

Figure 4.11 displays the calculated roughness from the tin surface of the float glass as a function of scattering vector, using the BWA. From these data, a clear oscillation can be seen in the deduced roughness. From simulations performed in section 6.4.4 these beats can be attributed to the presence of a surface layer. If such a layer has a component of uncorrelated roughness at its interface then the fringes in the diffuse and specular scatter are of different magnitudes. In consequence a sinusoidal variation is introduced into the I_{diff}/I_{spec} relationship, which follows through into the calculated roughness.

If a closer examination of the roughness deduced from the BWA as a function of scattering angle is made, it seems likely that there is another period present. Strong evidence for this is the reduction in the overall calculated roughness for higher scattering vectors. Theoretically, as was shown in section 3.2.21, this should increase and saturate for higher scattering vectors as more of the diffuse is seen. However, as the calculated roughness is falling it would imply that it is being forced down artificially. The most likely cause for this is that the specular scatter is being increased due to the presence of a Kiessig maximum with a large period. This period would be approximately a factor of five greater than the one corresponding to the 20 Å thick layer and thus must arise from a layer of 4 Å. Such double layers have been observed in other surface studies of float glass [11], however in our case the thinner one would appear to be only 1 atom thick.

In section 6.4.4, the mean interfacial roughness, weighted slightly by that on the top surface will be obtained for a layered sample. This is done by taking the mean of the roughness given in the roughness versus scattering vector plot and correcting it using the DWBA. However, only a single layer was present upon those samples. In the case of the Pilkington glass it would appear that at least two layers are present on the surface. Furthermore it would appear that one of the layers is so thin that only a small fraction of the interference fringe system associated with it is visible. From theoretical calculations of diffuse scatter from graded systems given in section 3.2.21, it is known that the Born wave approximation is hardly affected by the presence of a surface grading. As a result,

First 3 point taken on GXR1
Last 5 points taken at a synchrotron
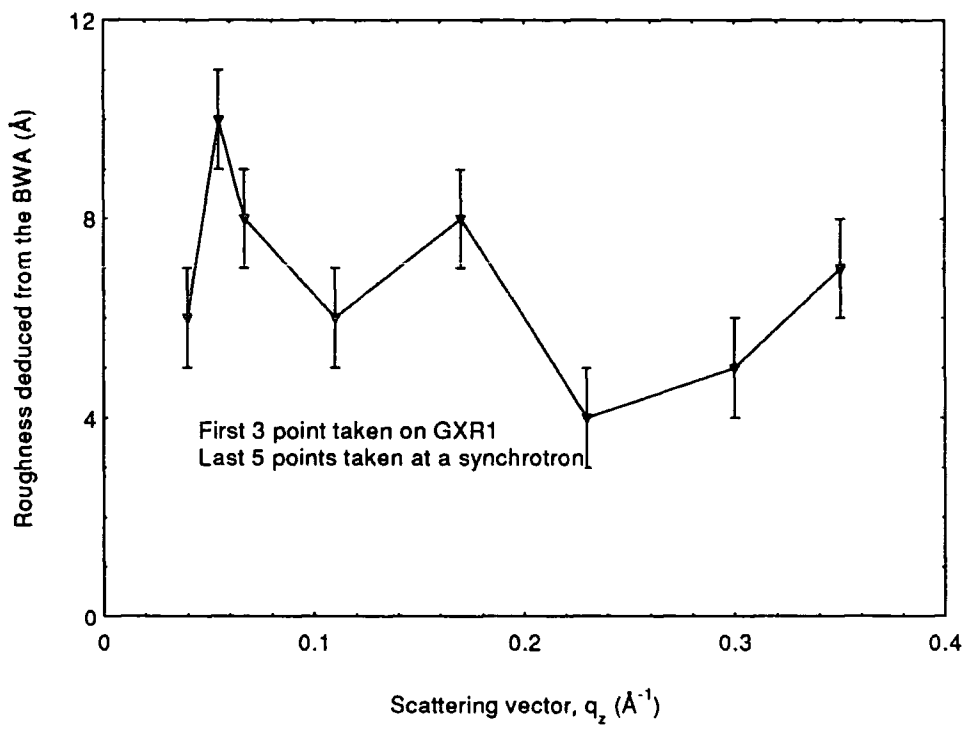
Fig 4.11   Variation in the deduced surface roughness as a function of scattering
angle using the Born wave approximation.

the failure of the Born wave approximation to give sensible values of interfacial roughness must be related to the presence of long period fringes in the specular scatter. If these fringes were much larger than the range of scattering vectors probed, then no accurate average value of the specular could be obtained.

4.2.5 Specular and diffuse scattering measurements from container glass

In order to verify whether the existence of a layer was completely general to glass, a second set of glass specimens was studied. In this case, the origin of the glass must remain confidential, but it was known to be 'container glass'. Again, grazing incidence x-ray scattering measurements were performed on the GXR1. Shown in figures 4.12 and 4.13 are typical specular scans from the surface of the glass with their respective best fits. As with the simulations of the float glass samples, taken on the GXR1, fits were obtained by assuming a single surface. It is interesting to note that very similar roughness values were obtained to those from the air side of the Pilkington float glass specimens. The calculated roughness from the specular scatter simulations are shown in table 4.3.

Sample	Surface roughness (Å)
S2	15.5 Å ± 1 Å
S6	14.5 Å
S12	13 Å
S13	13.5 Å

Table 4.3   The surface roughness predicted from the speculars of the container glass
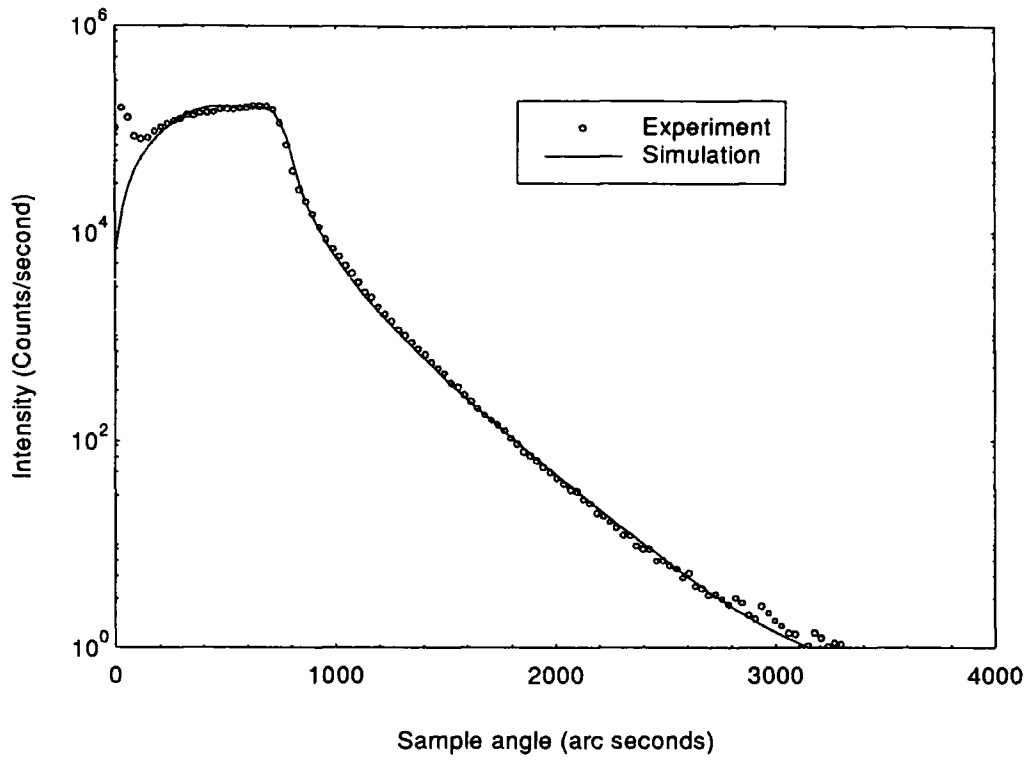
Fig 4.12   Specular scatter from sample S2 with its best fit simulation
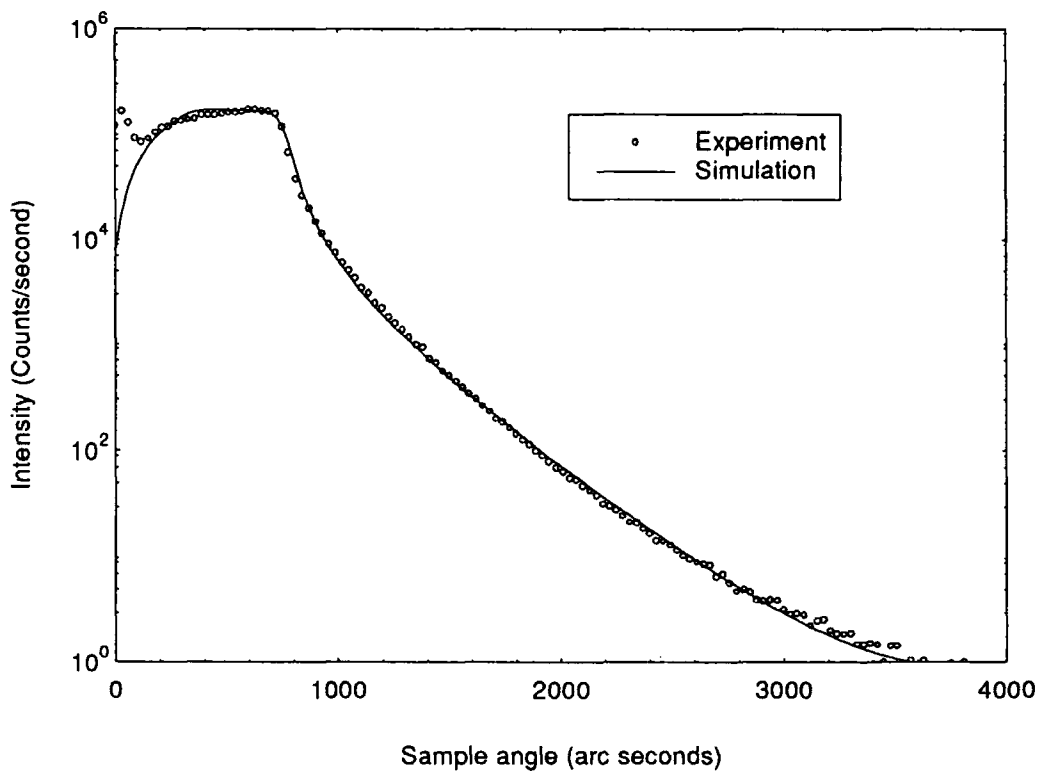
Fig 4.13   Specular scatter from sample S13 with its best fit simulation

When transverse diffuse scans were performed, it was noted that there was a slight density change from sample to sample. These predicted surface densities, from the two Yoneda wings of each sample are shown below in table 4.4.

Sample	Density from left wing	Density from right wing
S2	2.6 g/cc ± 0.1 g/cc	2.5 g/cc ± 0.1 g/cc
S6	2.5 g/cc	2.6 g/cc
S12	2.6 g/cc	2.5 g/cc
S13	2.4 g/cc	2.4 g/cc

Table 4.4 Predicted surface densities from the two Yoneda wings of the container glass

Born wave analysis of the diffuse scatter as a function of scatting angle was again performed. The results of this analysis are given below in table 4.5.

Sample	Scattering angle			
	2500"	3000"	3500"	4000"
S2	3.6 Å ± 1Å	4.6 Å	5.6 Å	6.2 Å
S6	3.0 Å	4.2 Å	4.4 Å	5.2 Å
S12	2.0 Å	2.6 Å	3.2 Å	3.9 Å
S13	2.7 Å	3.2 Å	4.0 Å	4.7 Å

Table 4.5 Surface roughness of the container glass as deduced from the BW analysis

From this table, it can be seen that a distinct rise is present in the roughness deduced from the Born wave approximation as a function of scattering angle. Such a rise is very similar to that predicted from theoretical calculations in section 3.2.21 and is in complete contrast to what was seen in the Pilkington specimens. In order to calculate the true

roughness values, corrections employing the 'look-up table', calculated from the DWBA, were again used and the results displayed in table 4.6.

Sample	Corrected roughness (Å)
S2	10.5 ± 1.5
S6	8 ± 1.5
S12	6 ± 1.5
S13	8 ± 1.5

Table 4.6   Corrected surface roughness for the container glass samples

Scattering angle = 3500 arc seconds.

Another difference observed between these, and the Pilkington samples, is that the surface roughness, as measured from the diffuse scatter, is less than from the specular.   In the case of the Pilkington samples, it appears that the extremely large roughness was due to the break down of the BWA.   However in this case, it would appear that no such breakdown has taken place.   Such a discrepancy in the results of the specular and diffuse scatter can only be attributed to the presence of a vertical electron density grading at the surface of these samples.

4.2.6 Simulations of the diffuse scatter from container glass samples

In order to verify the results of the Born wave analysis, simulations of the diffuse scatter from the samples S2 and S13 were undertaken.   These specimens were chosen, as they had the cleanest diffuse scatter and thus would give the most reliable results.   In order to be confident that a unique solution was obtained, several scans were fitted simultaneously until a consistent set of parameters were obtained with no scaling factors.   The simulations of samples S2 and S13 are shown in figures 4.14 and 4.15 respectively, whilst the result of the simulations are shown in table 4.7.   Both samples showed excellent fits assuming a single surface model with a combination of true roughness and surface
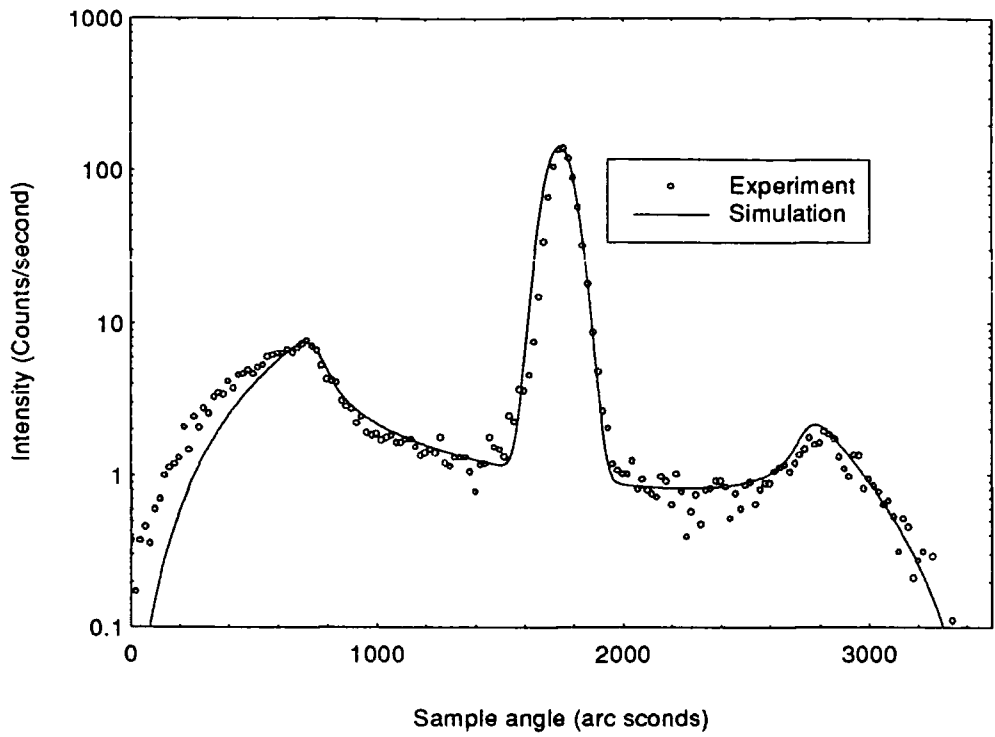
Fig 4.14a   Transverse diffuse scan and best fit simulation for sample angle S2
Scattering angle of 3500"

Fig 4.14b   Transverse diffuse scan and best fit simulation for sample S2.
Scattering angle of 4000"
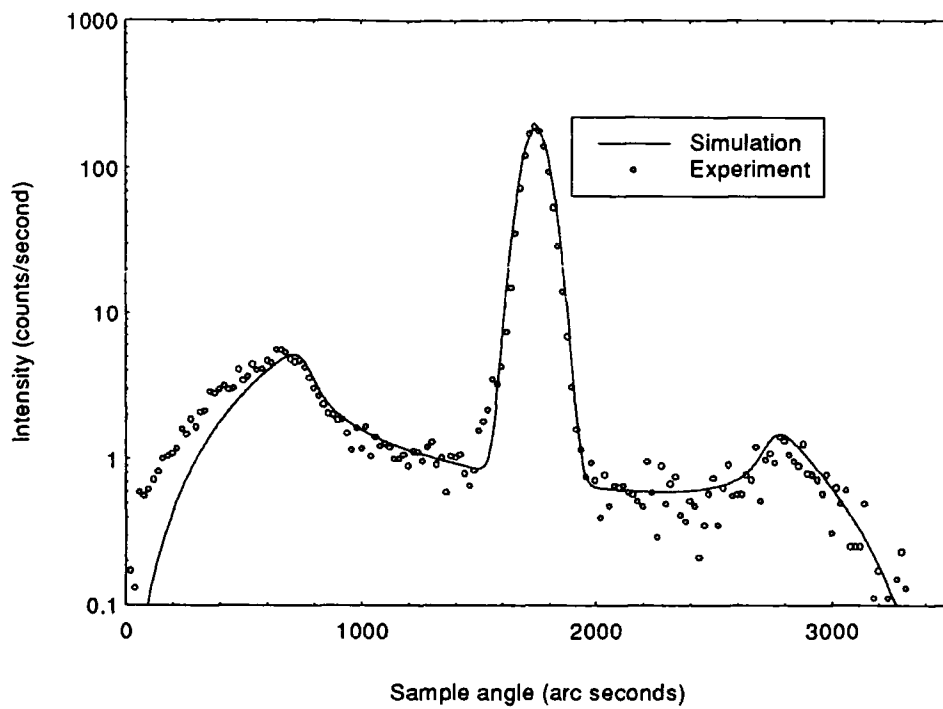
Fig 4.15a   Transverse diffuse scan and best fit simulation for sample angle S13
Scattering angle of 3500"
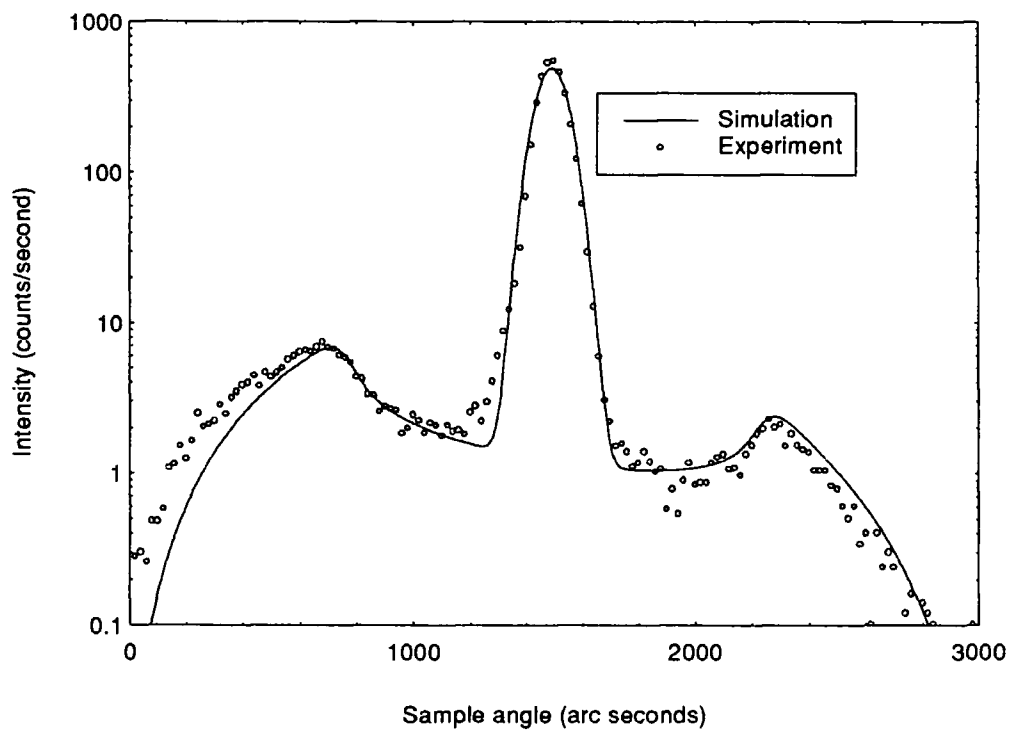
Fig 4.15b   Transverse diffuse scan and best fit simulation for sample angle S13
Scattering angle of 4000"

grading. Within the table, the convention used is that, σ_{total}, is the roughness as measured in the specular, σ_{grade} is the width of the vertical grading and σ_{true} is the true rms roughness. The lateral correlation length is ξ and the fractal exponent is given by h.

Sample	σ_{total}	σ_{grade}	σ_{true}	ξ	h
S2	15.5 Å ± 1 Å	12 Å ± 1 Å	9.5 Å ± 1 Å	550 Å ± 50 Å	0.4 ± 0.05
S13	13.5 Å	11 Å	7.5 Å	550 Å	0.4

Table 4.7   Simulation parameters obtained from multiple fitting of the container glass

From the simulations it is immediately apparent that the roughness deduced from the corrected Born wave approximation is equal to that given by the simulations. This gives strong weight to the argument that in these samples no surface layer has formed. Such a view is supported by the multiple fits which were obtained to the data, assuming that no surface layers were present. In consequence, the argument that this container glass surface is layer free, but has a vertical electron density gradient, appears completely vindicated. Such an electron density grade has subsequently been observed by us in other glassy materials [12], and as such it can be tentatively implied that such a grading is present in all glass surfaces.

4.2.7 Summary

Systematic studies of glass as a function of position across a float glass line have been performed using specular and diffuse scatter. Such investigations have shown that the tin side of the glass, within the top 50 - 75 Å, is consistently denser than the air side across the entire float line. By assuming an extra 6% concentration of SnO_2 in the tin side, this density difference can be explained. Such findings are in complete agreement with other element sensitive investigations relating to the surface composition of float glass. In addition it has been found that the float glass line produces a glass which is homogeneous in terms of density across the whole of the ribbon. Specular and offspecular reflectivity

measurements have revealed the existence of a thin surface layer of thickness approximately 20 Å, which is assumed to be comprised of carbonaceous material. In addition, it has been shown that this does not contribute to the density as measured by the Yoneda wings.

Measurements using the GXR1, on a series of glass samples from a different source have revealed that the existence of a layer is not completely general to all glasses. On these specimens, excellent agreement has been obtained between the results produced by fitting of the diffuse scattering data, and those deduced from the corrected Born wave approximation. Such agreement shows that once corrected, the Born wave analysis developed by Lagally *et al* and extended by our group, can be used to provide rapid analysis of the roughness of samples. From both methods of analysis the true roughness, as deduced from the diffuse scatter, is substantially lower than that given by the specular. This implies that within the surface of a glass sample, a vertical variation in electron density is in existence. Finally, it can be concluded that using a laboratory based source, the analysis of the roughness and density of single surfaces can be performed in minutes, so long as the lateral correlation length is within certain bounds. The possibility of extending such a technique to 'off line' production control would seem extremely promising.

4.3 Introduction to surface coatings on float glass

In the past decade, reports of surface coatings on glass have become increasingly frequent [13,14]. These include dirt resistant coatings, electrically conducting coatings and coatings to increase the thermal insulating properties of glass. The great advantage of being able to apply coatings to a glass is that properties are able to be imparted to it without having to alter the glass itself. In addition, since only a standard float glass substrate is needed, no expensive, dedicated float glass lines are required.

The first attempts to modify the surface of glass were performed in 1967 when the electro-float process was developed by Pilkingtons [1]. This process used the effect of

ion replacement from the tin and in doing so changed the near-surface properties of the glass. The effect of this process was to produce small, but economically viable, quantities of heat rejecting glass. This was termed Spectra Glass® and found uses in buildings and the prototype sun roofs in cars.

The electro-float process worked well, but was not able to produce glass in large quantities. As a result, the next attempts to alter the surface properties of glass were done by depositing thin layers onto it by CVD.

One example of the deposition of layers onto the surface of a float glass by CVD is Pilkington K glass®. This is thermally insulating and works by enhancing the natural 'greenhouse' properties of the glass. The product consists of a float glass substrate, on to which is deposited 700 Å of a Si/C/O mixture and then 3400 Å of SnO_2 by CVD. The Si/C/O is the 'active' layer, whilst the SnO_2 is a protective coating to prevent removal of the Si/C/O compound.

As mentioned previously, in order for a product to be able to be sold it must appear to have no 'haze' on its surface. As a result the refractive index of the Si/C/O coating has been carefully matched to that of the glass substrate at optical wavelengths and the interface roughness reduced to a minimum.

The technique of grazing incidence x-ray scattering provides a unique method to be able to characterise these layers and interfaces, and as result a series of **specially prepared** (i.e. **NON STANDARD**) samples were sent for x-ray analysis. This series of samples for the purposes of this report will be called 'therm'.

4.4 X-ray scattering studies of CVD deposited layers on float glass

4.4.1 Studies of the specular scatter from the CVD specimens

Grazing incidence x-ray scattering measurements were initially performed at Warwick by D.K. Bowen on a GXR1 reflectometer. Figure 4.16 shows the specular scatter from a typical 'therm' sample. It is clear from the rate of fall of the specular scatter that the top surface of the sample is extremely rough. When transverse diffuse scans were taken it was discovered that no specular component was present, even at the smallest angles (figure 4.17).

In order to overcome this problem, further 'therm' samples were produced by Pilkingtons and then polished with a 0.25 µm diamond paste. This time the samples were sent to Durham, since we had ready access to synchrotron facilities and this would vastly increase the signal to noise from the samples.

Grazing incidence x-ray scattering measurements were again performed. For all measurements the wavelength of the S.R.S. was set to 1.3926 Å, for consistency with the laboratory GXR1. Figure 4.18 shows the specular and off specular scatter from a typical, polished, 'therm' sample. This time very clear fringes are seen in the specular scatter. However, when the offspecular longitudinal diffuse scans are considered, no such fringes are seen. As a result, it can be concluded that no correlation in the roughness exists between the top and bottom interfaces, within the CVD layers.

Shown in figures 4.20 and 4.19 is the specular scatter taken on two different samples and from two positions on the same sample respectively. It is immediately apparent that the curves over lay each other exactly (apart from the first hump). Such reproducibility of the specular scatter indicates that the degree of control of the thickness of the layers on these samples is to the order of 1 Å. This is highly impressive when it is considered that such layers are deposited at a rate of 3 m^2/sec!
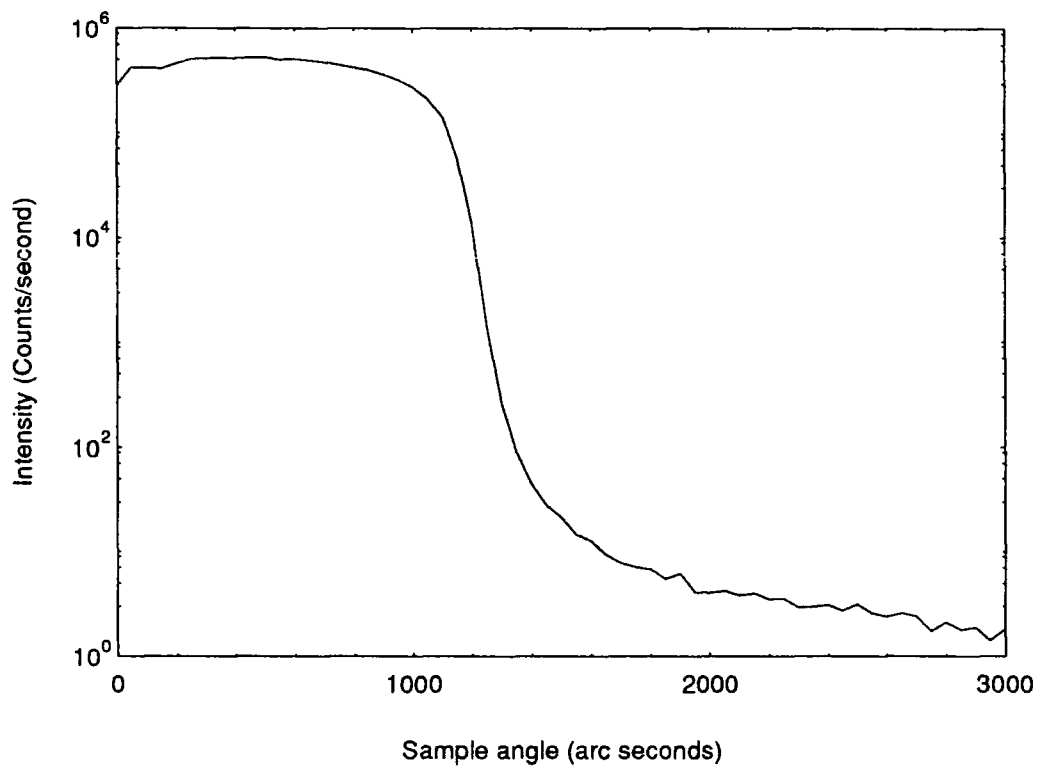
Fig 4.16   Specular scatter from an unpolished 'therm' sample
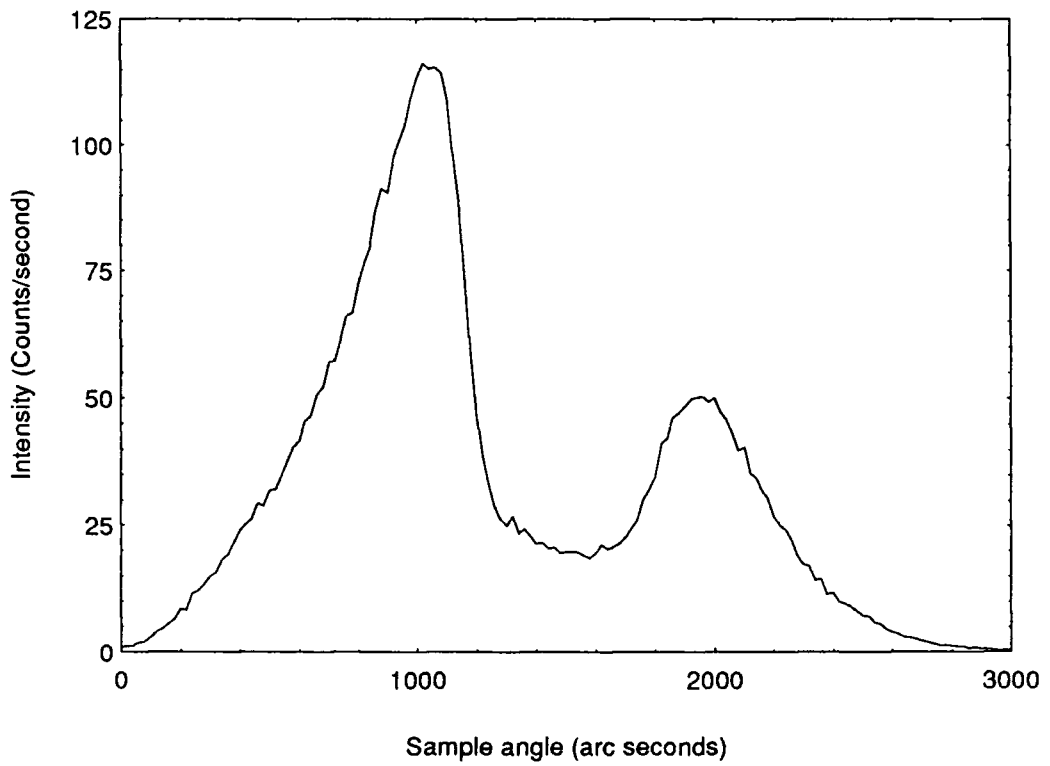
Fig 4.17   Transverse diffuse scan from an unpolished 'therm' sample.
Scattering angle = 3000 arc seconds
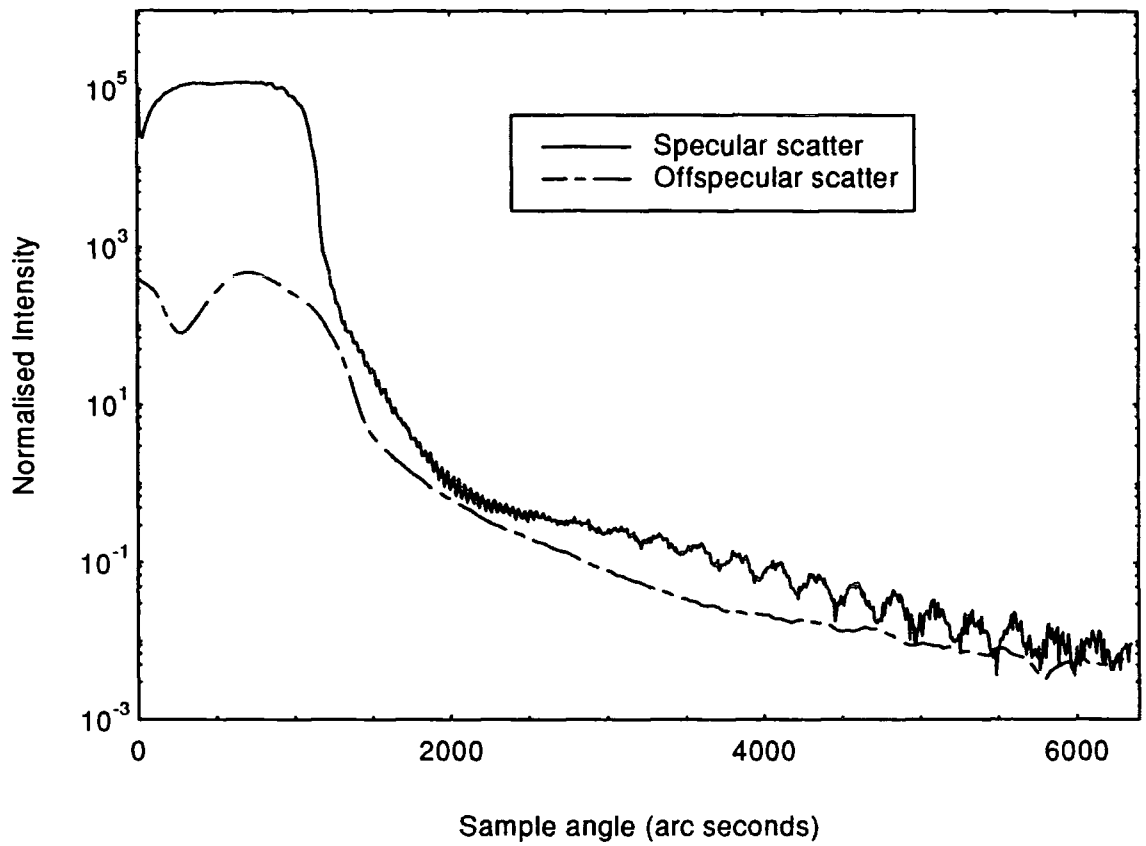
Fig 4.18   Comparison of the specular and offspecular scatter from a
              typical polished 'therm' sample
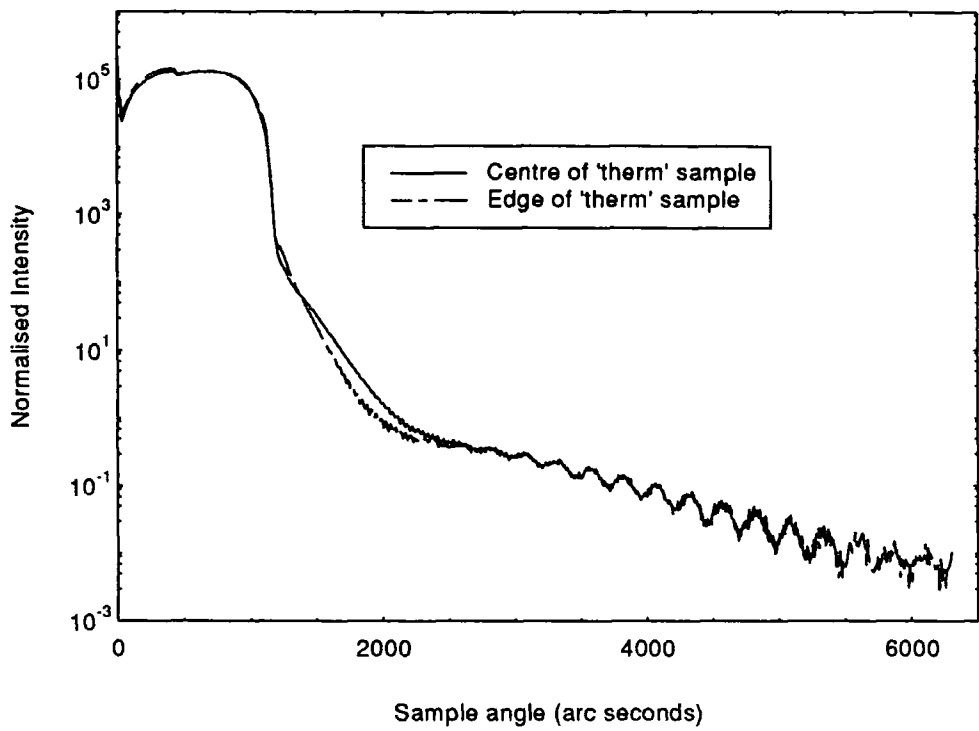
Fig 4.19   Comparison of the specular scatter taken from two
areas of the same polished 'therm' sample
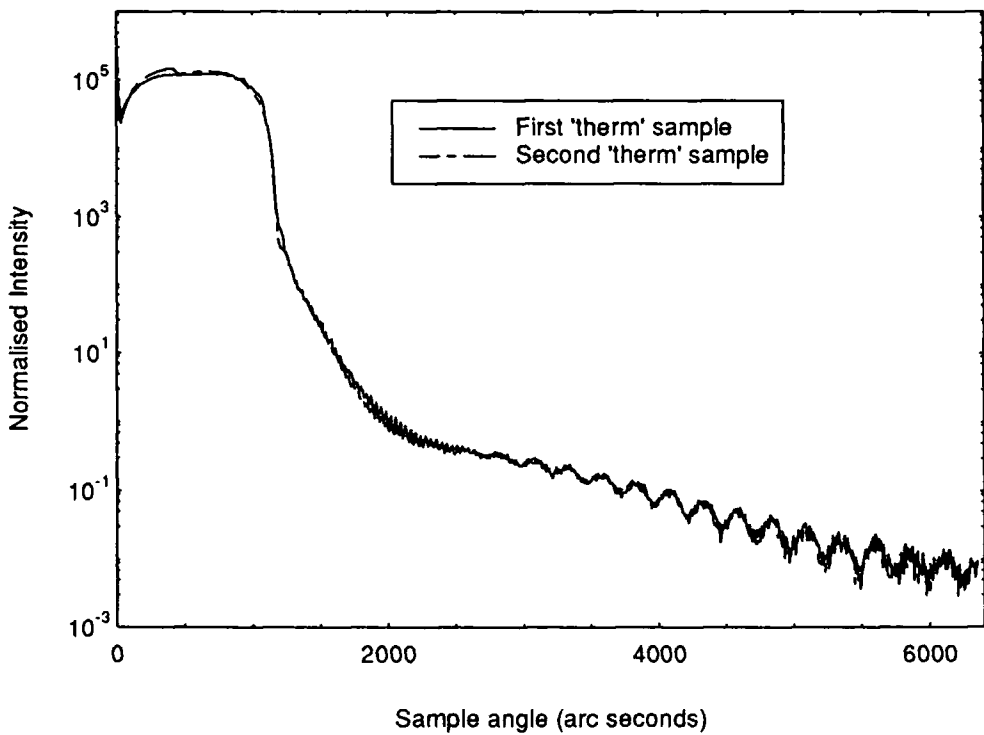
Fig 4.20   Comparison of the specular scatter taken from two separate
polished 'therm' samples

Simulations of the specular scatter were initially attempted using the REFS specular simulation code written by M. Wormington at Bede Scientific [15]. Figure 4.21 shows typical experimental data with its best fit simulation, whilst the simulated structure is shown in figure 4.22. During simulations, it quickly became apparent that the nominal structure could not reproduce the fringe pattern. In all cases, the initial hump, just after the critical angle was missing. This was resolved as arising from an additional 80 Å layer of material on top of the layers given in the nominal structure. From further specular reflectivity measurements, performed on the GXR1, it became clear that this layer was formed as a result of polishing (figure 4.23). For purposes of simulations it was assumed to be carbonaceous in origin since the polishing particles were diamond. The irreproducibility of this layer between samples is related to the polishing process and in no way detracts from the high quality of the 'as deposited' CVD layers.

A large problem that was encountered with the simulations of the polished 'therm' samples was that of top surface roughness. It was found that even with the maximum amount of roughness allowed by the DWBA, and a large amount of grading, that the initial fall off could not be reproduced. Since no other method existed for calculating the reflectivity other than the DWBA, the only way forward was to remove the $q_z^2\sigma^2 < 1$ criteria and simulate the structure, even though we knew that there was a problem with the breakdown of the Taylor expansion [16,17].

Shown in figure 4.24 is the same experimental curve with its best fit simulation using the DWBA, but disregarding its limitations. This time excellent agreement was obtained between the experimental and the simulated curves. It is reassuring to note that the same structure was obtained as for the simulations with the REFS code except that a top surface roughness of 37 Å ± 1Å was required. The consistency of the fits between the two codes suggests that although the roughness values of the top surface were higher than conventionally allowed within the DWBA, they were not so large as to break down the approximation significantly.
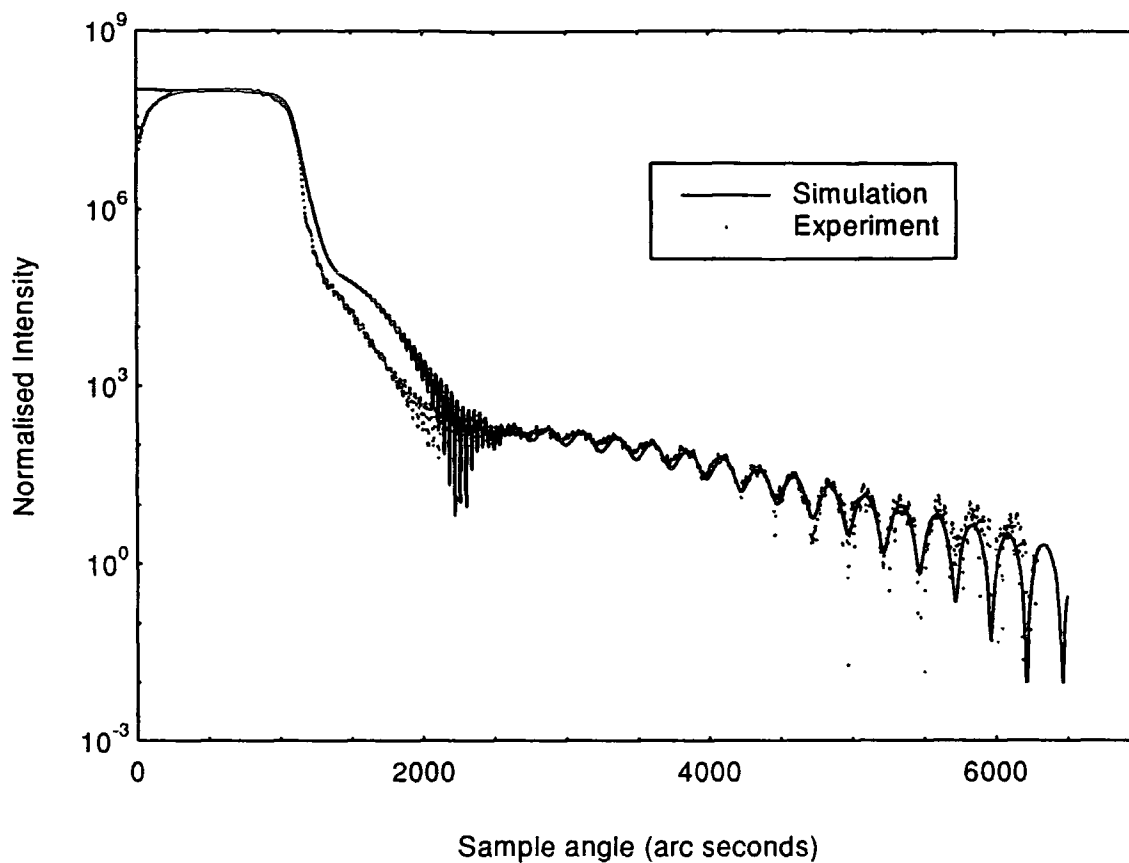
Fig 4.21   Specular scatter from a polished 'therm' sample with its best fit simulation

Layer thickness (± 1 Å)   Interface roughness' (± 1 Å)

C (80 Å)	← 32 Å
SnO₂ (3200 Å)	← 32 Å
Si/C/O (570 Å)	← 9 Å
Float Glass Substrate	← 4 Å

Fig 4.22   Results of the best fit simulation of the polished 'therm' samples
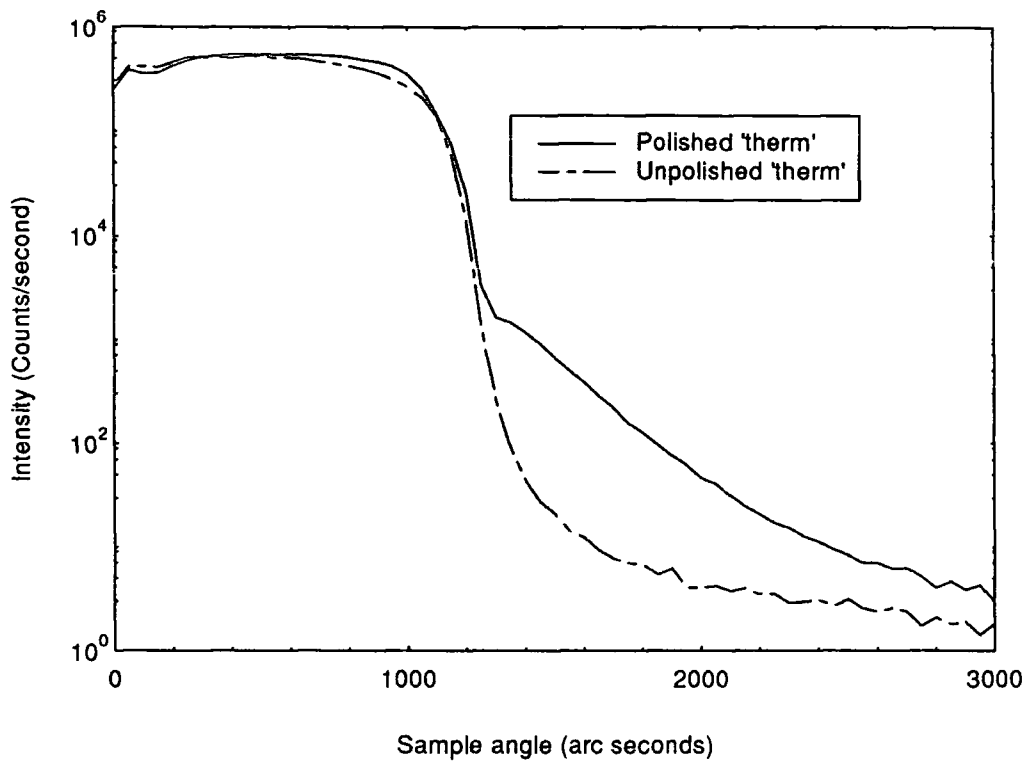
Fig 4.23   Comparison of the specular reflectivity from a polished and unpolished
'therm' sample.   Data taken on the GXR1
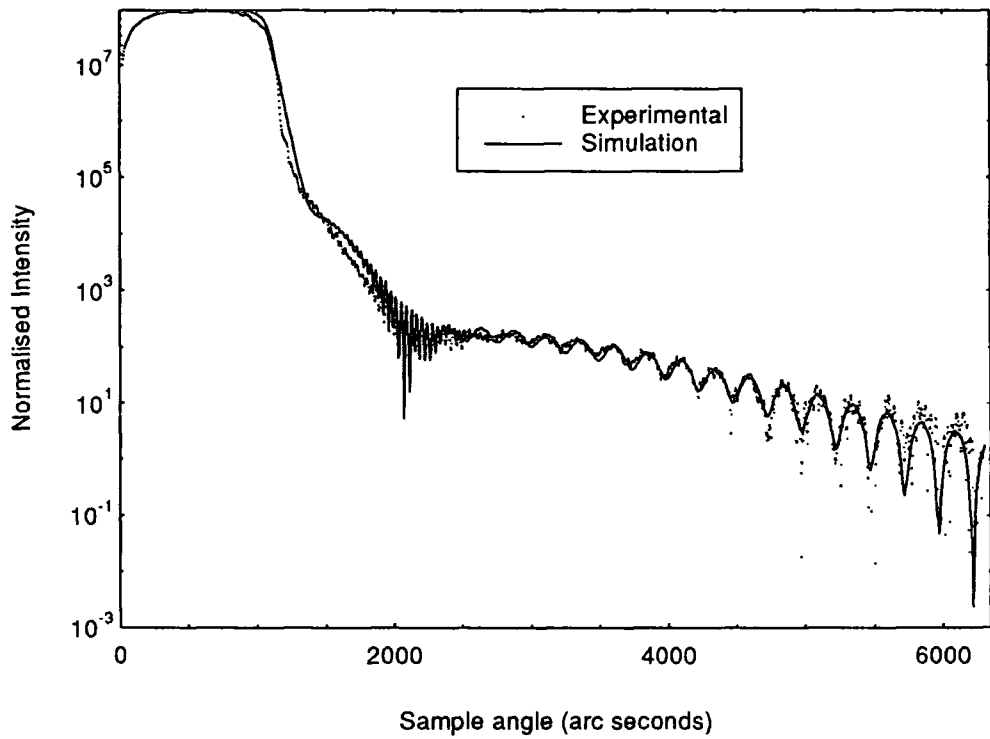
Fig 4.24 Simulation of the specular reflectivity from a polished 'therm' sample with
the $q_z^2\sigma^2 \leq 1$ criteria removed

4.4.2 Studies of the diffuse scatter from the CVD specimens

Although excellent fits were obtained to the data, the exact values of the surface roughness could not be relied upon. This was due to the lack of sensitivity in specular scans to the amount of grading present in the structure. In order to overcome this, transverse diffuse scans were taken at several scattering angles in the hope that a consistent simulated data set may have be obtained. Again a high level of reproducibility was seen between samples (figure 4.25), suggesting Angstrom level control of interface roughness. A striking feature in the data was the appearance of two critical angles in the transverse diffuse scans. The wing at 1060 arc seconds was well understood. This corresponded to the Yoneda wing observed in unpolished 'therm' samples, and gave a top surface density of 6.4 g/cc. Although this density was significantly less than the 6.9 g/cc expected for bulk SnO_2, it can be explained by Ultrasonic Force Microscopy measurements taken on similar SnO_2 layers by O. Kolosov at Oxford University. These showed that the top surface of the unpolished 'therm' samples consisted of micron sized grains. As with the ceramics, such a structure would be averaged over by the x-rays, and a density related to the grain to pore ratio would be predicted. Such a measured surface density would suggest that 8% of the top 50 - 75 Å below the carbonaceous material was in actual fact air.

In contrast, the Yoneda wings corresponding to a critical angle of approximately 700 arc seconds were completely new and also very much broader than the wing corresponding to SnO_2. Additionally, it was noted that these two Yoneda wings did not predict the same critical angle on either side of the transverse diffuse scan (tables 4.8 and 4.9). Such behaviour was completely dissimilar to the two Yoneda wings, corresponding to the SnO_2 layer which were seen to predict the same critical angle (and therefore density) for both incident angles. Similarly, this SnO_2 critical angle in the unpolished 'therm' showed no

variation as predicted by the Yoneda wings on either side of the transverse diffuse scans (table 4.10). The Yoneda wings referred to in the tables below are indicated in figure 4.26.

Detector angle	L.H. Critical 1 (± 20 arc sec.)	R.H. Critical 1 (± 20 arc sec.)	L.H. Critical 2 (± 10 arc sec.)	R.H. Critical 2 (± 10 arc sec.)
3816 arc sec.	695 arc sec.	810 arc sec.	1062 arc sec.	1073 arc sec.
4428 arc sec.	677 arc sec.	806 arc sec.	1048 arc sec.	1062 arc sec.

Table 4.8   First polished 'therm' sample. Data taken at the S.R.S.

Detector angle	L.H. Critical 1 (± 20 arc sec.)	R.H. Critical 1 (± 20 arc sec.)	L.H. Critical 2 (± 10 arc sec.)	R.H. Critical 2 (± 10 arc sec.)
3816 arc sec.	706 arc sec.	792 arc sec.	1055 arc sec.	1058 arc sec.
4428 arc sec.	684 arc sec.	767 arc sec.	1048 arc sec.	1058 arc sec.

Table 4.9   Second polished 'therm' sample. Data taken at the S.R.S.

Detector angle	L.H. Critical angle (± 30 arc seconds)	R.H. Critical angle (± 30 arc seconds)
3000 arc sec.	1047 arc sec.	1045 arc sec.

Table 4.10   Original unpolished 'therm' sample. Data taken on the GXR1.
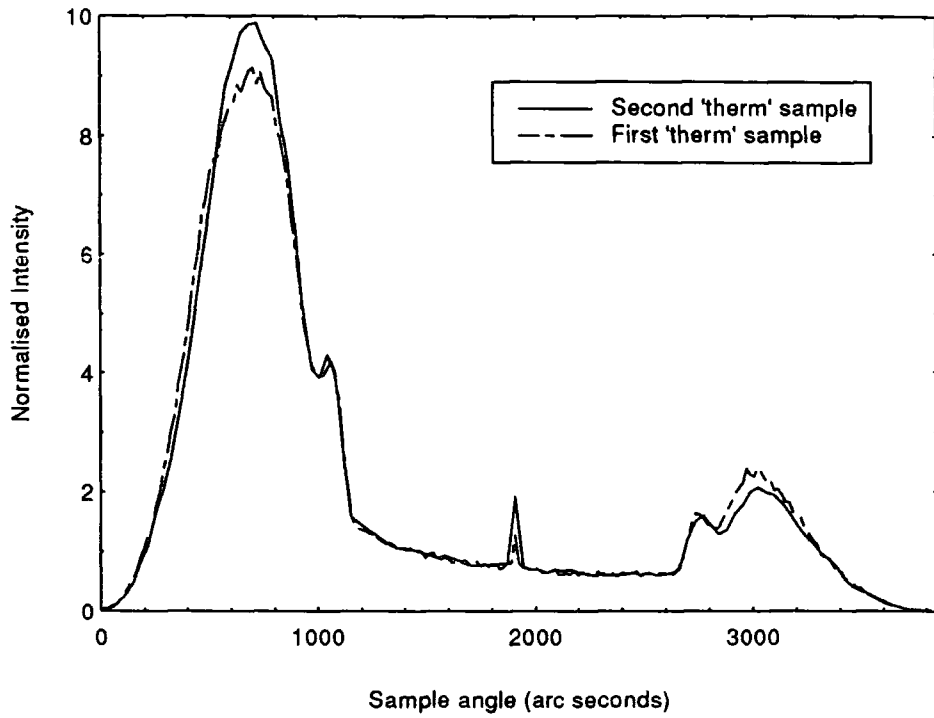
Fig 4.25 Comparison of transverse diffuse scans taken from two polished 'therm' samples. Scattering angle = 3600 arc seconds
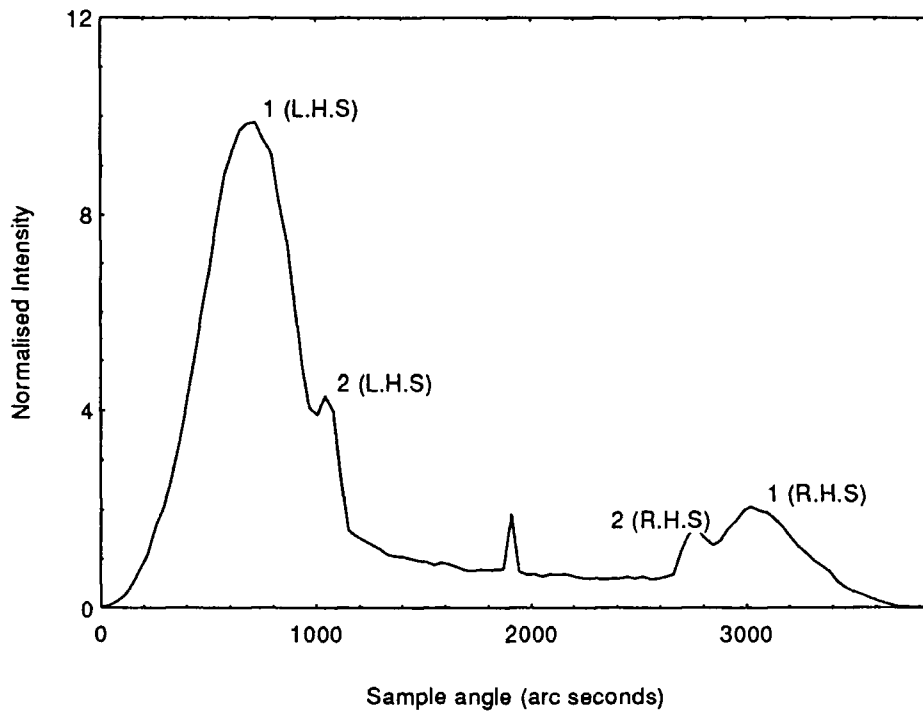
Fig 4.26 Graphical representation of the notation used in tables 8 and 9 for the two sets of Yoneda wings observed in the 'therm' samples

4.4.3 Two critical angles?

Simulations of the diffuse scatter could not reproduce the two sets of Yoneda wings for any combination of top surface roughness as indicated in figures 4.27 to 4.29. These simulations were performed using the structure shown in figure 4.22 with a lateral correlation length of 500 Å and a fractal exponent of 0.3. Although split Yoneda wings had been seen in simulations of Cu on Si, as shown in figure 7.21, these were only in highly correlated systems and were thus an interference effect. As shown in figure 4.18, no correlated roughness existed in these samples and so this effect could be eliminated. Further more, as the top surface of the 'therm' samples was carbon, it was less dense than the SnO_2 layer beneath. From simulations shown in section 4.2.3, it was seen that in such a system no effect on the position of the Yoneda wing was produced for any thickness of the top carbon layer. As a result, the existence of the two Yoneda wings must be related in some way to the SnO_2 layer not the top surface.

As the existence of the two sets of Yoneda wings could not be explained by using a simple layer model other explanations had to be sort. If the second observed critical angle was not a result of interference (and therefore not a critical angle at all) it must be real! In order for two Yoneda wings to be in existence, regions of the surfaces greater than the coherence length must exist which have significantly different densities. Two possibilities exist that could give rise to this effect.

The first possibility is that during polishing the surface coating has been ripped off in 'patches' of size greater than the projected coherence length of the x-rays (0.5 mm). This would expose the bare float glass underneath, which would scatter independently from the surface. As a result, two sets of Yoneda wings would be observed.

The second possibility is that during polishing, for some reason, different areas of surface density had been produced. Again these regions would have to be greater than the coherence length of the x-rays and so greater than 0.5 mm in diameter. As a result, the
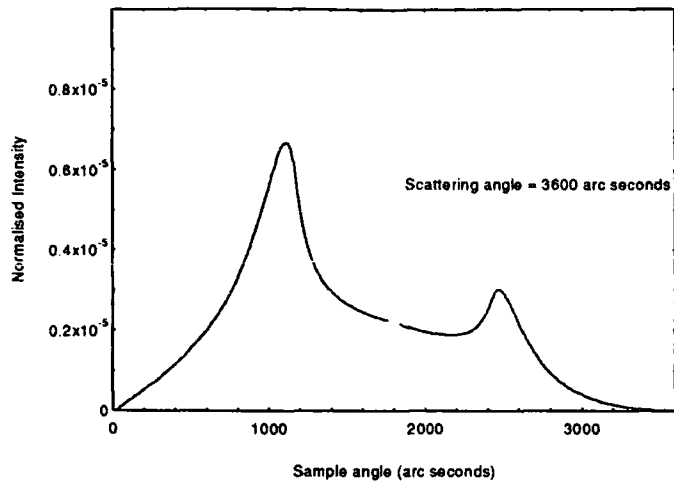
Fig 4.27 Simulation of a 'therm' sample with 5 Å roughness on the top two interfaces.
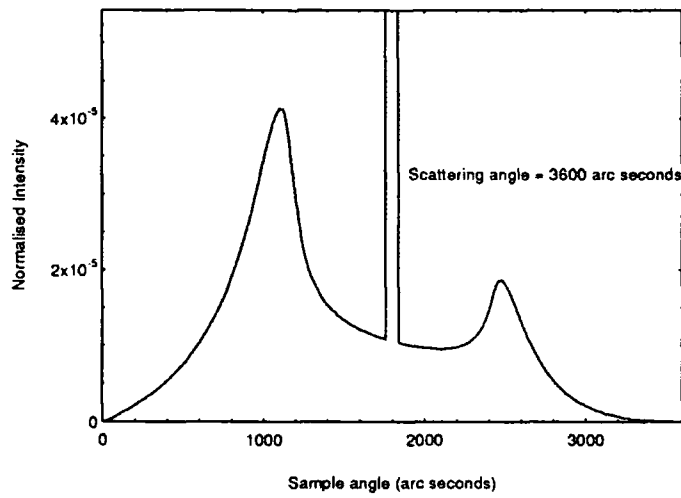
Fig 4.28 Simulation of a 'therm' sample with 15 Å roughness on the top two interfaces
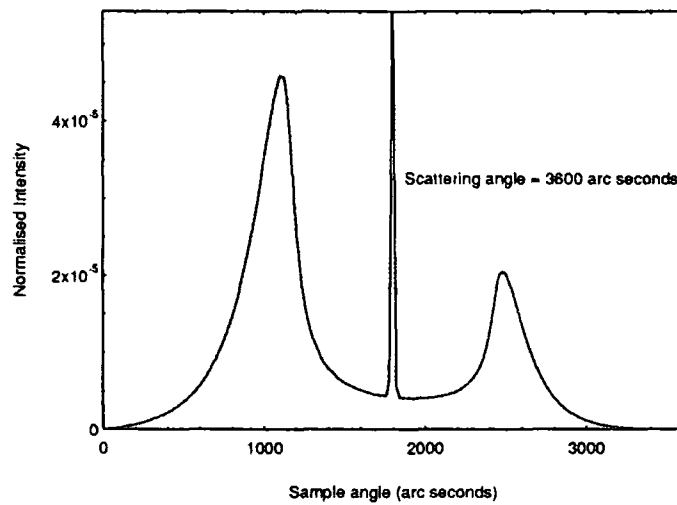
Fig 4.29 Simulation of a 'therm' sample with 35 Å roughness on the top two interfaces

separate regions would scatter independently and two separate Yoneda wings would again be observed.

In order to verify whether the surface coating had been removed in places, Normarski phase contrast measurements were made in Durham and Talystep measurements were performed at Logitech by M. Robertson.

Normarski phase contrast is an extremely sensitive optical technique for the sensing of height differences. Typically, it can sense such variations down to less than 1% of the wavelength of light that is being used. As a result, for our measurements a sensitivity of better than ± 5 Å would be expected. This is several orders of magnitude smaller than the 4000 Å which would be seen if the surface layer had been removed. The complimentary scanning probe technique of Talystep is also extremely sensitive to height variations, typically giving reliable results on vertical heights down to a few angstroms.

Results from both the Normarski phase contrast microscopy and the Talystep measurements revealed that no large 'craters', corresponding to the removal of the surface layers, existed. As a result, the model of a surface from which large chunks had been removed could be discounted. In consequence, the existence of the two separate sets of Yoneda wings, and therefore critical angles, imply that the surface is one in which lateral inhomogeneities are present. Such inhomogeneities are larger than the lateral projected coherence length of the x-rays and so on the 0.5 mm scale. Since in the unpolished samples, only one set of Yoneda wings was present, it may be inferred that the polishing of the samples has produced these lateral density variations on the surface. It is difficult to see that there could have been any intermixing between the two deposited layers, since the 'as polished' top layer was still several thousand angstroms thick. However, since the polishing process works by the incorporation of the polishing particles into the softer material, it may be speculated that the existence of lateral density inhomogeneities arose from the inclusion of carbon, in certain regions, from the residue of the polishing process. The second set of Yoneda wings, corresponding to the unpolished SnO_2 would therefore be arising from regions where such contamination had not taken place. Since the size of

this extra set of Yoneda wings in the diffuse scatter is much greater than those from the SnO_2, it can be inferred that a significant fraction of the surface has undergone this contamination. On to this 'patchwork' surface the carbonaceous layer is later deposited.

4.4.4 Sinθ corrections and the need for detector only scans

The variation of the measured critical angle on either side of the transverse diffuse scan was initially thought to be due to the sine theta corrections in the scans. This would cause the maxima of broad sets of Yoneda wings like those found at the critical angle of approximately 700 arc seconds to experience a shift to the left. As the critical angles are measured from the two edges of the scan, the resulting density as predicted from the left hand and right hand side Yoneda wings would be reduced and increased respectively. In contrast, the positions of the narrower 1060 arc second Yoneda wings would not be affected so much. In consequence, these Yoneda wings would predict the same density.

In order to eliminate the effect of the sine theta correction, detector only scans were performed. These scans give a constant projected coherence length, since the sample angle is fixed and the detector is scanned. In addition, as the beam footprint is a constant, there is no associated sine theta correction to the position of the Yoneda wing. As a result, the critical angle measured relates to the true density of the surface.

A typical detector only scan is given in figure 4.30, whilst the critical angles measured from the second polished 'therm' sample for several different angles of incidence is given in table 4.11. The convention used in this table to label the Yoneda wings is identical to
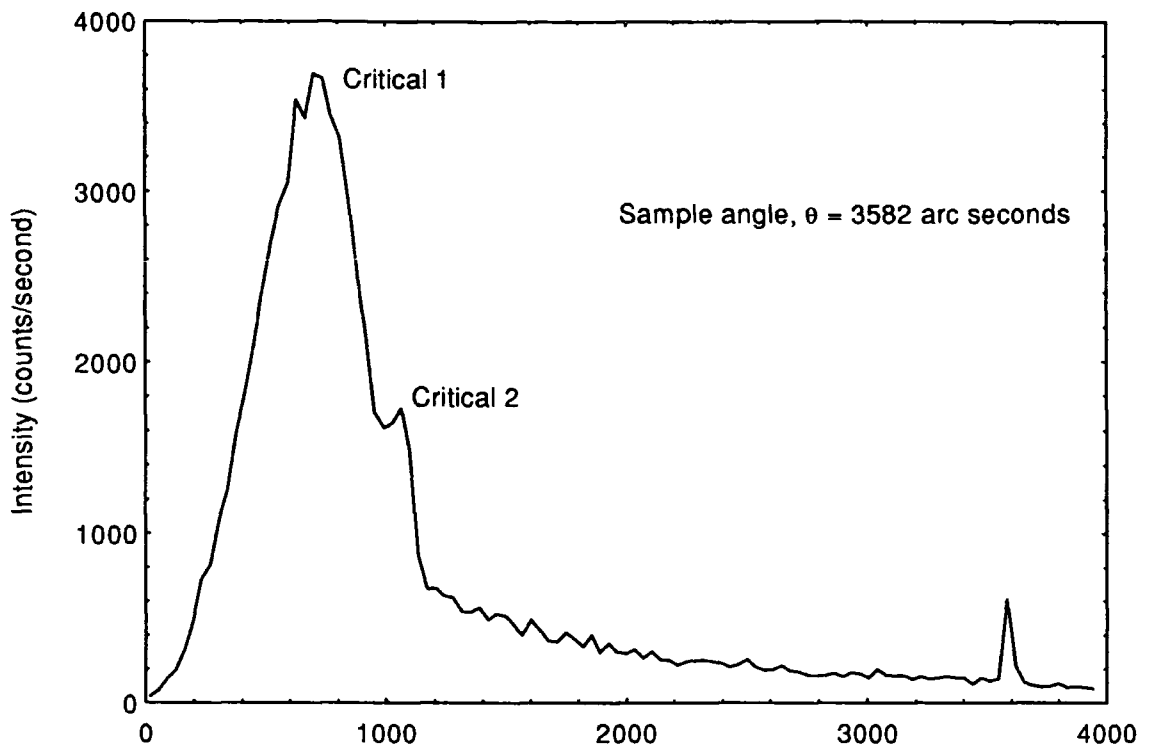
Fig 4.30   Example detector only scan to demonstrate the two critical
angles referred to in the text

that used in the transverse diffuse scans. For clarity, the two Yoneda wings have also been labelled in figure 4.30.

Sample angle (arc seconds) (fixed)	Critical 1 (arc seconds) (± 20 arc seconds)	Critical 2 (arc seconds) (± 20 arc seconds)
1386	871	Unreliable data
1908	770	1040
2214	745	1040
3582	713	1055

Table 4.11   Second polished 'therm' sample. Data taken at the S.R.S.

It is clear from the data in the table that again the critical angle corresponding to the SnO_2 is constant as a function of projected coherence length whereas the other Yoneda wing is not. However, this time the predicted surface density from the Yoneda wing corresponding to approximately 700 arc seconds decreases for increasing sample angle and therefore decreasing projected coherence length. This trend was completely buried by the sine theta 'roll off' of the wings in the transverse diffuse scans.

4.4.5 The possibility of lateral density variations

From these values of the surface density deduced from the Yoneda wings for different projected coherence lengths, inferences can be made as to the type of distributions that exist within the density patches. As the projected coherence length of the x-rays is altered the Yoneda wings can be used to probe the type of density variations on the surface. The Yoneda wings corresponding to SnO_2 predict the same critical angle for all projected coherence lengths. This implies that the 'patches' of surface density, giving these are constant, or are made up of density variations very much smaller than the coherence length of the x-rays. On the other hand the Yoneda wings corresponding to the lower density ($\rho \approx 2.9$ g/cc) predict a critical angle which varies as a function of projected

coherence length. This implies that the 'patches' of density giving rise to this Yoneda wing are themselves made up of a distribution of densities which are smaller, but close to the size of the x-ray coherence length. For the density observed, calculations showed that approximately 90% of the top 50 to 75 Å below the top layer must in fact have been carbon.

During the studies of ceramics (sections 5.2 to 5.5) variations of the measured surface density with coherence length were also observed. In this instance the density was seen to decrease for increasing coherence length. This was due to the scatter arising solely from the regions where grains existed and is explained in section 5.5. However, in the case of the 'therm' samples, the density is seen to increase for increasing coherence length. In order to explain this, the lower density material must occupy the majority of the surface. In this case, as the coherence length is increased, more of the sparsely populated denser patches are included and the average density is increased. This conclusion is consistent with the above findings that 90% of the top surface must have been carbon.

Returning to the transverse diffuse scans. Theoretically, since the regions of varying density, giving rise to the two sets of Yoneda wings, are greater than the lateral coherence length of the x-rays, they can be treated as kinematical scatterers. As a result, if the ratio of the two types of material are known on the surface, then simulations can be performed on the sample. This is done by simulating the two regions separately and then adding the diffuse curves together, before comparing them with the experimental diffuse scatter. An unfortunate consequence of not being able to detect the presence of the density variations by any other technique is that no ratio of the amounts of the two regions can be deduced. In consequence, both the degree of roughness, and the amount of material present on the surface change the height of the diffuse scatter, and as such no simulations of this can be undertaken at the present time.

4.4.6 Summary

In summary, the CVD deposition of 'therm' leads to a highly reproducible layer structure both in terms of the layer thickness and the interface roughness. The interface structure of these samples is not measurable by optical techniques since the refractive index of the layers has been specifically designed to make them invisible to the eye! As a result, the additional contrast that is obtained at x-ray wavelengths makes x-ray reflectivity an ideal tool to study these materials. The layer thickness values are not exactly the nominal ones, but this is trivially a calibration problem. The initial surface roughness of the 'as deposited' 'therm' is too high for meaningful measurements using GIXS, but on polishing these can be performed. On polishing of the specimens, a thin top surface layer is observed to appear. This layer is not constant from sample to sample. However, such a variation infers more about the reproducibility of the polishing process that the original deposition of the layers and polishing residue layers have been observed in other studies (chapter 6). However, in addition it appears that by some mechanism, most likely inclusion of material, that lateral inhomogeneities in density have been introduced during polishing. It would appear that the surface consists of regions of largely uncontaminated SnO_2 on the order of 0.5 mm which are surrounded by regions which are impregnated by lower density material (figures 4.31 and 4.32). It is not known how deep such contamination penetrates, only that it is greater than the top 75 Å. In addition, since the top surface layer is almost certainly less dense than the bulk, it can be deduced that this observed density variation is from the SnO_2 itself. Such observations are evident on all the sample studied after polishing.
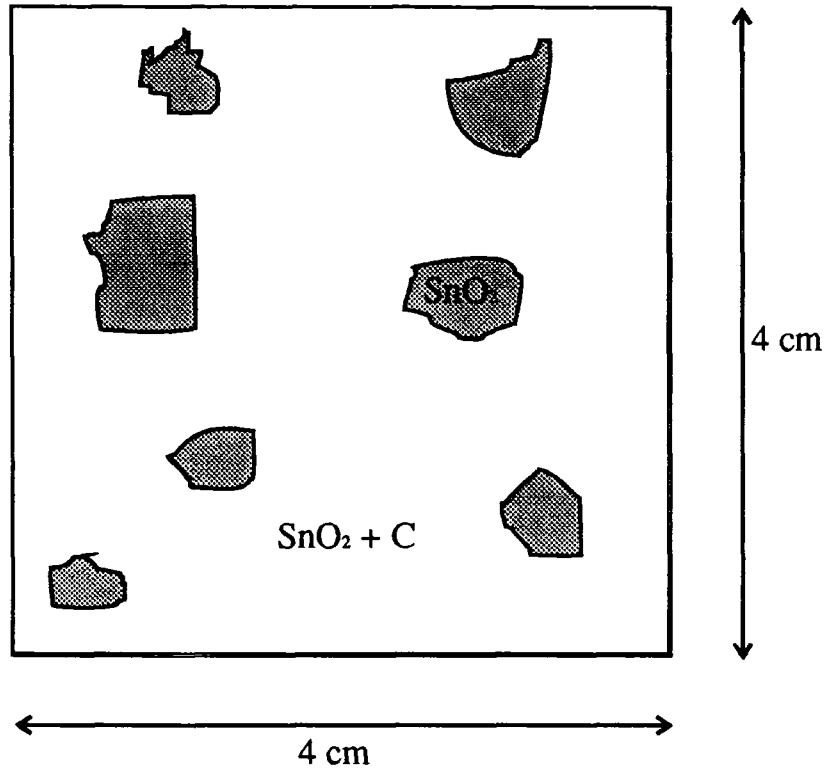
Fig 4.31   Model proposed for the top surface of the 'therm' samples after polishing
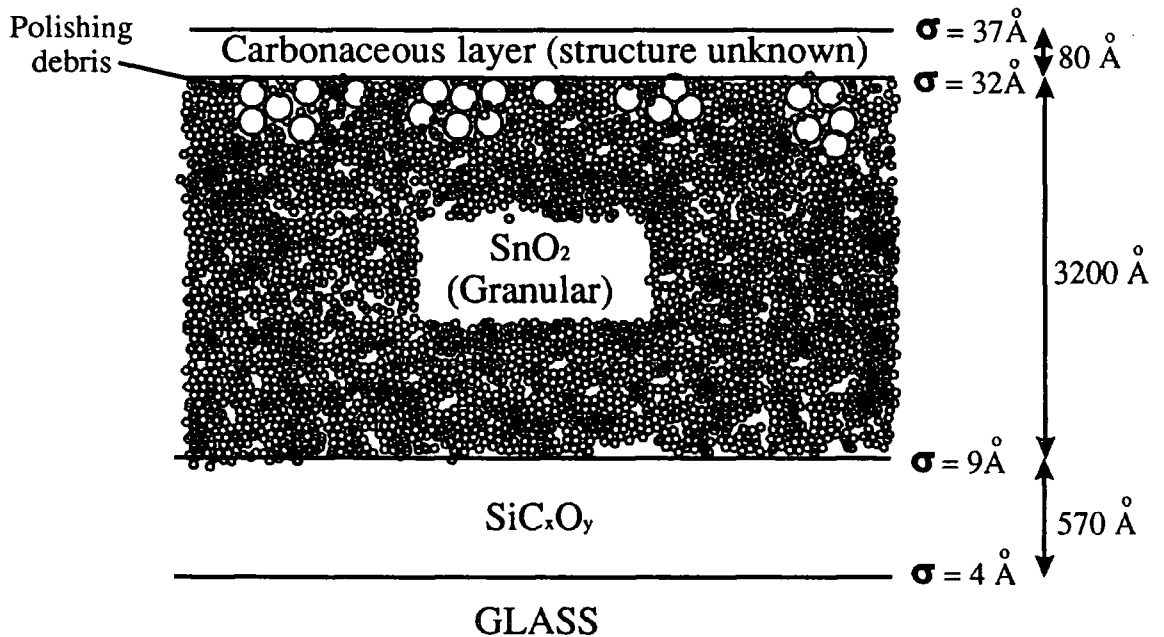
Fig 4.32   Cross section of the proposed structure for a polished 'therm' sample.
Errors on all layers and roughness values: ± 1 Å

Chapter V

X-ray scattering studies of ceramics as a function of processing conditions

5.1 The manufacture of ceramics

5.1.1 Introduction

Reference [1]

In modern day life mechanical seals are extremely important. These are found in a variety of devices from pumps to valves and a whole range of products from cars to washing machines. A drawback with the traditional vulcanised rubber or plastic seals is they wear relatively quickly, especially when the environment is hot or corrosive.

Over the past decade ceramics have appeared with increasing regularity in new applications, far removed from their traditional roles such as cements, basins and pottery. Ceramics are comprised of ionically bound, polycrystalline particles which have been pressed into shape and fired to give them strength. The result of the ionic bonding is that very few slip systems are available for plastic deformation and the resulting material is hard and brittle. These properties have been exploited in the industrial community and as such, ceramics have been used in a variety of applications such as high speed turbine blades, thread guides, engine blocks and valves.

A major expense in the manufacture of ceramic components is the grinding, lapping and polishing operations that must occur after the initial firing. The need for this extra processing is firstly due to the lack of control of the shrinkage of the particles during firing and secondly due to the pull out of grains from the ceramic surface. In order to compensate for this uncertainty in size, the 'as fired' ceramics are designed to be approximately 1 mm larger than required and the excess material is removed by grinding.

After grinding, ceramics cannot be used as mechanical seals due their extremely irregular surfaces. To overcome this difficulty, the ground ceramics are then subjected to various combinations of lapping and polishing until the desired surface finish is attained. As an example, tap plates which have not been sufficiently smoothed will have high points on their surfaces. Such regions will experience higher forces and are likely to cause early failure of the component. The result for the consumer is that the newly installed quarter turn tap leaks or sticks after only a few months! Fortunately this is rarely the case and with state of the art ceramic tap plates consumers can expect ten to fifteen years of useful life.

The requirements for grinding and polishing faced by the ceramics industry at the present time is completely analogous to the problems faced by the plate glass industry in the late 50's [2]. At this time glass was produced in plates and machined to size using a combination of grinding and polishing. With the invention of the float process in 1959, this whole stage of processing was removed and subsequently thousands of millions of pounds have been saved across the world. In this context it is clear how important the study of the grinding and polishing processes are in the processing of ceramics, since even if only the machining times are reduced, this will produce significant savings and increases in productivity.

A surface sensitive x-ray technique, developed at Bede Scientific which can be used on these materials is parallel beam x-ray diffraction (PBXRD). Work by Bowen *et al.* on 'as fired', ground, lapped and polished samples indicated that during grinding a clear increase in the stress within the near surface grains occurs. On polishing, these were seen to relax back to their values in the 'as fired' state. Apart from this work, to our knowledge, no grazing incidence x-ray measurements have ever been reported on the study of ceramics as a function of processing conditions.

5.1.2 Powder pressing

A powder containing a small amount of organic binder is compressed into shape within a metal die. This results in the particles rearranging themselves so as to minimise the amount of void space within the samples, but at no time does plastic deformation of the ceramic grains occur. In the case of the samples used in this study, uniaxial pressing was employed.

5.1.3 Firing

After the pressing process, the separate particles are held together only by the strength of the binder. The resulting 'green' ceramics lack mechanical strength and as a result, must undergo firing before they can be used in applications. During firing sintering takes place and necks form between the individual particles. In addition, the pore sizes between the particles shrink and as a result the average density increases. The transport of material from the bulk of the particles to the neck region during sintering is accomplished by diffusion which is highly efficient at these elevated temperatures. For the Al_2O_3 used in this study, firing took place between 1400 and 1600 degrees centigrade for a period of 3 to 4 hours.

5.1.4 Lapping and polishing

During lapping, a suspension of particles is introduced into the region between a plate and the sample surface. A force is then applied to the sample from above, typically in the region of 10 psi, which presses it against the plate and the particles underneath. The sample is fixed in a holder, but is free to rotate around its surface normal. As the plate rotates (10s rpm) particles roll between it and the sample surface, tearing pieces out of the sample as they pass. Due to the rotation of the sample, no preferential direction is introduced in this procedure. The hardness of the plate is carefully matched to that of the sample, otherwise the particles will get embedded in the softer material.

In contrast to the lapping process, polishing takes place with a softer plate, into which the polishing particles become embedded. During subsequent rotations the particles 'plane' pieces off the sample surface. In conjunction with the different plate, approximately half the force is applied as compared to lapping, and the plate rotates at a slightly slower rate. All this leads to a more gentle process which removes material in a much slower and more uniform manner than lapping. In lapping typically half a millimetre is removed in the time that polishing takes to remove a few micrometers.

5.1.5 Grinding

In grinding, a lubricated wheel is again used in conjunction with abrasive particles, to remove material from the surface of samples. However, this time the abrasive particles are resin bonded to the wheel and tear large chunks out of the surface as they move across it. The size of the abrasives is in the region of one hundred micrometers.

In the case of the ceramics ground here, two different grinding processes were used, namely unigrinding and horizontal surface grinding. There are two main differences between these processes. Firstly the unigrinding process has a preferred direction, whereas in horizontal surface grinding no such direction exists. Secondly, during horizontal surface grinding, the surface of the material is ground once, whereas in the unigrinding a second stage takes place. During this, a second shallower cut is performed in which any grains that have 'sprung back up' after the initial sweep are plucked out. The uniground process is expected to be, in general a better finish, since the second sweep, which just clips the surface, removes damage more gently than the first deep cut.

Although grinding is very effective in removing large amounts of material quickly, the highly energetic removal of particles inevitably introduces a large amount of subsurface damage in the samples. As a result, the finished samples also underwent a 5 minute 6 μm lap with diamond particles followed by a 15 minute polish with 3 μm cerium oxide.

5.2 X-ray scattering studies of ceramics performed on the GXR1

5.2.1 Estimation of the errors associated with the measurements

Grazing incidence x-ray scattering measurements were initially performed on the GXR1. All samples were too rough for analysis by the DWBA and there was no specular scatter present. As a result, transverse diffuse scans were made for constant incident intensity and scattering vector. For purposes of reproducibility of the samples on the production line, three nominally identical samples were studied for each change in processing conditions.

In order to observe the surface density of the ceramics as a function of polishing conditions the positions of the Yoneda wings were measured. As described in sections 3.2.1 and 3.2.7, the position of the Yoneda wings is related to the critical angle and therefore the surface density of the samples. Experimental errors associated with the measurement of the surface density arose due to the uncertainty in the position of the Yoneda wings. This was estimated to be in the region of ± 0.1 g/cc.

For measurements of the surface roughness, the integrated intensity of the diffuse scatter was recorded. As this scatter arises due to the roughness on the surface of the samples, it was hoped that its variations could be related to the effects of the processing on the samples. The error on the integrated intensity originated in the uncertainty in removing the background. This produced errors which varied from 4%, for integrated intensities of 1×10^5 c/s.arc second to 8% for integrated intensities of 1×10^4 c/s.arc second.

In order to study the effect of each stage of the processing, x-ray diffuse scattering measurements were made at different stages of production. No x-ray reflectivity data were available from the samples which had undergone horizontal surface grinding followed by lapping for various times due to time restrictions within the LINK nanotechnology programme.

5.2.2 Lapping of the Uniground brown alumina samples

A series of samples of 96% brown alumina were uniground and then lapped for different times. Figure 5.1 shows the surface density as a function of lapping time. It can be seen that no significant change occurred in the surface density as a function of lapping time. However it was noticed that it was of a value significantly lower than from 'as fired', bulk ceramics, which have a surface density of 3.86 g/cc. It was also noted that there was a negligible amount of spread in the data from the nominally identical samples.

The variation of integrated diffuse scatter as a function of lapping time is shown in figure 5.2. In contrast to the surface density data, a slight reduction of integrated intensity with increased lapping time was observed.

5.2.3 Polishing of the 'Uniground and lapped' brown alumina samples

To study further the unigrinding process, uniground samples were subjected to a standard lap and then polished for various times. The variation of surface density with polishing time is shown in figure 5.3. In this case a clear rise and early saturation to 3.55 g/cc, close to the fired density was observed. In addition, the spread of the data from the nominally identical samples is very small, in all cases less than the experimental error on the x-ray measurements.

The variation of integrated diffuse intensity with polishing time is shown in figure 5.4. No trends were observed in the data, but it was noted that the integrated diffuse scatter was a factor of five higher than in the lapped samples.
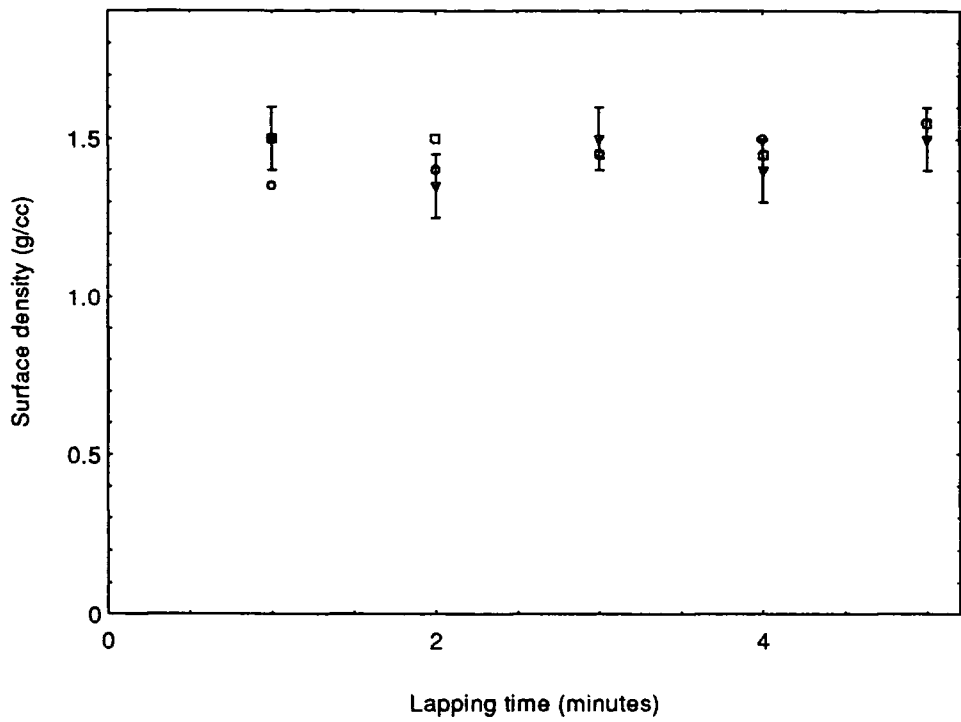
Fig 5.1   Variation of surface density of uniground samples with lapping time
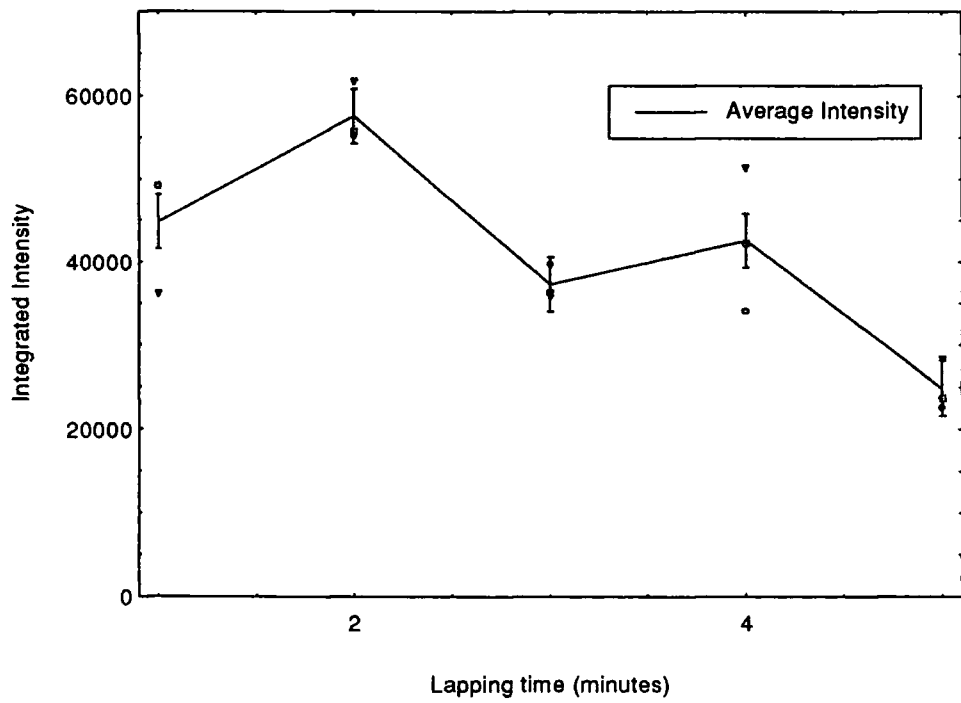
Fig 5.2   Variation of the integrated intensity from uniground samples as a
function of lapping time
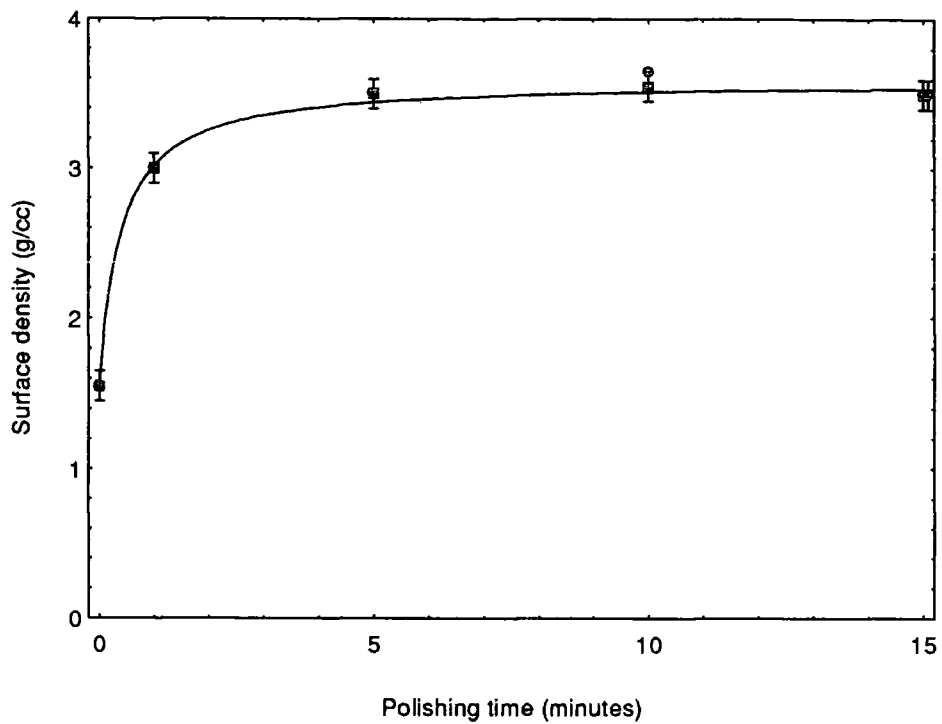
Fig 5.3   Variation of the surface density for 'uniground and lapped' samples as a function of polishing time
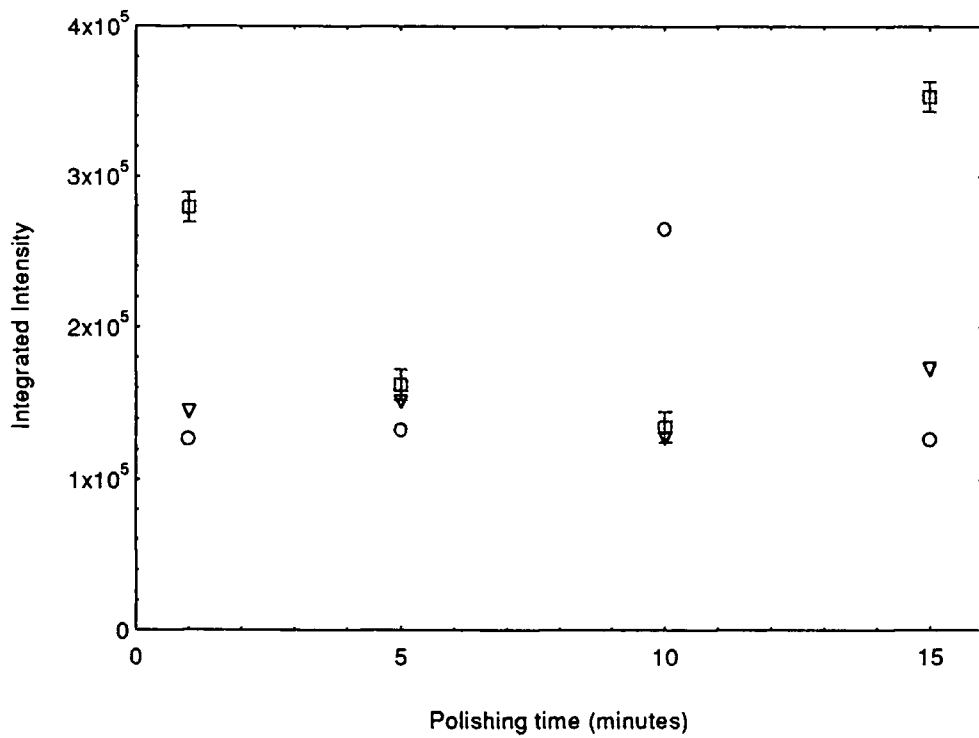
Fig 5.4   Variation of the integrated intensity from the 'uniground and lapped' samples with polishing time

5.2.4 Polishing of the 'Horizontal surface ground and lapped' samples

A similar series of measurements were performed on samples which had been horizontally surface ground, lapped and polished for various times. Figure 5.5, displays the variation of top surface density with polishing time. The curve is strikingly different from that of the uniground samples, with a plateaux of density 1.5g/cc, followed by a sharp rise at 7.5 minutes. However, even at 15 minutes, the polishing process had only increased the density to 2.9 g/cc and no saturation had occurred. Accompanying the rise in surface density was a greater variability in the nominally identical samples. Their variations changed from just above the experimental error of the x-rays, for polishing times less than 7.5 minutes, to variations well in excess of the experimental error for later times.

The integrated intensity of the samples, shown in figure 5.6, has a similar variation with time as had the surface density variations of the samples. As shown in figure 5.7, there is a clear trend between the measured surface density and the integrated intensity. It is unfortunate that the lack of data in the mid density region means that the exact relationship cannot be determined with certainty.

5.3 Bearing area measurements on the lapped and polished samples

5.3.1 The technique of bearing area measurements

The bearing area of the ceramic samples were measured by Morgan Matroc Ltd, using optical reflectivity. As the flat, polished, top surface of the grains reflected the light specularly these showed up as white. Conversely the unpolished surface between the grains scattered the light diffusely and appeared dark. By comparing the ratio of light to dark, the relative area of flat, polished, top surface could be calculated. This is known as the 'bearing area'.
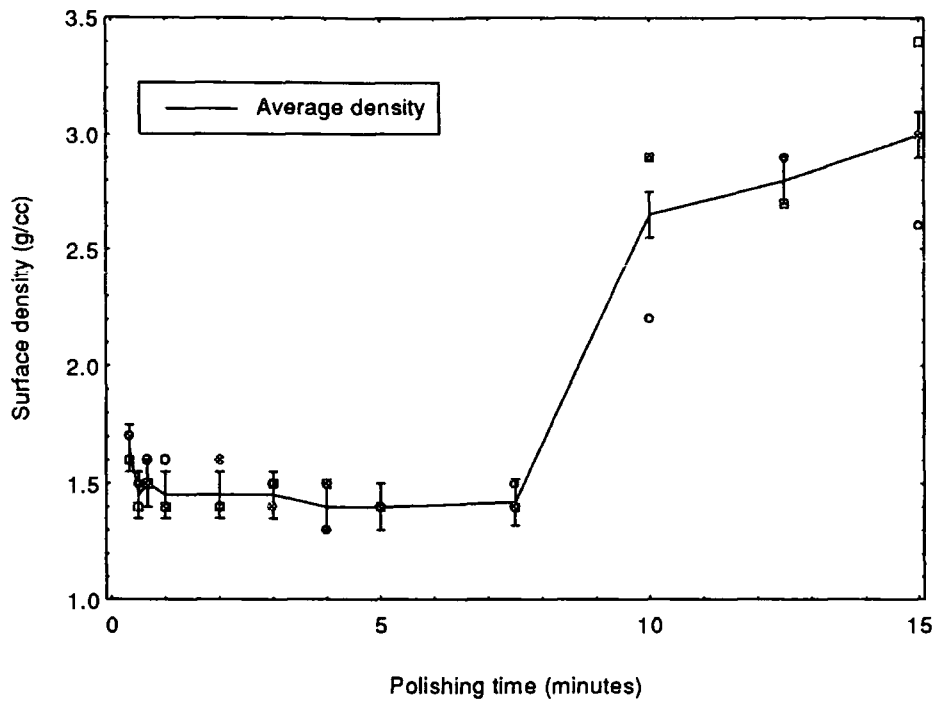
Fig 5.5   Variation of the surface density of 'horizontal surface ground and lapped' samples as a function of polishing time.
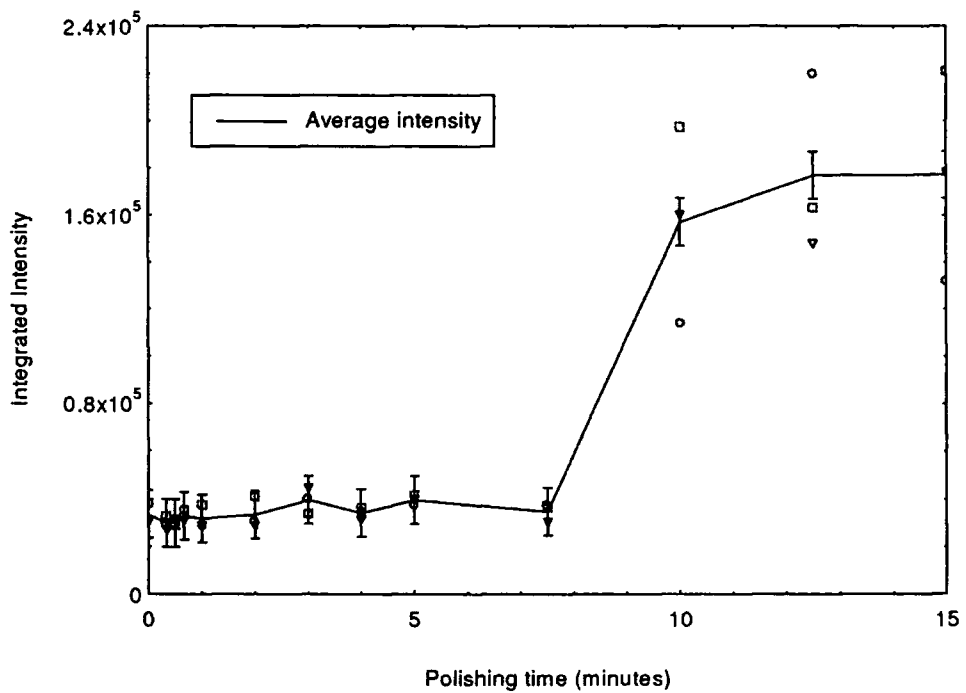
Fig 5.6   Variation of the integrated intensity from 'horizontal surface ground and lapped' samples for a variety of polishing times

5.3.2 Measurements on the Uniground samples

The results of the bearing area measurements made on the samples that had been subjected to unigrinding, a standard lap and then a variety of polishing times are shown in figure 5.8. Clear similarities between these measurements and the surface densities calculated from the positions of the Yoneda wings in GIXS (figure 5.3) are immediately apparent. Comparisons of the bearing area measurements and the surface density measurements are shown in figure 5.9. Here it is clear that a strong trend is in evidence between the surface density and the bearing area measurements. However, although a straight line fit is easily obtained to the data, caution must be urged before stating that a linear trend exists between these two quantities. The reason for this comes from the optical microscopy measurements made at Oxford (section 5.7). From these, the surfaces of the 'uniground and lapped' and 'horizontal surface ground and lapped' samples appears to be strikingly similar in the polishing stage. In both cases a transition from an island to a planar surface is seen, albeit at a different polishing time. When it is also considered that the 'horizontal surface ground, lapped and polished' samples do not show a linear trend between surface density and bearing area (figure 5.11); it is hard to justify the statement that a linear relationship is present between the two parameters in the 'uniground, lapped and polished' samples with so few data points in the mid range.

5.3.3 Measurements on the Horizontal surface ground samples

Bearing area measurements made on samples which had undergone horizontal surface grinding, a standard lap and had been polished for a variety of times are shown in figure 5.10. This time a marked difference is seen between these and the surface density measurements. For short polishing times, a slow, but continuous rise is observed in the bearing area. However, as the polish times reach 7.5 minutes, a more rapid rise is seen. This is seen to slow slightly, but never reaches saturation. When the surface density measurements are compared with the bearing area (figure 5.11), it is clear that although there is qualitative agreement for large polishing times, no systematic trend is observed across the entire polishing range. This is again true,
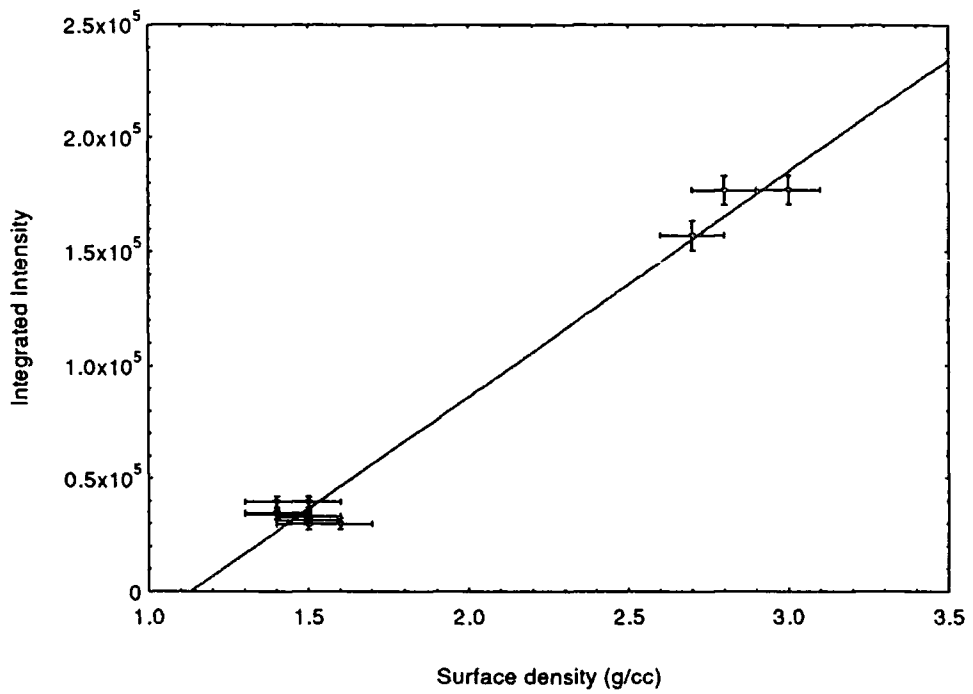
Fig 5.7   Comparison of the surface density and integrated intensity during polishing of a 'horizontal surface ground and lapped' sample.
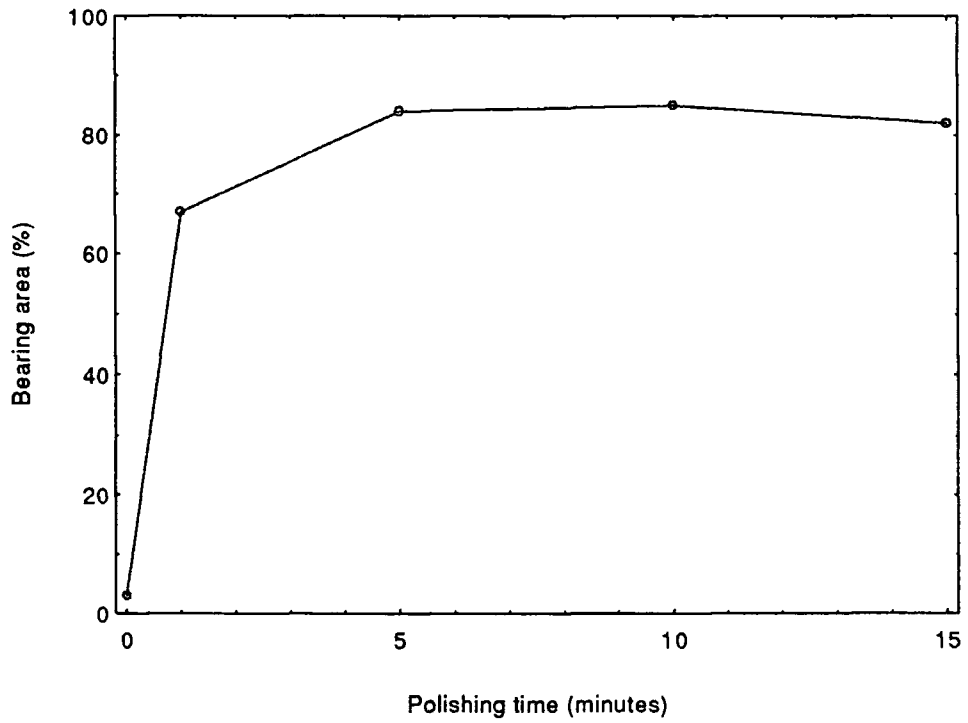
Fig 5.8   Variation of bearing area as a function of polishing time for 'uniground and lapped' samples
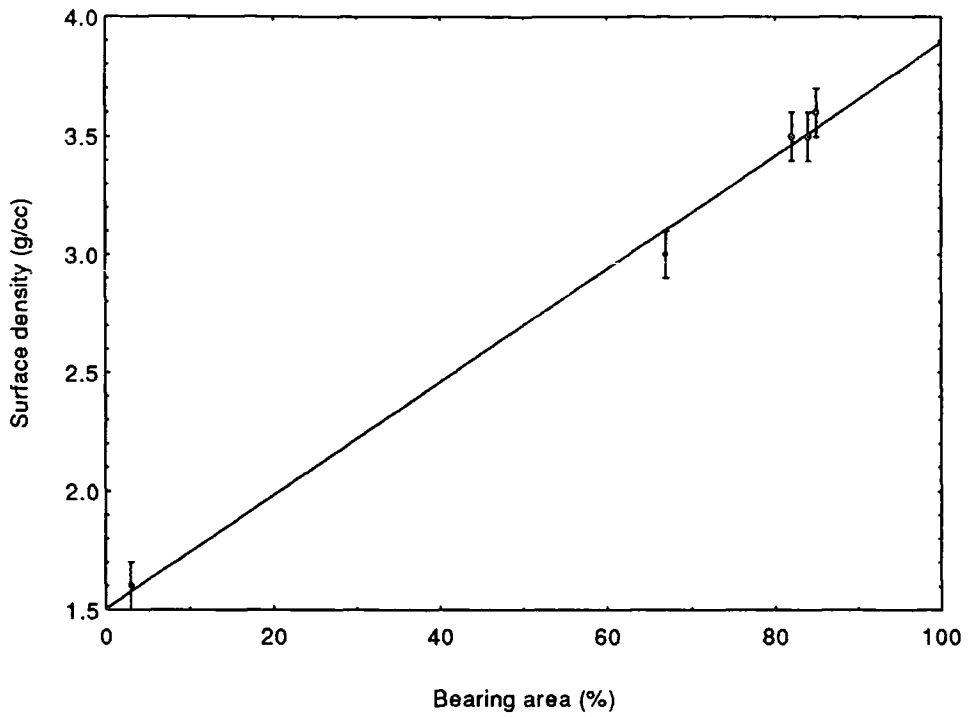
Fig 5.9   Comparison of the surface density and bearing area from 'uniground and lapped' samples during polishing.
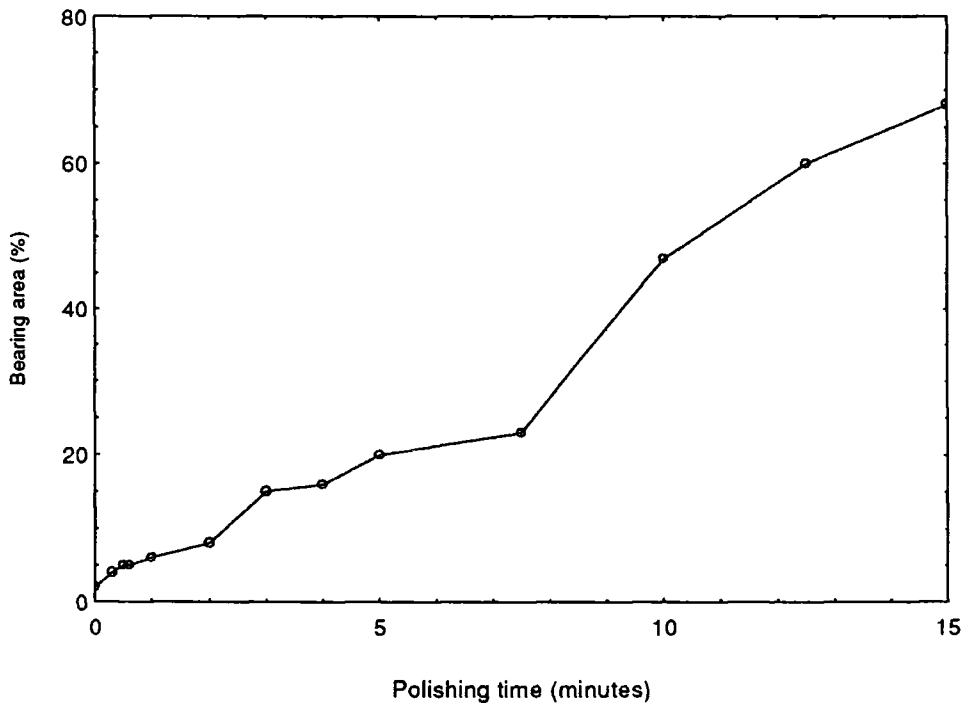
Fig 5.10   Variation of the bearing area from 'horizontal surface ground and lapped' samples as a function of polishing time.

when the bearing area is compared with the integrated intensity as is seen in figure 5.12.

5.4 Comparison of the surface density and bearing area measurements

Although direct relationships cannot be determined from the above observations, it is clear that qualitative trends exist between the predicted surface density and the bearing area. Using a kinematical model, this seems extremely strange. From this model, it would be expected that halving the amount of sample surface would be equivalent to halving the beam size and so the intensity should drop, but the shape of the diffuse curve should remain the same. However, if the grains were on a scale smaller than the coherence length of the x-rays, then dynamical effects would take over and simple scaling relationships break down. Within their coherence length, x-rays have a 'knowledge' of their surroundings [3,4]. This is the link between wave and particle theory and the reason why discrete photons can interfere to give the observed diffuse scatter. In order to explain the above observations, it must be concluded that the x-rays are sampling the average surface density of the medium within their coherence length. Since the coherence length of the GXR1 at the critical angle is of the order of 80 μm and the grain sizes varies between 2 and 30 μm it is clear that the coherence length is indeed able to extend over a number of grains and as such an average can take place.

One deviation from this is for very low bearing areas. At this point even the qualitative agreement between the bearing area and surface density breaks down. At such levels the measured bearing area continues to decrease, whereas the measured surface density reaches a lower limit and stops. This effect is most apparent in the variation of polishing time for horizontal surface ground samples (fig 5.5), but is also in evidence for the zero polish time in the unigrinding experiment (fig 5.3) and the lapped samples (fig 5.1). Inclusion of denser material in the surface can be ruled out, since the polishing particles were diamond, which have a lower density than Al_2O_3 and any other contaminant would have had to be present in extremely large amounts. Another possible cause could be the finite coherence length of the x-rays. If the separation of the surface grains became greater than the coherence length of the x-rays
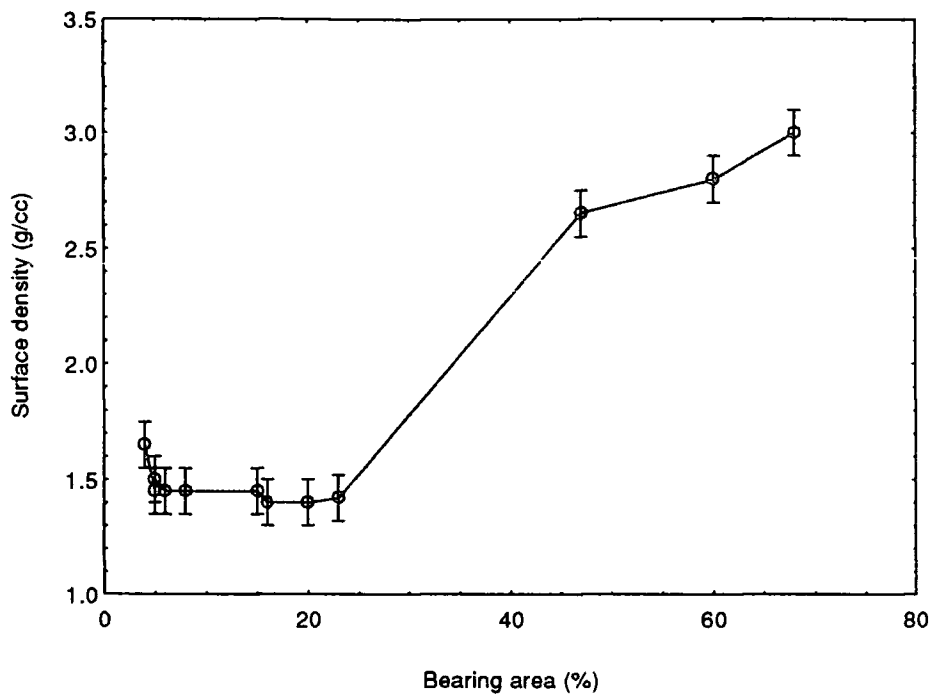
Fig 5.11   Comparison of the surface density and bearing area from 'horizontal surface ground and lapped' samples during polishing
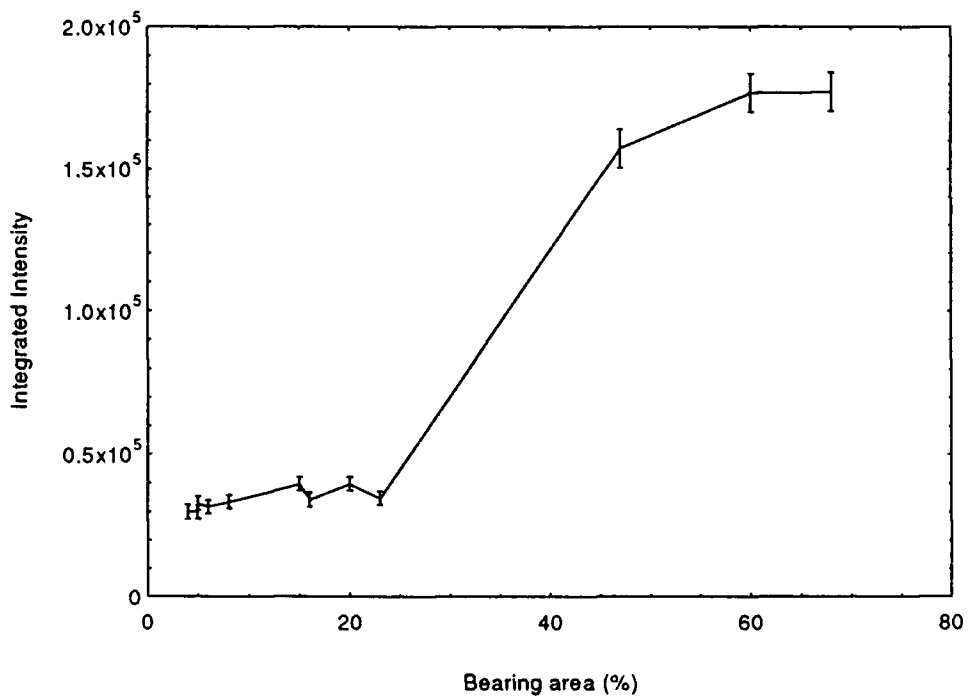
Fig 5.12   Comparison of the integrated intensity and bearing area from 'horizontal surface ground and lapped' samples during polishing.

at very low bearing areas, no interactions between the individual grains could occur. As a result, the x-rays would take an average of the grain-to-air ratio within their coherence length (figure 5.13). From this point on, further separations of the grains would not decrease the measured surface density.

5.5 X-ray scattering measurements performed at the Daresbury SRS

In order to test whether the plateaux in the x-ray results was a coherence length problem, GIXS measurements were performed on the same 'horizontally surface ground and lapped' samples, at the Daresbury S.R.S. Due to the large sample source distance (section 3.2.6), this has a coherence length a factor of ten greater than in the laboratory. As a result, if the lower observed density limit had been due to a finite coherence of the x-rays, then the bearing area at which the coherence length was just sampling the grain-to-air ratio would have been reduced. The larger coherence length of the SRS would mean that grains could be separated by a factor of ten more than in the laboratory before they lost knowledge of each other. In consequence, one would expect bearing areas a factor of one hundred less than in the laboratory to be able to be measured. Experimentally this would have been observed as a drastic lowering of the cut off in the x-ray measurements and the confinement of the plateaux to the very smallest polishing times.

The results of the density measurements, are shown in figure 5.14. Although there is a slight general drop in the measured surface density, no change in the starting position of the first plateaux is seen. The general fall is the result of an average being taken over a large population of grains. In the extreme case, it would be expected that for near zero coherence lengths, no air-to-grain average can be taken and only the grains would contribute to the diffuse scatter. As a result, the predicted intensity would be that of the bulk. However, for an infinite coherence length the sample would be completely averaged over and one might expect the predicted density to be equal to the optically measured bearing area. As a result, increasing the coherence length should shift the predicted density towards the bearing area measurement and thus to a lower level. This is the opposite to what was observed in the polished 'therm' samples (section 4.4.5). However, in that instance a different population of density

Coherence length

Separate grains on the surface of the ceramic

a)   Grain separation less than the coherence length of the x-rays

Coherence length

Average taken over this region

Separate grains on the surface of the ceramic

b)   Grain separation greater than the coherence length of the x-rays
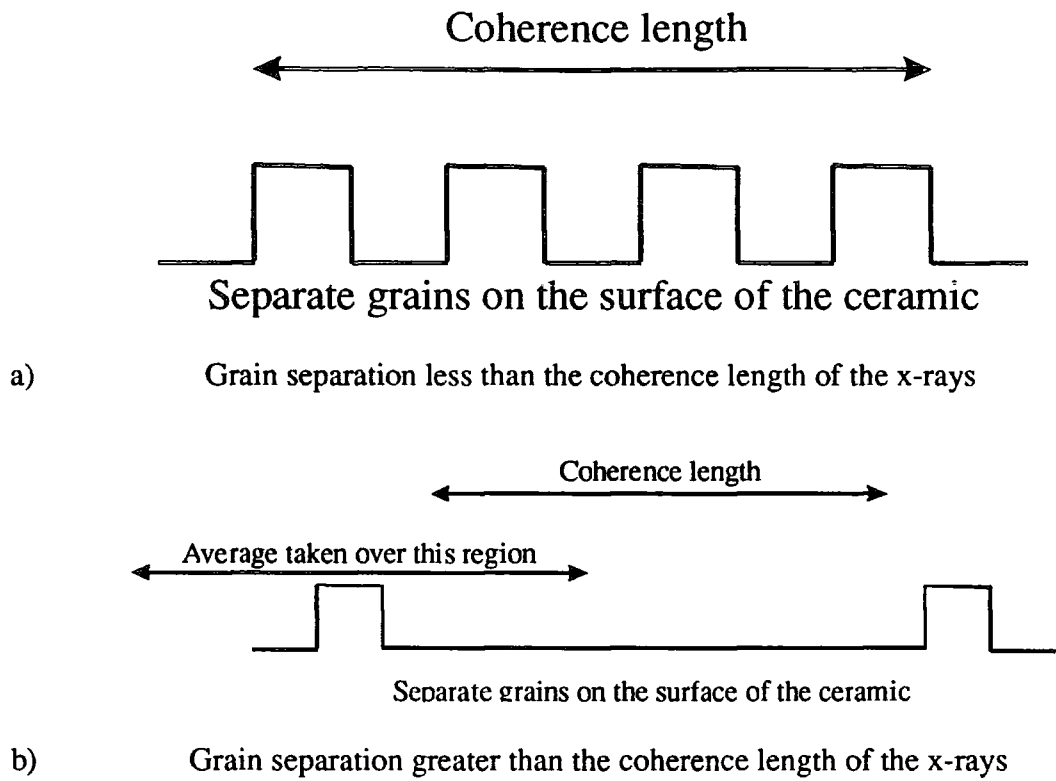
Fig 5.13 The average surface density is taken within the coherence length of the x-rays
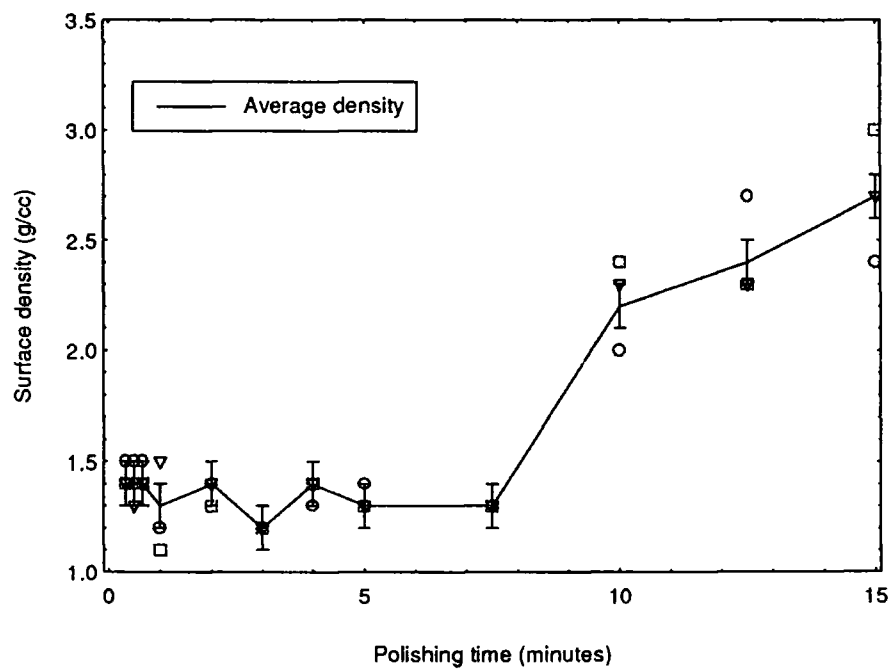
Fig 5.14   Variation of surface with polishing time for the 'horizontal surface ground and lapped' samples - data taken at Daresbury S.R.S.

variations was present on the surface and the two sets of results were shown to be completely consistent.

As can be seen from the data taken at the SRS the plateaux is still in place. In consequence it can be concluded that the finite coherence length of the GXR1 is not responsible for creating the lower limit cut off given in the GIXS measurements.

5.6 Model for the plateaux in the surface density measurements

Apart from the coherence length the only other difference between the x-ray and optical techniques is the types of surface that they are able to detect. The (optical) bearing area measurements are completely insensitive to the material between the polished grains. As mentioned previously, this is because the rough, unpolished surfaces in the pits scatters light diffusely and as a result are not observed. However, in the x-ray case, (figure 5.15), below a certain bearing area, x-rays can both reach the bottom surface and get back out. Although this is using a simple box model, the result that below a certain density, the amount of material removed from the top surface is equal to the amount of extra material being seen from the bottom surface can be carried over to the distribution. So long as this material is within the coherence length of the x-rays, it will be taken into the averaging of the density, and will keep the lower observed density limit fixed.

In summary, as the bearing area is reduced, a value is reached where the x-rays can 'see' the bottom surface. From this point onwards, although the optical technique continues to measure solely the scatter from the top, polished surface, the x-rays begin to become sensitive to the regions between the grains. As a result a lower limit cut off is observed in the GIXS measurements of surface density.

5.7 Optical microscopy measurements

X-ray diffuse scattering was not the only tool used to probe the surface of the polished ceramic plates. Evaluation of the surface of the 'horizontally ground and lapped' samples was also made using optical microscopy at Oxford University. For short polishing times, the surface displayed an island-like structure, with discrete polished, flat areas. As the polishing time was increased, these were seen to increase in size and density. However, for polishing times greater than 7.5 minutes a sudden change in surface morphology was seen. At this point the discrete islands began to converge quickly, creating a single surface randomly interspersed with holes. It is at this same point that both the surface density and bearing area measurements showed the steepest rise.

Optical microscopy was also performed on the 'uniground and lapped' samples. Again the same transition from island to plane surface morphology was observed. However, the only samples available were for 1 minute polishing time intervals. Thus it can only be said that the transition took place within the first minute of polishing within these samples.

5.8 Surface acoustic wave measurements (SAW)

5.8.1 Measurement of surface damage using SAW

Apart from the studies of the surface of the samples, near surface damage was also probed. This was again performed at Oxford University by using surface acoustic waves (SAW) and a schematic diagram of the experiment is shown in figure 5.16.

The acoustic waves, with frequency of 225 MHz, are produced by a piezoelectric cell. These travel down a lens and are introduced into the surface via a coupling fluid (water). At one particular angle (the Brewster angle) these are able to excite Rayleigh waves in the surface of the sample. These travel along the surface, emitting waves as they progress. Two waves are able to enter the lens and reach the piezoelectric cell. The first is the wave that is emitted vertically from directly below the cell and the
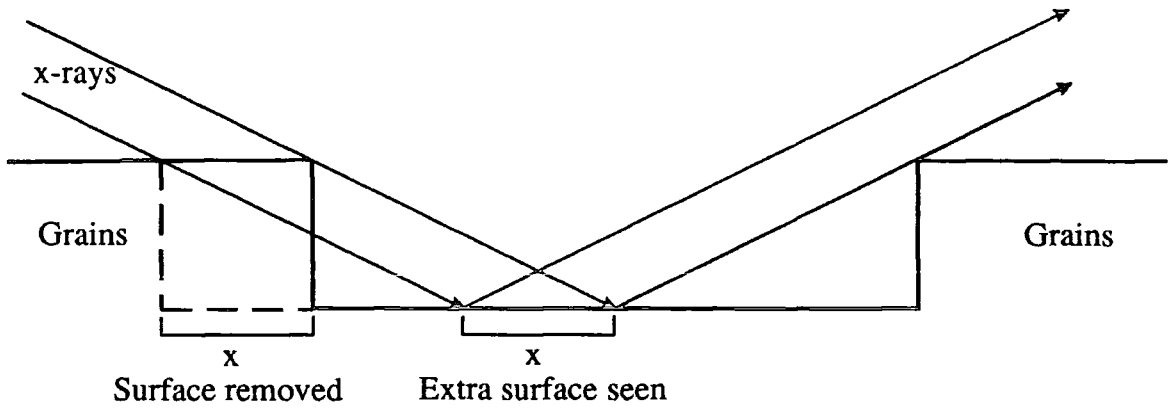
Fig 5.15 This diagram depicts the point at which x-rays are just able to detect the bottom of the pits. For further increases in grain separation, the amount of top surface removed is equivalent to the amount of extra bottom surface seen. As a result the average density remains constant and therefore so does the position of the critical angle.
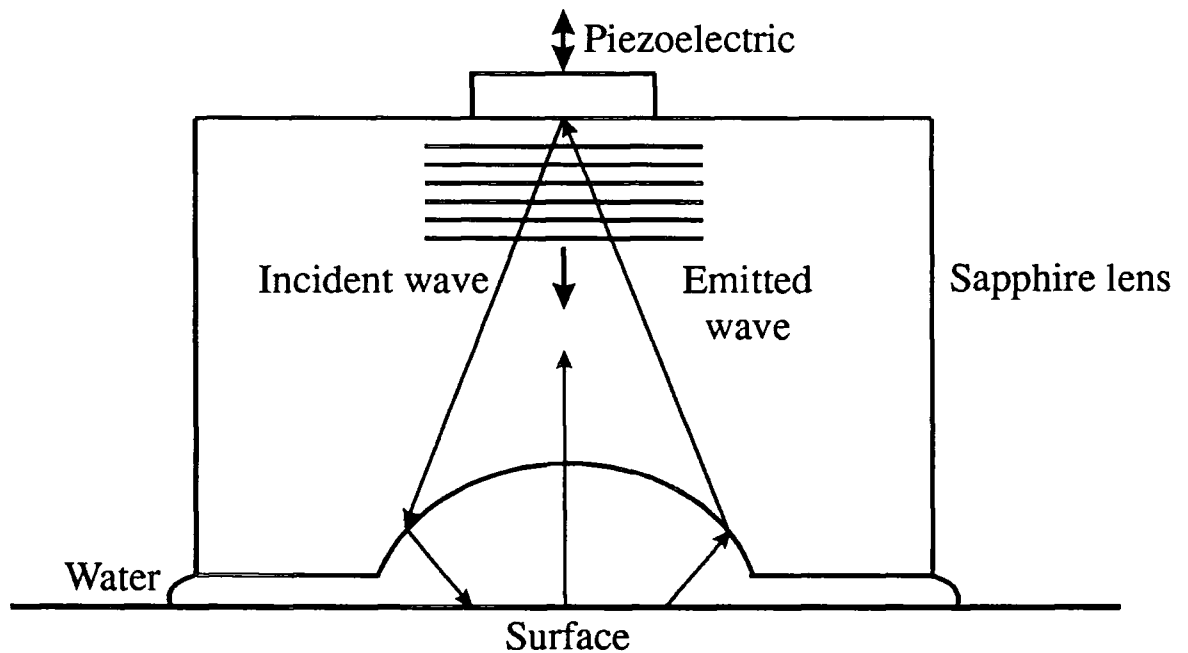
Fig 5.16 Apparatus for the generation and detection of surface acoustic waves

second is the wave that enters the lens at the 2nd Brewster angle. These produce vibrations in the piezoelectric transducer which are converted into electrical oscillations and interfere. As the distance the wave had to propagate between the two secondary sources is known, the velocity of the wave in the medium can be calculated. This is in turn affected by the presence of the holes and cracks in the samples surface.

5.8.2 SAW measurements on the Uniground samples

Surface acoustic waves were used initially to investigate the uniground samples that had been subjected to a standard lap and then polished for a variety of times. Twenty measurements were performed on each sample. Readings were taken at four separate points with five different readings at each point. Although an increase in velocity is seen with polishing time (figure 5.17), qualitatively the data does not follow the observations from the surface density and bearing area investigations. Also when recalling the arguments against stating that a linear trend was in evidence in figure 5.9; no relationship can be reliably determined from these results, due to the sparseness of the data points (figure 5.18).

5.8.3 SAW measurements on the Horizontal surface ground samples

Surface acoustic waves were used also to investigate horizontally surface ground samples that had been subjected to a standard lap and then polished for a variety of times. Fifty measurements were performed on each sample. Measurements were taken at 10 separate points with 5 measurements at each point. At the onset of polishing a rapid rise was seen (figure 5.19). This was followed by a plateaux which continued for the first 6 ± 1 minutes. For longer polishing times, a rapid rise was
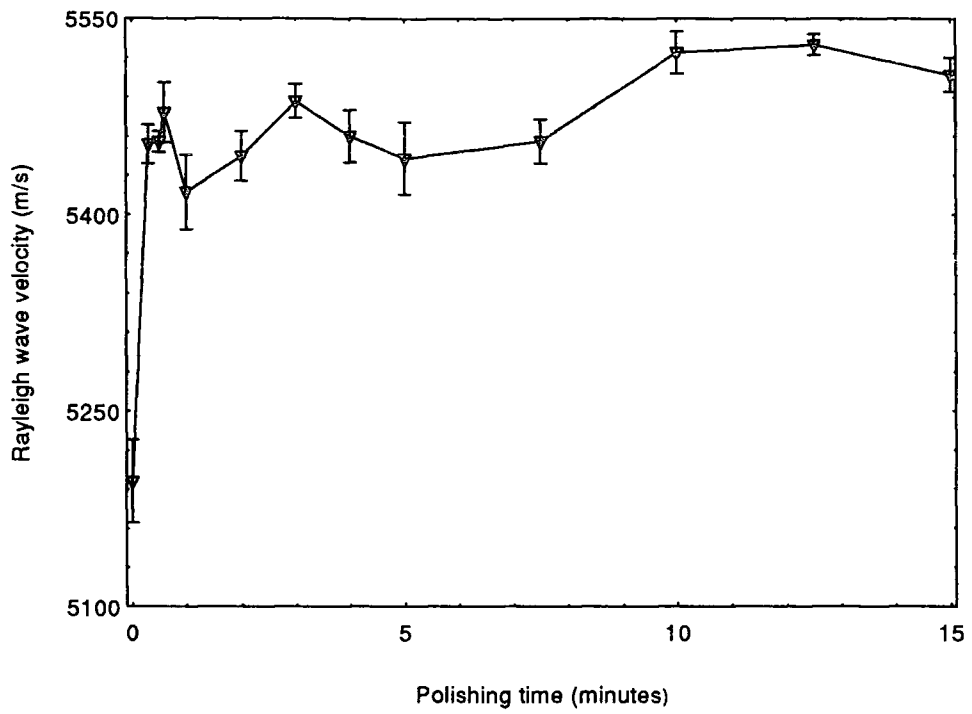
Fig 5.17   Rayleigh wave velocities measured from 'uniground and lapped' samples
for various polishing times
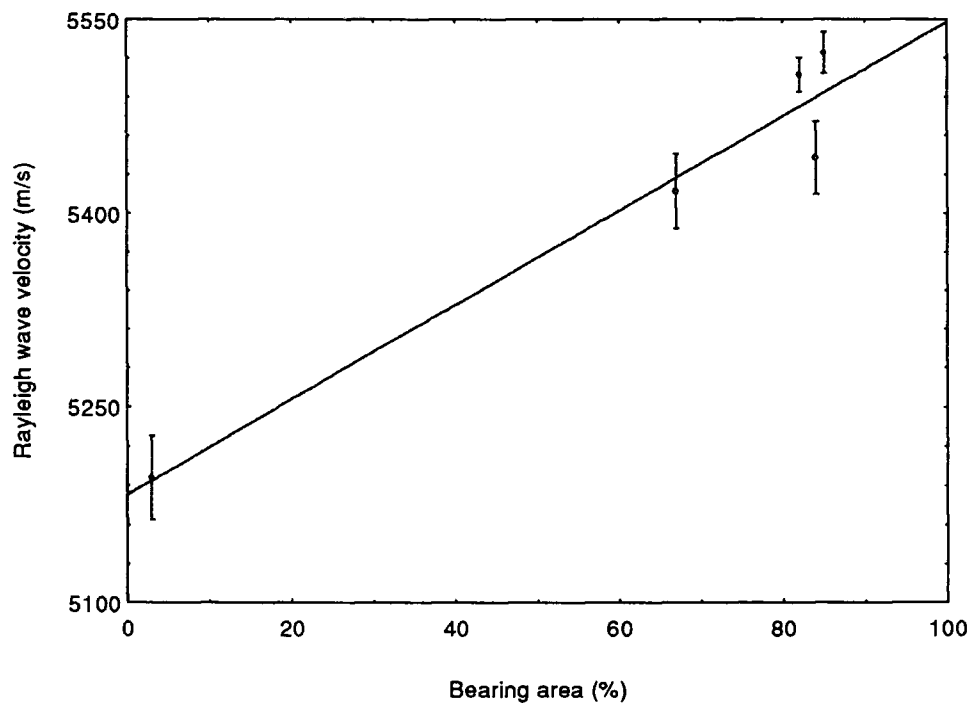
Fig 5.18 Comparison of the Rayleigh wave velocity and bearing area from 'uniground and
lapped' samples for a variety of polishing times.

observed, which although slowing, continued for all polishing times studied. This time many data points were available for comparison with the bearing area results (figure 5.20) and it can be said conclusively that although a strong trends exists it is not wholly linear.

5.9 Model proposed for the surface of the ceramics

A possible model, which combines the various observations is that of a surface which is comprised of a distribution of grain sizes. For low bearing areas this gives rise to a surface with a distribution of islands of a variety of width and depth (figure 5.21).

In the case of horizontal surface grinding a very large amount of damage has been introduced deep into the surface. Thus the initial lapping was not able to remove all of the gross defects and for short polishing times large grains stick up above the damaged surface and take a large amount of time to be removed. This is observed as the islands in the optical microscopy measurements and, in addition, gives rise to the observed slow increase in bearing area. Since these large grains are widely separated, the highly damaged bottom surface can be seen to some extent by the x-rays. This leads to an initial lower cut off on the density as described above. In addition, since variations in the samples on this level are not detectable, the error on the readings are machine limited. As a result, the observed fluctuations in density are all within the experimental error of the measurements (this is also the case in the 'as lapped' samples). The initial plateaux, also observed in the Rayleigh wave velocity, suggests that at such low bearing areas, acoustic waves are confined to the regions between the grains since there is no continuous top surface to support their existence.

When these initial large defects are removed the surface tends to the regime of a single interface, interspersed with holes. This is the observed transition in topography as reported from optical microscopy. In addition, the x-rays are no longer able to reach the surface at the bottom of the now small pits and the measured density reflects more the bearing area as measured by optical reflectivity. The rapid rise in the Rayleigh wave velocity also suggests that the waves are now able to propagate around the holes at the surface, rather than having to travel via bottom of the pits. As a result, as fewer
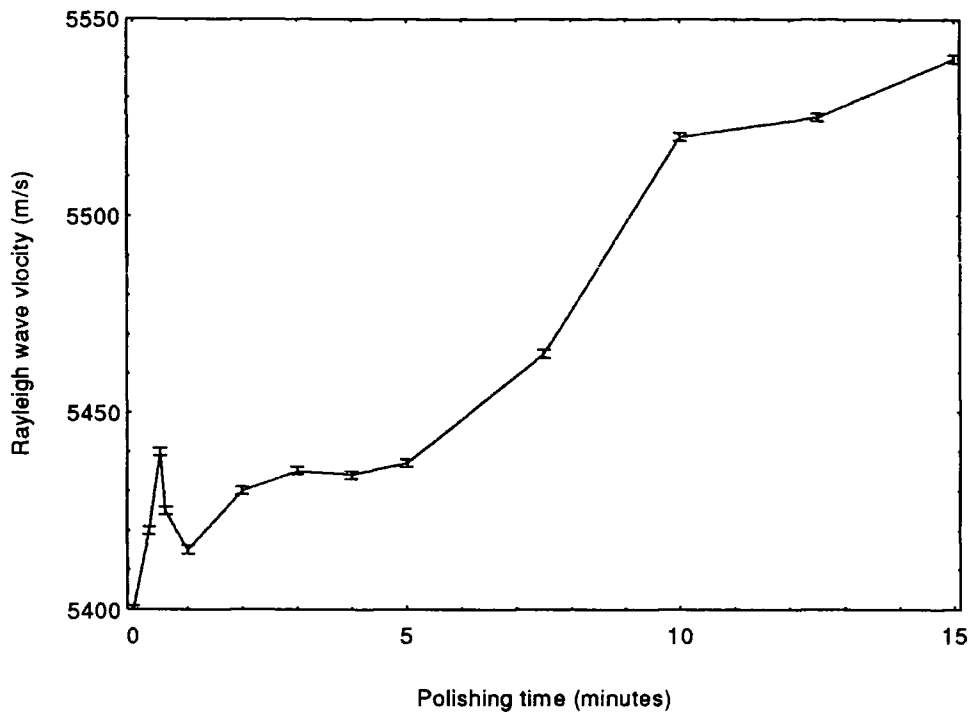
Fig 5.19   Rayleigh wave velocities taken from 'horizontally surface ground and lapped' samples for a variety of polishing times.
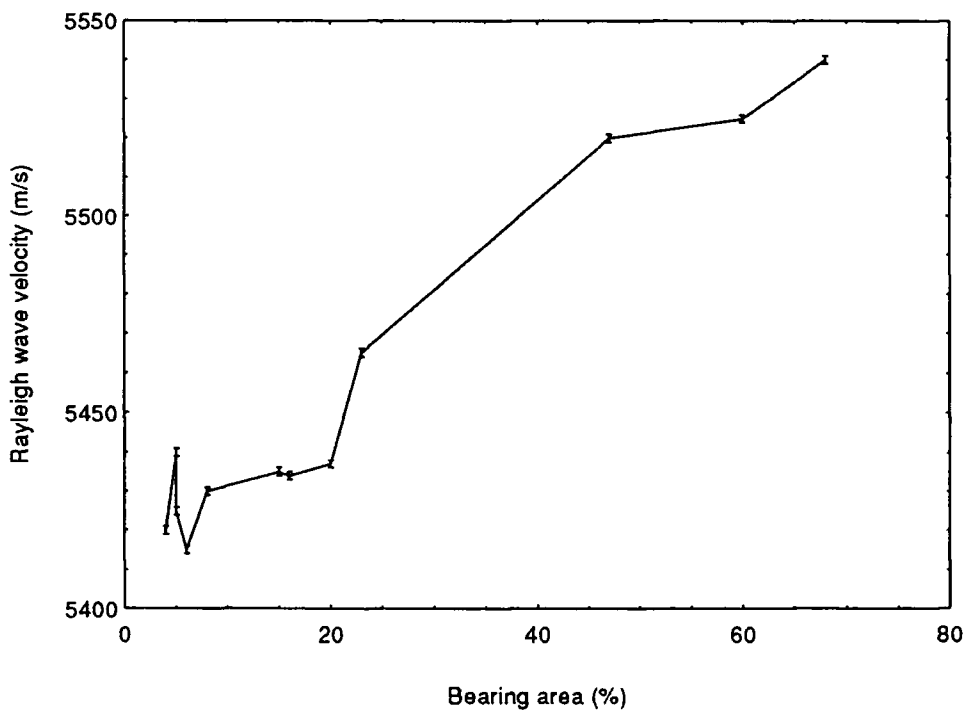
Fig 5.20   Comparison of the Rayleigh wave velocity and bearing area taken from 'horizontal surface ground and lapped' samples for a variety of polishing times.

a)   Sample surface before polishing

b)   Sample surface just before rapid rise in surface density

c)   Sample surface at point of rapid rise in surface density

d)   Sample surface just before saturation in surface density

e)   Sample surface when saturation in surface density has occurred
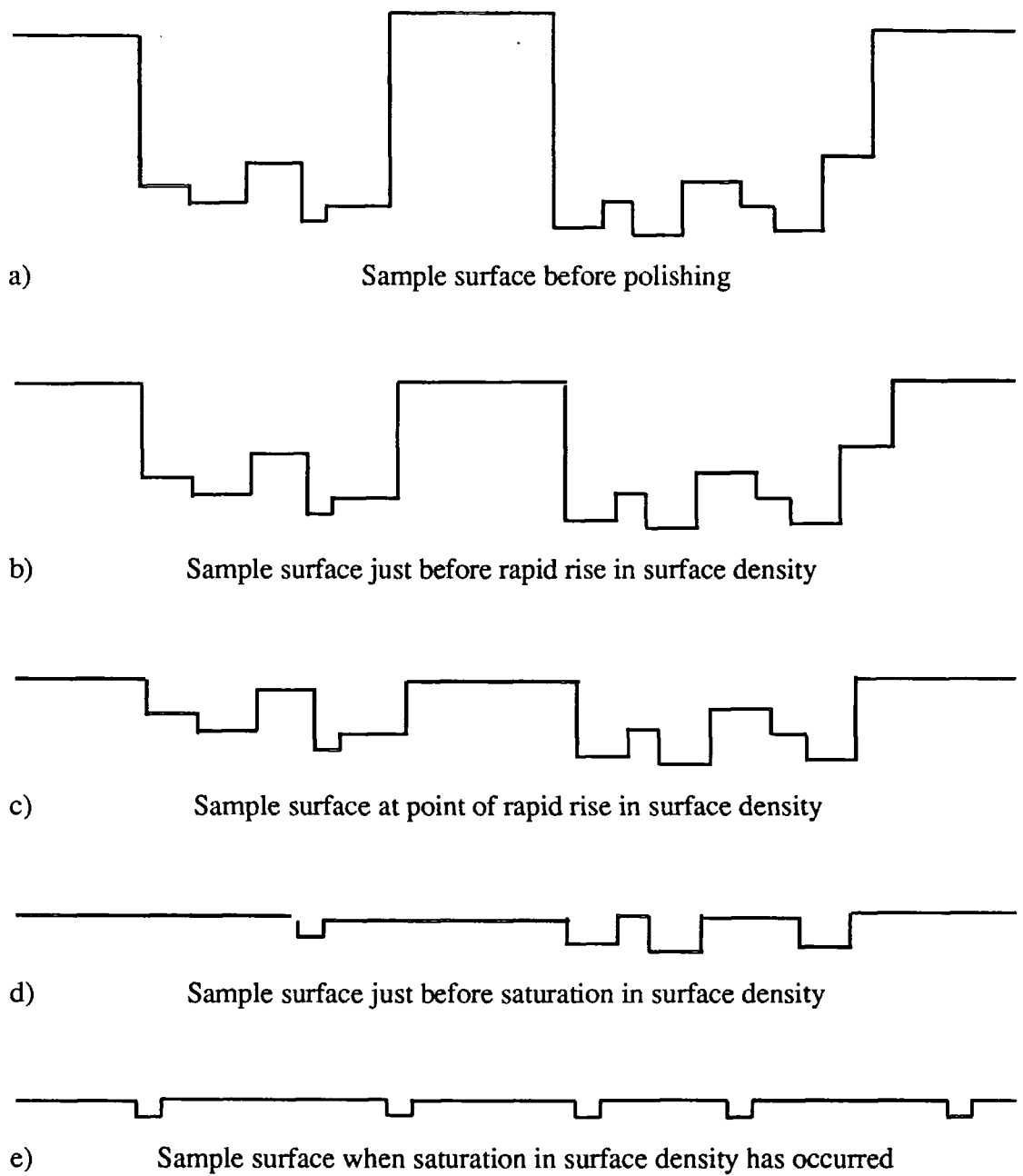
Fig 5.21   Model for the surface of a ceramic sample at various stages during the polishing process.

holes are left, the speed of propagation of the waves increases as is expected for a medium with fewer 'cracks'.

For larger polishing times, the holes which are left are slowly polished away, and the corresponding bearing area, surface density and Rayleigh wave velocity continue to increase but more slowly.

Although in many cases the observed diffuse scatter is seen to follow the general trend of the surface density, it is found not to follow it exactly. This can be understood when it is remembered that these discrete surfaces are scattering within the coherence length of the x-rays. As a result, interference between the scattered waves takes place and they do not necessarily have to obey what is expected from the kinematical model. In addition, the integrated diffuse scatter is seen to show a marked increase for higher polishing times. For angstrom level roughness this would be interpreted as a general roughening of the sample. However, in this case, the level of roughness is so great that no specular scatter exists. As the diffuse scatter arises from extra energy being scattered out of the specular peak, in this instance roughening the sample will not increase the diffuse scatter. In addition the increased roughness will lead to more shadowing. As a result, the observed order of magnitude increase in the diffuse scatter is due to a smoothing of the surface as polishing progresses. Again, the reason for the lack of variation in the diffuse scatter for very low bearing areas is that the x-rays are sensitive to the bottom surface and as a result, the measurements are instrument limited. Consequently, any variations in the nominally identical samples, will not be detected for the lowest bearing areas, whereas they will be in the case of the highest bearing areas.

As described in the introduction, the unigrinding process is very much more gentle than the horizontal surface grinding process and therefore the damage introduced is not as deep. In addition the second sweep of the grinding wheel removes the bulk of the gross defects introduced during the initial, coarse, sweep. In consequence, the amount of damage in the 'as ground' samples is much less and the subsequent lapping and polishing processes are more of a clean up operation. As a result, a much better control of the surface density between nominally identical samples was attained. In

97

addition, the graph of bearing area and surface density as a function of polishing time reaches the point of rapid increase in the first few seconds of polishing, and has time to reach saturation. This corresponds to the point in which the number of holes being removed is equivalent to the amount of damage being introduced due to the polishing process. In the same way, the integrated intensity has also saturated, and what is observed experimentally is the variations in nominally identical samples for the highest bearing areas only. These conclusions were re-enforced when optical measurements were made upon the 'uniground and lapped samples' as a function of polishing time. In these, the surface was seen to vary in a similar manner to the horizontal surface ground samples. The only difference being that the transitions between the island and the planar structure occurred within the first minute, as opposed to 7.5 minutes as observed in the 'horizontal surface ground and lapped' samples.

5.10 Summary

Grazing incidence x-ray scattering measurements have been performed on Al_2O_3 which had been ground in different ways, lapped and then polished for a variety of times. As the samples were very rough, no specular scatter was present and transverse diffuse scans were performed on the GXR1 reflectometer for constant incident intensity. Two types of grinding processes were used, namely unigrinding and horizontal surface grinding. From previous studies, it was known that unigrinding removed material more gently than horizontal surface grinding, leaving a better surface finish.

Surface density measurements, as given by the positions of the Yoneda wings, showed a strikingly different shape as a function of polishing time for the samples ground by the two techniques. The uniground samples showed a rapid rise in surface density, which was seen to slow and saturate close to the 'as fired' bulk density of the material. In contrast, a plateaux in surface density was observed for short polishing times in the horizontal surface ground samples. Even though the density rose sharply after 7.5 minutes of polishing, it never reached saturation.

When optical bearing area (surface to pit ratio) measurements were performed, further differences were observed between the samples ground by the two methods. It was noted that the bearing area of the uniground samples looked qualitatively similar to that of the surface density measurements. This was attributed to the x-rays averaging over the density of the grains and pits within their coherence length, so reflecting the bearing area measurements. In contrast the bearing area measurements performed on the horizontal surface ground samples continued to fall for polishing times less than 7.5 minutes.

Qualitatively the correlation between the bearing area and the surface density measurements appeared quite different between the two grinding techniques. However, a closer inspection of the data revealed that the density of the plateaux in the horizontal surface ground samples corresponded to the lowest density displayed in the uniground specimens. Thus it was proposed that a lower limit cut off existed in the measurements of surface density using x-rays. Initially, it was assumed that this cut off was due to the finite coherence length of the x-rays being less than the separation of the grains at the lowest bearing areas. In order to verify this, GIXS measurements were performed on the horizontal surface ground samples at the Daresbury SRS. This provided a coherence length one order of magnitude greater than that available in the laboratory. Thus surface densities a factor of ten lower should have been able to be measured. However, when the surface density of the samples was calculated from this data it showed an almost identical behaviour to that given in the laboratory. As a result, the cut off was clearly not an x-ray optical effect. In order to explain this, a geometrical model was proposed for the lower limit cut off in terms of x-rays being able to detect the surface in the pits. This was seen to explain satisfactorily the observed discrepancy between the x-ray and optical measurements for low bearing areas.

Optical microscopy measurements revealed that the surface morphology of the uniground and horizontal surface ground samples looked remarkably similar on polishing. In both cases the surface was transformed from one which contained isolated islands to one which was essentially planar and interspersed with randomly sized pits. The only difference between the two sets of samples was that the

horizontal surface ground samples took 7.5 minutes to reach the transition whereas the uniground samples altered within the first minute.

From the above measurements a model was proposed for the surface of the Al_2O_3. This was one in which the 'as ground' surface consisted of large grains which stuck up above a surface containing of a smaller distribution of pits. As the polishing process continued, the grains were worn away and the surface density rose slowly. Since the unigrinding process was less energetic than horizontal surface grinding the damage introduced by it was much lower. In consequence, the rate of damage removal by the polishing was higher in these samples and the rise of the surface density and bearing area was correspondingly faster.

Chapter VI

X-ray scattering studies of GaAs polished by

various techniques

6.1 Introduction

Reference [1]

In integrated circuits the dominant semiconductor in use today is silicon. This is due to it being cheap and able to be grown up to 12 inches in diameter without significant numbers of dislocations present. Further more, when polished, high surface finishes can be obtained, in many cases in the region of 1 Å. For devices that operate at high frequencies, a better choice of material is GaAs. This can be doped to have a higher mobility than silicon and as such can be used in applications running at several Ghz. In addition to this, it can be used in electro-optic devices such as AlGaAs lasers. Unfortunately, one drawback associated with GaAs is that it is difficult to grow. This is partly due to its critical resolved shear stress being one third of that in silicon, and partly due to the loss of the relatively volatile arsenic during growth.

In the past, horizontal Bridgman with an over pressure of arsenic has been used to grow GaAs. However, the resulting 'D' shaped boule is difficult for the electronics industry to deal with, since its technology has evolved around Czochralski grown silicon. In the past decade, two other methods have emerged which can grown GaAs with relatively low dislocation densities. These processes are namely liquid encapsulated Czochralski (LEC) and vertical gradient freeze (VGF). The LEC technique is similar to that of Czochralski grown silicon, except a capping layer of B_2O_3 is used to contain the volatile As and an over pressure of inert gas is applied. One difficulty that accompanies the LEC technique is that of control of crystal width. In this, the usual feedback method, relating the weight of the growing crystal to its width, is hampered by the large surface tension of the B_2O_3. In consequence, a Si_3N_4 'coracle' is sometimes used. This floats at the GaAs/B_2O_3

interface and defines the width of the growing crystal. The resulting technique produces growth rates of 10mmh^{-1} and near dislocation free crystals up to a few centimetres in diameter.

In the VGF technique, the melt is held in a vertically mounted vessel and radio frequency heated. In order to initiate growth, a seed crystal is placed at the bottom of the chamber. The rate of growth is controlled by a temperature gradient which is moved slowly along the vessel by controlling the power on the RF heaters. In this way high quality crystals can again be grown dislocation free up to a few centimetres in diameter.

After growth of the crystals, the resulting boules are cut into slices using a diamond saw and any surface damage removed by a combination of grinding lapping and polishing. A review of these three machining operations has been given in section 5.1.

6.2 Sample preparation

The (001) GaAs used in this study was provided by MCP wafer technology and grown by the VGF technique. The dopant used was silicon and the resulting GaAs was therefore n type, giving a dislocation density of typically 300cm^{-2}. In order to minimise variations in substrate quality, each piece of GaAs used was cut from the same block and then polished in different ways. Polishing of the wafers was done at Logitech Ltd., using four different polishes, namely:

a) Peroxide Alkaline (PA) polish: hydrogen peroxide/ammonia solution;

b) Bromine Methanol;

c) 0.3 μm Chemlox: proprietary hypochlorite-based abrasive (Al_2O_3 in this instance) polish and;

d) 1.0 μm Chemlox.

6.3 X-ray diffraction measurements performed on polished GaAs

6.3.1 Symmetric reflections

The x-ray diffraction data from these were compared with that from an as-lapped sample. One set of GaAs crystals were square with dimensions 6x6x1 mm, while another was in the form of wedges 12.5 mm from apex to base.

Initially, symmetric triple axis (004) reciprocal space maps were taken from the samples. Data was collected from the square and wedge shaped samples using the Bede model 200 and D3 (in high resolution mode) diffractometers respectively. Discussions of these diffractometers have been given elsewhere [2,3] (section 2.2), whilst the triple axis technique has been reviewed in sections 3.1.5 to 3.1.9. The wavelength used on both machines was Cu $K_{\alpha 1}$.

Full width half maximum (FWHM) and full width fiftieth maximum (FW1/50M) widths of the diffraction peaks were made in the q_z and q_y directions. As mentioned in section 3.1.5 the q_z direction probes the components of normally resolved strain in the sample, whilst the q_y direction corresponds to the lattice tilts. In symmetric scans, the q_z and q_y reciprocal vectors are probed by performing $\theta/2\theta$ and θ scans respectively. When asymmetric scans are performed, the $\theta/2\theta$ scan moves radially away from the 000 point in reciprocal space. In this way it maps out the strain component at an angle to the q_z direction and thus the surface normal.

Shown in figures 6.1 to 6.4 are the reciprocal space maps taken from the four wedge shaped samples. The results of the analysis of the FWHM and FW1/50M for the $\theta/2\theta$ and θ scans are given in tables 6.1 to 6.4. The error bars shown correspond to the step size of the full reciprocal space maps from which the peak widths were measured.
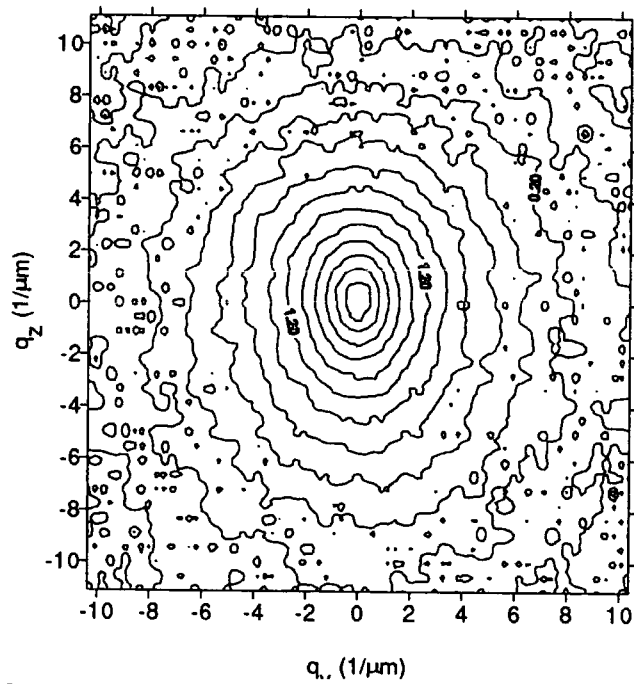
Fig 6.1 Full reciprocal space map of the symmetric (004) reflection from the 'as lapped' sample. The observed diffuse scatter is one order of magnitude greater than the polishes.

Fig 6.2   Full reciprocal space map of the symmetric (004) reflection from the
0.3 μm Chemlox polished sample.

Fig 6.3   Full reciprocal space map of the symmetric (004) reflection from the bromine methanol polished sample.
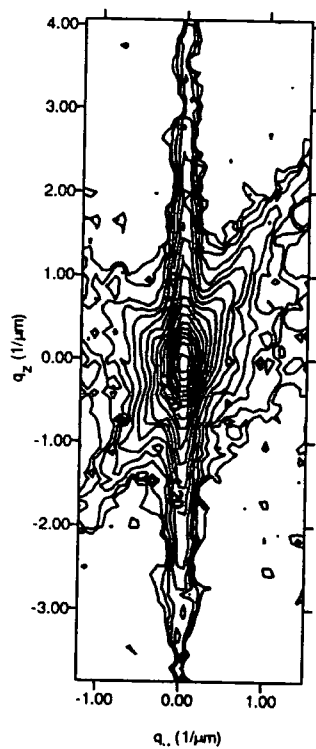
Fig 6.4   Full reciprocal space map of the symmetric (004) reflection from the PA polished sample

θ/2θ Scans	as-lapped (arc seconds)	0.3 μm Chemlox (Reference)	Bromine Methanol	PA Polish
FWHM	41 ± 10	9 ± 1	8 ± 1	9 ± 1
FW1/50M	224 ± 10	30 ± 1	30 ± 1	29 ± 1

Table 6.1   Variation of the θ/2θ 004 peak widths of the wedge samples run on the D3 diffractometer

θ Scan	as-lapped (arc seconds)	0.3 μm Chemlox (Reference)	Bromine Methanol	PA Polish
FWHM	52 ± 10	6 ± 1	6 ± 1	5 ± 1
FW1/50M	363 ± 10	18 ± 1	23 ± 1	15 ± 1

Table 6.2   Variation of the θ 004 peak widths of the wedge samples run on the D3 diffractometer

θ/2θ	1 μm Chemlox (arc seconds)	0.3 μm Chemlox	Bromine Methanol	PA Polish	0.3 μm Chemlox (Reference)
FWHM	34 ± 2	31 ± 2	31 ± 2	31 ± 2	34 ± 2
FW1/50M	104 ± 2	93 ± 2	95 ± 2	93 ± 2	98 ± 2

Table 6.3   Variation of the θ/2θ 004 peak widths of the square samples taken on the Model 200 diffractometer

θ Scan	1 μm Chemlox (arc seconds)	0.3 μm Chemlox	Bromine Methanol	PA Polish	0.3 μm Chemlox (Reference)
FWHM	19 ± 2	13 ± 2	27 ± 2	10 ± 2	12 ± 2
FW1/50M	96 ± 2	47 ± 2	95 ± 2	31 ± 2	33 ± 2

Table 6.4   Variation of the θ 004 peak widths of the square samples taken on the Model 200 diffractometer

From tables 6.1 to 6.4, it is clear that there are significant variations in the FWHM and FW1/50M of the θ scans as a function of polishing conditions. The values of the θ/2θ scans, however, stay constant within the error bars of the experiment. This shows that polishing affects the distributions of tilts, but leaves the distributions of strain component normal to the surface constant. It is not expected that the roughness of the crystal interface gave an important contribution to the θ/2θ results, since typically its effects are most apparent for larger q values [4], and secondly the chance of it exactly compensating the differences in strain is remote. From these data, it was noted that the distribution of tilts in the bromine methanol polished samples was larger than those polished with the hypochlorite based abrasive polish. In addition, it appeared that the smaller diameter particles gave the smaller distribution of tilts in the crystalline lattice of the samples. Of all the polishes, the hydrogen peroxide/ammonia solutions gave the lowest range of tilts.

One sample deviated from this trend. The $1 \mu m$ Chemlox polish appeared to show some variation in strain as well as tilts. This could be attributed to the $1 \mu m$ polishing particles producing some degree of lapping of the surface of the sample. When it is recalled that the $3 \mu m$ 'as lapped' sample gave a distribution of diffuse scatter an order of magnitude greater in both the q_z and q_y directions than the polished samples, any lapping effect may be expected to break down the relationship observed above.

6.3.2 Asymmetric reflections

In order to characterise the in plane strain component, 224 asymmetric reflections were performed on the wedge shaped samples. All scans were performed on the D3 diffractometer, aligned in the same configuration as for the symmetric 004 reflections. Such scans are sensitive to both the in and out of plane strains and in addition, probe a smaller depth below the surface than the 004 reflections. Shown in figures 6.5 to 6.7 are the asymmetric reflections taken from the samples polished by PA, 0.3 μm Chemlox and bromine methanol respectively. The FWHM and FW1/50M taken from the θ/2θ and θ scans are given in tables 6.5 and 6.6. Again, it is clearly evident that whilst there are
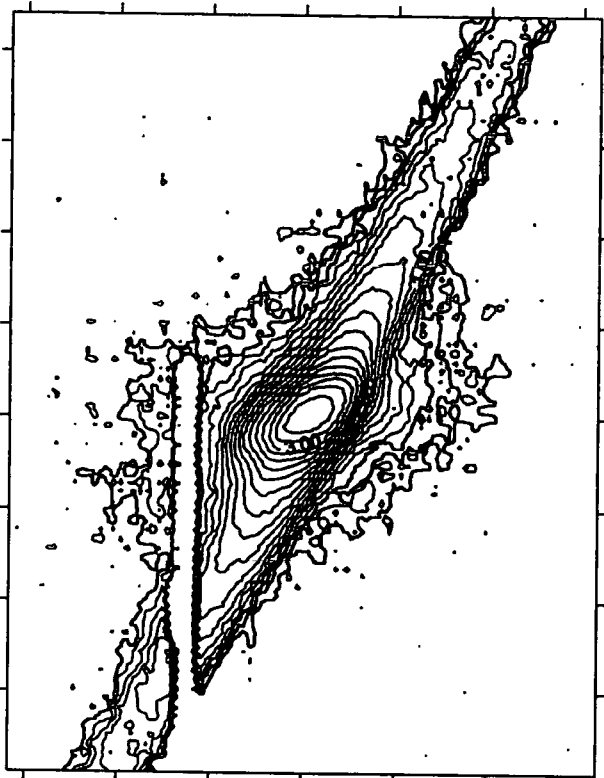
Fig 6.5   Full reciprocal space map of the asymmetric (224) reflection from the PA polished sample.
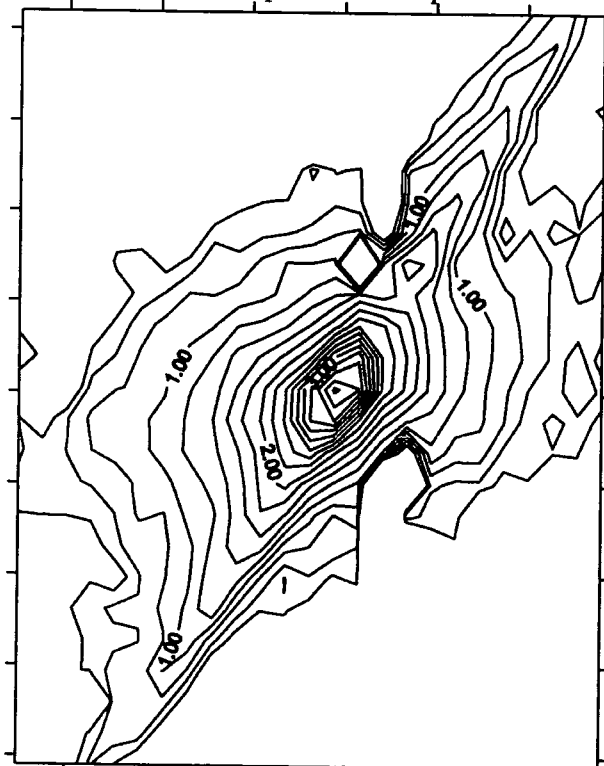
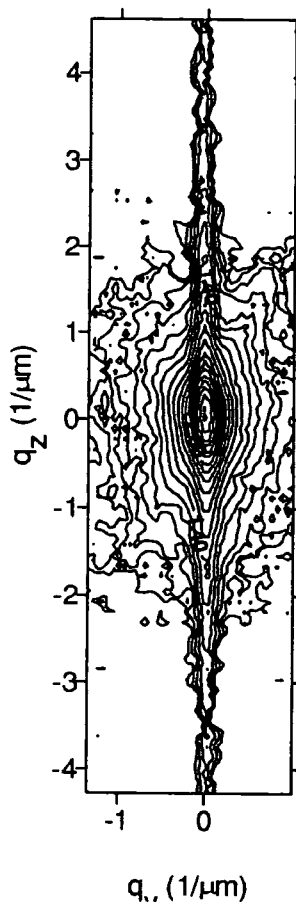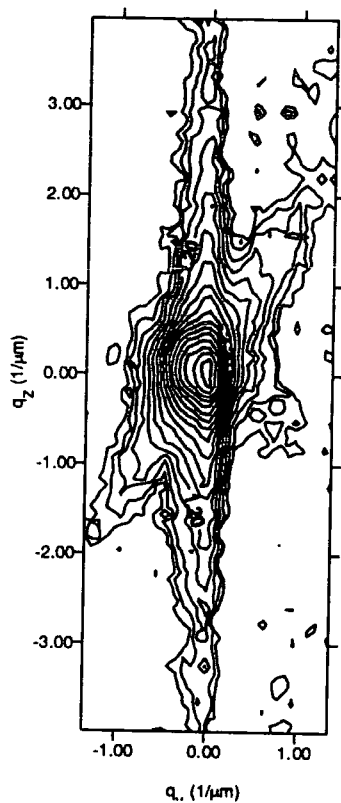Fig 6.6   Full reciprocal space map of the asymmetric (224) reflection from the 0.3μm Chemlox polished sample.
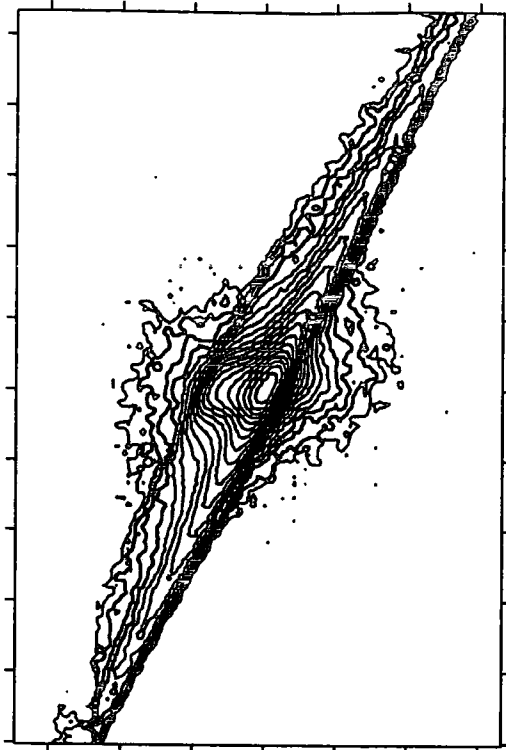
Fig 6.7   Full reciprocal space map of the asymmetric (224) reflection from the bromine methanol polished sample.

significant variations in the tilts, there are no variations in the distributions of strains in any of the samples. As a result, it may be concluded that the distribution of both vertical and horizontal strains are constant as a function of the polishing process. Visible in the full reciprocal space maps are bars of missing data. Within the data files, lines of zero counts are recorded in the θ/2θ scans for a range of θ values. As the background of the detector is 0.15 c.p.s., shadowing of the scatter from the sample can be ruled out. It is most likely that this effect arose from a software bug in the control program, as it was under test at the time.

θ/2θ Scan	0.3 μm Chemlox (Reference)	Bromine Methanol	PA Polish
FWHM	9 ± 1	9 ± 1	10 ± 1
FW1/50M	22 ± 1	22 ± 1	25 ± 1

Table 6.5   Variation of the asymmetric 224 θ/2θ scan peak widths
of the wedge samples

θ Scan	0.3 μm Chemlox (Reference)	Bromine Methanol	PA Polish
FWHM	11 ± 1	9 ± 1	17 ± 1
FW1/50M	32 ± 1	35 ± 1	36 ± 1

Table 6.6   Variation of the asymmetric 224 θ scan peak widths of the wedge samples

From these data it is noted that the tilt distribution within each sample vary much more but have a much lower spread between samples than in the symmetric reflections (table 6.2). Although the strain within the samples can be thought of in terms of vector quantities, it is not obvious why tilts can vary as a function of direction. A more convincing explanation is that the tilt distribution varies as a function of depth, the higher values in the asymmetric scans corresponding to a higher level of damage in the near surface region.

Another interesting point is that the tilt distribution in the PA polish is now similar (or even worse than) that in the bromine methanol. It is possible, that the higher surface sensitivity may be giving a larger contribution from the thicker oxide layer present on the PA polished material.

6.3.3 Model proposed for the near surface of the polished GaAs

The absence of strain and the presence of a distribution of tilts in the near surface layer could be interpreted in one of two ways. A possible model could be of low angle boundaries consisting of rows of edge dislocations between small mosaic blocks of otherwise perfect material. For low dislocation densities, such boundaries could give rise only to tilt and have little associated long range strains. These edge dislocations would presumably correspond to relaxed microcracks extending from the surface into the material being polished.

The second model which could give rise only to a tilt distribution is one of material removed by the abrasive being redeposited epitaxially in unstrained mosaic blocks. Whilst in sections 6.4.1 and 6.4.2, there is evidence from the x-ray reflectivity for a redeposited surface layer, it is only a few nanometers in thickness and even if epitaxial would not give sufficient signal. However, the two processes are not incompatible and propagation of microcracks beneath the abrasive particles, followed by subsequent removal and partial redeposition would be consistent with both the reflectivity and diffraction data. Bromine methanol is believed to deepen such cracks, removing material very quickly and thus leaving a surface which is smooth on the x-ray length scales but tilted on length scales of greater than 0.5 mm. Conversely, the peroxide/alkaline polish produces a passivating oxide layer at the surface which inhibits the crack propagation, resulting in the lowest distribution of tilts.

6.4 Specular and diffuse x-ray scattering measurements

6.4.1 Specular and diffuse simulations of the bromine polished sample

To test further the model, grazing incidence x-ray scattering measurements were performed at the Daresbury SRS, using a wavelength of 1.3926Å. Shown in figure 6.8 is the specular reflectivity curve recorded from the bromine methanol polished wedge sample along with its best fit simulation. From the fringe present in this data, it is clear that a layer of different density exists on the surface. Simulations revealed that this layer was of the order of 24 Å thick and had associated with it a top and substrate roughness of 6 and 7 Å respectively.

Grazing incidence transverse diffuse scans were also recorded from the sample. Shown in figure 6.9 is one such scan taken at a scattering angle of 5400 arc seconds. It is immediately apparent that the specular is extremely broad, but is still a Gaussian. This indicates that a large number of tilts are present on the surface, which have a Gaussian distribution of angles with respect to the average plane. Such a broadening is also seen on the left hand side Yoneda wing. As the projected x-ray coherence length is a large fraction of a millimetre at these highly glancing angles, it can be concluded that surface tilts present are on the half millimetre scale. Such a surface can be seen by eye and has been reported previously on GaAs polished by bromine methanol [5]. The most likely cause of such a surface is the highly energetic etching action of bromine. This will not only etch the surface of the samples, but will also etch down and therefore open up, any micro cracks present. The resulting interface will consist of large mounds, extending between the larger cracks on the surface. This action may also give rise to tilts in the crystalline lattice of the sample which would be in agreement with the findings of the diffraction data.

In addition to the broadness of the Yoneda wings, it was noticed that they corresponded to a density less than that of bulk GaAs. Simulations of the positions of these revealed that the surface corresponded to a density of 80% bulk GaAs. In this case the width of the
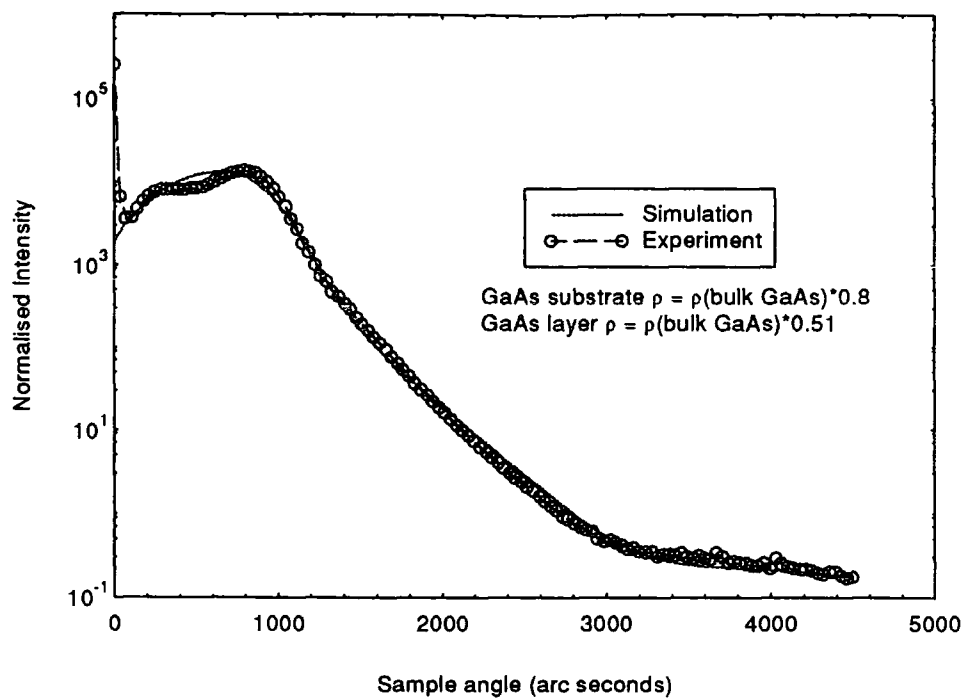
Fig 6.8   Specular scan of the bromine methanol polished sample with its
best fit simulation
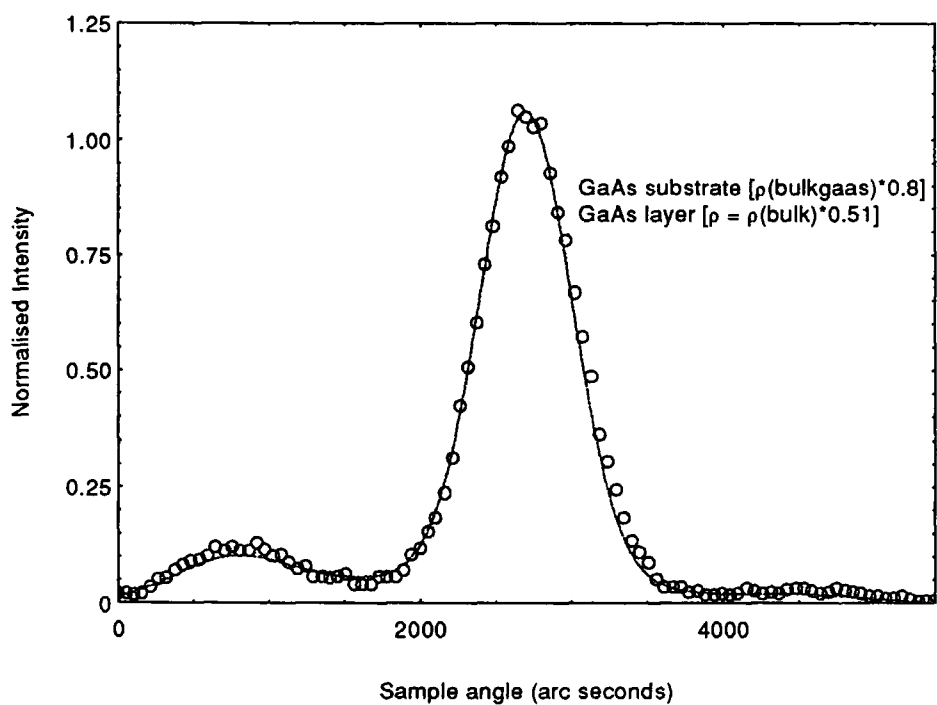
Fig 6.9   Transverse diffuse scan from the bromine methanol polished sample along
with its best fit simulation.   Scattering angle = 5400 arcseconds.

Yoneda wings in the simulated curve were the same as that in the experimental data. As a result, the sinθ correction observed in the CVD glass section (section 4.4.2) would be the same on both the simulated and experimental curve. In this way the observed low density is not a geometrical artefact. From similar calculations to that presented in section 4.2.3, it can be concluded that this lower density region must exist over a depth of several thousand angstroms and as such may well be indicative of grading.

Although it was known that the action of other mechanical polishes gave rise to lateral correlation lengths in the order of several thousand angstroms, it was not known what effect the bromine would have on the surface of the sample. From intuition one might expect that the dissolution of features on the surface would be strongly related to their surface to volume ratio. As such, the smallest irregularities would disappear first leaving only the largest length scales. Some evidence for this is seen in the optically visible roughness on the surface. However, it is not clear what the intrinsic form of the microscopic roughness on the post etched sample may be. Simulations of the diffuse scatter proved relatively inaccurate, due to its highly broadened nature. The results of the best fit simulations are shown in table 6.7, whilst the simulation is given in figure 6.9. Within the table, σ_{total} is the roughness as measured in the specular scan. As the specular simulations are sensitive only to vertical variations in electron density, they are not able to distinguish between vertically correlated roughness, σ_{cor}, uncorrelated roughness, σ_{uncor}, and vertical grading in the electron density, σ_{grade}. These last three parameters can all be extracted by simulating the diffuse scatter as has been done here [6]. In addition, from these diffuse scatter simulations, the lateral correlation length of the roughness and the fractal exponent can also be determined. It is interesting to note that in the GaAs a vertical grading in electron density is present. This grading is also present in the other polished samples presented in this thesis (section 6.4.2) and also in parallel studies of InP as a function of polishing conditions [7]. Thus from these data, it may be implied that such a vertical electron grading exists at all polished interfaces.

Interface	σ_{total} (Å)	σ_{uncor} (Å)	σ_{grade} (Å)	ξ (Å)	h
Substrate	7 ± 1.5	6	4	1200 ± 400	0.2 ± 0.2
Top surface	6	5	3	1200	0.2

Table 6.7   Simulation parameters for the bromine methanol polished GaAs

Such a low fractal exponent is indicative of a surface which has a component of extremely high frequency roughness present upon it. It may be tentatively inferred that these high frequency modulations are in some way related to the atomic scale etching process of the bromine. In addition, since the etch had been performed for 30 minutes it may also be suggested that the observed correlation length may be intrinsic to the etching process.

6.4.2 Specular and diffuse simulations of the PA polished sample

In order to try to avoid the highly energetic etching process associated with bromine methanol, Logitech Ltd. developed the PA polish. This was designed to produce a insoluble oxide of gallium which would form within the microcracks and thus prevent further removal of material. In contrast, the action of the rotating polishing pad would continuously remove the surface oxide and as a result, a uniform etch was hoped to be obtained.

Shown in figure 6.10 is the specular scatter recorded from the PA polished wedge sample with its best fit simulation. The broad hump in the scatter as a function of angle indicates the presence of a layer on the surface of the sample. Results of the simulations gave a layer thickness of 49Å with a substrate and top surface roughness of 17 Å and 9 Å respectively. When offspecular longitudinal diffuse scans were taken, no such hump was seen corresponding to the position in the specular scatter (figure 6.11). As such within these samples, little or no conformality existed between the top and bottom surfaces. The simulations of the diffuse scatter taken at 5400 arc seconds is shown in figure 6.12 and the results given below in table 6.8. For the simulation all the roughness was assumed to
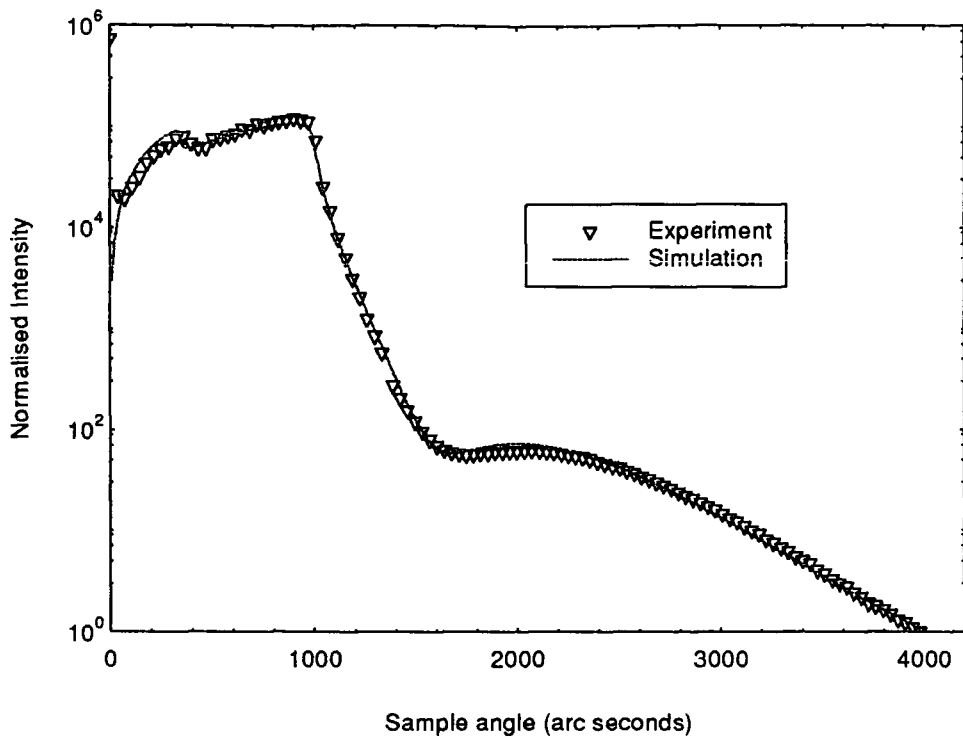
Fig 6.10   Simulation of the specular scatter from the PA polished sample
with its best fit simulation
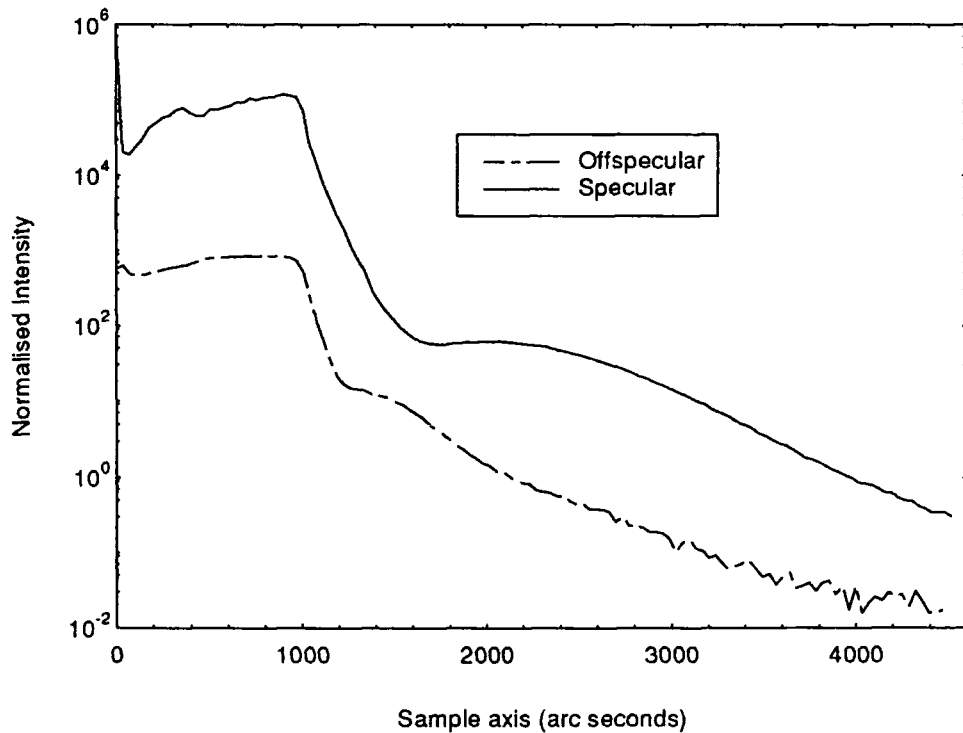
Fig 6.11   Comparison of the specular and offspecular scatter from
the PA polished sample

be non-conformal and gave a corresponding correlation length of 3000 Å, with a fractal exponent, h of 0.5.

Interface	σ_{total} (Å)	σ_{uncor} (Å)	σ_{grade} (Å)	ξ (Å)	h
Substrate	17 ± 1.5	12	12	3000 ± 250	0.55 ± 0.1
Top surface	9	6.4	6.4	3000	0.55

Table 6.8   Simulation parameters for the PA polished GaAs

6.4.3 Variations in specular scatter from the PA polished sample with time

One year later, a further specular scan was recorded.   As can be seen in figure 6.13, a fringe is again seen which is in the same angular position as before but is of greater amplitude.   The constant position of the fringe indicates that the layer present is of the same thickness as before.   In addition, the larger amplitude suggests that it has larger electron density contrast with respect to the substrate than previously.   It is difficult to see how the density of the already formed oxide can change with time.   However, it may be possible that in the original layer, some small regions of GaAs still remained.   As time progressed, oxygen, diffusing through the existing oxide would oxidise the remaining GaAs and change the observed density.   Alternatively the roughness of the buried interfaces may have altered, thus changing the amount of specular scatter from the bottom surface and therefore the fringe contrast.   Since the thickness of the layer did not change, it may be concluded that no significant oxygen diffusion could occur through an oxide of 50 Å thickness.   Unfortunately, no diffuse scatter data was available for simulations.
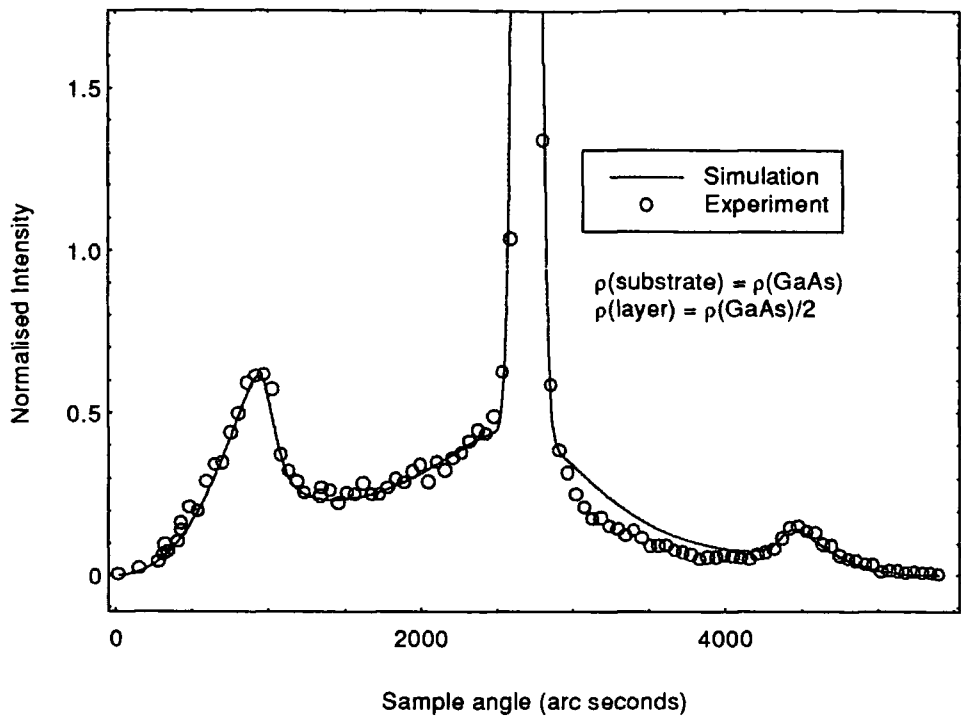
Fig 6.12   Transverse diffuse scan taken from the PA polished sample with its best fit simulation.   Scattering angle = 5400 arc seconds
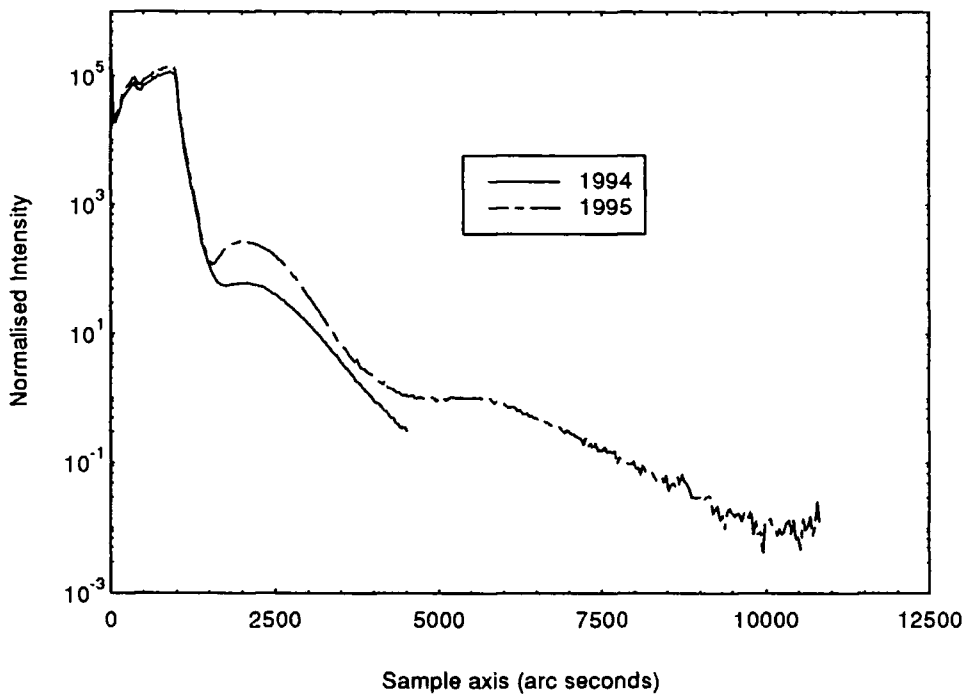
Fig 6.13   Variation of the specular scatter recorded from the PA polished sample over a period of one year

6.4.4 Born wave analysis of the diffuse scatter from the PA polished sample

Determination of roughness by full simulation is time consuming and in order to see if it was possible to extract the roughness of the samples without simulations, the Born wave analysis (BWA) introduced by Lagally *et al* was employed [8]. This method has been discussed previously both in section 3.2.21 and section 4.2.1. The resulting equation is given below:

$$\frac{I_{diff}}{I_{spec}} = \exp(q_z^2 \sigma^2) - 1 \qquad\qquad 6.1$$

In the Born wave approximation it is assumed that all the diffuse scatter is seen. However in reality the range of q_y that is able to be probed is cut off by the sample edges. Thus for larger scattering angles, it is expected that the deduced roughness will be higher than for small scattering angles. In section 3.2.21 and section 4.2.1 corrections for this effect were performed by producing 'look up' tables from the distorted wave Born approximation (DWBA). Built into this 'look up' table is information on the critical angles and therefore it can be used to predict the amount of diffuse scatter visible for any particular scattering angle.

In this section however, a second method will be demonstrated to try and determine the interfacial roughness. The roughness given by the BWA from the diffuse scatter in a real experiment will be plotted as a function of scattering vector and compared with a simulated surface for many scattering angles. Such plots were first introduced in section 3.2.21 and show graphically the increase in deduced roughness as a function of scattering vector. In order to extract the true roughness of the experimental surface, a simulation of a single surface is performed using the DWBA over the same scattering vector range. Using these simulated data, the roughness is deduced from the simulated diffuse scatter in the same manner as was done in the experimental case. This second roughness verses scattering vector plot is then compared with that as given by the real

surface and the roughness of the simulation changed iteratively until the two curves fit over the entire scattering vector range.

In this study, Born wave analysis was applied to the PA polished sample for a variety of scattering vectors ranging from 0.007 Å^{-1} to 0.055 Å^{-1}. The results of the BWA are shown in figure 6.14 along with the predictions from the DWBA over the same q_z range for a sample with 8.0 Å surface roughness. It is clear that there is reasonable agreement between experiment and theory except that the experimental curve dips at 0.018 Å^{-1} and 0.05 Å^{-1}. These dips can be seen to correspond approximately to the peaks in the specular scatter. As there is little correlation within the surface layer, when the specular increases due to a beat of the layer, the diffuse scatter cannot rise to compensate for it. In consequence, the ratio of specular to diffuse in equation 6.1 does not give the true roughness. Such an effect has been modelled assuming a 50 Å single layer of Ga_2O_3 with 5 Å of uncorrelated roughness on both its bottom and top interfaces. As can be seen from figure 6.16, there is a clear oscillation in the deduced roughness value. This can be seen to correspond exactly with the positions of the fringes in the specular curve (figure 6.15).

A second observation from the data was that the roughness deduced from the Born wave approximation appeared to be an average of the individual roughness values on the interfaces (section 6.4.2). However, a further complication was introduced when, in a separate study, simulations were performed in conjunction with P. Normile, on layers of Indium deposited on float glass. The structure used in these simulations was 100 Å of In on float glass, whilst the correlation length of the roughness was 1500 Å and the fractal exponent was 0.5. The scattering angles of the simulations were large and as a result the vast majority of the diffuse scatter would have been observed. Thus the values deduced from the diffuse simulations using the Born wave analysis had already reached there saturation values. In all cases the roughness values shown are an average of those taken
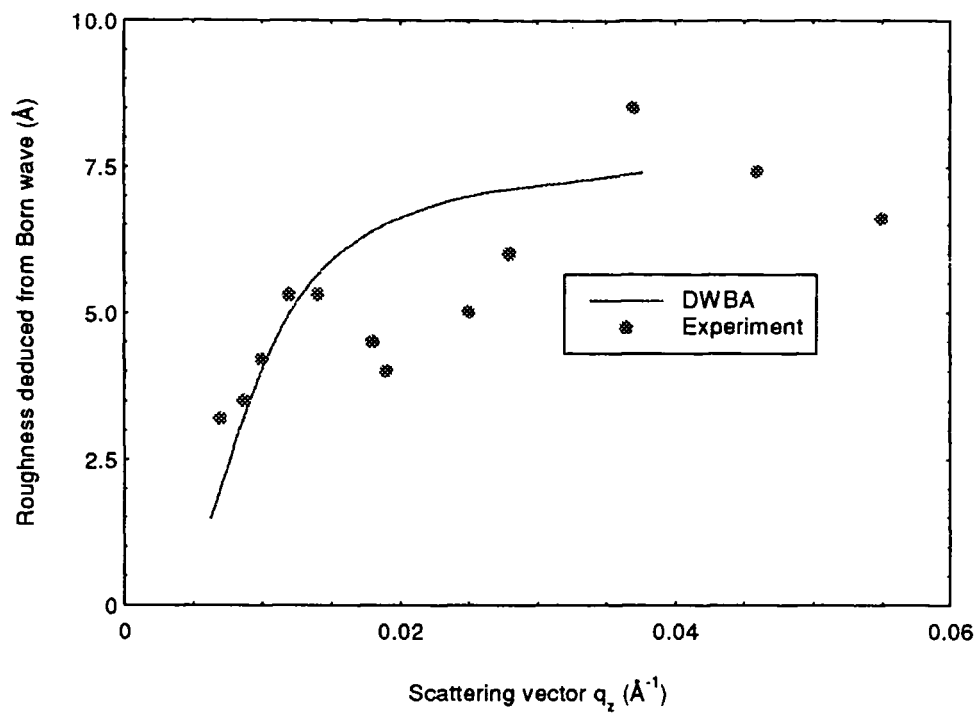
Fig 6.14 Comparison of the roughness deduced using the BWA from transverse diffuse scans taken from the PA polished samples with that from a simulated surface.
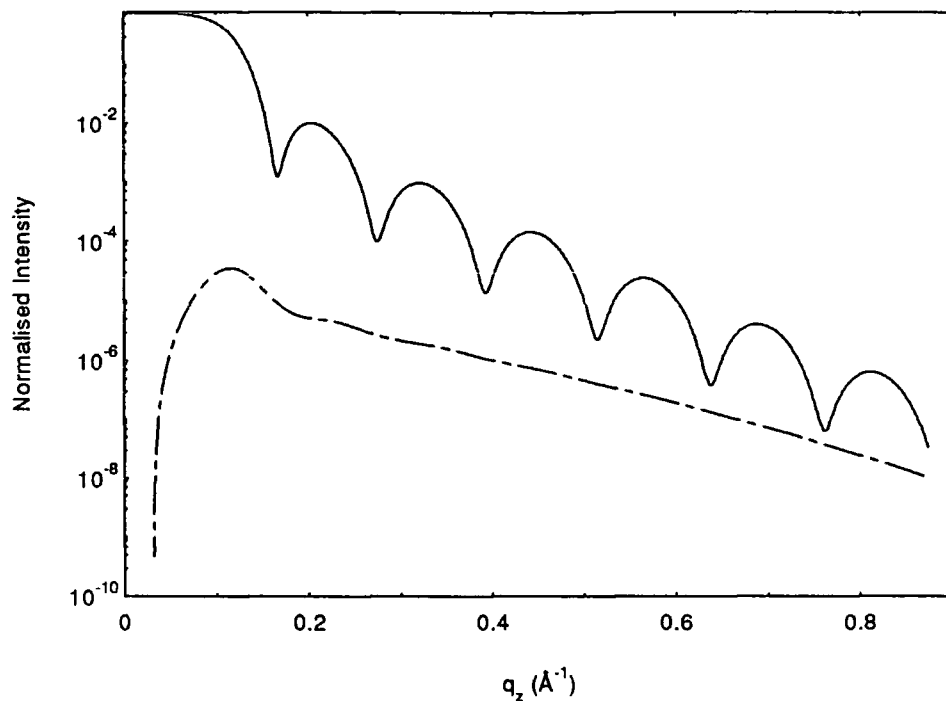
Fig 6.15   Simulation of the specular and offspecular scatter from a single 100 Å copper layer on a silicon substrate
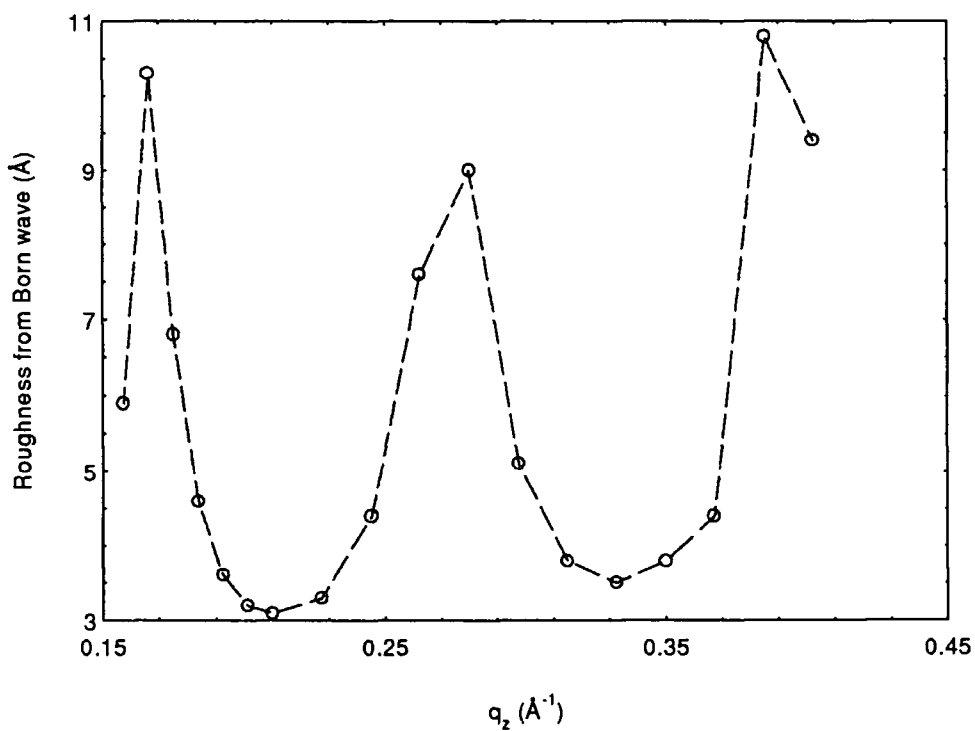
Fig 6.16 Roughness predicted from the data shown in figure 15 using the Born wave approximation.   Clearly visible are beats relating to the fringes in the specular scatter.

from a Kiessig fringe maximum and minimum. In consequence, any errors associated with the presence of the fringes in the specular scatter should be negligible. The results from the study are shown below in table 6.9.

Top surface roughness (Initial simulation)	Bottom surface roughness (Initial simulation)	Roughness deduced from Born wave approximation
5 Å	5 Å	5 ± 0.5Å
3 Å	7 Å	3 ± 0.5Å
0 Å	10 Å	1 ± 0.5Å

Table 6.9   The roughness values deduced using the Born wave approximation from simulations of a layer of indium on glass.

From these simulations it is clear that the deduced roughness is approximately equal to that of the top surface. However, in this case it was also observed that the fringes in the specular scatter were very weak, suggesting that the scatter from the buried interfaces was being strongly absorbed by the indium. Accordingly, it must be concluded that in the case of single layers, the deduced roughness is that of the average interface, weighted by the top surface. Although, in the case of the PA polished sample, it appears that the correct average roughness has been deduced, in general it is not known to what degree the top surface is biasing the results. Thus although the method appears to work for thin, weakly absorbing layers, in general it is unclear what the results mean without full simulation of the diffuse data.

6.5 Summary

In conclusion, symmetric and asymmetric diffraction studies have been performed on GaAs polished by a variety of different techniques. These studies have revealed that the distribution of strain within the samples is independent of polishing technique, whereas the lattice tilts are not. Such findings are not restricted to GaAs and have been observed by our group in similar studies of InP as a function of polishing conditions [7]. A model has been put forward to explain these findings in terms of a surface consisting of

unstrained mosaic blocks, separated by cracks. It is suggested that these cracks originated during the lapping stage of the sample. Grazing incidence x-ray scattering measurements have revealed the presence of a thin surface layer on all samples. In addition, a long lateral length scale surface figuring has been observed on the bromine methanol polished sample. It is believed that this has arisen from the action of the bromine opening up the microcracks formed during lapping. In contrast, no such figuring has been noted on the PA polished sample. It is implied that the passivating oxide layer associated with this polish has stopped the opening of the microcracks and so left a flat surface. These results are consistent with the x-ray diffraction findings, which show the bromine methanol polished samples to have a much higher distribution of crystalline tilts than the PA polished samples.

An investigation into the validity of using the Born approximation to deduce the roughness on buried interfaces has been undertaken. In this study a method of curve fitting was employed as described in section 6.4.4. This was done by altering the surface roughness in the simulated curve until it passed through the mean of the fringes in the experimental curve for the whole range of scattering vectors. It was found that as the layer was made increasingly thick that the roughness deduced tended to that of the top surface. However, it was believed that in the PA polished GaAs sample, this had not occured and that a true average roughness had been obtained.

An unfortunate problem associated with the curve fitting method is that the multiple simulations required to produce the fits over a large q_z range take a great deal of time. Thus realistically, for one or two layer systems, there is no advantage in terms of time in using the BWA as opposed to simulating the diffuse scatter from a couple of angles. This is especially true when it is noted that there is an uncertainty as to what degree the top surface is biasing the results. In contrast, in the case of the container glass (section 4.2.5) where there were no layers present, the BWA was orders of magnitude faster than the standard simulations. At the other extreme, in the case of the annealed multilayers (section 7.2.3), the BWA gave a trends in the samples within a few minutes, whereas simulations of multiple angles of such a multilayer would have taken days.

When analysing the annealed multilayers, no curve fitting was employed. Fortunately, the transverse diffuse scans from which the uncorrelated roughness values were calculated, were all taken at the average position in the specular fringes. Thus the errors that would have been introduced into the deduced roughness values as a result of the fringes in the specular scatter would have become negligible in this instance. In the annealed samples, anomalous dispersion was used to highlight the buried interfaces. As a result a large diffuse Bragg peak was observed and it can be said conclusively that diffuse scatter from the buried interfaces was being probed. It is accepted that this average interfacial roughness is biased towards the top layers. In the case of the Pilkington glass (section 4.2.1), it was clear that the Born wave analysis broke down. However, it appears that in these samples there is more than one layer present. As a result, it is possible that only a fraction of a period of one of the layers is visible. In consequence, the averaging through several periods which is required for accurate calculations cannot be performed and this may be the reason why the method predicted such high roughness values.

Chapter VII

Giant Magnetoresistance in magnetic multilayers

7.1 Introduction

Giant Magnetoresistance (GMR) is the name given to the large fractional decrease in resistivity, $\Delta\rho/\rho_0$, exhibited by certain layered structures on the application of a magnetic field. Since its discovery in the late 80's, great excitement has been generated in the industrial and academic sectors, due to it's possible uses, in applications that require the sensing of magnetic fields. Such applications have been widely reviewed [1-5] and include read heads, motion sensors, non-volatile memories and magnetic transistors.

In 1986, Grunberg [4,5,6] was studying iron layers with a non magnetic spacer of chromium sandwiched between them. He noticed that some of his iron layers were aligned ferromagnetically and others antiferromagnetically with respect to one another. The following year, Fert [4,5], observed that the electrical resistivity of an antiferromagnetically coupled iron/chromium superlattice, dropped by a factor of two, when a sufficiently high magnetic field was applied. In 1988, Baibich [7] reported that the magnetoresistance of a superlattice of Fe(001)/Cr(001) could be increased by making the Cr spacer thinner. He also speculated that this effect was some form of spin dependent transport. In 1990, Parkin [8,9], working on superlattice systems of Co/Cr, Co/Ru and Fe/Cr, observed that as the non magnetic spacer layer was thickened, the magnetoresistance showed an oscillatory behaviour. He ascribed this finding to an RKKY [10] type interaction (figure 7.1), modulated by the spacer layer thickness to give a larger period due to aliasing (figure 7.2) [1,8]. In the RKKY interaction, an electron with the same spin as the atom, 'wants' to sit as close to it as possible. As a result it's wavefunction is a maximum at the atom. The converse is true for an electron of opposite spin.
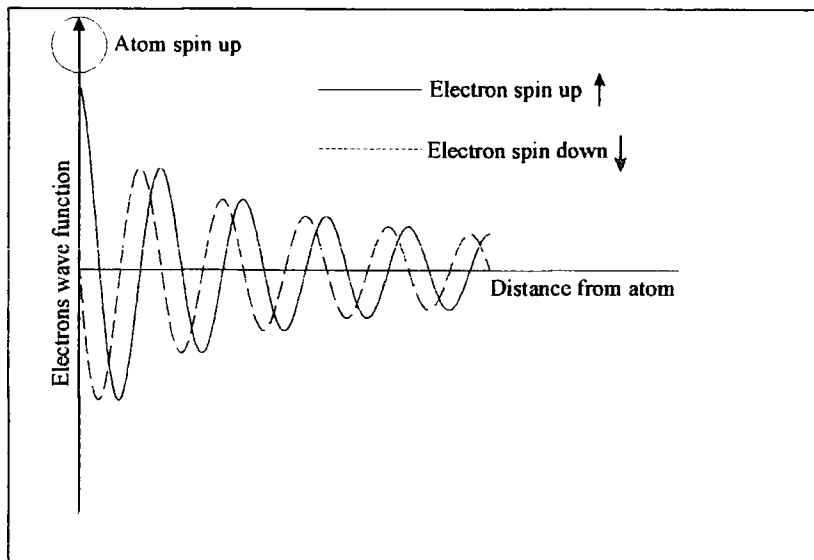
Figure 7.1   The effect of a spin polarised atom on the wavefunctions of
electrons in the vicinity
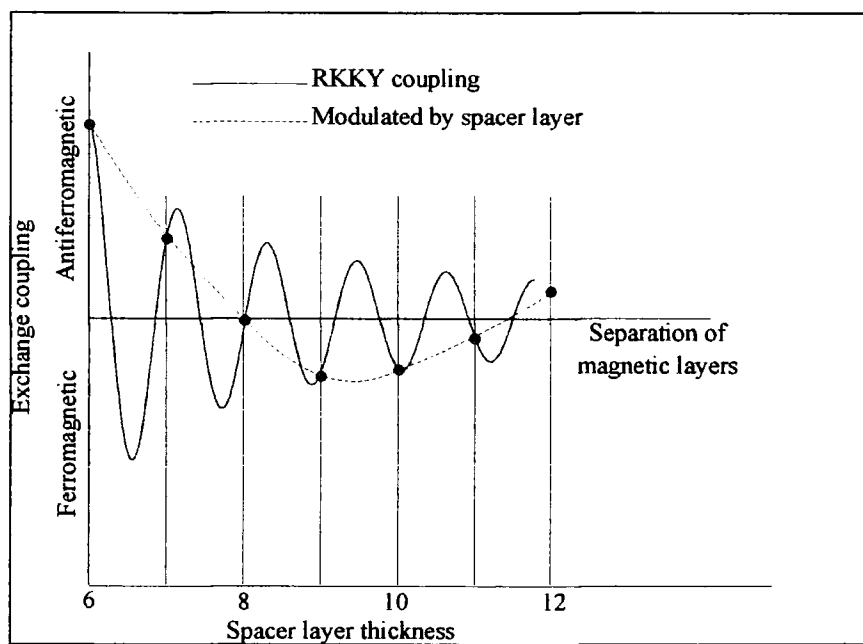
Figure 7.2   The RKKY type interaction proposed by Parkin

In 1989, Camley [11] put forward a model for the GMR effect in multilayers. The model followed the idea of Baibich that some form of spin dependent scattering was occurring. Further papers were written, from which Mathon [12] produced a review article. In this he proposed his own model. This followed the same ideas as the paper written by Camley, but lead to a simple analytical result. This is summarised below.

Scattering of electrons takes place due to defects, impurities etc. For an electron to be able to be scattered, it must have states of its own spin available to it (ignoring spin relaxation [13]). In addition electrons can only scatter into states within an energy interval of K_bT. As a result only the density of states very close to the Fermi level are active within the scattering process, and the resistance of the material becomes proportional to the density of states in the region of the Fermi level.

If the situation is restricted to a non magnetic spacer, sandwiched between two magnetic layers as shown in figure 7.3, it can be seen that two possible configurations can occur. Either the two magnetic layers can be 'ferromagnetically' (figure 7.3a) aligned, or 'antiferromagnetically' aligned (figure 7.3b) with respect to one another. Due to the oscillatory behaviour of the coupling, the thickness of the spacer layer can be chosen to give antiferromagnetic alignment as the zero field state. In this case, the system can be caused to flip from this to the ferromagnetic case, on the application of a magnetic field.

Within the system, two independent channels of electrons are present, spin up and spin down. In the first configuration (figure 7.3a), the conduction electrons of both spins passing through the structure experience the same strength of scattering. This is due to there being the same number of states available for them to scatter into, somewhere in the medium. In the second configuration (figure 7.3b) only one of the spins of the conduction electrons is scattered strongly whilst the other is not. Mathon showed, by treating these two spins as parallel resistors, that in the antiferromagnetically aligned state, the total resistance of the system was higher than the resistance in the ferromagnetically aligned configuration. As a result a qualitative model for GMR emerged.

The magnitude of the observed GMR is a function of temperature. As the temperature is increased scattering of the conduction electrons with magnons causes spin mixing and the independence of the two conduction channels is decreased. In addition, as the temperature approaches the Curie temperature the magnetic properties of the layers vanishes and therefore so does the GMR. As a result, all GMR measurements made in this chapter were performed in liquid helium at 4.2K. The measurements were made at Leeds University by H. Laidler and K. Wellock, using a 4 probe, DC method with the current in the plane (C.I.P) and the 4T field applied perpendicular to the layers.

Multilayers are not the only type of structure that exhibits GMR. Indeed a number of other, more easily manufactured, structures exists. A close relation of the multilayer is the spin valve [2,14]. This has two magnetic layers separated by a (thick) non magnetic spacer. One of the layers is magnetically pinned to a substrate (strong coupling) whilst the other is free to change the orientation of its magnetisation. On changing the magnetisation of the top layer, the resistance of the system changes as described above. Due to the small amount of coupling between the two magnetic layers the device can be made to flip between states using an extremely small field. This is a disadvantage with multilayers, since although they posses the highest GMR, very large fields (typically in the region of 4T) can be required to cause them to change state.

Granular GMR structures also exist [4], where magnetic particles are embedded in a sea of non magnetic spacer, whilst hybrid structures of multilayers embedded with granules are also under investigation.

Several systematic studies have been performed by our group on the effects of structural changes on the measured GMR. These include the effect of interface doping, the type of growth technique [15], the effect of buffer and capping layers [16-18], the effect of substrate temp during growth and the effect of annealing of the samples [19,20]. The last of these was actually the first study to be performed, in 1993, using Cu-Co multilayers as a starting point. Although the main driving force to study Cu-Co systems was their large GMR, another factor was that they were known

to be immiscible [21]. As it turns out this was a good choice since there is a large body of evidence in the literature to support that, in Cu-Co, little bulk interdiffusion occurs below 400°C [22-30] and that in layers over 4ML very few pin holes exist.

7.2 Effects of annealing on the structure and GMR of Cu/Co multilayers

7.2.1 Sample preparation

Co/Cu multilayers were grown on polished, single crystal, sapphire substrates oriented normal to the [11$\bar{2}$0] direction. The sapphire substrates were 1mm thick and the layers were deposited on their rectangular 12 mm x 10 mm faces. All samples were grown at Leeds University in the VG80M MBE facility with a base pressure of 3×10^{-11} mbar. To achieve a high degree of uniformity across the samples they were rotated at 1 Hz during growth. In order to obtain good growth on the sapphire substrates, two underlying buffer layers were used, 60Å of Nb, deposited directly onto the sapphire substrate at 950°C followed by a 30Å Cu layer at 375°C. The 20 period multilayers, nominally 11.5Å Co/7Å Cu, were grown at room temperature, and capped with nominally 40Å of Au to prevent the top layer of Cu from oxidising. The sapphire wafers were cut into 2 mm by 8 mm pieces using a diamond saw. The resulting samples were annealed in a stream of oxygen-free nitrogen for 45 minutes at 200, 260, 290, 320°C respectively. A fifth sample was left unannealed.

7.2.2 Specular and diffuse x-ray reflectivity measurements

Grazing incidence x-ray scattering measurements were made using the two circle powder diffractometer on station 2.3 at the Daresbury SRS. Details of the experimental configuration and the alignment procedures are given in sections 2.1.1 and 2.1.2.

Figure 7.4 shows a set of specular scans performed at the Cu edge (λ = 1.3801 Å), taken from this series of annealed samples. For annealing temperatures below 290°C, no variations are observed in the data. Two significant changes occur above 290°C however. Firstly there is a more rapid fall in the intensity for small scattering angles
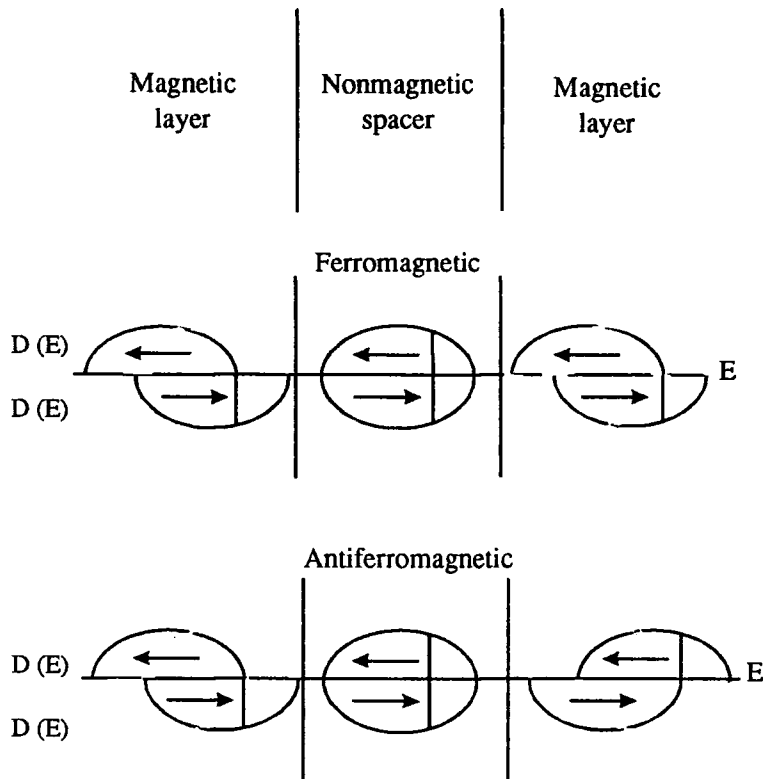
Fig 7.3 Density of states for electrons within a trilayer for various magnetic alignments
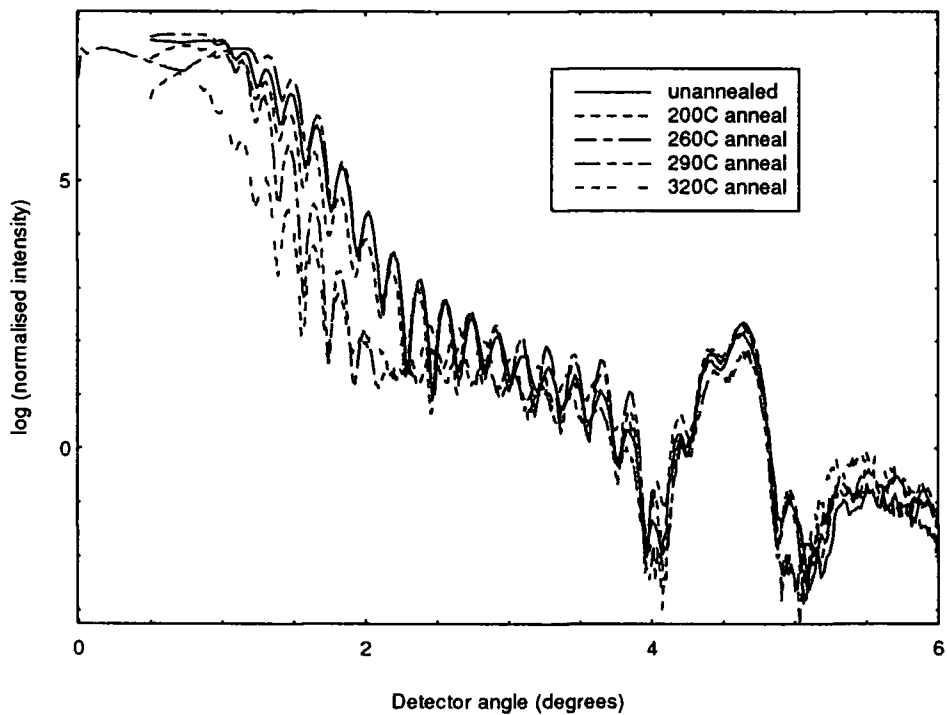
Fig 7.4 Comparison of specular scatter taken from samples which have undergone
annealing for various amounts of time

and secondly, there is an increase in the period of the Kiessig fringes in the region between 2 and 4 degrees.

The second of these observations is related to a decrease in overall stack thickness from 438 Å ± 2Å to 425 Å ± 2 Å. In addition the stable position and height of the Bragg peak suggests that no changes have occurred within the multilayer itself. As a result, it must be concluded that one of the buffer or cap layers has reduced in thickness.

In order to clarify whether the more rapid fall off of the specular was due to increased top surface roughness or interdiffusion, transverse diffuse scans were performed. These were taken at, and away, from the Bragg Peak and are shown in figures 7.5 and 7.6 respectively. From figure 7.5 it is clear that there is little change in the diffuse scatter around the Bragg peak for any annealing temperature studied. Figure 7.6 however, shows a significant drop in the diffuse scatter away from the Bragg peak for annealing temperatures of $290^{\circ}C$ and above.

Qualitatively, the lack of change in the specular scatter and the fall in the intensity of the diffuse scatter taken away from the Bragg peak on annealing at $290^{\circ}C$, indicate that the amount of uncorrelated roughness within the sample has dropped. Conversely, the stability of the transverse diffuse scans taken at the Bragg peak, indicates that there is negligible change in the correlated component of roughness within the stack on annealing. From this lack of change in the transverse diffuse scans taken across the Bragg peak, interdiffusion can be eliminated as a cause of the increased fall-off in the specular scatter. If interdiffusion had occurred, both the transverse diffuse scans would have displayed a marked drop in intensity (section 3.2.19) and changes would have been seen in the specular scatter.
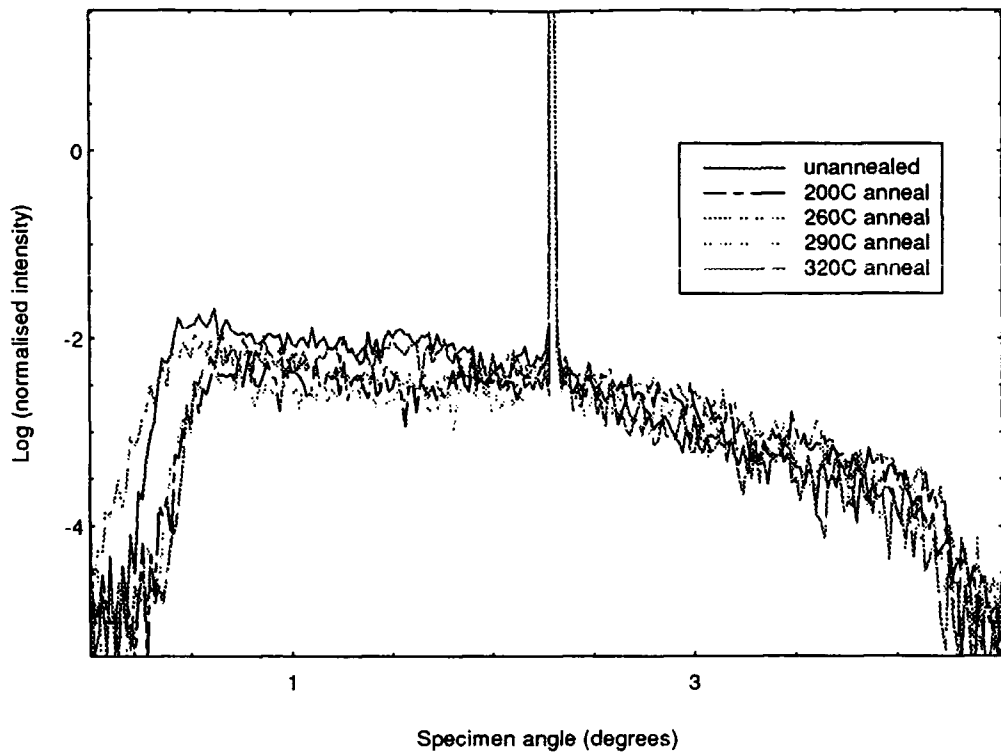
Fig 7.5   Transverse diffuse scans through the first order Bragg peak
for various annealing conditions
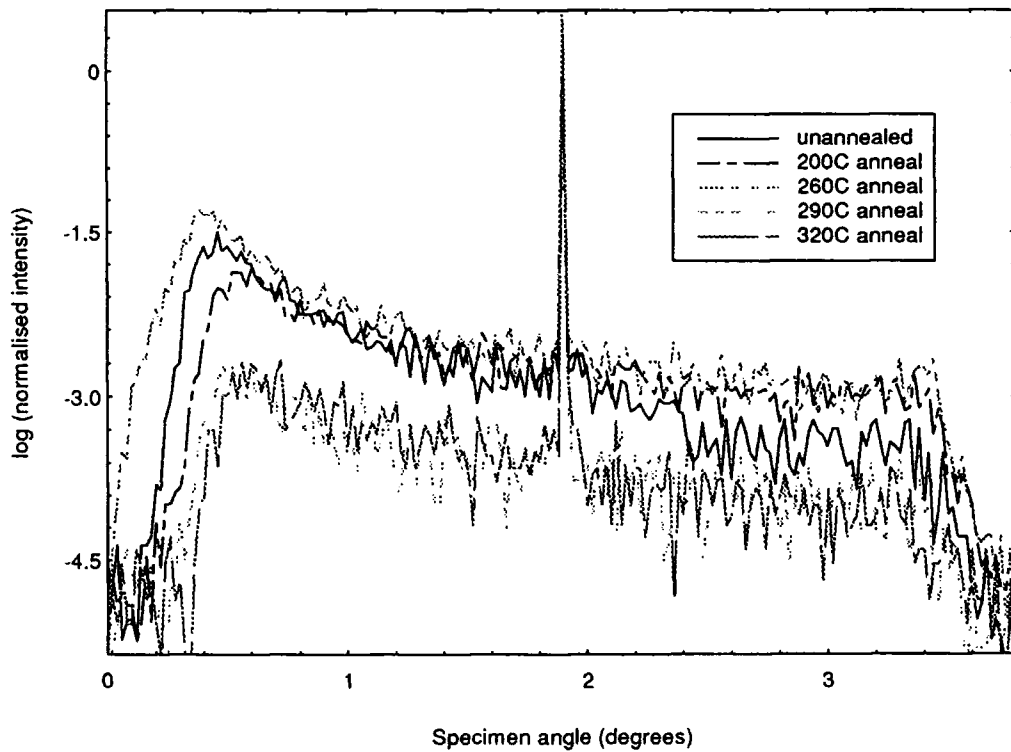
Fig 7.6 Transverse diffuse scans taken away from the Bragg peak for various annealing
conditions

7.2.3 Born wave analysis of the transverse diffuse scans

A method of analysing quantitatively the diffuse scatter from multilayers was developed by Lagally *et al* [31] in 1991. By assuming Gaussian roughness and a kinematical model, they showed that the roughness could be split into its correlated and uncorrelated components, if a periodic structure was present. For uncorrelated roughness, the absence of vertical periods associated with replications through the multilayer stack, means that the diffuse scatter is spread out 'evenly' in reciprocal space. (Obviously, there is a general fall off with q_z and so only one q_z value must be chosen.) However, for correlated roughness, a strong vertical period is present. In consequence, the diffuse scatter is channelled into certain q_z values, i.e. the diffuse Bragg peaks. As a result, a transverse diffuse scan taken far away from the Bragg peak will probe mainly the uncorrelated component of the roughness. However, a diffuse scan taken through the Bragg peak will be dominated by correlated roughness in the stack. Within the Born approximation, the equations for the correlated (7.1) and uncorrelated (7.2) components respectively are:

$$I_{diff}/I_{spec}(\text{Bragg peak}) = \{\exp(q_z^2\sigma_c^2)\}-1 \qquad 7.1$$

$$I_{diff}/I_{spec}(\text{Away}) = \{\exp(q_z^2\sigma_u^2)\}-1 \qquad 7.22$$

Here q_z $(= [4\pi/\lambda]\sin[\phi/2])$ is the momentum transfer vector perpendicular to the surface. σ_c and σ_u are the correlated and uncorrelated components of roughness respectively, where σ is the total roughness within each layer ($\sigma^2 = \sigma_u^2 + \sigma_c^2$). I_{diff} and I_{spec} are the integrated intensities of the diffuse and specular scatter for a fixed q_z value.

As these equations are derived from the Born wave approximation, it is assumed that all the diffuse scatter is seen (section 3.2.21). However, in reality, the diffuse scatter is cut off by the shadow of the sample edges. As a result, the roughness deduced from these equations is slightly below its actual value. This shift is approximately a constant scaling factor for each curve and so does not affect the actual trends in the data.

Simulations of the specular and diffuse scatter from surfaces with singles layers deposited on them were performed in section 6.4.4. Born wave analysis of this simulated data revealed that the deduced roughness had a sinusoidal variation as a function of scattering vector, q_z. Such variations were attributed to the amplitude of the fringes in the specular and diffuse scatter being of different magnitudes. These fluctuations produced periodic variations in the I_{diff}/I_{spec} relationship, shown in equations 7.1 and 7.2, which followed through into the deduced roughness. In order to compensate for this periodicity, an average of the roughness values over a couple of periods proved to be necessary.

From the specular scatter in this study, it is clear that such oscillations are present. In consequence, theoretically for a reliable uncorrelated roughness value to be deduced, such an averaging must take place. However, the transverse diffuse scans from which the uncorrelated roughness was calculated were taken at the mean point of the specular fringes for all annealing conditions. Thus the errors associated with the increase and decrease of the specular scatter relative to the diffuse are in this instance negligible.

Also shown in section 6.4.4 was that the Born wave approximation tended to be biased towards the roughness of the top surface when a layer was present on samples. However in this case, anomalous dispersion was used to increase the scatter from the buried layers. The presence of a diffuse Bragg peak indicates that correlated roughness from the multilayer is being probed. If this scatter is being observed then the diffuse scatter arising from the uncorrelated component is also able to escape. However, the values obtained will still be weighted by the upper layers.

The results of the Born wave analysis are shown in figure 7.7. It can be seen that whilst there is a fall in uncorrelated roughness at 290°C, the correlated component does not vary beyond experimental error. In order to double-check these results, a second set of transverse diffuse scans was performed, this time, close to, and away from the Cu absorption edge. Such scans close to the edge enhance the scattering for the Cu-Co interfaces, due to anomalous dispersion. Since in these samples, the Cu-Co layers make up the multilayer, this allows scattering from the periodic layers and from
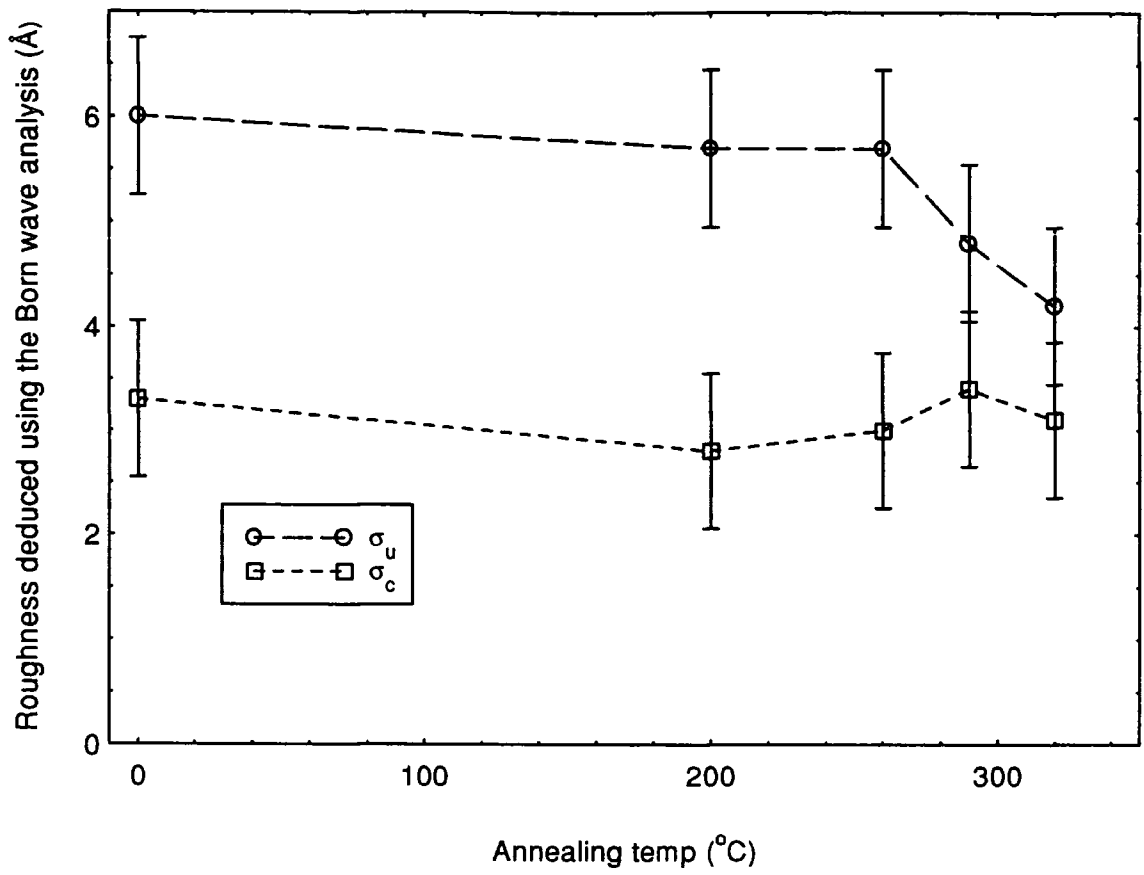
Fig 7.7 Amount of correlated and uncorrelated roughness within each layer of the
annealed samples deduced by the Savage (Born wave analysis) method

the buffer layers to be distinguished. For scattering angles corresponding to the Bragg peak (figure 7.8), a large increase in the diffuse scatter is observed on tuning the wavelength to the edge. However when transverse diffuse scans are taken away from the Bragg Peak (figure 7.9), little change occurs. The absence of change in the latter scan shows that the uncorrelated roughness which gives rise to the scatter does not exist within the Co/Co multilayer stack. On the other hand the enhanced diffuse scatter at the Bragg peak shows that there is a large amount of correlated roughness present through the multilayer. If these two conclusions are combined with the roughness deduced from the Lagally analysis it can be concluded that the 4Å of uncorrelated roughness measured must be confined to the buffer layers and the cap.

Another observation from the transverse diffuse scans is that the positions of the Yoneda wings move to a higher angle for samples annealed at 290°C and above. This indicates that the electron density of the top surface is increasing.

7.2.4 HRXRD and magnetotransport measurements

High angle x-ray diffraction (HRXRD) scans taken by Helen Laidler at the University of Leeds, showed that little changes occurred in the crystallographic structure of the Co/Cu layers on annealing [19]. However, a significant change in diffracted intensity occurred in the angular range between the sapphire substrate peak and the Co/Cu (111) peak. This took the form of a new peak at 41 degrees, for annealing temperatures of 290°C and above, which could not be simulated by any change in layer thickness. The peak was finally identified by Laidler as corresponding to the lattice parameter of a $Au_{35}Cu_{65}$ alloy. This composition is consistent with the thickness of the Au cap and last Cu layer. Since the $Au_{35}Cu_{65}$ alloy has an electron density higher than either Au or Cu alone [32], this explains the observed increase in electron density of the top surface beyond 290°C in the grazing incidence measurements. The reduction in thickness of the top layers, observed in the specular scans, is consistent with this increase in surface density due to the formation of an intermetallic. Further evidence for a alloyed top layer can be found in section 7.4.2, where the detailed simulation of a sample with solely a gold cap gave the wrong critical angle. The only way the model could be made to fit was to include a AuCu alloy as suggested above.
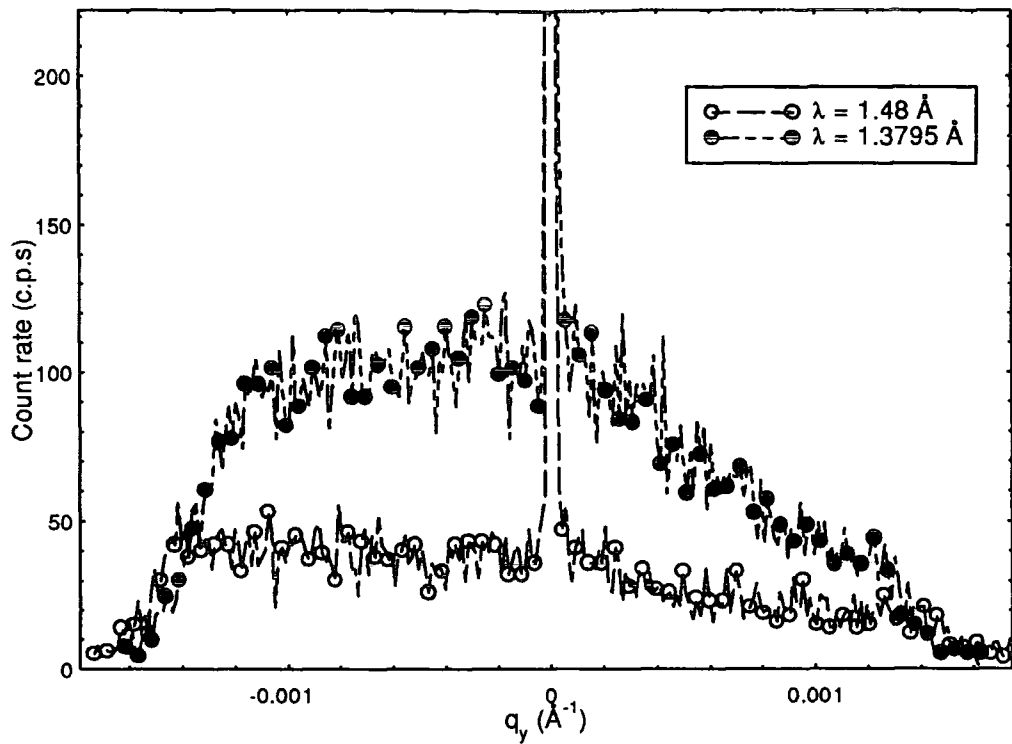
Fig 7.8 Transverse diffuse scans taken through a first order Bragg peak at ($\lambda = 1.3795$ Å) and away ($\lambda = 1.48$Å) from the absorption edge
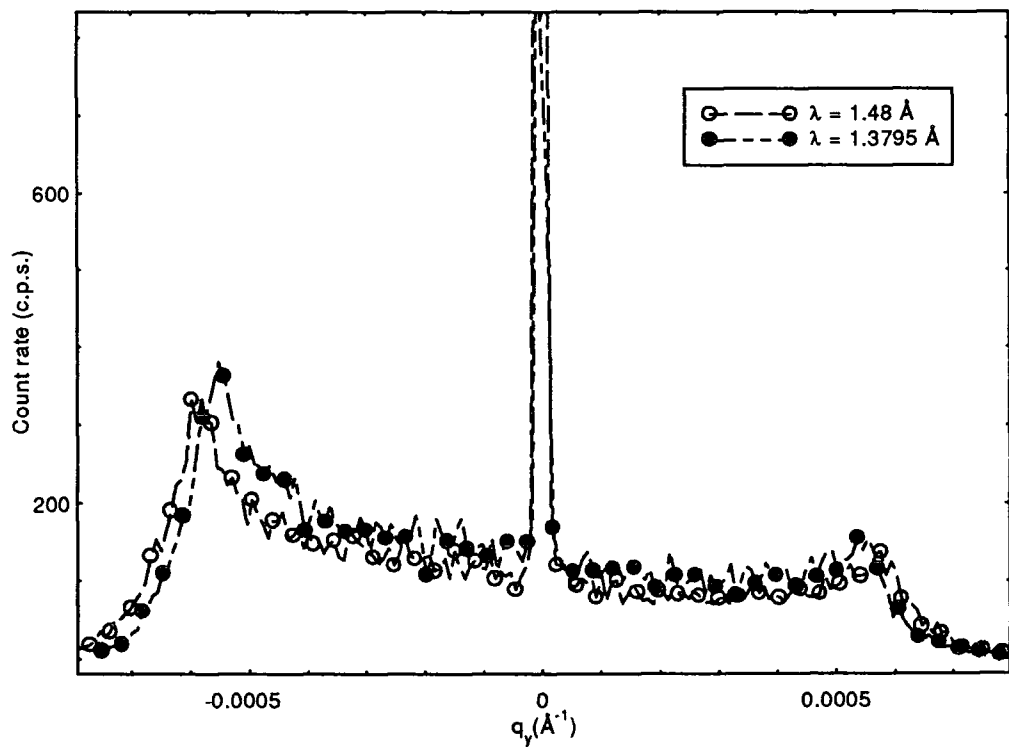
Fig 7.9   Transverse diffuse scans taken away from the first order Bragg peak at ($\lambda = 1.3795$ Å) and away ($\lambda = 1.48$Å) from the absorption edge

In order to further test the argument that an alloy or intermetallic compound had formed, another sample was grown but this time the multilayer was terminated with a Co instead of a Cu layer followed by the Au cap [19]. The phase diagram for Co and Au shows that these elements are largely immiscible [21] and there is no stable alloy. This sample was annealed at 320°C as before and high angle x-ray data taken. This time no peak at 41 degrees became visible, reinforcing the argument that a AuCu alloy was forming in the other samples. As a result, both the high and low angle x-ray results agree that little change is occurring within the multilayer on annealing. The stability of the system is explained by the immiscibility of both the multilayer and the buffers and the use of a non-oxidising cap.

The results of the magnetotransport data are shown in Table 7.1.

Annealing Treatment	ρ_s ($\mu\Omega$ cm)	$\Delta\rho$ ($\mu\Omega$ cm)	MR (%)
Unannealed	8.2	3.0	36.6 ± 0.75
200°C	9.0	3.4	37.8
260°C	12.0	4.4	36.7
290°C	14.4	4.7	32.6
320°C	18.6	5.8	31.1

Table 7.1 Magnetotransport data as a function of annealing temperature

Although the GMR is seen to be constant as a function of annealing temperature, this is due to the $\Delta\rho$ and ρ_s components scaling by the same amounts. The 225% increase in room temperature resistivity is surprisingly high for a sample in which no structural changes have taken place within the Cu/Co multilayer. Previous work on AuCu alloys found that the resistivity of a CuAu alloy increases by 0.3 $\mu\Omega$cm per atomic percent of Au in Cu [19]. This implies that the resistivity of the cap region should increase by about 10$\mu\Omega$cm. Work by K. Wellock, at Leeds University showed that the normal two spin dependent channel model was inappropriate when including buffer layers. Instead he showed that a better model was one proposed by Maxwell, which treated

the conductivity as an average of the separate conductances of the layers weighted by their respective thickness'. It was shown that this model was consistent with the findings observed in these samples.

7.2.5 Summary

The conclusion that should be drawn from the above is that for the immiscible Cu/Co system, annealing up to at least 300°C can take place without significant degradation of the sample. Even when changes finally do start occurring, these are mainly confined to the buffer and capping layers. In the particular case here, the measured GMR, is unaffected by annealing temperatures up to 300°C. Finally, the GMR would appear to bear no relation to the uncorrelated component of roughness within the samples.

The use of the uncorrected Born wave analysis would appear to provide information on the correlated and uncorrelated component of roughness within the samples. In order for meaningful results to be drawn out of the deduced roughness, the lateral correlation length within the samples must remain constant. The consistent shape of the diffuse scatter within these samples has shown this to be the case. Finally, in order to alleviate the effects of the fringes in the specular scatter on the deduced roughness, the transverse diffuse scans should be taken at the average positions of the fringes. This should avoid any scaling effects associated with the fringes.

7.3 Effect of substrate temperature during growth on the measured GMR in Cu/Co multilayers

An extension to the above findings that the GMR was not a function of uncorrelated roughness was produced the following year when studies were made on the effect of the substrate temperature during growth on the GMR [33]. In this investigation Co/Cu multilayers, grown by MBE on sapphire substrates were studied for a variety of substrate temperatures during growth. An increase was observed in the value of the GMR as the amount of correlated roughness in the samples was reduced. However, studies of samples grown on 111 silicon using a new type of buffer showed a higher

GMR than predicted from this trend (figure 7.10). As a result, a further study was undertaken into what difference, in the structure of these samples, caused them to behave differently from the multilayers grown on sapphire. This study is presented below.

7.4 Cu/Co multilayers grown on Si(111) with a Cu₃Si buffer layer

7.4.1 Sample preparation

The samples studied were twenty period Co-Cu multilayers grown on polished silicon substrates orientated normal to the [111] direction. The silicon substrates were 10 mm square with a thickness of 1 mm. All samples were grown at the University of Leeds in the VG80M MBE facility with a base pressure of 3×10^{-11} mbar. During deposition, the pressure remained below 1×10^{-10} mbar and some samples were rotated at 1 Hz. The sample shown here was not rotated, but the data shown is representative of all specimens.

The 20 period multilayers, nominally 11.5Å Co/7Å Cu, were grown on a 10Å Cu layer, deposited directly onto the silicon substrate at 150°C. This formed a Cu₃Si compound [32] onto which a 15Å Au layer was deposited. Finally a nominally 15Å thick Au cap was laid to prevent oxidation of the top layer of copper.

7.4.2 Specular and diffuse x-ray reflectivity measurements

Grazing incidence x-ray scattering measurements were again made using the two circle diffractometer on station 2.3 at the Daresbury SRS. Four types of measurements were made, namely specular, off-specular longitudinal, transverse diffuse and detector only scans.

Due to their closely matched scattering factors, poor contrast occurs between layers of Co and Cu in x-ray reflectivity measurements. As a result, anomalous dispersion was used, to enhance the scattering from these layers compared to the other interfaces. X-ray measurements were then performed close to and far away from the Cu
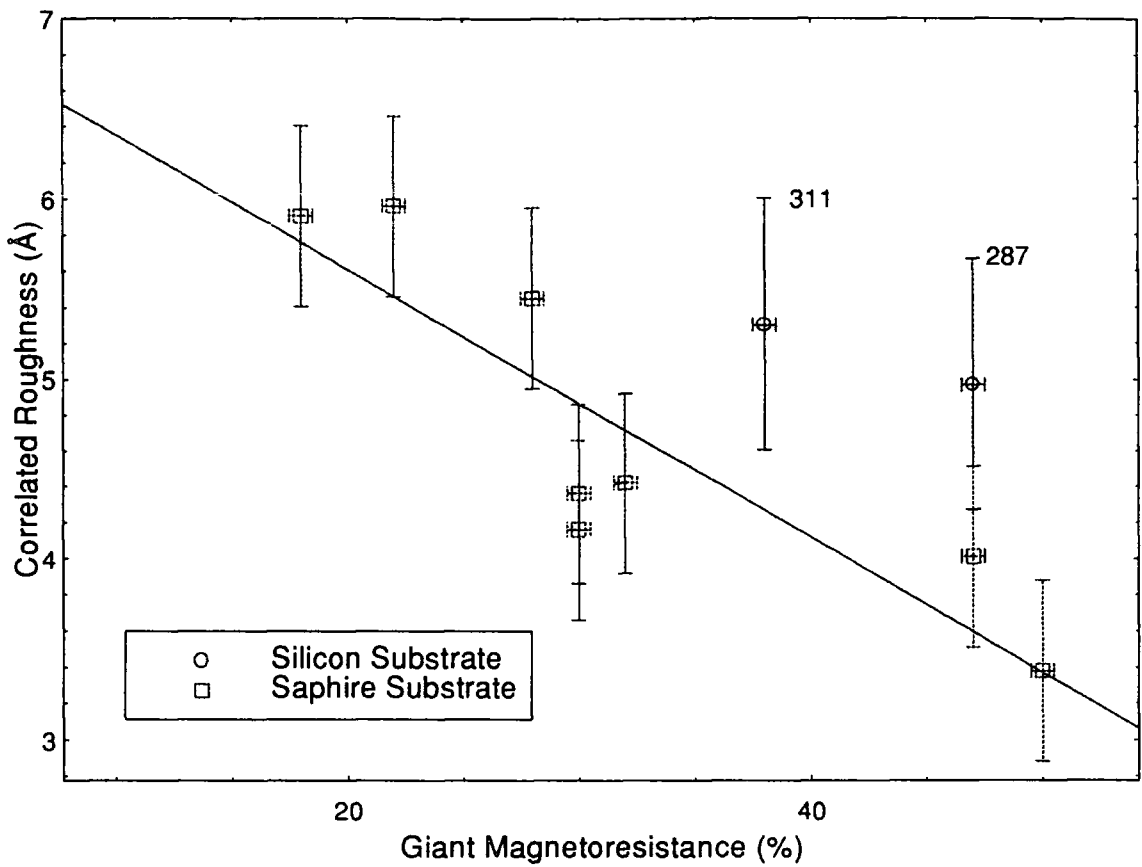
Fig 7.10   A graph of GMR vs correlated roughness for multilayers grown on
silicon and sapphire

absorption edge, yielding more easily the buried structure of the Co-Cu interfaces via simulations.

The simulation of the x-ray specular and diffuse scatter was performed on a 486 PC, using code written by Matt Wormington working at Bede Scientific. This code, based on the distorted wave Born approximation, uses the fractal description of surfaces [34,35] to simulate the diffuse scatter from a model of the structure. These simulations are then compared with the data, the model refined, and iterations performed until the specular and several diffuse scans fit simultaneously. This process of multiple fitting is advantageous in complex systems since it reduces the number of possible solutions to the data. Despite this advantage, to our knowledge, this method has only been applied by a few people other than our group [36-39].

Figure 7.11 shows the specular curve for sample 311, corrected for its diffuse background, with its best fit simulation. The structure deduced from the simulations is shown in figure 7.12.

As with the annealing experiment (section 7.2), it proved necessary to use a Au-Cu alloy for the cap, suggesting interdiffusion between the top Cu layer and the Au had occurred. Since the Au-Cu alloy has a higher density than either Au or Cu alone, omission of this interdiffusion from the model led to a false prediction for the position of the critical angle. In addition the interference fringes were out of phase since the oscillations begin at the critical angle.

Figure 7.13 a-d, shows a series of transverse diffuse scans, taken through the 1st order Bragg peak, for different rotations of the sample about its surface normal. The diffuse scatter is seen to peak sharply on one side of the specular ridge. On rotation of the sample the diffuse scatter peak moved round the specular sinusoidally as shown in figure 7.14. No change in the specular curve was observed on rotation (figure 7.15). Such asymmetries in diffuse scatter which are a function of the direction of the input beam $(+q_y,-q_y,+q_x,-q_x)$ have been observed by many other researchers [40-44]. In all cases they have been ascribed to a preferential direction on the surfaces and by implication terracing within the multilayers. Unlike the other investigations, a single
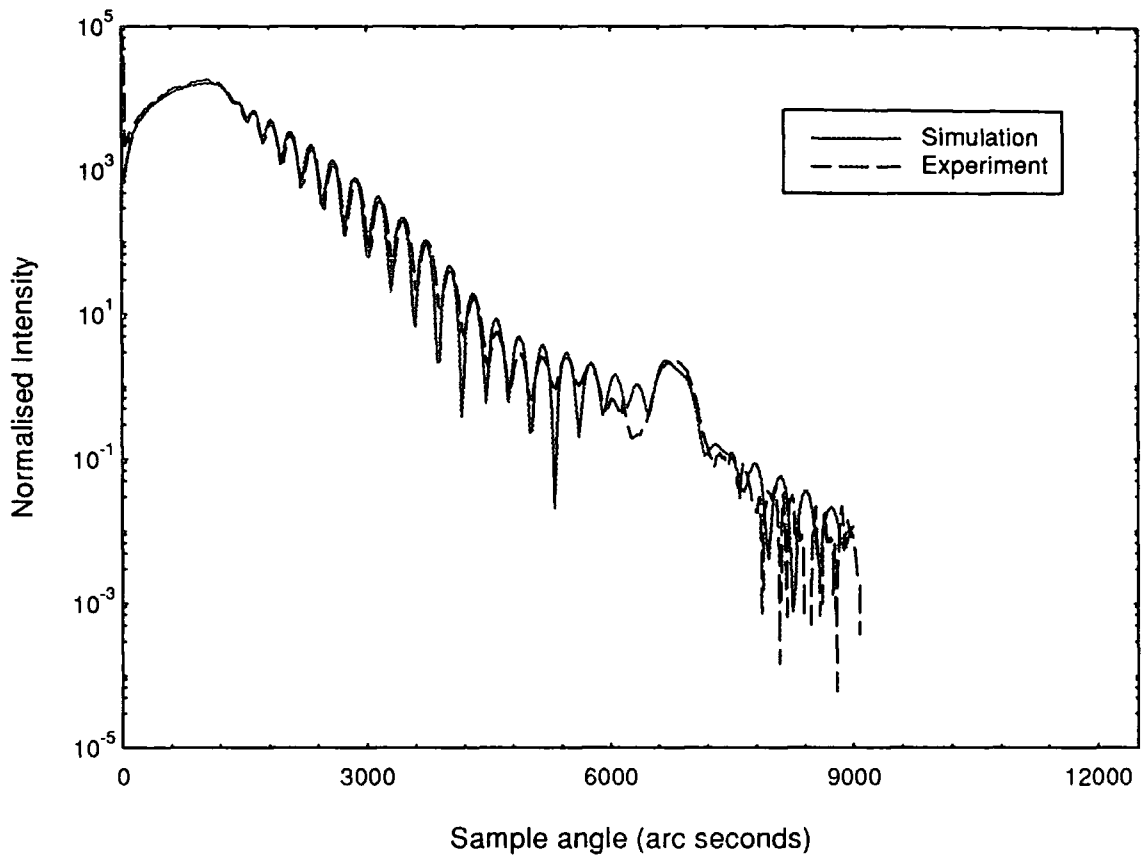
Fig 7.11   Specular scan and simulation from sample 311

Layer
thickness
($\pm$ 1 Å)

Interface
roughness
($\pm$ 1 Å)

$Au_{0.8} Cu_{0.2}$ (31 Å)
Co (14.5 Å)
Cu (6.5 Å)
Co (15 Å)
Au (21.5 Å)
Cu_3Si (15 Å)
Si Substrate

←7.0 Å rms
←6.5 Å rms
←7.0 Å rms   x 19
←6.5 Å rms
←6.0 Å rms
←6.0 Å rms
←6.0 Å rms

Fig 7.12   Structure of the Cu-Co multilayer deduced from the above simulation
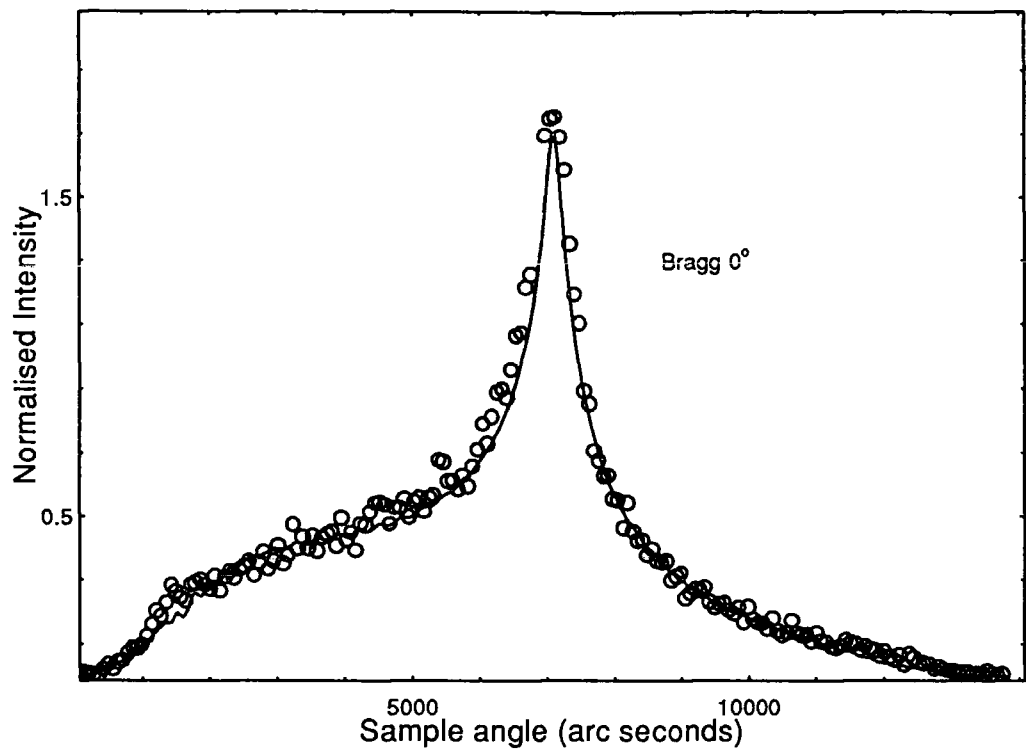
Fig 7.13a Transverse diffuse scan taken through the first order Bragg peak for 0 degrees
rotation about the sample's surface normal
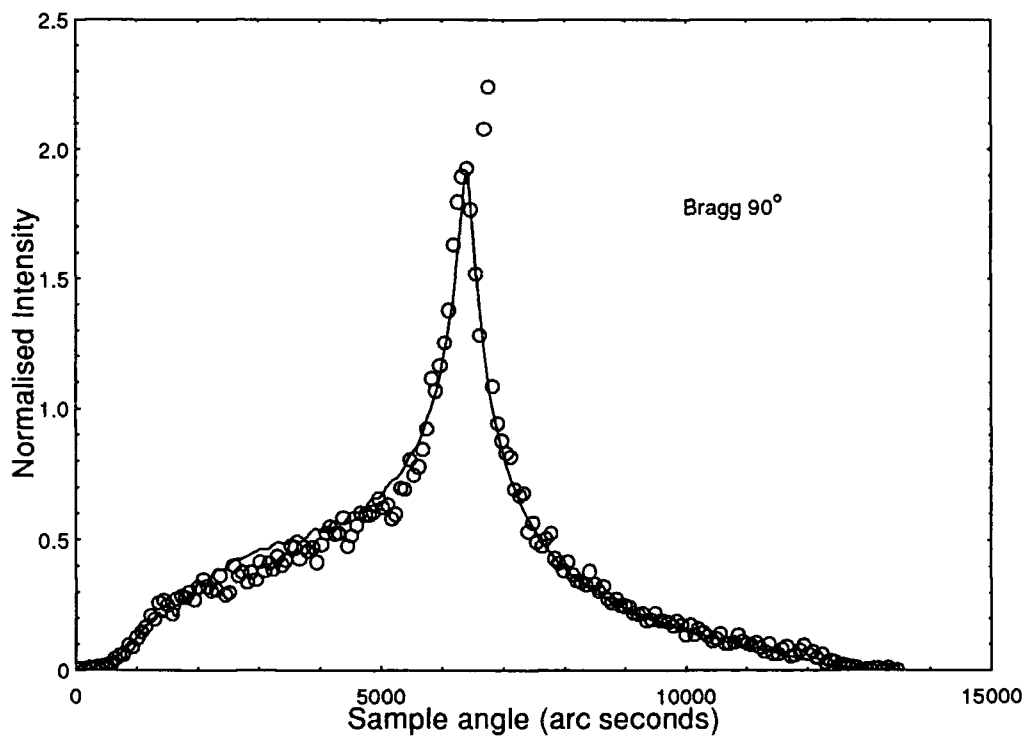
Fig 7.13b Transverse diffuse scan taken through the first order Bragg peak for 90 degrees
rotation about the sample's surface normal
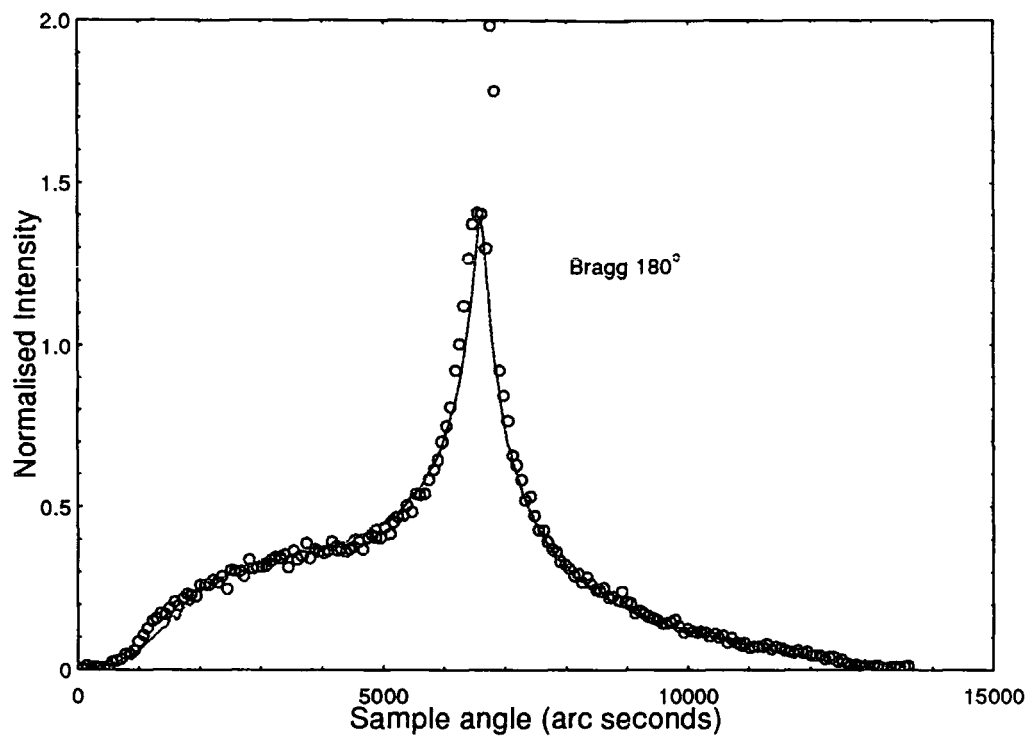
Fig 7.13c Transverse diffuse scan taken through the first order Bragg peak for 180 degrees rotation about the sample's surface normal
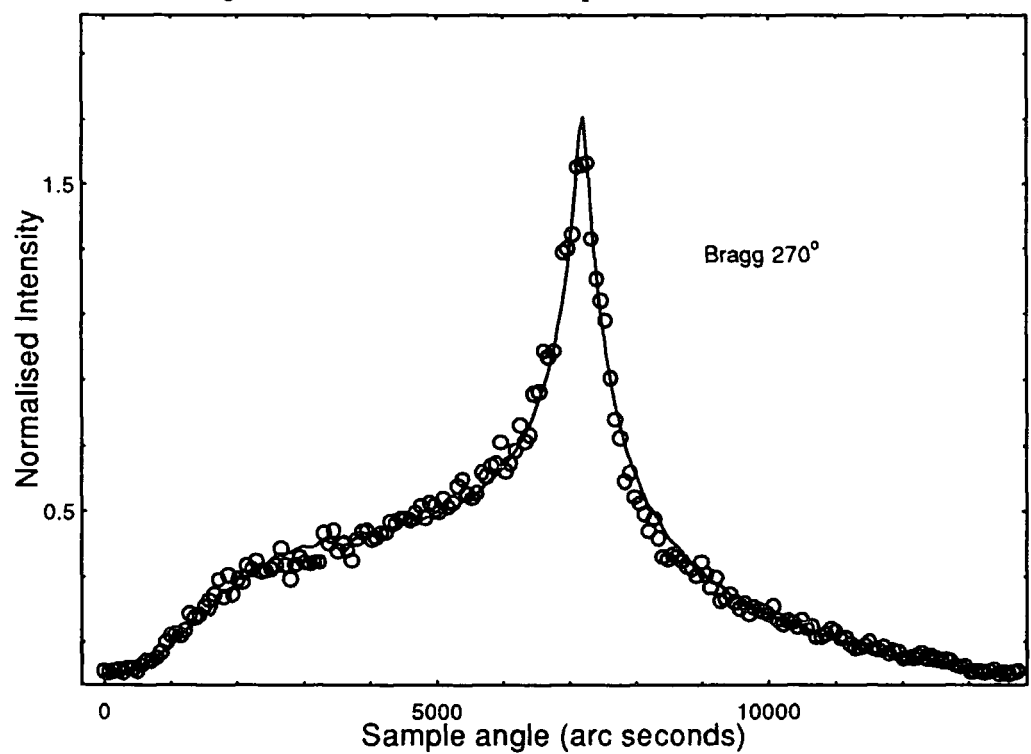
Fig 7.13d Transverse diffuse scan taken through the first order Bragg peak for 270 degrees rotation about the sample's surface normal
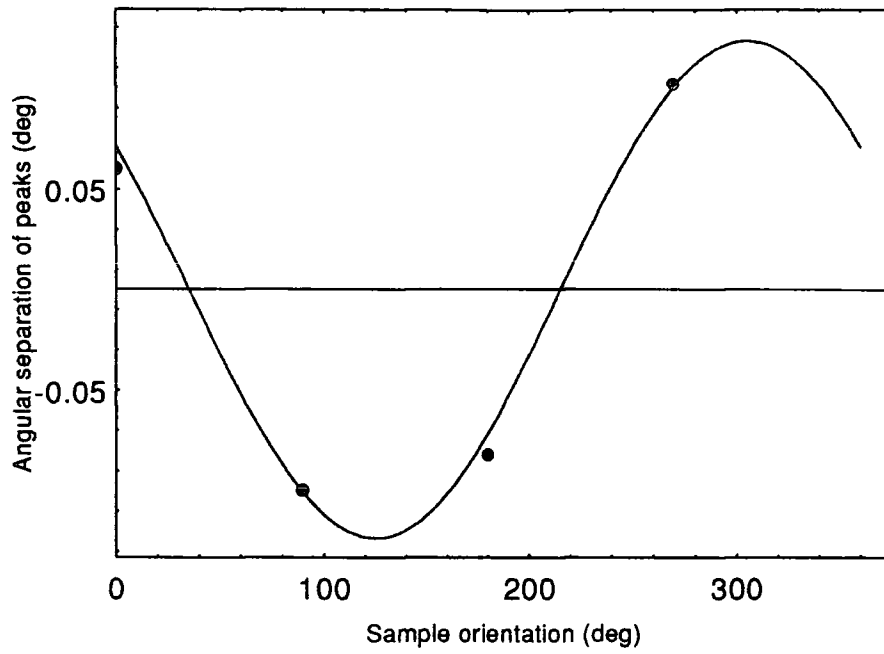
Fig 7.14 Separation of diffuse hump from specular peak as a function of sample rotation about it's surface normal
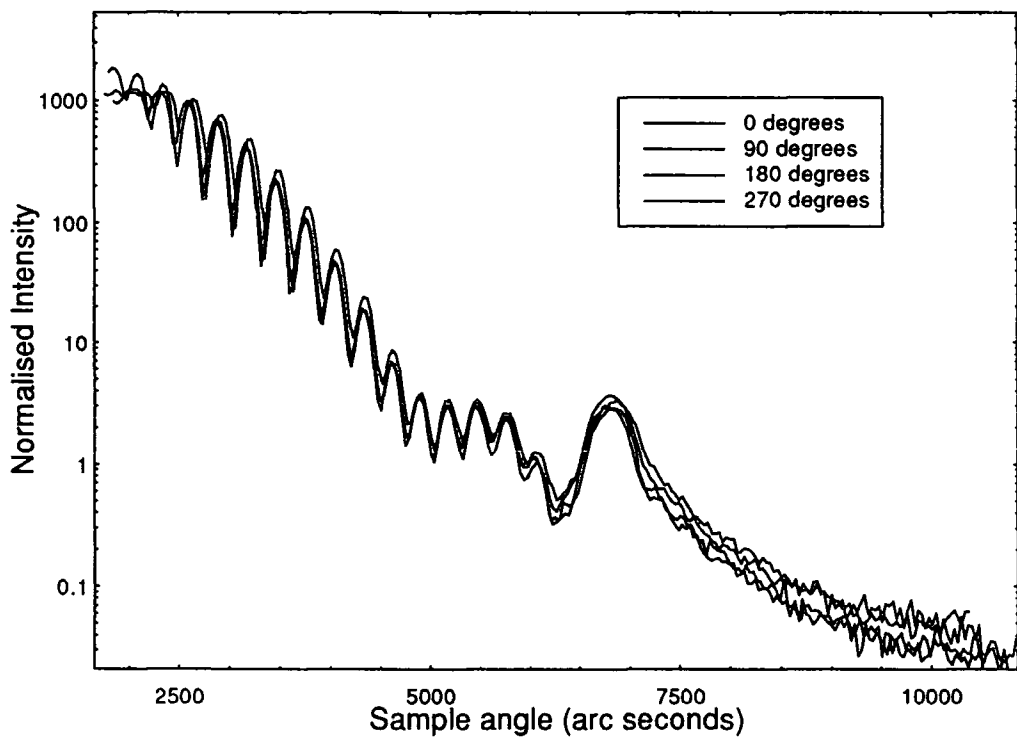
Fig 7.15 Variation of specular scatter as a function of sample rotation about it's surface normal

off cut, giving rise to regular terraces, cannot be the case here, or we would expect to see two humps either side of the specular peak, i.e. a diffraction grating [45].

On rotation about the surface normal, in contrast to the peak in the diffuse scatter, it is interesting to note that the Yoneda wings are not a function of sample angle (figure 7.16). As far as we are aware, this is not in the literature, but can be understood in the following way. The observed diffuse scatter intensity arises as an interference function of scattered x-rays, originating from roughness in the sample. As a result, if the roughness has a preferential direction, as in the case of terracing, this will be mirrored in the diffuse scatter. In contrast, the Yoneda wings arise as an increase in diffuse scatter at the critical angles, due to the matching of the waves across the interface. We have observed in other systems (sections 5.2 and 5.3), that the E-M waves in the system match across the average surface within their coherence length. Since the coherence length is very much greater than the terrace length the specular and Yoneda wings match across the average surface. As a result they are independent of the rotation of the sample about its surface normal. This lack of variation in the positions of the Yoneda wings and specular in the transverse diffuse scans was included by M. Wormington in the simulations through modification of the electric field vectors in the standard GIXS diffuse scatter code.

The simulations of the transverse diffuse scans taken through the Bragg peak as a function of sample rotation are also shown in figure 7.13. Fits were obtained to the data using the structure of the multilayer obtained from the specular scan. From the shape of the transverse diffuse scatter, fits could be obtained to the data for correlation lengths ranging from 300 to 1300 Å and corresponding fractal exponents of 0.5 to 0.2.

In order to increase the accuracy of the fits, more angles were simulated to try and obtain a consistent data set. Transverse diffuse scans taken through a Kiessig maximum and a Kiessig minimum are shown in figures 7.17 and 7.18 respectively along with their simulations. Increasing the number of transverse diffuse scans dramatically reduced the number of possible solutions to the data. In the main the lateral correlation length settled down to a value of 450Å ± 50Å and h remained
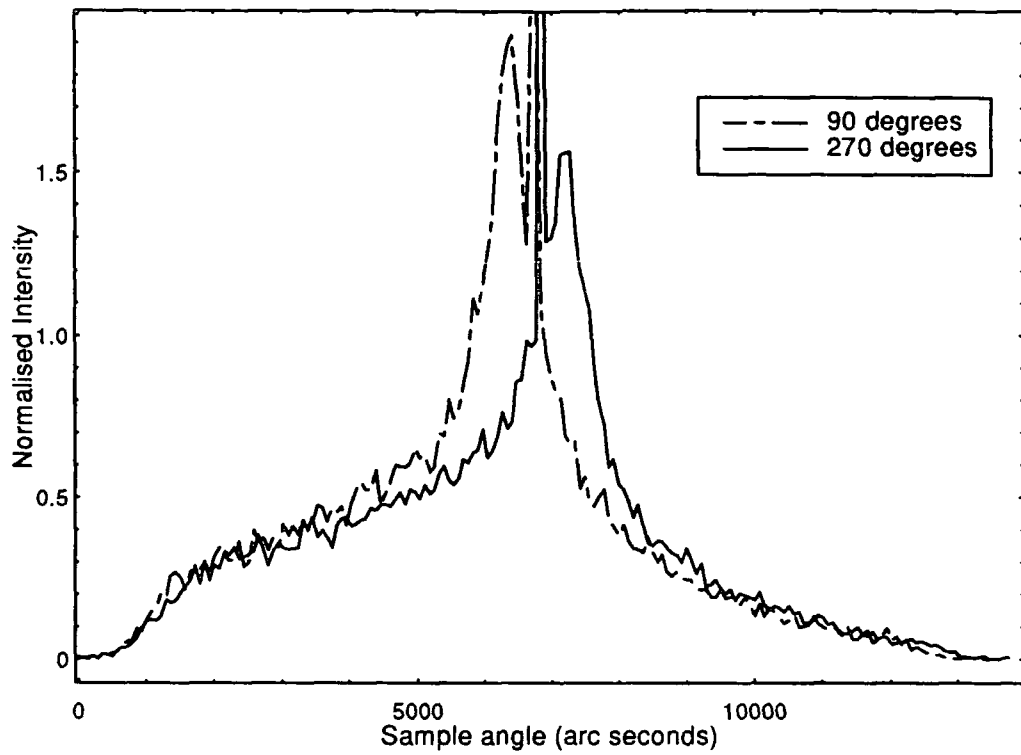
Fig 7.16 Variation of the diffuse scatter through the Bragg peak as a function of sample rotation about it's surface normal.
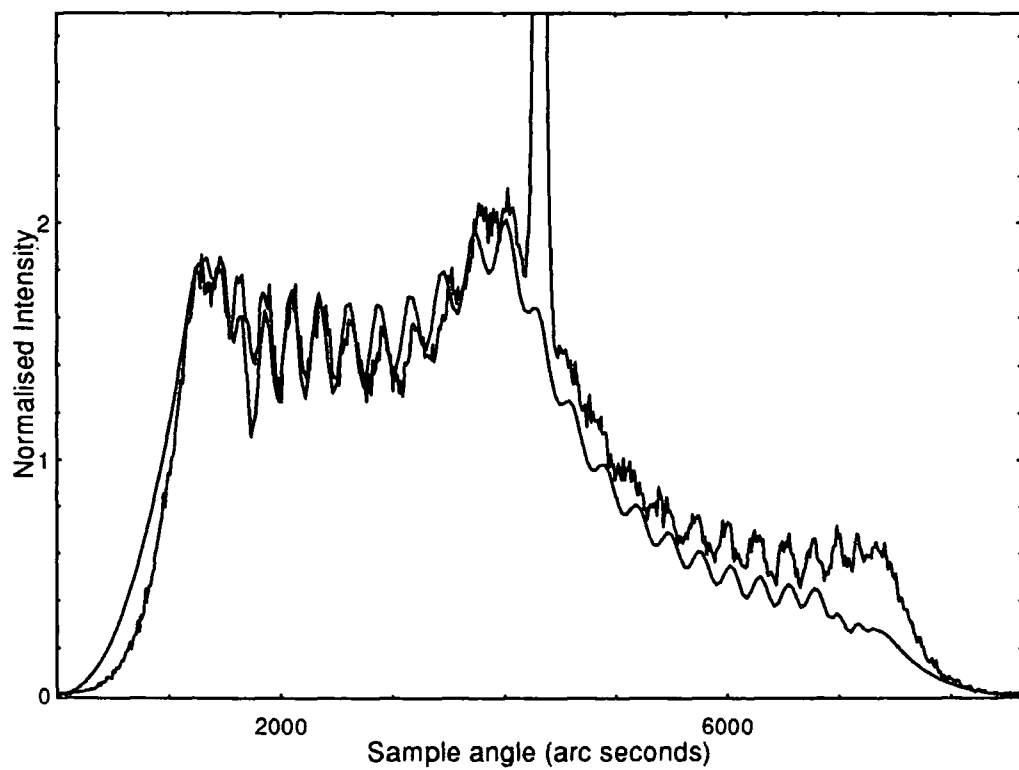
Fig 7.17 Transverse diffuse scan taken through a Kiessig maximum with the best fit simulation

constant at 0.28 ± 0.05. In all, a consistent data set was obtained over six simulations at wavelengths of 1.38Å and 1.48 Å.

To obtain a good fit to the diffuse scatter, it was necessary to assume that the ratio of correlated to uncorrelated roughness was 60:40. The top surface showed more correlated roughness, the ratio being 70:30. This increase in top surface correlation is clearly unphysical and may be related in some way to a failing of the model to describe the system exactly. This anomaly is discussed further in section 7.4.3. The ratio of correlated to uncorrelated roughness in the multilayer, determined from the amplitude of the Kiessig interference fringes and the Bragg peak in the off-specular, longitudinal scans (figure 7.19) is also in the ratio 60:40, in agreement with the fits to the transverse diffuse scan data.

7.4.3 Peculiarities with the simulations of the Cu/Co multilayers

There was one transverse diffuse scan which did not fit to exactly the same parameters. For the best matches, simulations of the Kiessig minimum required a correlation length of 250Å $\pm$ 25Å and a h of 0.28 ± 0.05. This was required in order to suppress the sharp peak in the diffuse scatter, which although lower than in the other transverse diffuse scans, was still present to some degree.

Although the fractal exponent was identical to that in the other scans, the lower correlation length was a matter for concern. In order to try to simplify the situation, simulations of a single Cu layer (on Si) of comparable thickness to the Cu/Co multilayer were performed. This layer was 600 Å thick and had 4 Å of roughness on its top and bottom surface with a correlation length of 1000 Å and a fractal exponent, h, of 0.5. Using these simulations it was found that a suppression of the peak in the Kiessig minimum could be obtained by increasing the degree of correlation between the top and bottom surface (figures 7.20 and 7.21). From the nature of reciprocal space, it would be expected that increasing the degree of correlation between the top and bottom surface would give rise to periodicities in the q_z direction, extending out as bars in q_y (section 3.2.22). However, it is not so obvious how the presence of a vertical spatial periodicity can affect the shape of the diffuse scatter in the q_y direction.
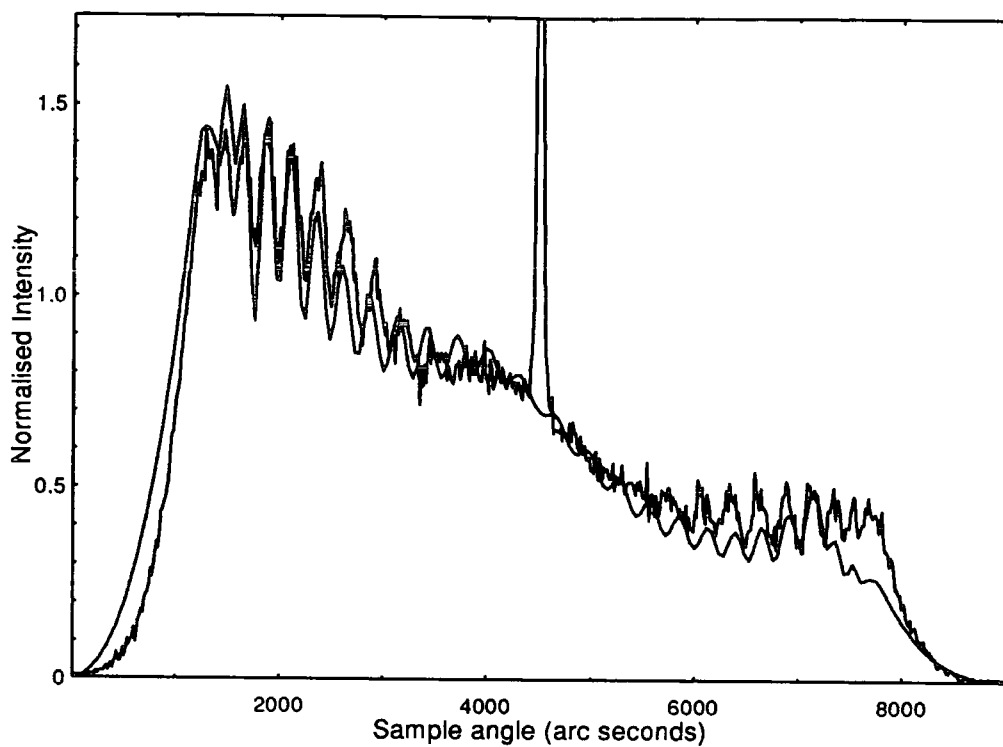
Fig 7.18 Transverse diffuse scan taken through a Kiessig minimum with the best fit simulation
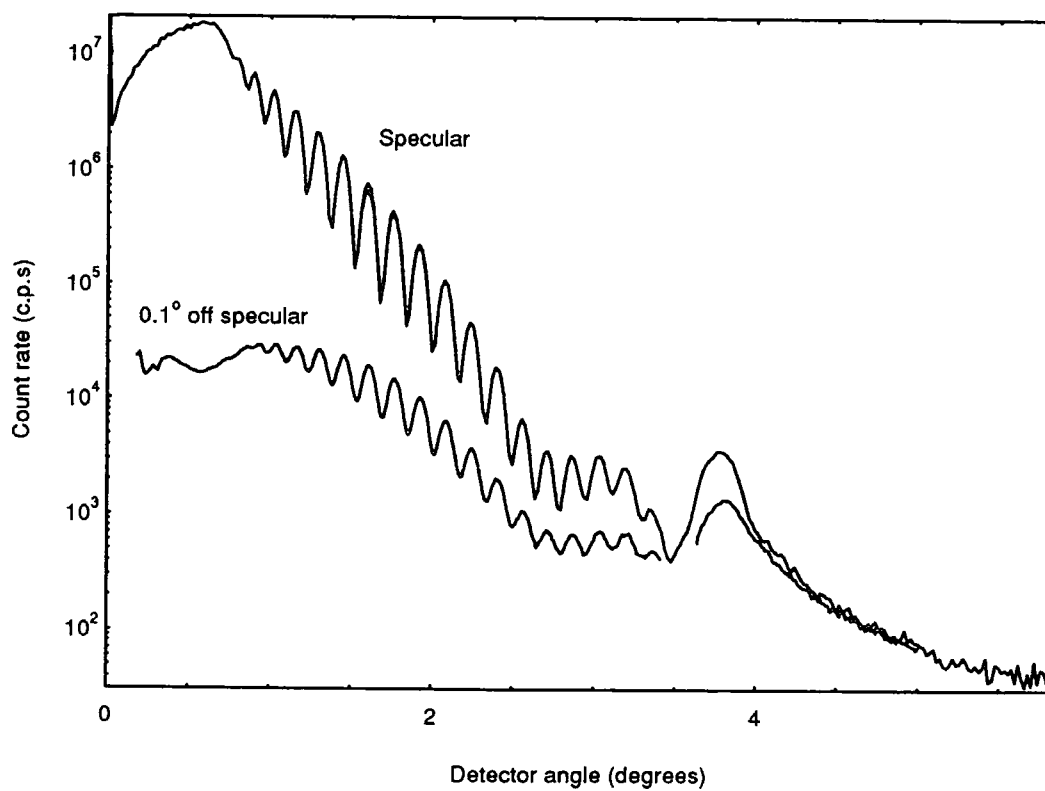
Fig 7.19   Comparison of specular and offspecular scatter taken from the silicide sample 311
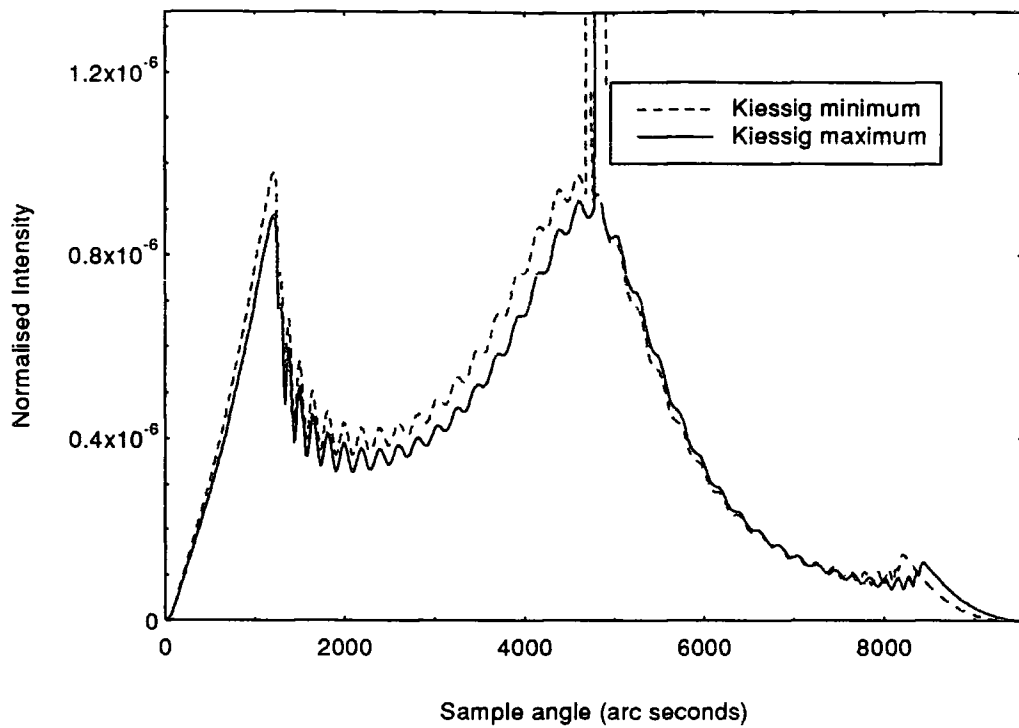
Fig 7.20   Comparison of transverse diffuse scans taken through a Kiessig maximum and minimum for a sample which contained solely uncorrelated roughness.
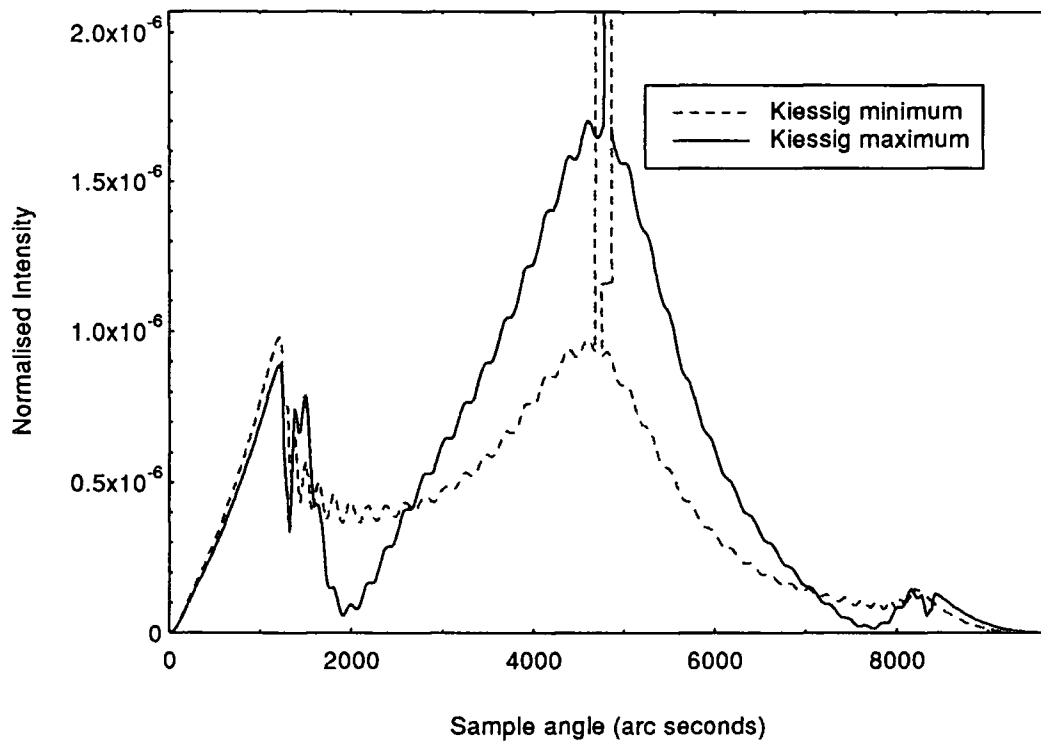
Fig 7.21   Comparison of transverse diffuse scans taken through a Kiessig maximum and minimum for a sample which contained solely correlated roughness.

The most likely cause for this variation of the diffuse scatter in q_y as a function of vertical correlation is from the allowed penetration depth of the x-rays. At the centre of the transverse diffuse scan, x-rays entering the material can easily reach the bottom surface. As a result, changes in the degree of correlation between the top and bottom surface lead to changes in the intensity of the diffuse scatter. In contrast, close to the Yoneda wings the penetration depth is limited, and the effect of vertical roughness correlations is negligible. This results in the diffuse scatter being dominated solely by the top surface, and as such it is a constant shape, unaffected by the correlations through the stack below. The effect of this is to confine the change in intensity due to variations in the correlated roughness to the centre of the transverse diffuse scan. As, a result, a change in its shape as a function of q_y is observed as the degree of conformal roughness is altered.

From the above arguments, it would appear that a fit to all scattering angles should be possible if the correct degree of surface to substrate roughness correlation could be found. However, in reality this solution was never attainable. In addition, as the rest of the stack required a correlation in the ratio 60:40, it is difficult to produce a physical explanation of how solely the correlation between the top and bottom surfaces could be increased. Such an increase in conformal roughness would also have produced fringes in the offspecular longitudinal diffuse scans which were too large. Thus, it would appear that another explanation may be required for the anomaly in the conformal roughness.

As mentioned previously, a second explanation that may reproduce the above findings is that of a limitation of our model. Within this it is assumed that when vertical correlations are present they extend equally over all frequencies of roughness defined within the correlation length. Thus, ignoring the optical effects of the Yoneda wings, all of the diffuse scatter in q_y is changed by the same amount on the introduction of vertical correlations in the roughness. However, in reality this is not always the case [31] and it may be expected that the shorter periods of roughness get washed out by the random deposition noise as they propagate vertically though the stack. As a result, the effect of vertical correlations would become less apparent for the higher q_y values which correspond to the shorter periods of surface roughness. The effect of

this would be to produce a rise in the centre of the transverse diffuse scan through the Kiessig maximum, in addition to that already produced by the optical penetration depth described above. Consequently, when this was modelled using our code it would give a longer correlation length than in reality. In contrast, at the Kiessig minimum, the centre of the transverse diffuse scan would be suppressed more than expected by our model and an underestimate of the correlation length would be produced. Such a type of correlation would then satisfactorily explain the observations in our simulated data. Unfortunately, the use of a separate correlation function for each layer would have increased our simulation time by two orders of magnitude; thus it was not possible on this sample.

A second peculiarity that existed in the data was a scaling factor of 1.5 (± 25%) which was required in all diffuse scans. This was not due to grading for two reasons. Firstly, if grading had been present, the predicted diffuse intensity would have been too high. In our case, it was too low, as if more roughness was required in the diffuse than was seen in the specular! Secondly, the effect of grading would be to cause a different scaling factor for each angle studied, which was not the case.

The final peculiarity in the data was that whilst Yoneda wings are present in the transverse diffuse scans taken around the Kiessig fringes; no clear Yoneda wings are visible at the Bragg peak. On reflection, this is hardly surprising, since the Yoneda wings arise due to the increase in scattering solely from the top surface; whereas the diffuse scatter through the Bragg peak is due to the regularly spaced layers below. As a result, the factor of four increase in intensity from the top surface is easily swamped by the order of magnitude increase in scatter arising from the 40 coherently scattering layers. Our simulations match very well this loss of Yoneda wings.

7.4.4 True diffuse scatter or a bent sample?

One other possibility may exist for the subsidiary peak next to the specular ridge other than diffuse scatter. If the sample surface possessed a 'tilt' on a length scale greater than the coherence length of the x-rays then a second specular ridge would be produced. If the sample were to be rotated about its surface normal, this extra peak would move sinusoidally around the main specular ridge, just as observed in the above data.

In order to resolve the question of whether the subsidiary peak was specular or diffuse in origin, detector only scans were employed. The effects of scatter arising from a figured (or bent) sample and genuine off centred diffuse scatter originating from a terraced multilayer is shown in figure 7.22. The motion of the detector only scan through reciprocal space for various (fixed) sample angles is shown by the dotted lines. If the extra peak were specular in origin, then it is obvious that its separation from the main specular ridge would increase as the sample angle was increased. However, if the scatter was due to terracing, then the separation of the two peaks would become closer.

When the experimental detector only scans are examined (figure 7.23), it is clear that the latter is the case. For scans taken at larger sample angles, the two peaks in the scan are moving closer together and finally coalesce when the detector is fixed at the sample's Bragg angle. In this way figuring can be ruled out and so the extra peak in the diffuse scatter must be interference generated, and as a result, from an asymmetry in the roughness profile, i.e. terracing.
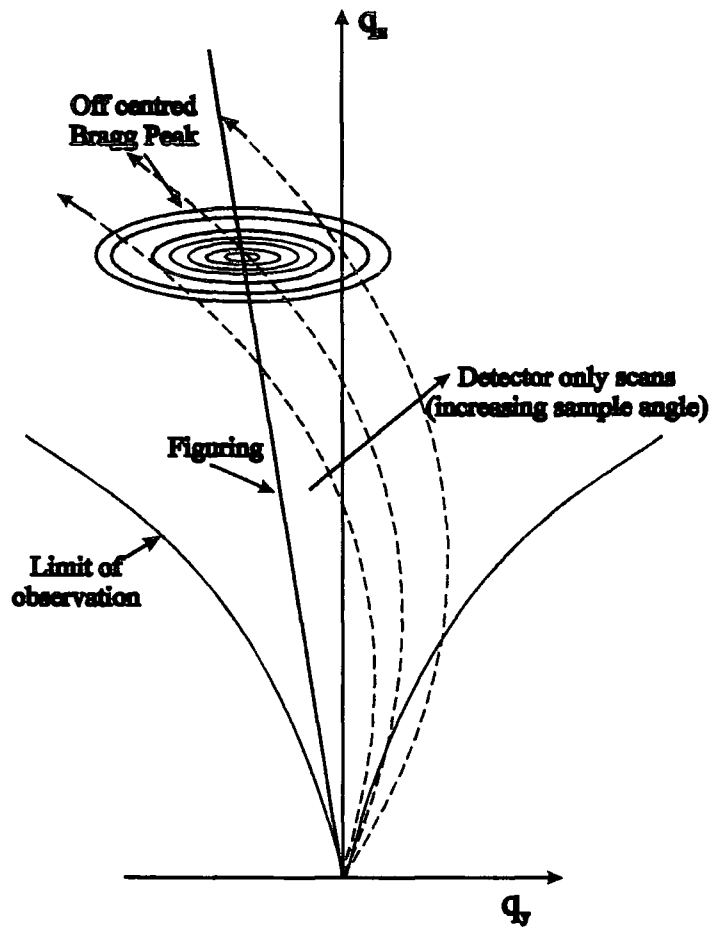
Fig 7.22 Figuring and off centred diffuse scatter displayed in reciprocal space
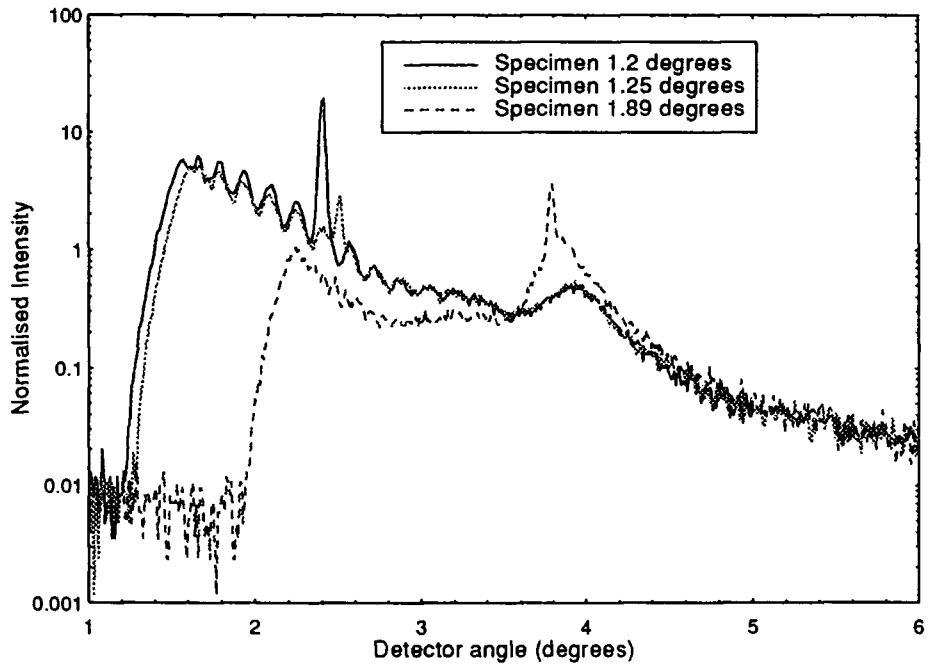
Fig 7.23 Experimental detector only scans taken for various (fixed) sample angles

7.4.5 Arguments for the use of self affine models in MBE systems

Self affine systems have been reviewed in sections 3.2.13 to 3.2.15 and we use the results to examine the applicability of the model to MBE systems in this section.

In growth systems, even simple ones, there are too many variables for every particle to be followed until it comes to rest. As a result, the details of the growth mechanisms are ignored and equations of the form

$$\frac{\partial h(x,t)}{\partial t} = G(h,x,t) + \eta(x,t) \qquad 7.3$$

used [46] to describe growing surfaces. $G(h,x,t)$ is a general function that depends on the interface height, position and time and $\eta(x,t)$ is a noise term.

Initially any term is allowed to exist within $G(h,x,t)$ to determine how the interface behaves and then successive symmetry arguments are used to exclude many of them. Out of these arguments, growth equations emerge, which although much simpler than reality, may capture the main processes which determine the scaling behaviour of systems (i.e. define the basic universality classes).

One such equation is the Edward Wilkins (EW) equation. This describes a random deposition process (ballistic rather than columnar), with surface relaxation. (i.e. slight lateral diffusion,$v\nabla^2 h$, a conservative process in terms of particles).

$$\frac{\partial h(x,t)}{\partial t} = v\nabla^2 h + \eta(x,t) \qquad 7.4$$

The Kardar-Parisi-Zhang (KPZ) equation is the similar to the EW equation except it has a built in a non linearity term, $(\lambda/2)(\nabla h)^2$, which allows irregularities on the surface to grow out laterally. This term is non conservative in terms of particles.

$$\frac{\partial h(x,t)}{\partial t} = \nu \nabla^2 h + \left(\frac{\lambda}{2}\right)(\nabla h)^2 + \eta(x,t) \qquad 7.5$$

Both equations show a distinct self affine scaling behaviour and from them two (of several) distinct Universality classes can be defined.

MBE itself is a thermally driven, non equilibrium system. It comprises many temperature dependent terms such as bond breaking (diffusion), the distance that an atom will travel before it sticks, and the number of sites that an atom must find before it is held securely [46-49]. In addition there are many crossovers in growth processes, which create great problems in determining the universality class to which MBE should belong. Despite all these problems surrounding the exact equation which governs the behaviour of MBE systems many researchers have found self affine type scaling properties of MBE grown surfaces [46,50,51].

A problem which comes out of growth studies concerns the 'Schwoebel barrier', a potential barrier which tends to deter atoms from jumping down a step edge [46] (figure 7.24). As a result any irregularities that develop on the surface, say due to a local disturbance in the deposition rate, can blow up to create large mounds. These mounds are not self affine in nature and dominate the surface profile. In consequence, the self affinity of the surface is destroyed. Experimentally these mounds have been observed in MBE systems [46,52,53]. However, at the present time, no-one knows on what time scales these structures develop and the MBE surfaces certainly appear to be self affine, in certain cases, if the time of growth is not extremely long.
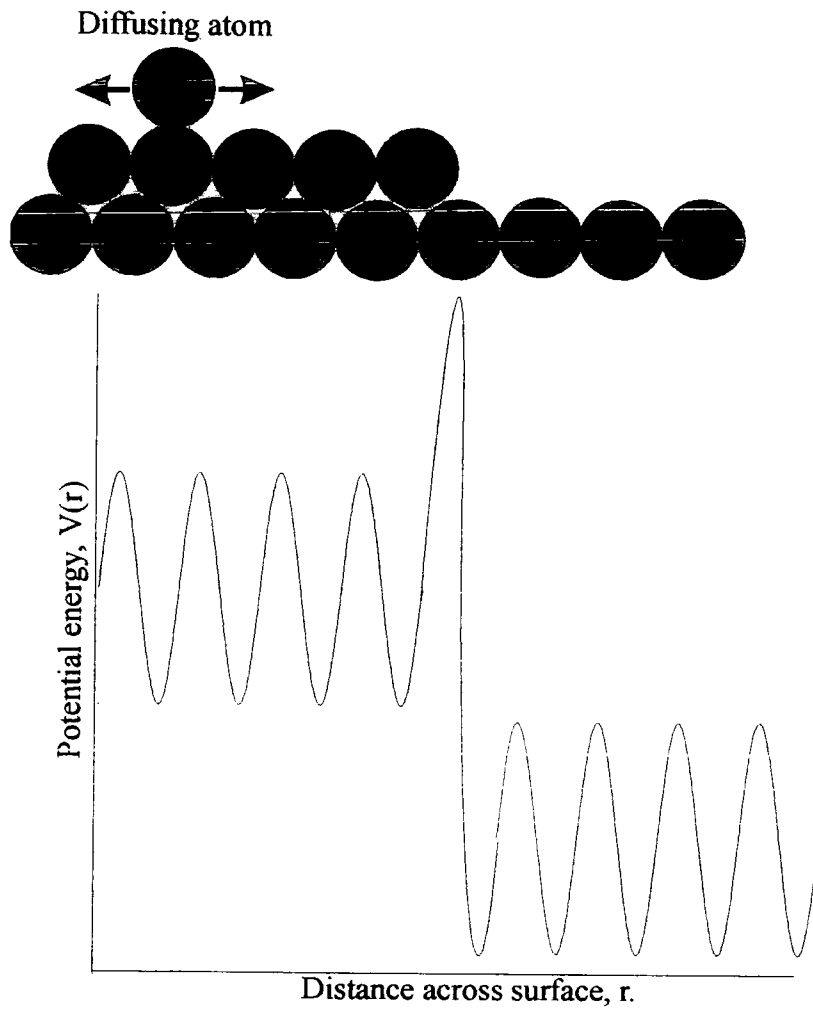
Fig 7.24   The effect of an atomic step on the movement of a diffusing atom
(Schwoebel barrier)

7.4.6 The limitation of the self affine description of a surface with regards to terracing and the proposal of a new model

In the past there have been several attempts to simulate terraced surfaces by using a fractal model [54,55]. However, in the last year or so, it has become widely believed that a terraced surface cannot be described by such a model [56,57], due to such a surface not scaling in a self-affine way. As a result, new models are being devised such as roof, terrace, and castallation models to account for these effect [56,57].

With regards to the Co/Cu multilayers grown on silicon, a simple off cut cannot be the case for two reasons. Firstly, the diffuse scatter is symmetric on rotation of the sample about its surface normal, and secondly, such a simple model would give rise to a diffraction grating effect [40].

The symmetry of the diffuse scatter strongly suggests that whatever is causing the offset from the specular peak, it is symmetric, about the surface normal [58]. In addition, the local tilts within this structure, must be at an angle to the average sample surface. This is required so that the diffuse peak is offset from the specular position. Furthermore, there can be no periodicities within this structure, since no grating effects are seen.

Simple islanding can be ruled out, since such a structure is seen to produce specular and offspecular interference fringes which are 180° out of phase [56,59]. However, islanding with randomly terraced walls, would give both the symmetry required and the offset. This type of structure is termed step-bunching. Unfortunately, such a system, like any other with complete symmetry about the surface normal, would be expected to give two symmetric diffuse humps; one from each side of the island. In order to compensate for this, the symmetry required must be relaxed to two directions only. Such a surface is shown in figure 7.25 a,b and is seen to explain satisfactorily the symmetry of the observed diffuse scatter.

An apparent anomaly is reached at this point. The above model is clearly not a self affine system, and yet such a model is seen to give a reasonable fit to the experimental
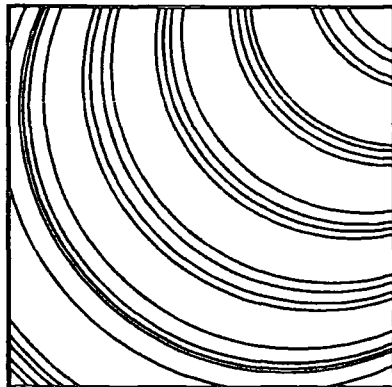
Fig 7.25a The type of step bunching required to give to observed symmetry in the diffuse scatter
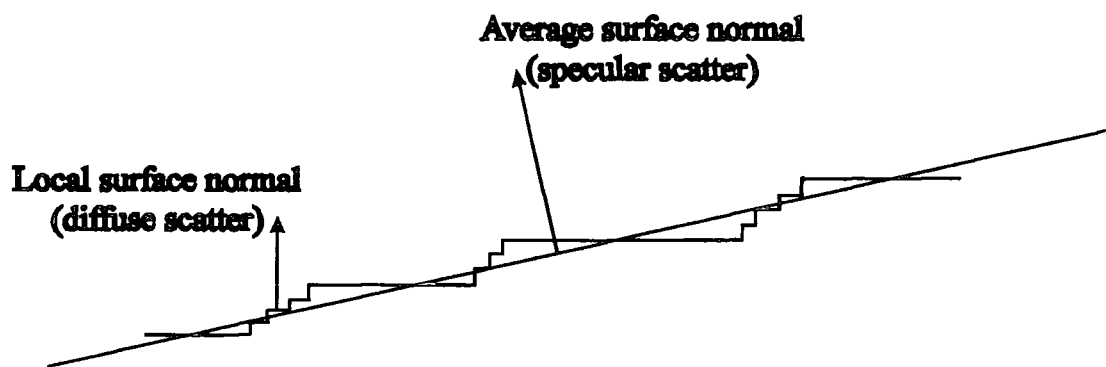
Fig 7.25b One dimensional cross section of the above steps showing large terraces separated by bunched steps.

data. To resolve this, consideration must be given to where the bulk of the diffuse scatter is arising. From figure 7.25b it is clear that the surface is most rough in the region of the step bunching. As a result, although it is clear that the macroscopic surface is not scaling in a self affine manner, it may be possible that on smaller length scales, within the bunches themselves, such scaling is present. Thus, the self affine model can provide a satisfactory fit to the observed diffuse scatter from certain microscopic regions on the sample if they are seen to dominate the diffuse scatter.

In order to confirm the actual morphology of the samples, it is clear that they must be examined also by other techniques such as TEM and AFM. An unfortunate consequence of the age of the present samples is that grease and dirt has accumulated on the surface. As a result, AFM measurements from MBE grown samples, have tended to reveal more about the growth exponent of grease than the initial MBE surface! Cleaning of the samples with IPA merely redistributed the grease and more energetic cleaning methods would have either changed the surface morphology or removed the layers entirely. Even if satisfactory cleaning could have been achieved, scanning probe measurements examine only the top (AuCu) surface and cannot be relied upon to provide information on the Cu/Co interface structure.

It must not be forgotten that whatever is causing this asymmetry is not confined solely to this sample, as was mentioned at the beginning of the chapter (figures 7.26). In order to investigate this further multilayers were grown on the same piece of Si(111). The critical difference between the samples was in some a copper silicide buffer was used, whilst in others it was cobalt silicide. From these data it was noted that the samples grown on copper silicide showed a much stronger asymmetry in their diffuse scatter. When the $\sin\theta$ roll off was corrected it was doubtful whether any preferential terracing was in existence within the cobalt silicide samples (figure 7.27 and 7.28). As a result, it may be inferred that it is the formation of the Cu_3Si buffer layer that has something to do with the initiation of this pseudo-terraced structure.

Finally, the question posed at the beginning of this section (section 7.3) was. 'Why is it that the Cu/Co multilayers grown on Si/Cu_3Si lie above the GMR vs correlated roughness line for multilayers grown on sapphire/Nb?' To give a possible answer to
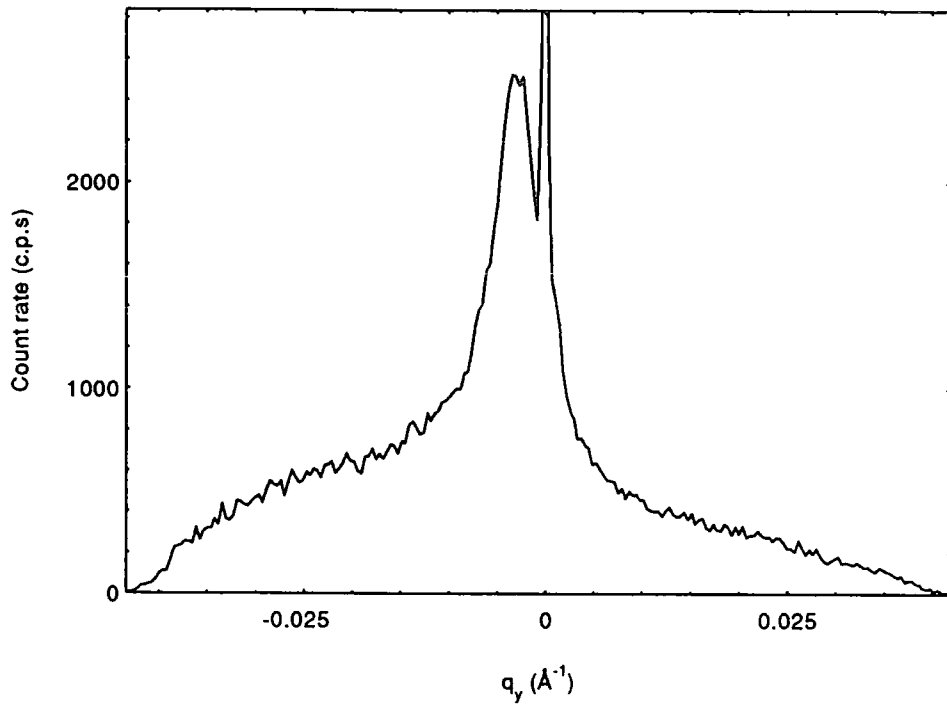
Fig 7.26 Transverse diffuse scan taken through the first order Bragg peak of a second
Cu/Co multilayer (287) grown on silicon with a Cu_3Si buffer.
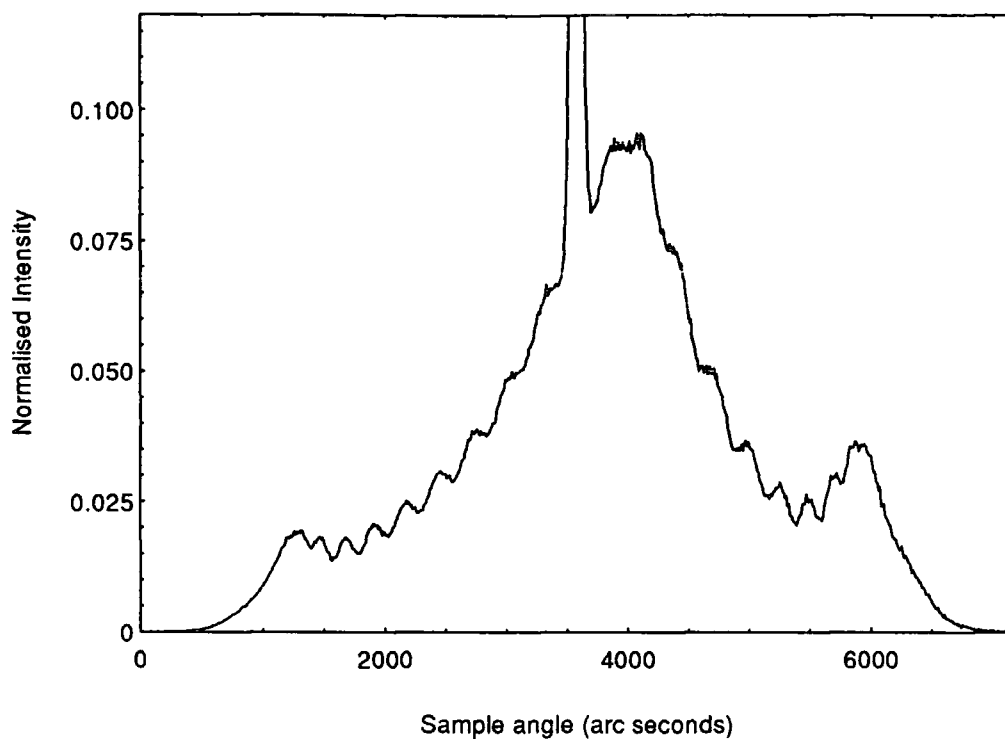
Fig 7.27   Transverse diffuse scan through a Kiessig maximum of a copper-cobalt
multilayer grown using a copper silicide buffer.   Scattering angle = 1.8 degrees
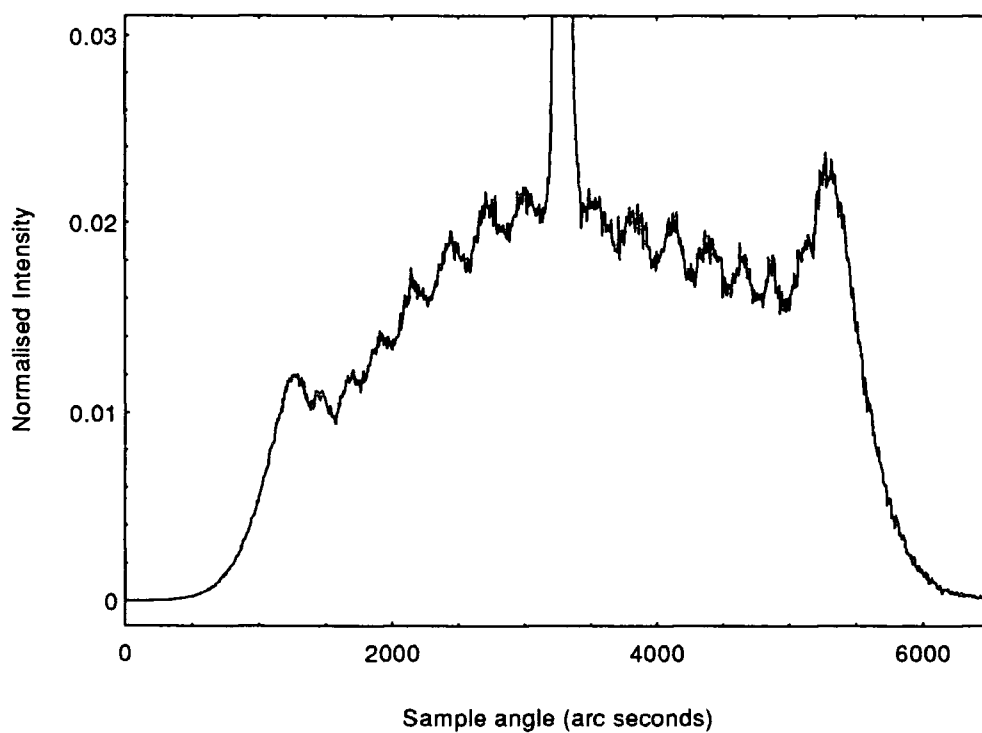
Fig 7.28   Transverse diffuse scan through a Kiessig maximum of a copper-cobalt
multilayer grown using a cobalt silicide buffer.   Scattering angle = 2.0 degrees

this question some other work on multilayers must be considered. From such work it is known that in growth, only the longest periods propagate vertically through the stack. This is due to the shorter periods being 'washed out' by random noise or lateral diffusion. Since the diffuse scatter arising from the silicon substrate multilayers is interference generated, then the shape of the diffuse scatter must still be linked to the length scales present on the surface. Taking the full width half maximum of the diffuse Bragg peak, it is found that this width in reciprocal space ($2x10^{-4}$ $Å^{-1}$) corresponds to a length scale on the sample of the order of $1x10^4$ Å. As the mean free path of the electrons in the medium is of the order of 100 Å, at 4.2K [60] then this means that the majority of the correlated roughness is not "seen" by them. However the x-rays, which have a coherence length on the order of $1x10^6$ Å, will see all this roughness. When it is noted that the other samples in the study had a much shorter correlation length, it may be assumed that the electrons interacted with much more of the roughness and so shifted the line with respect to the silicon substrate multilayers.

7.4.7 Summary

Grazing incidence x-ray scattering measurements have been performed on Cu/Co multilayers grown on silicon using a Cu_3Si buffer. Clearly evident in the diffuse scatter was an asymmetry, which processed sinusoidally around the specular ridge on rotation of the sample about it's surface normal. Excellent fits were obtained to the data for several scattering vectors, using a slight modification to the self affine model. This allowed the diffuse scatter to be offset from the average surface. The applicability of using a self affine surface to describe a terraced system was explained in terms of step bunching from which the majority of diffuse scatter would arise. As such bunches may be self affine in nature, it is possible that the observed diffuse scatter can be described by a self affine model even when the surface on the whole is not.

Chapter VIII

Conclusions

The conclusions drawn from this thesis can be split into two distinct categories. Within each chapter, grazing incidence x-ray scattering (GIXS) has been performed in order to characterise some structural feature of the samples under investigation. A summary of the results obtained can be found at the end of each study, and in consequence it is felt inappropriate to repeat these here. During the course of this work, many of the samples had structures far removed from ideal layers with nanometer scale roughness, as commonly required by GIXS. In consequence, a great deal of knowledge was gained about the limitations of the GIXS technique and the interpretation of the scatter arising from it.

Grazing incidence x-ray scattering measurements were performed in chapter 4 to characterise polished CVD layers deposited on float glass. From these measurements, it was noted that two sets of Yoneda wings were present in the transverse diffuse scans. These could not be simulated using any combination of roughness, or lateral correlation of the interfaces. In consequence, it was concluded that density patches existed on the surface, which were larger than the projected coherence length of the x-rays.

In chapter 5, GIXS measurements were performed on ceramic samples which had been polished for different times. From these data it was found that the surface density of the samples, as measured from the positions of the Yoneda wings, increased for longer polishing times. Bearing area measurements, which correspond to the fraction of the surface which has been transformed from rough pits to a smooth planar interface, were also performed using optical microscopy. When these were compared with the x-ray data, qualitative agreement was found between the two sets of results. In order to explain this agreement, it was concluded that the x-rays were probing an average surface density, and so the electromagnetic waves must be matching over the mean interface within their coherence length. Furthermore, from these measurements it was shown that useful

information could be extracted using GIXS from surfaces which were orders of magnitude rougher than could be simulated using the DWBA.

In chapter 7, grazing incidence x-ray scattering measurements were again employed for studying a Cu/Co multilayer grown on Si 111 using a Cu_3Si buffer layer. From this data it was noticed that an asymmetry was present in the diffuse scatter. This took the shape of a sharp peak, which processed sinusoidally around the specular on rotation of the sample about it's surface normal. In order to explain these observations, it was proposed that the interfaces within the multilayer were terraced in nature. When simulations of the data were obtained for several scattering vectors, with a single parameter set, the model of a terraced structure had to be reviewed. This was due to it being known that a periodic stepped surface could not be simulated using a self affine model. The revised model was one in which the majority of the diffuse scatter arose from regions in which step bunching had occurred. Such bunches were known to be self affine in nature and thus the resulting diffuse scatter could be described by the usual model.

The need for a vertical electron density gradient in some simulations was demonstrated when container glass and GaAs were studied in chapters 4 and 6 respectively. When simulations were performed, it was found that satisfactory scaling could only be obtained between the specular and diffuse scatter if such grading was included.

In general it can be concluded that GIXS is a very sensitive technique for the study of thin layer structures. The simulation of specular scatter alone is adequate for the determination of the thickness of layers, but is not able to give reliable roughness values due to the possibility of grading. In order to determine what fraction of the observed roughness in the specular scatter is 'real', diffuse simulations must be employed. From this data it is possible to determine both the lateral correlations of the roughness on an interface and the vertical correlations between interfaces. Unfortunately, diffuse simulations are more sensitive to geometrical factors within the experiment than specular scatter. Thus it is vital that the geometry of the reflectometer is well characterised and that the input intensity is known accurately. Even when all this is done, the simulation of

one scattering vector does not always give conclusively a unique solution. As a result, multiple scattering vectors must be simulated. This leads to a high degree of confidence in the simulation parameters but is very time consuming. For this reason, automated fitting is needed before this can become a viable analysis technique for use on the production line. Fortunately, such algorithms for 'auto fitting' are already under development.

In an attempt to produce a short cut in the determination of the interface roughness, the Born wave analysis technique, developed by Lagally, was investigated. It was found that the value of roughness deduced from the approximation increased quickly and saturated for larger scattering vectors. This was due to the Born wave approximation assuming that the diffuse scatter produced by all frequencies of roughness was being probed. However, due to the shadow of the sample edges, at the small scattering vectors only the shortest q_y values can be observed. As a result, much of the diffuse scatter arising from the higher frequencies of roughness is missed and the roughness deduced is an underestimate. In order to overcome this, calibration tables were calculated using the distorted wave Born approximation (DWBA). This gives a better description of the wavefields around the sample and also has the positions of the Yoneda wings built in. It can therefore predict the observed diffuse scatter for a range of scattering vectors.

The most successful applications of the Born wave analysis (BWA) was in chapter 4 when it was applied to layer free container glass. In this study, it was clear that the method developed by Lagally followed exactly that which was predicted from theory. Once corrected for the fraction of the diffuse scatter cut off by the sample edges, the BWA was seen to deduce a constant roughness for all scattering vectors probed. Simulations of the specular and several scattering vectors were found to give the same value of roughness within experimental error. As a result, it was shown that for layer free samples, the combination of the BWA and look-up tables was orders of magnitude faster than standard simulations.

The applicability of the BWA to samples which possessed a single layer was investigated in chapter 6. In this chapter, the diffuse scatter arising from a single layer on a GaAs substrate was calculated using the DWBA. The roughness used in these simulations was assumed to be totally uncorrelated and therefore, unlike the fringes in the specular scatter, the diffuse scatter displayed no modulations in intensity as a function of scattering vector. This discrepancy between the intensity of the specular and diffuse scatter then affected the equation derived by Lagally for deducing the amount of roughness within the samples. Thus the value of roughness deduced was seen to oscillate in phase with the fringes in the specular scatter.

The application of the BWA technique to real samples containing a single layer was assessed when diffuse scatter measurements were performed on PA polished GaAs. From these measurements, experimental evidence was provided for the oscillations induced in the deduced roughness due to fringes in the specular scatter. To calculate the roughness of the sample, the usual method of look-up tables was not employed. Instead a method of curve fitting was used between the deduced roughness from the experimental diffuse scatter and that from a DWBA simulation. In this, the roughness given by the BWA from the diffuse scatter in a real experiment was plotted as a function of scattering vector and compared with that from a DWBA simulation. The roughness value in the simulation was changed until the two deduced roughness curves fitted over the whole scattering vector range. At this point, the roughness required in the simulations was equal to the roughness on the surface of the sample.

When specular and diffuse simulations were performed on the PA polished sample, it was found that the best fits gave a roughness of 6 Å and 12 Å ± 1.5 Å for the top and bottom surfaces respectively. Born wave analysis of the sample gave a roughness value of 8 Å which was approximately the average roughness of the two interfaces. Further studies using simulated diffuse scatter from other materials revealed that as the layer was thickened, the value of roughness deduced from the Born wave analysis tended to that of the top surface. This introduced an uncertainty into the values of roughness deduced by this method. In consequence it was concluded that although the average value of

interfacial roughness had been correctly deduced in the case of the PA polished sample, in general it may not be the case. When this was combined with the time taken to perform the curve fitting on the results of the Born wave analysis, it was felt that little was gained for single layers as compared to standard diffuse scatter simulations.

Extensions of the technique to multilayers was performed in chapter 7. Here, the method of calculating the correlated and uncorrelated component of roughness within the multilayer, introduced by Lagally, was employed. The use of synchrotron radiation allowed the wavelength to be tuned to excite anomalous dispersion and highlight the scatter from buried interfaces. In this instance it was clear that the diffuse scatter was being observed from the buried interfaces due to the presence of a diffuse Bragg peak. From these data, it was found that trends could be observed in the interfacial roughness as a function of annealing temperature, so long as the lateral correlation length remained approximately the same. In addition, it was shown that the effect of Kiessig fringes on the deduced roughness could be neglected if the diffuse scans were taken at the position half way between a Kiessig maximum and minimum. Using standard simulation techniques of the specular and diffuse scatter, the time taken to extract the trends in the interface roughness in the five multilayers would have taken days. As a result, the fact that the BWA gave trends in minutes can be interpreted as a success and a good indication that the technique is well suited for studying multilayers.

In this thesis many materials have been studied using the technique of GIXS. As most of these were in some way too challenging for routine analysis, a great amount has been learnt about the interpretation of the scattered intensity. However, in numerous cases, further work is needed before complete characterisation of the samples or the processes is possible. This ranges from a repeat of the same measurements on different samples, to the inclusion of results from a different technique in order to further the simulations of the x-ray data. In order to give a flavour of what extensions to the present work is planned, the most interesting areas are dealt with in the following chapter.

Chapter IX

Further work

Further work on the float glass samples could include the identification of the surface layer. If this layer was due to the adsorption of water, then heating the sample to $150^{\circ}C$, using a heated sample stage, would drive it off. Elemental analysis of the surface layer could be performed using x-ray photoelectron spectroscopy (XPS). This would require fresh samples to be cut by Pilkingtons to a size of 5mm square. In addition, the samples would have to be transported without any carbonaceous material touching the surface, as this would bias the results.

In chapter 4, it was believed that the SnO_2 layer consisted of density patches greater than the coherence length of the x-rays. Simulations of the transverse diffuse scans could have been performed by calculating the diffuse scatter produced from the separate density regions. These would have been weighted by the fraction of the surface they occupied and added together kinematically. An unfortunate drawback with this method was that it was not known in what ratio the two regions of density were present on the surface. Attempts to perform EDAX (energy dispersive analysis of x-rays) measurements on the samples were hampered, when it was found that it was not possible to cut them to the correct size without serious damage. Thus further work should be carried out on freshly prepared samples, cut to 1 cm square before the deposition of the layers. A repeat of the specular and diffuse measurements should be made, and EDAX measurements performed so that good diffuse simulations can be obtained.

The most interesting extension of the study of GaAs (chapter 6) would be to see if similar variations in the surface and crystal structure could be detected in silicon. This is used much more widely in the electronics industry and would therefore produce a much greater amount of interest. However, the higher crystalline quality of silicon would mean that the variations in the diffraction peak widths would be significantly smaller. Thus it would be correspondingly more difficult to deconvolute the instrument function of the

diffractometer. In order to overcome this, 224 grazing exit reflections could be performed to increase the natural width of the rocking curve.

Grazing incidence x-ray scattering (GIXS) measurements performed on these samples would also be difficult, due to the high surface finish of the crystals. Typically, the surface roughness of silicon is one angstrom and so very little diffuse scatter is produced. This is especially significant, as only measurements made on a laboratory source would be of use in the electronics industry. A factor of five increase in intensity on the GXR1 could be obtained, by replacing the monochromating crystal with one cut to select Cu K_α. Another factor of two could be obtained by running the tube to its limit, whilst the background could be kept low by including a second set of slits, placed in front of those shielding the detector. These would be set to reduce the line of slight of the detector to exclude everything but that arising from the sample. With these changes, a signal to noise of 10 million may be possible.

When studying the ceramics (chapter 5), an interesting area only just touched on was the effect of wear on the surface quality. Preliminary measurements have shown that after long periods of use, a specular peak is observed in the x-ray scatter. This would suggest that the surface, or at least regions of it are rough on the scale of tens of angstroms. It may be possible that this is a contributing factor to the increase in stiffness observed towards the end of a tap plate's useful life. Secondly, it would be useful to repeat the surface density measurements on the ceramic samples as a function of polishing time, for different degrees of lapping. In this way, it may be possible to optimise the total time of the process, by tuning the separate machining operations. Finally, on the subject of ceramics, it is vitally important that the techniques of x-ray reflectivity, optical microscopy and surface acoustic waves are used in conjunction with one another. These give complementary information on the surface and near surface of the samples, which is vital in the interpretation and modelling of the structure.

Further work is needed on the Cu/Co multilayers, grown on silicon using a Cu_3Si buffer layer, to investigate the exact nature of the terracing within the samples (chapter 7). One

method to do this would be to perform transmission electron microscopy (TEM). Using this technique it may be possible to image the step bunches, which we believe are responsible for the observed asymmetry in the diffuse scatter. It is noted that the TEM technique has a limited ability to image very large length scales. In consequence, many separate photographs may be required to show conclusively that step bunching is occurring. Finally, it would be interesting to see if the correlation between conformal roughness and the measured GMR is valid in other systems apart from Cu/Co. At the moment work is beginning to shift to Fe/Au samples which may be able to show whether this trend can be generalised or not.

Bibliography : Chapter I

1   Feidenhans'l, R., Surface Science Reports, **10**, 105 (1989)

2   Renaud, G., HERCULES, J. Baruchel, Editor. 1995, Springer-Verlag : London. A14

3   Hinder, A.B., Thin Solid Films, **77**, 272 (1981)

4   Laidler, H., J. Mag. Mag. Mat., **154(2)**, 165, (1996)

5   Morgan Matroc, Tap plate wear tests, work in progress (1997)

6   Fert, A., Physics World, p34 Nov (1994)

7   Analysis of Microelectronic Materials and Devices, M. Grasserbauer, Editor. 1991, John Wiley & Sons : Chichester.

8   Authier, A., X-ray and Neutron Dynamical Diffraction, Tanner, B.K. Editor. 1997, Plenum Press : New York and London, p 1.

9   Colella, R., X-ray and Neutron Dynamical Diffraction, Tanner, B.K. Editor. 1997, Plenum Press : New York and London, p 323.

10   Robinson, I.K., Phys. Rev. B, **33(6)**, 3830 (1986)

11   Lucas, C.A., J. Appl. Phys., **63(6)**, 1936 (1988)

12   Fewster, P., X-ray and Neutron Dynamical Diffraction, Tanner, B.K. Editor. 1997, Plenum Press : New York and London, p 269.

13   Etgens, V.H., Phys. Rev. B, **47(16)**, 10607 (1993)

14   Moore, C.D., Il Nuovo Cimento (in press)

15   Ryan, T.W., Semicond. Sci. Technol, **2**, 241 (1987)

16   Marra, W.C., J. Appl. Phys. **50(11)**, 6927 (1979)

17   Marra, W.C., Phys. Rev. B, **46(16)**, 1081 (1981)

18   Hect, E., Optics, B. Spatz, Editor.1987, Addison-Wesley : Wokingham

19   De Boer, D.K.G., X-ray Spectrometry, **24**, 91 (1995)

20   Sinha, S.K., ACTA Physica Polonica A, **89(2)**, 219 (1996)

21   Vineyard, G.H., Phys. Rev. B., **26(8)**, 4146 (1982)

22   Sinha, S.K., Physica B, **173**, 25 (1991)

23   Sinha, S.K., Physica B, **174**, 499 (1991)

24   Waseda, Y., Lecture Notes in Physics, Araki, H, Editor. 1984, Springer-Verlag : Berlin.

25   Joyce, D.E., Work in progress (1997)

26   Holy, V., J. Phys. D, **28**, A220 (1995)

Bibliography : Chapter II

1   Collins S.P., Rev. Sci. Inst. **63**(1), 1013 (1992)

2   Cernik R.J., J. Appl. Cryst. **23**, 292 (1990)

3   Cernik R.J., Nuclear Instruments and methods, **A281**, 403 (1989)

4   Raoux, D., HERCULES, Baruchel, J., Editor. 1996, Springer-Verlag : London.

5   Cockerton S., Adv. X-ray Anal. **38**, 371 (1995)

6   Waseda, Y., Lecture Notes in Physics, Araki, H, Editor. 1984, Springer-Verlag : Berlin.

7   Hudson J.M., Thesis, University of Durham (1994)

8   Loxley, N., Adv. X-ray Anal. **38**, 361 (1995)

9   Freund, A., HERCULES, Baruchel, J., Editor. 1995, Springer-Verlag : London. p79.

10   Tanner, B.K., X-ray Diffraction Topography, Pamplin, B., Editor. 1976, Pergamon Press : Oxford.

11   Miltat, J., Characterization of Crystal Growth Defects by X-ray Methods, Tanner, B.K., Editor. 1979, Plenum Press : New York.

12   Loxley, N., Adv. X-ray Anal. **37**, 145 (1994)

Bibliography : Chapter III

1   Kittel, C., Introduction to Solid State Physics, 6th Edition. 1986, John Wiley & Sons : Chichester.

2   Authier, A., X-ray and Neutron Dynamical Diffraction, Tanner, B.K. Editor. 1997, Plenum Press : New York and London, p 1.

3   Tanner, B.K., X-ray Diffraction Topography, Pamplin, B., Editor. 1976, Pergamon Press : Oxford.

4   Kreyszig, E., Advanced Engineering Mathematics, 6th Edition. 1988, John Wiley & Sons : USA.

5   Tanner, B.K., Journal of Crystal Growth **126**, 1 (1993)

6   Fewster, P., X-ray and Neutron Dynamical Diffraction, Tanner, B.K. Editor. 1997, Plenum Press : New York and London, p269.

7   Robinson, I.K., Phys. Rev. B, **33(6)**, 3830 (1986)

8   Feidenhans'l, R., Surface Science Reports, **10**, 105 (1989)

9   Renaud, G., HERCULES, J. Baruchel, Editor. 1995, Springer-Verlag : London. A14

10   Marra, W.C., J. Appl. Phys. **50(11)**, 6927 (1979)

11   Marra, W.C., Phys. Rev. B, **46(16)**, 1081 (1981)

12   Hect, E., Optics, B. Spatz, Editor.1987, Addison-Wesley : Wokingham

13   Vineyard, G.H., Phys. Rev. B, 26(8), 4146 (1982)

14   Dosch, H., Phys. Rev. lett., 56(11), 1144 (1986)

15   DeBohr, D.K.G., X-ray Spectrometry, **24**, 91 (1995)

16   Sinha, S.K., Acta Physica Polonica A, **89(2)**, 219 (1996)

17   Parratt, L.G., Phys. Rev., **95(2)** 359 (1954)

18   Yoneda, Y., Phys. Rev., **131(5)**, 2010 (1963)

19   Sinha, S.K., Phys. Rev. B., **38(4)**, 2297 (1988)

20   Cernik, R.J., J. Appl. Cryt., **23**, 292 (1990)

21   Savage, D.E., J. Appl. Phys., **69(3)**, 1411 (1991)

22   Savage, D.E., J. Appl. Phys., **71(7)**, 3283 (1992)

23   Phang, Y.H., Appl. Phys. Lett., **60(24)**, 2986 (1992)

24   Phang, Y.H., J. Appl. Phys. **72(10)**, 4627 (1992)

25   Phang, Y.H., J. Appl. Phys. **74(5)**, 3181 (1993)

26   Savage, D.E., J. Appl. Phys. 74(10), 6158 (1993)

27   Garoff, S, J. Chem. Phys. **90(12)**, 7505 (1989) refs therein

28   Holy, V., Phys. Rev. B., **47(23)**, 15896 (1993)

29   Kopecky, M., J. Appl. Phys. 77(6), 2380 (1995)

30   Holy, V., Phys. Rev. B., **49(15)**, 10668 (1994)

31   Holy, V., Appl. Phys. A., **60**, 93 (1995)

32   Holy, V., Physica B, **198**, 249 (1994)

33   Kaganer, V.M., Phys. Rev. B., **52(23)**, 16369 (1995)

34   Metzger, T.H., Appl. Phys. Lett., **61(8)**, 904 (1992)

35   Zheludeva, S.I., Rev. Sci. Instr., **63(1)**, 1 (1992)

36   Palasantzas, G., Phys. Rev. B., **48(5)**, 2873 (1993)

37   Palasantzas, G., Phys. Rev. B., **48(19)**, 14472 (1993)

38   Palasantzas, G., Phys. Rev. B., **49**(15), 10544 (1994)

39   Barabasi, A.L., Fractal concepts is surface growth, Cambridge University Press, 1995.

40   Stommer, R., J. Phys. D., **28** A216 (1995)

41   Holy, V., Proceedings of X-Top'96, Palermo, Italy, Il nuovo cimento-D (in press).

42   Rauscher, M., Phys. Rev. B., **52(23)**, 16855 (1995)

43   Salditt, T., Phys. Rev. Lett., **73(16)**, 2228 (1994)

44   Salditt, T., Mat. Res. Soc. Symp. Proc., **355**, 269 (1995)

45   Salditt, T., J. Phys. D., **28**, A236 (1995)

46   Salditt, T., Phys. Rev. B., 51(9), 5617 (1995)

47   Holy, V., X-ray and Neutron Dynamical Diffraction, Tanner, B.K. Editor. 1997, Plenum Press : New York and London, p33.

48   Salditt, T., Z. Phys. B., **96**, 227 (1994)

49   Grubel, G., ESRF Newsletter Report number 2 (1994)

50   Lorrain, P., Electromagnetic Fields and Waves, 3rd Edition. 1988, W.H. Freeman and Company : New York.

51   Lengler, B., Photoemission and Absorption Spectroscopy of Solids and Interfaces with Synchrotron Radiation, M. Campagna, Editor. 1990, North Holland.

52   Wormington, M., Mat. Res. Soc. Symp. Proc. **238**, 119 (1992)

53   Tanner, B.K., IEEE Transactions on Magnetics., **28(5)**, 273 (1992)

54   Als-Nielsen, J., HERCULES, Baruchel, J., Editor. 1996, Springer-Verlag : London. Vol. 1, p. 28

55   Eisberg, R., Quantum Physics, 2nd Edition. 1985, John Wiley & Sons, Inc. : USA

56   Wormington, M., Private Communications. (1995)

57   Stanglmeier, F., Acta Cryst., **A48**, 626 (1992)

58   Lengeler, B., Phys. Rev. B., **46(12)**, 7953 (1992)

59   Gibaud, A., Phys. Rev. Lett., **74(16)**, 3205 (1995)

60   Palasantzas, Y.P., Phys. Rev. B., **49(7)**, 4902 (1994)

61   Lengler, B., Phys. Rev. B., **46(12)**, 7953 (1992)

62   Wormington, M., Phil. Mag. Letts **74**, 211 (1996)

Bibliography : Chapter IV

1   Pilkington, L.A.B., Proc. Roy. Soc. Lond. **A 314**, 1 (1969)

2   Edge, C.K., Ceramic Bulletin, **71(6)**, 936 (1992)

3   Callister, W.D., Materials Science and Engineering, 3rd Edition. 1994, John Wiley & Sons, Chichester.

4   Stella, A., Mikrochim. ACTA. **114/115**, 475 (1994)

5   Verita, M., 16th International Congress on Glass, Madrid, 31-C, Vol. 6,1992.

6   Kuban, B., 16th International Congress on Glass, Madrid, 31-C, Vol. 6,1992.

7   Sieger, J.S., J. of Non-Crystalline solids **19** 213 (1975)

8   Pantano, C.G., Fundamentals of Glass Science and Technology - ESG 1993, Venice.

9   Bettley, W., Glass Technology **35(5)**, 193 (1994)

10   Savage, D.E., J. Appl. Phys. **69(3)**, 1411 (1991)

11   Lengler, B., J. Appl. Phys. **75(2)**, 785 (1994)

12   Wormington, M., Phil. Mag. Letts **74**, 211 (1996)

13   Hinder, A.B., Thin Solid Films **77**, 272 (1981)

14   Wulff, H., Surface and Interface Analysis **23**, 148 (1995)

15   Wormington, M., Mat. Res. Soc. Symp. Proc. **238**, 119 (1992)

16   Sinha, S.K., Phys. Rev. B. **38(4)**, 2297 (1988)

17   Salditt, T., Phys. Rev. B., **51(9)**, 5617 (1995)

Bibliography : Chapter V

1   Callister, W.D., Materials Science and Engineering, 3rd Edition. 1994, John Wiley & Sons, Chichester.

2   Pilkington, L.A.B., Proc. Roy. Soc. Lond. A. **314**, 1, (1969)

3   Salditt, T., Z. Phys. B., **96**, 227 (1994)

4   Hect, E., Optics, B. Spatz, Editor.1987, Addison-Wesley : Wokingham

Bibliography : Chapter VI

1   Semiconductiors and Semimetals, Willardson R.K., Editor. 1984, Academic Press, Inc., London. Vol. 20.

2   Hudson J.M., Thesis, University of Durham (1994)

3   D3 Application notes, Bede Scientific Instruments Ltd.

4   Robinson, I.K., Phys. Rev. B, **33(6)**, 3830 (1986)

5   Logitech Ltd., IIIV's Review, **7(2)**, 21 (1994)

6   Wormington, M., Phil. Mag. Letts **74**, 211 (1996)

7   Moore, C.D., Il Nuovo Cimento (in press)

8   Savage, D.E., J. Appl. Phys., **69(3)**, 1411 (1991)

Bibliography : Chapter VII

1   Smits, J., Physics world, Nov. p48 (1992)

2   Awschalom, D., Physics world, Sep. p31 (1993)

3   Daughton, J., I.E.E.E., **29**, 6, 2705 (1993)

4   Barthelemy, A., Physics world, Nov. p34 (1994)

5   Rodgers, P., New scientist, Feb. p34 (1996)

6   Grunberg, P., Phys. Rev. B. **39(7)**, 4828 (1989)

7   Baibich, M.N., Phys. Rev. Lett., **61(21)**, 2472 (1988)

8   Parkin, S.S.P, Phys. Rev. Lett., **64(19)**, 2304 (1990)

9   Parkin. S.S., Phys. Rev. Lett., **67(25)**, 3598 (1991)

10   Crangle, J., Solid State Magnetism, 1991, Edward Arnold, London.

11   Camley, R.E., Phys. Rev. Lett., **63(6)**, 664 (1989)

12   Mathon, J., Contemporary Physics, **32(3)**, 143 (1991)

13   Prinz, G.A., Physics today, Apr. p58 (1995)

14   Parkin, S.S.P., J. Appl. Phys. **69(8)**, 4774 (1991)

15   Tanner, B.K., Submitted to Adv. X-ray Analysis. **40,** (1997)

16   Saffa, M., J. Mag. Mag. Mat. **150(3)**, L290, (1995)

17   Pape, I., J. Mag. Mag. Mat. **156(1-3)**, 373, (1996)

18   Tanner, B.K., Synch. and neutron investigations **12(1)**, 1179, (1996)

19   Laidler, H., J. Mag. Mag. Mat. **154(2)**, 165, (1996)

20   Laidler, H., J. Mag. Mag. Mat. **156**, 332, (1996)

21   Massalski, T.B., Binary Alloy Phase Diagrams. ISBN 08717026(22/30), 1986.

22   Li, H., Surface science, **237**, 141 (1990)

23   Madakson, P., J. Appl. Phys. **68(5)**, 2121 (1990)

24   Chen, Q., Thin solid films, **196**, 103 (1991)

25   Madakson, P., J. Appl. Phys. **70(3)**, 1374 (1991)

26   Shih, D.Y., J. Appl. Phys. **70(6)**, 3052 (1991)

27   Schmid, A.K., Phys. Rev. B. **48(4)**, 2855 (1993)

28   Mankey, G.J., J. Vac. Sci. Technol., A9(3), 1595 (1991)

29   Zhang, H., J. Appl. Phys., 75(10), 6534 (1994)

30   Lin, C.L., J. Appl. Phys., 79(1), 282 (1996)

31   Savage, D.E., J. Appl. Phys., **69(3)**, 1411 (1991)

32   Laidler, H., Private communications (1996)

33   Hase, T.P.A., Work in progress. Durham University. (1997)

34   Sinha, S.K., Phys. Rev. B., **38(4)**, 2297 (1988)

35   Holy, V., Phys. Rev. B., **47(23)**, 15896 (1993)

36   Geer, R.E., Phys. Rev. Lett., **71(9)**, 1391 (1993)

37   Holy. V., Phys. Rev. B., **49(5)**, 10668 (1994)

38   Schlomka, J.P., Phys. Rev. B, **51(4)**, 2311 (1995)

39   Stommer, R, J. Phys. D, **28**, A216 (1995)

40   Lagally, M.G., Phys. Rev. B, **50(19)**, 14435 (1994)

41   Shen, Q., Phys. Rev. Lett., **64(4)**, 451 (1990)

42   Sinha, S.K., Physica B, **198**, 72 (1994)

43   Zabel, H., Appl. Phys. Lett. **43(1)**, 59 (1983)

44   De Bohr, D.K.G., X-ray Spec. **24**, 91 (1995)

45   Hect, E., Optics, B. Spatz, Editor.1987, Addison-Wesley : Wokingham

46   Barabasi, A.L., Fractal concepts is surface growth, Cambridge University Press, 1995.

47   Lagally, M.G., Physics today, Nov., (1993)

48   Hilger, A., 'Growth and characterisation of semiconductors' (1991)

49   Das Sarma, S., Phys. Rev. Lett., **66(18)**, 2348 (1991)

50   Palasantzas, Y.P., Phys. Rev. B, **49(7)**, 4902 (1994)

51   Lengeler, B., Phys. Rev. B, **46(12)**, 7953 (1992)

52   Whitehouse, J.L., Appl. Phys. Lett. **59(25)**, 3282 (1991)

53   Cotta, R.A., Phys. Rev. Lett. **70(26)**, 4106 (1993)

54   Sinha, S.K., Physica B, **198**, 72 (1994)

55   De Bohr, D.K.G., J. Phys. D, **27**, A227 (1995)

56   Sinha, S.K., ACTA Physica Polonica, 89(2), 219 (1996)

57   Holy, V., X TOP'96, Palermo, Italy. (1996)

58   Holy, V., Private communications (1996)

59   Wormington, M., Private communications (1996)

60   Ryan, P., Private communications (1996)